

Advances in Civil Engineering

Advancements in Design and Analysis of Protective Structures

Lead Guest Editor: Chiara Bedon

Guest Editors: Michel Arrigoni, Filipe Santos, and Lucia Figuli





Advancements in Design and Analysis of Protective Structures

Advances in Civil Engineering

Advancements in Design and Analysis of Protective Structures

Lead Guest Editor: Chiara Bedon

Guest Editors: Michel Arrigoni, Filipe Santos, and Lucia Figuli



Copyright © 2018 Hindawi. All rights reserved.

This is a special issue published in “Advances in Civil Engineering.” All articles are open access articles distributed under the Creative Commons Attribution License, which permits unrestricted use, distribution, and reproduction in any medium, provided the original work is properly cited.

Editorial Board

- Maria Cruz Alonso, Spain
Serji N. Amirkhanian, USA
P. Ch. Anastasopoulos, USA
Venu G. M. Annamdas, Singapore
Pedro Arias-Sánchez, Spain
Farhad Aslani, Australia
Chiara Bedon, Italy
Rafik Belarbi, France
Hugo C. Biscaia, Portugal
Melina Bosco, Italy
Alberto Campisano, Italy
Francesco Canestrari, Italy
D. Castro Castro-Fresno, Spain
Robert Černý, Czech Republic
Constantin Chalioris, Greece
Noel Challamel, France
Daniel W.M. Chan, Hong Kong
Edwin H W Chan, Hong Kong
Carlos Chastre, Portugal
Ghassan Chehab, Lebanon
Francesco Colangelo, Italy
Ottavia Corbi, Italy
Mario D'Aniello, Italy
Jorge de Brito, Portugal
Gianmarco de Felice, Italy
Angelo Di Egidio, Italy
- Luigi Di Sarno, Italy
Ahmed Elghazouli, UK
Flora Faleschini, Italy
Giovanni Garcea, Italy
Agathoklis Giaralis, UK
Kirk Hatfield, USA
Khandaker Hossain, Canada
Dong-Sheng Jeng, Australia
Thibaut Lecompte, France
Eul-Bum Lee, Republic of Korea
Dongsheng Li, China
Li Li, Canada
Sui Pheng Low, Singapore
Lyan-Ywan Lu, Taiwan
Eric Lui, USA
Lorenzo Macorini, UK
Yann Malecot, France
John Mander, USA
Giuseppe Carlo Marano, Italy
Fabio Mazza, Italy
Ahmed Mebarki, France
Hossein Moayedi, Iran
Fabrizio Mollaioli, Italy
Ayman S. Mosallam, USA
Giuseppe Oliveto, Italy
Alejandro Orfila, Spain
- Togay Ozbakkaloglu, Australia
Alessandro Palmeri, UK
Fabrizio Paolacci, Italy
Arnaud Perrot, France
Christophe Petit, France
Giuseppe Piccardo, Italy
Prodromos Psarropoulos, Greece
Damien Rangedard, France
Dimitris Rizos, USA
Geoffrey W. Rodgers, New Zealand
Hamid Reza Ronagh, Australia
Pier Paolo Rossi, Italy
Anna Saetta, Italy
Evangelos J. Sapountzakis, Greece
Halil Sezen, USA
Sanjay Kumar Shukla, Australia
Stefano Sorace, Italy
Flavio Stochino, Italy
Claudio Tamagnini, Italy
Yaya Tan, China
Yinshan Tang, UK
Cumaraswamy Vipulanandan, USA
Wei-Chau Xie, Canada
Michael Yam, Hong Kong
Victor Yepes, Spain
Mariano Angelo Zanini, Italy

Contents

Advancements in Design and Analysis of Protective Structures

Chiara Bedon , Michel Arrigoni, Filipe Santos , and Lucia Figuli
Editorial (3 pages), Article ID 7024982, Volume 2018 (2018)

Ductility Calculation of Prefabricated Shear Wall with Rabbet-Unbond Horizontal Connection

Chongfang Sun , Shuting Liang , Xiaojun Zhu, Yamin Song, and Dongyue Wu 
Research Article (12 pages), Article ID 5197125, Volume 2018 (2018)

Novel Crashworthy Device for Pier Protection from Barge Impact

W. Wang  and G. Morgenthal
Research Article (15 pages), Article ID 9385643, Volume 2018 (2018)

Dynamic Response of Steel Box Girder under Internal Blast Loading

Shujian Yao , Nan Zhao, Zhigang Jiang, Duo Zhang, and Fangyun Lu
Research Article (12 pages), Article ID 9676298, Volume 2018 (2018)

Seismic Response Analysis of Fully Base-Isolated Adjacent Buildings with Segregated Foundations

Khaled Ghaedi , Zainah Ibrahim , Mohammed Jameel , Ahad Javanmardi, and Hamed Khatibi 
Research Article (21 pages), Article ID 4517940, Volume 2018 (2018)

A Designer's Approach for Estimation of Nuclear-Air-Blast-Induced Ground Motion

Shashank Pathak  and G. V. Ramana
Research Article (12 pages), Article ID 3029837, Volume 2018 (2018)

Temperature Effect on Lime Powder-Added Geopolymer Concrete

Sandeep L. Hake , R. M. Damgir, and S. V. Patankar
Research Article (5 pages), Article ID 6519754, Volume 2018 (2018)

Uniaxial Compressive Test of High Ductile Fiber-Reinforced Concrete and Damage Constitutive Model

Mingke Deng , Jiaojiao Pan , and Xingwen Liang
Research Article (12 pages), Article ID 4308084, Volume 2018 (2018)

Protective and Blast Resistive Design of Posttensioned Box Girders Using Computational Geometry

Majid Aleyaasin 
Research Article (7 pages), Article ID 4932987, Volume 2018 (2018)

Strengthening of RCC Beams in Shear by Using SBR Polymer-Modified Ferrocement Jacketing Technique

Rajinder Ghai , Prem Pal Bansal, and Maneek Kumar 
Research Article (16 pages), Article ID 4028186, Volume 2018 (2018)

Access Control Points: Reducing a Possible Blast Impact by Meandering

Martin Larcher , Georgios Valsamos, and Vasilis Karlos
Research Article (11 pages), Article ID 3506892, Volume 2018 (2018)

Impact Force Evaluation of the Derailment Containment Wall for High-Speed Train through a Collision Simulation

Hyun-Ung Bae , Kyung-Min Yun , Jiho Moon , and Nam-Hyoung Lim 

Research Article (14 pages), Article ID 2626905, Volume 2018 (2018)

Structural Glass Systems under Fire: Overview of Design Issues, Experimental Research, and Developments

Chiara Bedon

Review Article (18 pages), Article ID 2120570, Volume 2017 (2018)

Study of Split-Flow Wall Located at Exit

Guomin Zhao, Min Li, Yunfeng Zhao, Qingsong Zhng, and Zhongxian Liu

Research Article (7 pages), Article ID 1374183, Volume 2017 (2018)

Editorial

Advancements in Design and Analysis of Protective Structures

Chiara Bedon ¹, Michel Arrigoni,² Filipe Santos ³ and Lucia Figuli⁴

¹University of Trieste, Trieste, Italy

²ENSTA Bretagne, Brest, France

³New University Lisbon, Lisbon, Portugal

⁴University of Žilina, Žilina, Slovakia

Correspondence should be addressed to Chiara Bedon; bedon@dicar.units.it

Received 4 February 2018; Accepted 6 February 2018; Published 17 April 2018

Copyright © 2018 Chiara Bedon et al. This is an open access article distributed under the Creative Commons Attribution License, which permits unrestricted use, distribution, and reproduction in any medium, provided the original work is properly cited.

The objective of this ADAP Special Issue volume is to provide an overview on the current trends and recent advancements in terms of design and analysis, including experiments and modelling, on protective structures.

From a structural point of view, such a definition includes multiple loading and boundary conditions that designers should be properly accounted when ensuring appropriate safety levels to people. In fact, protective structures and facilities are expected to optimally perform their function under severe loads, even when associated with mostly different threats. Extreme events like earthquakes, fire accidents, explosions (even nuclear), and high-rise natural hazards are the first reason of severe damages in constructed facilities and causalities. Impacts due to collisions of transportation means, on the other hand, should be also properly accounted when designing bridges or containment structures in general. A key role, in all the mentioned cases, is given to design optimization and mitigation of input forces/effects. Such a result can be achieved by both reducing the magnitude of applied loads on structures, that is, via active, passive, and semiactive additional devices, and by enhancing the structural resistance and capacity, that is, via efficient materials and structural components.

Within a more general definition of protection and protective tools to improve security, different means are indeed accepted, being possible to achieve the final protective goal at the emergency management level rather than at the material/structural level only, hence suggesting a co-operation of multiple aspects and expertise.

In doing so, finite element (FE) and computational fluid dynamics (CFD) numerical simulations, as well as full-scale

experiments and analytical models, can represent valid tools for the analysis of emergency and hazard conditions.

The revised papers included in the final ADAP Special Issue booklet are related to various topics, including studies at the management, material, and assembly levels, under a multitude of loads.

In the paper from Larcher et al., security enhancements against terroristic attacks or explosive events in general are suggested for vulnerable areas via the use of protective wall systems. Such a strategy concept, numerically investigated by the authors by taking into account internal blast scenarios and access control points, relies on the prevention of blast wave propagation within a given building. The efficiency of rigid (meandering) walls is explored by taking into account a case study building system, giving evidence of their active contribution as effective risk-reduction measure.

As a preliminary requisite, protection of people in buildings under emergency scenarios should in fact generally account for appropriate evacuation plans and strategies. Congestion, as highlighted by Zhao et al., actually represents the major cause of crowd trample and crushing incidents. Shunt walls, in this sense, can also enhance the safety levels for pedestrians and occupants but should be properly designed via evacuation simulations, especially to account of large crowds.

Containment walls can be efficient within buildings but also for the minimization of transportation accidents, as in the case of trains, being typically associated to tragic scenarios when derailment and collision incidents occur. To this aim, refined 3D simulations are presented by Bae et al., to explore the impact configurations due to high-speed train

derailments, including various loading configurations. Possible recommendations to take into account in the design of containment walls or blocks are also provided, based on parametric studies.

Within the variety of “extreme” hazards that buildings and infrastructures should properly withstand, major threats often derive from explosions and high-strain impacts.

Bridges and tunnels can be potential targets of terroristic attacks since their collapse or severe damage is often associated with possible causalities, economic disaster, and panic scenarios. In this regard, protection of bridges to blast loads has attracted the interest of a large number of research studies, during the last years. In the paper by Yao et al., the dynamic performance of steel box girders is numerically investigated under the effects of internal explosions, by taking into account several scenarios. Through the parametric study, evidence is given to the typical local failure phenomena leading the box girders to collapse, including design suggestions to enhance their blast-resistance capability.

Optimal tendon profiles are suggested by Aleyaasin for posttensioned steel box girders, to optimize their structural performance and resistance, aiming to properly withstand accidental blast loads due to car bombs. A design method is also proposed and validated via a case study example.

Protection of bridges can also be required against different sources of hazards and accidents, as reported in the paper by Wang and Morgenthal, where the pier performance under barge impacts is investigated. A novel crash-worthy device, being representative of a sacrificial steel structure to mitigate high-rise impact effects on piers, is assessed and optimized, including a worked example. Major benefits of such a crash absorber derive from its large energy-dissipation capacity during impact, hence minimizing the forces that the piers should actually withstand.

In the paper by Ghaedi et al., the seismic performance of adjacent, base-isolated buildings with segregated foundations is explored via nonlinear time history analyses. Numerical simulations are reported to give evidence of the actual seismic performance of adjacent buildings with base isolation, with respect to fix-base solutions, as well as to emphasize the potential and benefits of base isolation, as a function of different separation gaps and input features.

The analysis of structures under extreme loads requires an accurate definition of loading scenarios. In this regard, Pathak and Ramana report on a closed-form expression for the estimation of nuclear air-blast-induced free-field ground displacements, by accounting for several key input parameters. The analytical model is validated against available nuclear test data, giving evidence of the potential of the mathematical formulations and including possible recommendations for design calculations.

Especially under extreme events, connections and details can have a key role for the global performance of a given system. This is the case, for example, of buildings under seismic loads (where governed damage and failure mechanisms should be preferred), and especially for prefabricated structures, where the structural interaction between the independent members can be crucial.

Sun et al., in this regard, explore a rabbit-unbond horizontal connection (RHC) for new reinforced concrete, prefabricated shear walls. Full-scale tests are reported, including discussion on the structural performance of the walls and damage propagation. Compared to conventional connection systems in use for the prefabricated systems under investigation, the presented RHC solution takes advantage of unbonded reinforcement to enhance the ductility capacity and energy dissipation of the so assembled structure. Even in presence of a limited number of test results, major effects and benefits are observed on the ultimate displacement of RHC specimens, with variations on the expected ductility ratio, hence suggesting further extended investigations.

The use of innovative materials and their optimal combination can have important effects for structural performance optimization approaches, both for the retrofitting of existing assemblies as well as for the design of novel constructions. In the first case, experimental studies are proposed in the paper by Ghai et al., where the authors report on the structural efficiency of polymer-modified ferrocement (PMF) jacketing technique for reinforced concrete beams in shear, by using styrene-butadiene-rubber (SBR) latex polymer. Even in presence of shear failure mechanisms in RCC beams typically associated with a combination of multiple aspects (such as load pattern, shear-to-span ratio, beam section, concrete strength, reinforcement type, and amount), Ghai et al. show that the PMF jacketing technique can improve the deformation, crack pattern, and ultimate shear load carrying capacity of initially damaged beams, hence representing a valid strengthening solution.

Deng et al. present uniaxial compressive tests on high ductile fiber-reinforced concrete (HDFRC), including the proposal of a damage constitutive model. Comparative results show the accuracy of their HDFRC damage evolution model, as well as the key role of fibers at the cracking stage.

Hake et al. investigate the temperature effects on lime powder-added geopolymer concrete. Different lime powder amounts are taken into account, giving evidence of the actual compressive resistance of concrete specimens as a function of different temperature scenarios.

Thermal loads in general can have crucial effects on most of the materials in use for buildings and infrastructures, hence requiring careful consideration to ensure appropriate safety levels. This is especially the case of structural systems under fire loading, where multiple aspects should be accounted at the design stage. In this regard, a state-of-the-art review is finally by Bedon, to assess the mechanical performance of structural glass systems and assemblies in fire conditions. Key aspects for their analysis and behavioral assessment are reported from the literature, giving evidence of material sensitivity to high temperatures, as well as presenting a summary of existing research studies at the small/full-scale levels, and including some general considerations on current design issues.

In conclusion, let us have some final considerations on this ADAP Special Issue project.

First of all, all the contributing authors are gratefully acknowledged for their support. The hope is that the readers

could find fruitful and high-quality research topics in the published papers.

Peer reviewers are also gratefully acknowledged for their hard work, ensuring the publication in this volume of high-quality scholarly journals. A final acknowledgement is also extended by the Lead Guest Editor to the full team of Guest Editors, for the support provided in the last months through the full process of submission and promotion of the call for papers, up to the publication of the ADAP Special Issue booklet in *Advances in Civil Engineering*.

Chiara Bedon
Michel Arrigoni
Filipe Santos
Lucia Figuli

Research Article

Ductility Calculation of Prefabricated Shear Wall with Rabbet-Unbond Horizontal Connection

Chongfang Sun ^{1,2}, Shuting Liang ², Xiaojun Zhu,³ Yamin Song,² and Dongyue Wu ⁴

¹Jinan Rail Transit Group Co. Ltd., Jinan, Shandong 250101, China

²School of Civil Engineering, Southeast University, Nanjing 210018, China

³Architectural Design and Research Institute Ltd., Southeast University, Nanjing 210018, China

⁴School of Civil Engineering and Architecture, Jiangsu University of Science and Technology, Zhenjiang 212000, China

Correspondence should be addressed to Shuting Liang; stliang@seu.edu.cn

Received 17 August 2017; Accepted 31 October 2017; Published 3 April 2018

Academic Editor: Chiara Bedon

Copyright © 2018 Chongfang Sun et al. This is an open access article distributed under the Creative Commons Attribution License, which permits unrestricted use, distribution, and reproduction in any medium, provided the original work is properly cited.

Considering the effect of confined end-zone and unbonded reinforcement, the yield curvature and ultimate curvature of rabbet-unbond horizontal connection (RHC) shear wall were calculated. Based on the curvature calculation result, the yield displacement and ultimate displacement were calculated using displacement superposition, which were compared with test values. The result showed that theoretical values were slightly smaller than test values; however, on the whole, both were in good agreement. The author studied the effect of unbonded reinforcement on yield displacement and ultimate displacement, and the result showed that the effect on ultimate displacement is more pronounced than yield displacement. The present work could be useful for the design of new prefabricated shear wall.

1. Introduction

In recent years, due to high industrialized level, good quality, convenient installation, energy conservation, and environment protection, the precast concrete structure is widely used. In particular, the prefabricated shear wall structure with large rigidity and great bearing capacity is the first choice for high-rise housings. In this regard, China has made policies to promote the development of the prefabricated shear wall structure [1], and many institutes and universities have carried out the relevant research [2, 3]; meanwhile, they cooperate with the national housing industrialization bases [4, 5] and applies the structure in some estate development projects as demonstration [6, 7]. What is more, the implementing subjects continue rise, for example, the prefabricated concrete shear wall structure system of Zhongnan Group [8]. For the prefabricated shear wall structure, the horizontal connection in the structure is the key to ensure structural integrity and seismic performance [9], and for this purpose, the authors invent a new horizontal connection [10] whose bearing

capacity has been studied; however, the ductility which unbonded reinforcement can improve has not been studied.

To date, addressing the ductility calculation of different shear wall structures, many engineers or scholars have made contributions. For the conventional cast-in-situ shear wall, Si et al. [11] proposed displacement ductility calculation method considering the effect of axial compression ratio, shear span ratio, confined end-zone, and stirrup eigenvalue. Park et al. [12] deduced the crack curvature, yield curvature, peak curvature, and ultimate curvature of flexure-dominated shear wall with concentrated end-zone reinforcements and uniformly web reinforcements along the cross section. For high-performance concrete shear wall, Liang et al. [13] deduced the crack-bending moment and curvature, yield-bending moment and curvature, peak-bending moment and curvature, and ultimate-bending moment and curvature. For prefabricated shear wall, Chen [14] deduced the formula of crack-bending moment and curvature, yield-bending moment and curvature, peak-bending moment and curvature, and ultimate-bending moment and curvature.

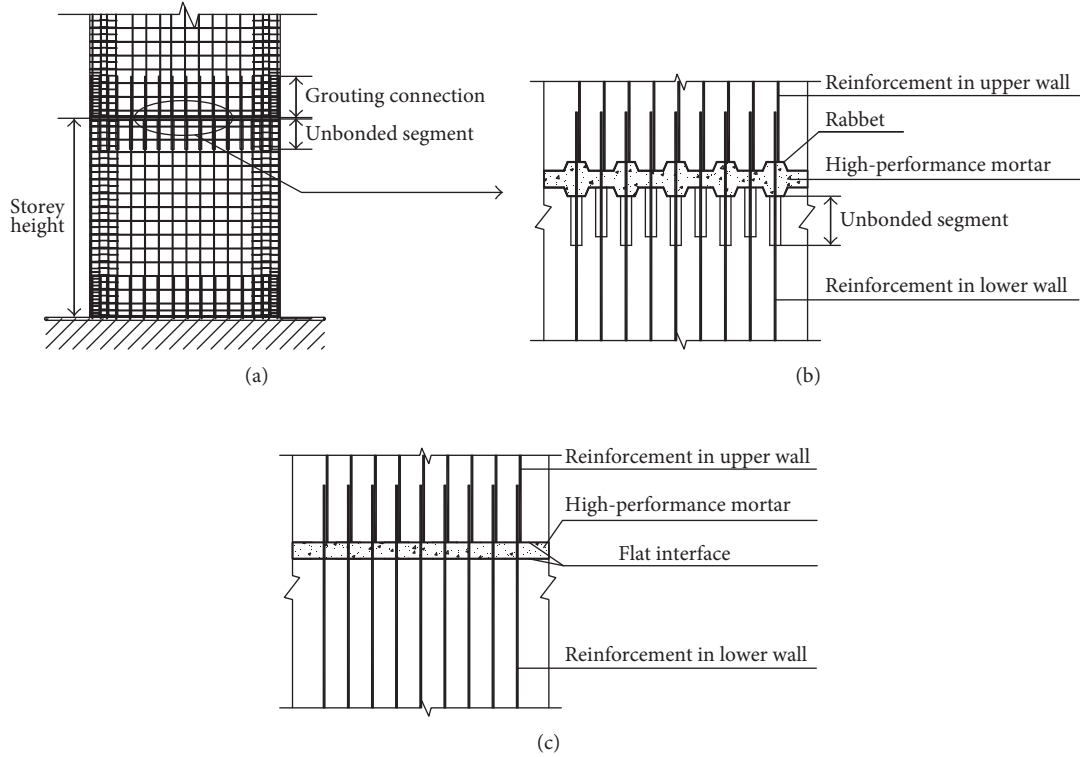


FIGURE 1: (a) Prefabricated shear wall, (b) the RHC details, and (c) conventional connection details. Note: For the sake of clarity, the lateral web reinforcements in the upper and lower walls are not shown in (b) and (c).

Therefore, here, firstly, for the newly horizontal connection, considering the effect of confined end-zone and unbonded reinforcement, yield curvature and ultimate curvature are calculated, which prepares for displacement calculation. And then, yield displacement and ultimate displacement are calculated using displacement superposition, which is verified by the test values. Finally, the effects of unbonded reinforcement on yield displacement and ultimate displacement are studied.

2. Rabbit-Unbond Horizontal Connection

The arrangement of the rabbit-unbond horizontal connection (RHC) is shown in Figures 1(a) and 1(b). The reinforcements reserved in the lower wall are connected with those in the upper wall by a well-developed grouting-connection technology. The two walls are integrated by filling high-performance mortar into the space between a pair of trapezoidal rabbets. Compared with the conventional connection (Figure 1(c)), a segment reinforcement of RHC in the lower wall is left unbonded to increase the ductility and energy dissipation of the assembled structure, and the trapezoidal rabbets are used to enhance the connection's shear capacity.

3. Curvature Calculation of RHC Shear Wall

This section calculates yield curvature and ultimate curvature considering effect of confined end-zone and unbonded reinforcement, meanwhile, which prepares for calculation of yield displacement and ultimate displacement in Section 4.

3.1. Deformation Coordination Equation

3.1.1. Strain Lag of Unbonded Reinforcement. According to test phenomenon of literature [15], compared with the bonded specimen, unbonded specimen's crack width and length are greater under the same loading, which states that the unbonded cross section's neutral axis is closer to compressed zone, as shown in Figure 2. Assuming that bending moments M of the two sections in Figure 2 are equal and the tensile reinforcements do not yield, we can get $A_s E_s \varepsilon_{s1} Z_1 = A_s E_s \varepsilon_{s2} Z_2 = M$, where A_s and E_s are the cross section's area and Young's modulus of the tensile reinforcement, respectively, $\varepsilon_{s1}, \varepsilon_{s2}$ are the tensile reinforcement strains in the bonded cross section and the unbonded cross section, respectively, Z_1 and Z_2 are the lever of the bonded cross section and the unbonded cross section, respectively, the subscripts 1 and 2 denote the bonded and unbonded. Apparently, under a constant moment M , $Z_2 > Z_1$ leads to $\varepsilon_{s2} < \varepsilon_{s1}$, and this is called "strain lag."

Regarding the "strain lag," the unbonded cross section's average strain distribution is no longer linear but bilinear (Figure 3).

3.1.2. Deformation Coordination Region. For the bonded shear wall, the ductility' calculation is based on the plane section assumption and the deformation coordination assumption between reinforcement and concrete. Because the maximum moment locates at the bottom of the shear wall, the plane section assumption regards a rectangular region at the bottom as the basic deformation coordination

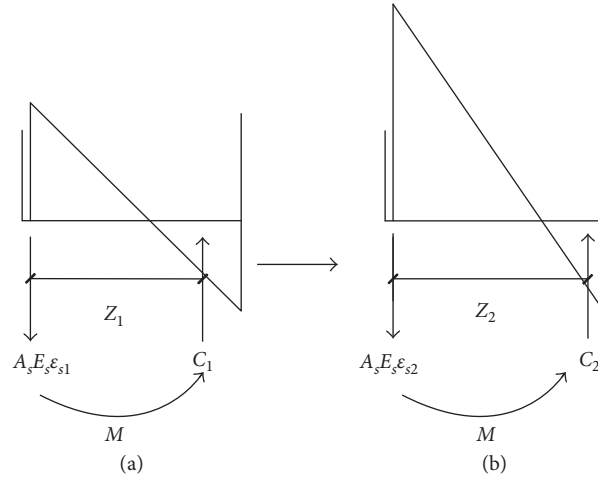


FIGURE 2: Force in (a) bonded cross section and (b) unbonded cross section. Note: C_1 and C_2 represent the resultant force of compressive concrete, respectively.

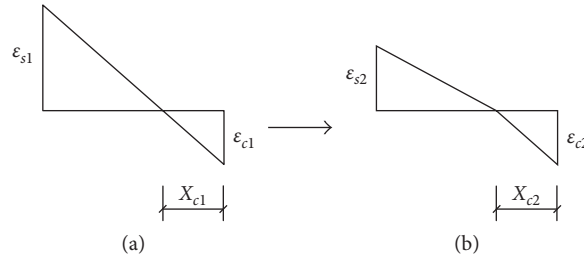


FIGURE 3: Average strain distributions in (a) bonded cross section and (b) unbonded cross section.

region (Figure 4(a)), and the deformation coordination equation is

$$\frac{x_{c1}}{h_0 - x_{c1}} = \frac{\epsilon_{c1} l_{c1}}{\epsilon_{s1} l_{s1}}, \quad (1)$$

where x_{c1} is the height of the compressed zone in the cross section of the bonded shear wall (Figure 3(a)). h_0 is the effective height of the cross section. ϵ_{c1} and ϵ_{s1} are the edge strain of the compressed concrete and the strain of the tensile reinforcement in the cross section of the bonded shear wall, respectively (Figure 3(a)). l_{c1} and l_{s1} are the heights of the compressed zone and the tensile zone of the deformation coordination region of the bonded shear wall, respectively (see Figure 4(a)). Because $l_{c1} = l_{s1}$, the deformation coordination (1) is reexpressed as

$$\frac{x_{c1}}{h_0 - x_{c1}} = \frac{\epsilon_{c1}}{\epsilon_{s1}}. \quad (2)$$

For the unbonded shear wall, we assume that in the compressed zone of the wall, the deformation of the unbonded reinforcement is consistent with the concrete deformation, but in the tensile zone of the wall, the deformation of the unbonded reinforcement is not consistent with the concrete deformation. In this regard, the traditional plane section assumption is no longer applicable, and the shape of the deformation coordination region is changed from the rectangular to the trapezoidal (Figure 4(b));

however, the strain of the tensile reinforcement in the trapezoidal is uniformly distributed.

3.1.3. Deformation Coordination Equation. For the sake of convenience, regard the concrete edge compressive strain of the maximum bending moment cross section as the calculated value, correspondingly, the equivalent compressive height of l_{c2} [16] is denoted as l_e . It is worth mentioned that the traditional plane section assumption is still applicable beyond trapezoidal deformation region, and the boundary condition of the region is linear. Thus, assuming that the deformation of the trapezoidal region also obeys the linear distribution along the cross section height, we can get the deformation coordination equation:

$$\frac{x_{c2}}{h_0 - x_{c2}} = \frac{\epsilon_{c2} l_e}{\epsilon_{s2} l_{s2}}, \quad (3)$$

where x_{c2} is the height of the compressed zone in the cross section of the unbonded shear wall (Figure 3(b)), ϵ_{c2} and ϵ_{s2} are the edge strain of the compressed concrete and the strain of the tensile reinforcement in the cross section of the unbonded shear wall, respectively (Figure 3(b)), l_{s2} is the height of the tensile zone of the deformation coordination region of the unbonded shear wall, and it equals the unbonded length, and l_e is the equivalent compressive height of the unbonded shear wall, derived from the loading tests of partial unbonded reinforced

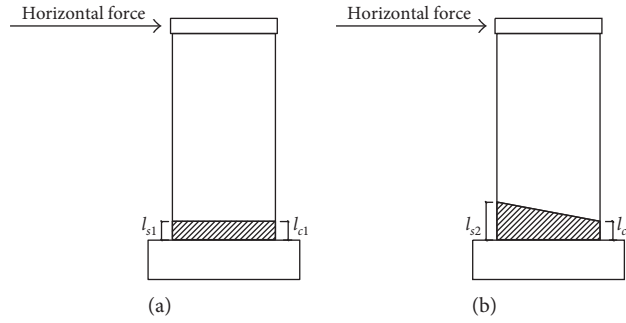


FIGURE 4: Deformation coordination region of (a) bonded shear wall and (b) unbonded shear wall.

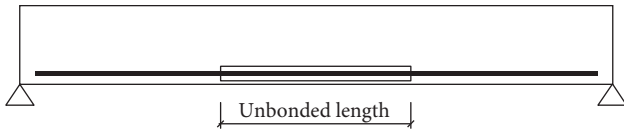


FIGURE 5: Partial unbonded reinforced concrete beam.

concrete beams with pure bending regions [16], as shown in Figure 5.

The formula of l_e is obtained in the following method: In tests of partial unbonded reinforced concrete beam, strain values of the top concrete under each level load are recorded, and the total deformation Δl_c of top concrete corresponding to unbonded length can be calculated. The average strain value of the top concrete under the same level load within pure bending region is expressed as ϵ_c . Divide Δl_c by ϵ_c , and we can get the equivalent compressive height. Take the average value of equivalent compressive heights under all level loads as the final equivalent compressive height. By fitting, the equivalent compressive height formula is expressed as

$$l_e = \begin{cases} 0.74l_{s2}, & 90 \text{ mm} < l_{s2} < 900 \text{ mm} \\ 32.81 + 0.09l_{s2}, & 900 \text{ mm} < l_{s2} < 1575 \text{ mm}. \end{cases} \quad (4)$$

Since the shear wall can be regarded as the cantilever beam, the author employs l_e to calculate the ductility of RHC shear wall. Here, ignore the effect of axial force acting on the shear wall.

3.2. Assumption. The assumptions to calculate the ductility of RHC shear wall are stated as follows:

- (1) The concrete is based on the plane section assumption and its tensile strength is not considered.
- (2) The compressed stress-strain curve of concrete and stress calculation of the vertical reinforcement refer to China code "Code for the design of concrete structures (GB 50010-2010, 2010)." The ultimate tensile strain of the vertical reinforcement is 0.01.
- (3) In compressed zone, the unbonded reinforcement deformation is coordinated with the concrete deformation.
- (4) The deformation coordination region in the unbonded segment is from rectangular to trapezoidal. The tensile reinforcement strain in the trapezoidal region is uniformly distributed. Deformation in the trapezoidal region obeys linear distribution.

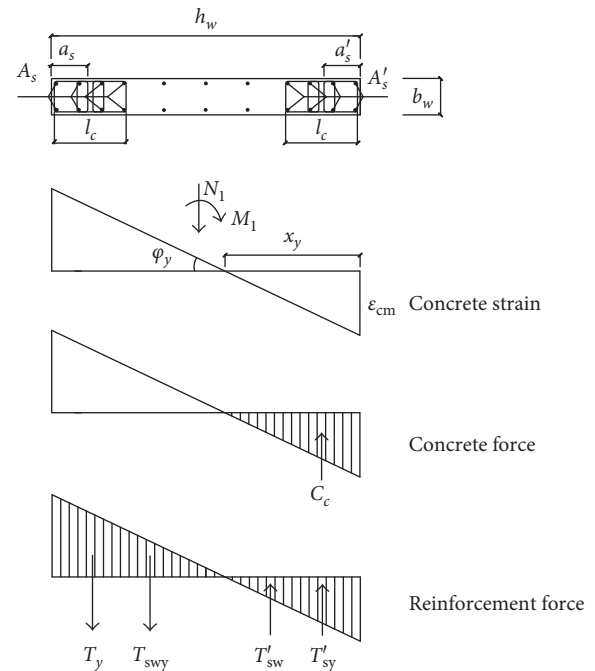


FIGURE 6: Stress and strain distribution profile in the yield state.

3.3. Yield Curvature. In the yield state, the lateral deformation of compressive concrete is small, so stirrup stress is small, and stirrup restraint in the confined end-zone is not considered. The stress-strain relationship of concrete adopts unconfined stress-strain relationship. Assume that when bonded reinforcement segments in confined end-zone yield, the shear wall yields. Stress of the compressive concrete is assumed to be the linear triangle distribution. Deformation of reinforcement and concrete in compressive zone is assumed to be consistent. Stress and strain distribution in the yield state is shown in Figure 6.

According to the force equilibrium, the following equation can be obtained as follows:

$$N_1 + T_y + T_{swy} = C_c + T'_{sw} + T'_{sy}, \quad (5)$$

where N_1 is the axial force acting on the shear wall's cross section in the yield state. T_y is the yield force of vertical reinforcement in the tensile zone which can be defined as $T_s = f_y A_s$, where f_y is the yield stress of tensile reinforcement. T_{swy} is the tensile force of web reinforcements in the

tensile zone which can be defined as $T_{swy} = \rho_w b_w (h_{w0} - x_y) f_{yw} / 2$, where ρ_w is the reinforcement ratio of web reinforcement; b_w is the cross section width; h_{w0} is the effective height of the cross section; x_y is the depth of compressive zone; and f_{yw} is the yield stress of web reinforcement. C_c is the compressive force of concrete in the compressive zone which can be defined as $C_c = b_w E_c x_y^2 \varphi_y / 2$, where E_c is the elastic modulus of concrete. T'_{sw} is the compressive force of web reinforcements in the compressive zone which can be defined as $T'_{sw} = \rho_w b_w (x_y - a'_s)^2 E_s \varphi_y / 2$, where a'_s is the distance of compressed reinforcement resultant force to compressed edge. T'_{sy} is the compressive force of vertical reinforcement in compressive constraint zone which here can be defined as $T'_{sy} = E_s (x_y - a'_s) \varphi_y A'_s$, where A'_s is the compressed reinforcement cross section area.

According to assumption (1), the deformation co-ordination equation is

$$\frac{x_y}{h_{w0} - x_y} = \frac{\varepsilon_{cm} l_e}{\varepsilon_y l_{s2}} \quad (6)$$

where ε_{cm} is the concrete compressive strain and ε_y is the yield strain of reinforcement.

Solve above equations and $\varphi_y = \varepsilon_{cm} / x_y$ can be calculated according to the concrete strain profile in Figure 6.

3.4. Ultimate Curvature. In the ultimate state, the lateral deformation of compressive concrete is great, so stirrup restraint in confined end-zone should be considered. The stress-strain relationship of concrete adopts the confined stress-strain relationship. Assume that when the compressive concrete strain in confined, end-zone reaches ultimate compressive strain and shear wall reaches the ultimate state. Deformation of reinforcement and concrete in compressive zone is assumed to be consistent. What is more, compressive reinforcements are assumed to yield. The compression effect of unconfined concrete is not considered. Stress and strain distribution in ultimate state is shown in Figure 7.

According to the force equilibrium, the following equation can be obtained:

$$N_2 + T_s + T_{swu} = C_{cc} + C_{uc} + T'_{su} \quad (7)$$

where N_2 is the axial force acting on the shear wall's cross section in the ultimate state. T_s is the tensile force of vertical reinforcement in the tensile constraint zone which can be defined as $T_s = \sigma_s A_s$, where σ_s is the tensile stress of vertical reinforcements in the constraint zone which can be defined as $\sigma_s = E_s \varepsilon_{ccu} l_e / l_{s2} (h_{w0} \beta / x - 1)$ from (6), where ε_{ccu} is the ultimate compressive strain of confined concrete; β is the coefficient corresponding to the rectangular stress block, refer to China code "Code for design of concrete structures (GB 50010-2010, 2010)"; x is the depth of the compressive zone in rectangular stress block which can be defined as $x = x_u \beta_1$. T_{swu} is the tensile force of web reinforcements in the tensile zone which can be defined as $T_{swu} = f_{yw} b_w \rho_w (h_{w0} - 1.5x)$. C_{cc} is the compressive force of confined concrete. C_{uc} is the compressive force of unconfined concrete. C_{cc} and C_{uc} have different formulas for different eccentric compression states. T'_{su} is the compressive force of vertical reinforcement in the

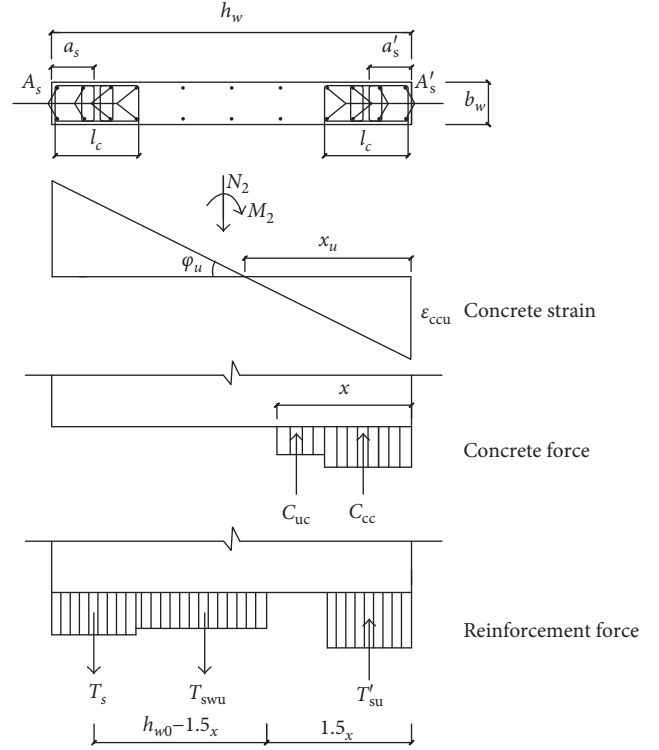


FIGURE 7: Stress and strain distribution profile in the ultimate state.

compressive constraint zone which here can be defined as $T'_{su} = \sigma'_s A'_s$, where σ'_s is the compressive stress of vertical reinforcements.

The constitutive law of confined concrete referring to literature [17] is as follows:

$$\begin{aligned} \varepsilon_{cc} &= (1 + 3.5\lambda_v)\varepsilon_{c0}, \\ \varepsilon_{ccu} &= (2.34 + 2.49\lambda_v^{0.73})\varepsilon_{cc}, \\ f_{cc} &= (1 + 1.79\lambda_v)f_c, \end{aligned} \quad (8)$$

where ε_{cc} is the peak compressive strain of confined concrete, λ_v is the stirrup eigenvalue, ε_{c0} is the peak compressive strain of unconfined concrete and it is set as 0.0018, f_{cc} is the axial compressive strength of confined concrete, and f_c is the axial compressive strength of unconfined concrete.

According to assumption (1), the deformation co-ordination equation is

$$\frac{x_u}{h_{w0} - x_u} = \frac{\varepsilon_{ccu} l_e}{\varepsilon_s l_{s2}} \quad (9)$$

From (7) and (9), x can be calculated. Different x leads to different eccentric compression states and different ultimate curvatures; then, the explanations are as follows:

- (1) When $x \leq x_b$, the wall is in large eccentric compression, $T_s = T'_s = f_y A_s$, where x_b is the boundary depth of the compressive zone. This situation consists of two states: $x_b > x > l_c$ and $x \leq l_c$.
 - (a) When $x_b > x > l_c$, $N_2 = C_{cc} + C_{uc} - T_{sw}$, where $C_{cc} = \alpha f_{cc} b_w l_c$, α is the coefficient corresponding

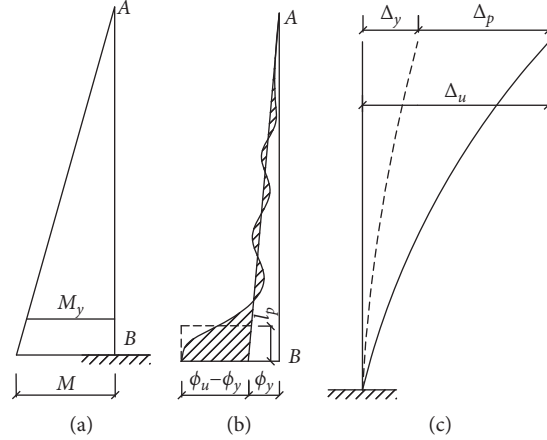


FIGURE 8: (a) Bending moment, (b) curvature, and (c) lateral displacement of cantilever shear wall.

to constraint zone length and it is set as 0.8 and l_c is the confinement depth. $C_{uc} = f_c b_w (x - l_c)$.

(b) When $x \leq l_c$, $N_2 = C_{cc} - T_{sw}$, where $C_{uc} = 0$, $C_{cc} = \alpha f_{cc} b_w x$.

(2) When $x > x_b$, the wall is in small eccentric compression, $N_2 = C_{cc} + C_{uc} + T'_s - T_s$, where here $T'_s = f'_y A'_s$. This situation consists of two states: $x > l_c$ and $x_b < x \leq l_c$.

(a) When $x > l_c$, $C_{cc} = \alpha f_{cc} b_w l_c$, $C_{uc} = f_c b_w (x - l_c)$, the equation about x can be obtained as:

$$f_c b_w x^2 + \left(\alpha f_{cc} b_w l_c - f_c b_w l_c + f'_y A'_s + A_s E_s \varepsilon_{ccu} \frac{l_e}{l_{s2}} - N_2 \right) \cdot x - A_s E_s \varepsilon_{ccu} h_{w0} \beta_1 \frac{l_e}{l_{s2}} = 0. \quad (10)$$

When $x_b < x \leq l_c$, $N_2 = C_{cc} + T'_s - T_s$, where $C_{uc} = 0$, $C_{cc} = \alpha f_{cc} b_w x$, the equation about x can be obtained as

$$\alpha f_{cc} b_w x^2 + \left(f'_y A'_s + A_s E_s \varepsilon_{ccu} \frac{l_e}{l_{s2}} - N_2 \right) \cdot x - A_s E_s \varepsilon_{ccu} h_{w0} \beta_1 \frac{l_e}{l_{s2}} = 0. \quad (11)$$

Solve the above equations, and finally we can obtain the ultimate curvature $\varphi_u = \varepsilon_{ccu} / x_u$.

4. Calculation of Displacement Ductility

The displacement ductility $\mu\Delta$ is defined as $\mu\Delta = \Delta_u / \Delta_y$, where Δ_u is the ultimate displacement and Δ_y is the yield displacement.

Assume that wall's displacement consists of two parts approximately: one part is the displacement that the wall generates resisting external force when all reinforcements are bonded, and assume the wall is not a rigid body and another part is the displacement that elongation of unbonded reinforcements leads the wall to

generate when the wall is RHC wall, and assume the wall is a rigid body.

$$\Delta_y = \Delta_{y1} + \Delta_{y2}, \Delta_u = \Delta_{u1} + \Delta_{u2}, \quad (12)$$

where Δ_{y1} and Δ_{u1} are yield displacement and ultimate displacement that the wall generates resisting external force when all reinforcements are bonded, and assume the wall is not a rigid body, respectively. Δ_{y2} and Δ_{u2} are yield displacement and ultimate displacement that elongation of unbonded reinforcements leads the wall to generate when the wall is RHC wall, and assume the wall is a rigid body, respectively.

4.1. Calculation of Δ_{y1} , Δ_{u1} . The shear wall can be regarded as a cantilever member. In a cantilever member, the curvature distribution of plastic hinge region is very irregular (Figure 8(b)). The height of plastic hinge region can be determined by the curvature distribution along the wall height.

Based on the displacement equivalent principle in maximum bending moment region, the curvature distribution of plastic hinge region can be simplified, which consists of two parts: the plastic deformation region and the elastic deformation region.

Curvature is defined as the corner angle unit height, so the corner angle relative to the base section at any height h can be expressed as $\theta_h = \int_0^h \varphi dx$.

Therefore, the lateral displacement relative to the base section at any height h can be expressed as $\Delta_h = \int_0^h x \varphi dx$.

Define that when the base section of cantilever shear wall yields, shear wall yields. The yield curvature is linear distribution along the wall height H (Figure 8(b)). The curvature in the top section is zero, and the curvature in the base section is the yield curvature φ_y (Figure 9), and the resulting equation can be expressed as $x/H = \varphi/\varphi_y$.

Applying above equations, the yield displacement can be derived as follows:

$$\Delta_{y1} = \int_0^H \varphi_y \frac{x^2}{H} dx = \varphi_y \frac{H^2}{3}. \quad (13)$$

Assume that when shear wall reaches the ultimate state, there is a equivalent plastic hinge region height l_p at

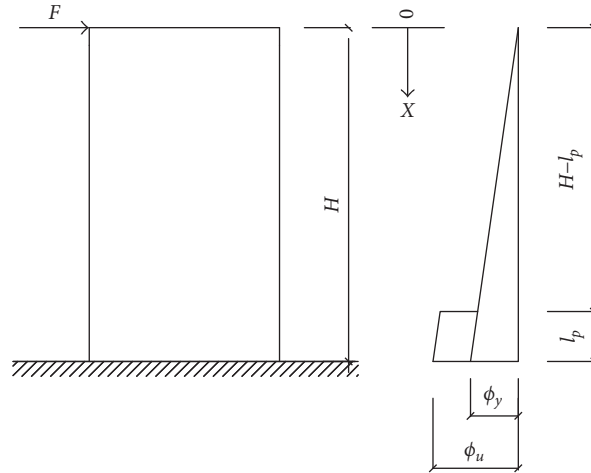


FIGURE 9: Curvature of cantilever shear wall.

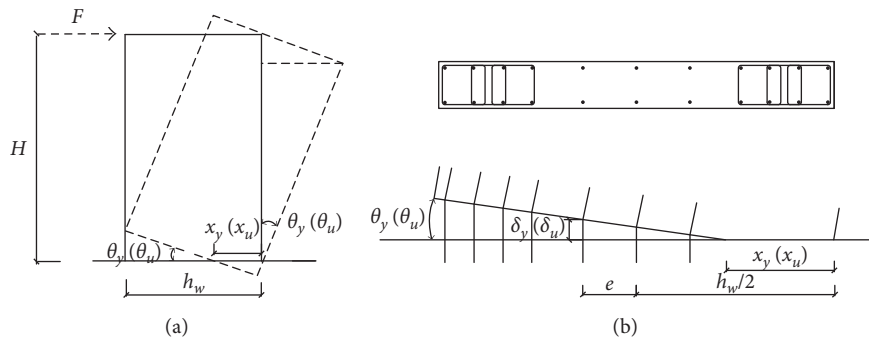


FIGURE 10: (a) Rigid body rotation and (b) unbonded reinforcement deformation of RHC shear wall.

the wall base, in which plastic curvature is equal to the largest plastic curvature φ_p , and the resulting equation can be expressed as $\varphi_p = \varphi_u - \varphi_y$.

Applying above equations, the ultimate displacement can be derived as follows:

$$\Delta_{u1} = \int_0^H \varphi_y \frac{x^2}{H} dx + \int_{H-l_p}^H (\varphi_u - \varphi_y) x dx = \varphi_y \frac{H^2}{3} + (\varphi_u - \varphi_y) \frac{2Hl_p - l_p^2}{2}, \quad (14)$$

where l_p is the equivalent plastic hinge region height which can be defined as $l_p = (0.20 + 0.044H/h_w)h_w$, where h_w is the cross section length. The formula of l_p is generally a good estimate for RC shear walls [9].

4.2. Calculation of Δ_{y2}, Δ_{u2}

4.2.1. Calculation of Δ_{y2} . When calculating Δ_{y2} , as shown in Figure 10(a), assume that the shear wall is a rigid body and the deformation of bonded reinforcement is ignored, the yield displacement can be expressed approximately as $\Delta_{y2} = \theta_y \times H$, where θ_y is the wall's corner angle, as shown in Figure 10(b), which can be expressed as

$\theta_y = \delta_y / h_w / 2 - x_y \pm e$, where x_y is the compressive zone depth in the yield state obtained by Section 3.3 approximately, e is the distance of unbonded reinforcement to the cross section's geometric center, and δ_y is the elongation of unbonded reinforcement.

When unbonded reinforcements in tensile confined end-zone yield, elongation of unbonded reinforcements can be expressed as $\delta_y = \varepsilon_y \times l_s$.

Applying above equations, the yield displacement can be derived as follows:

$$\Delta_{y2} = \frac{\varepsilon_y l_s H}{h_w / 2 - x_y \pm e}. \quad (15)$$

4.2.2. Calculation of Δ_{u2} . When calculating Δ_{u2} , as shown in Figure 10(a), assume that the shear wall is a rigid body and the elongation of bonded reinforcement is ignored, the ultimate displacement can be expressed approximately as $\Delta_{u2} = \theta_u \times H$, where θ_u is the corner angle at wall base, which can be expressed as $\theta_u = \delta_u / h_w / 2 - x_u \pm e$, where x_u is the compressive zone depth in the ultimate state obtained by Section 3.4 approximately and δ_u is the elongation of unbonded reinforcement.

For δ_u , according to the provision 4.2.4 in China code "Code for design of concrete structures (GB 50010-2010, 2010),"

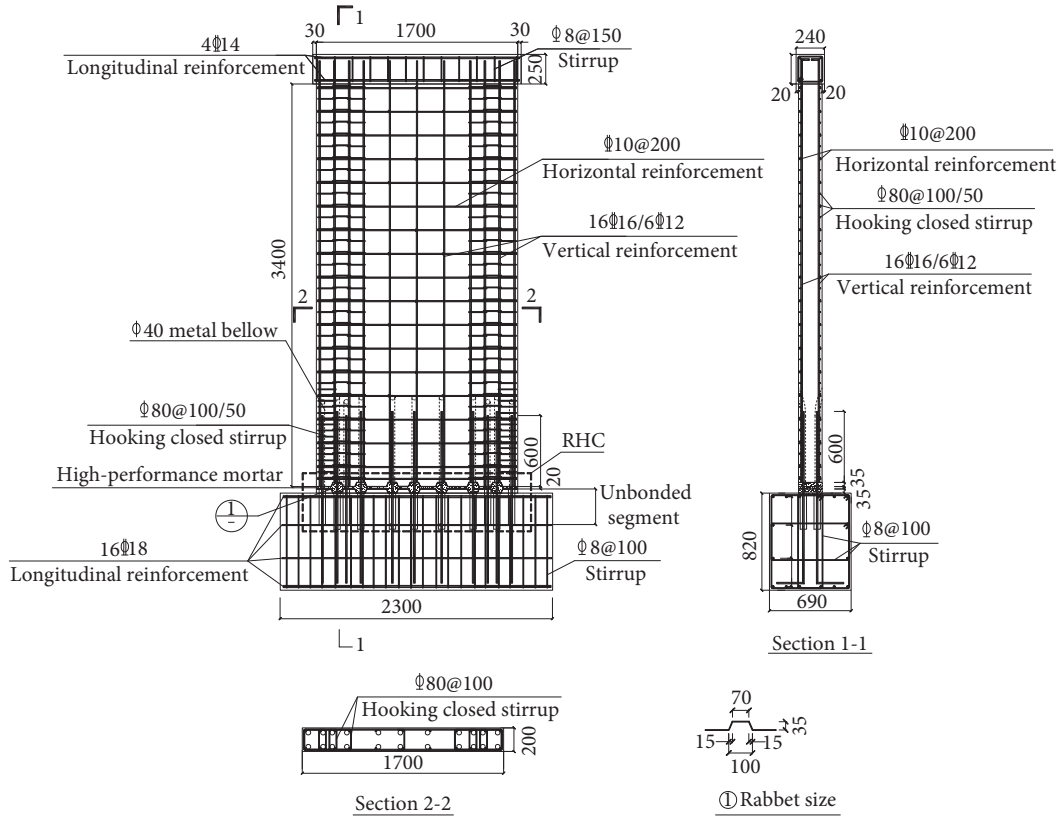


FIGURE 11: Dimension and reinforcement details of the RHC shear wall specimen (unit: mm).

the gross elongation of HRB400 ordinary reinforcement under the largest force should not be less than 7.5%. When calculating Δ_{u2} , we assume that the deformation of unbonded reinforcements in tensile confined end-zone reaches the minimum elongation percentage $\delta_{gt} = 7.5\%$; the elongation can be expressed as $\delta_u = \delta_{gt} \times l_s$.

Applying above equations, the ultimate displacement can be expressed as

$$\Delta_{u2} = \frac{\delta_{gt} l_s H}{h_w/2 - x_u \pm e} \quad (16)$$

5. Verification of Ductility

Two full-scale specimens (RHC-1, RHC-2) are designed and tested. The RHC specimen is composed of a base and a wall. The wall has a height, length, and thickness of 3.4 m, 1.7 m, and 0.2 m, as shown in Figure 11. The base has a length, width, and height of 2.3 m, 0.69 m, and 0.82 m. The grouting region is located in the wall. The unbonded segment at the vertical reinforcements is located in the base. Based on the finite element simulation results of specimens before test, select the unbonded length at the vertical reinforcement as 300 mm. The horizontal connection is located between the wall and the base. Considering the vertical reinforcement intensity of confined end-zones and construction of metal bellows, seven rabbets are set up symmetrically at connection. The rabbit's size is shown in Figure 11. High-performance mortar is grouted in metal bellows and connection. Two

specimens have the same details of reinforcement and size, and the difference is the axial compression ratio with 0.1 of RHC-1 and 0.2 of RHC-2.

5.1. Material Properties. All of the materials (concrete, steel, and mortar) employed in the tests are selected based on China code "Code for design of concrete structures (GB 50010-2010, 2010)." The grade of concrete is C35, which denotes that the ultimate compressive strength of the cubic concrete specimens (15 cm \times 15 cm \times 15 cm) cured in standard conditions is 35 MPa, and its Poisson's ratio is 0.2. Here, six cubic concrete specimens are tested.

The grade of steel in the tests is HRB400, where HRB denotes hot-rolled ribbed-steel bar and the number 400 denotes the yield strength. Its elastic modulus is 200 GPa and Poisson's ratio is 0.3, and three sets of steels with different diameters ($d = 10$ mm, 12 mm, and 16 mm) are tested.

The high-performance mortar is tested (160 mm \times 40 mm \times 40 mm) with a type of H-80, which is a characteristic of early strength, high strength, no shrinkage, and high fluidity.

The mechanical parameters of all materials are presented in Tables 1–3.

5.2. Test Setup. The quasistatic cyclic tests of the RHC shear wall are performed. Axial load is applied by tensioning pre-stressed reinforcement strands, and the lateral load is applied by the 150 t hydraulic actuator. The loading protocol employed

TABLE 1: Mechanical property of concrete.

Specimen number	Failure load (kN)	Compressive strength (MPa)	Average compressive strength (MPa)
1	880	39.11	
2	910	40.44	
3	822	36.53	
4	960	42.67	39.86
5	950	42.22	
6	860	38.22	

TABLE 2: Mechanical property of steel.

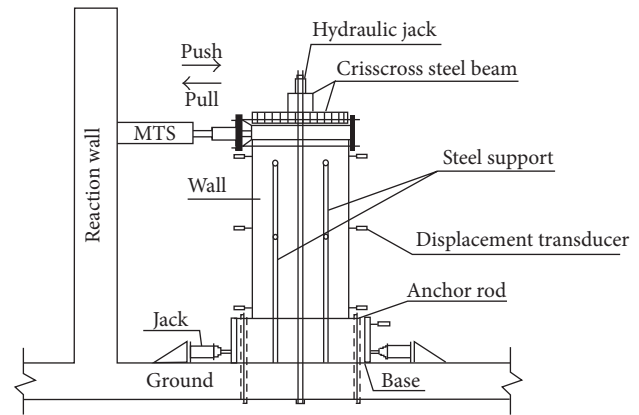
Specimen number	Steel diameter	Yield strength (MPa)	Ultimate strength (MPa)	Ratio of tensile strength to yield strength	Elongation (%)
1-1		445	625	1.4	24
1-2	10	455	615	1.35	24
Average value		450	620	1.375	24
2-1		445	575	1.29	25
2-2	12	460	585	1.27	25
Average value		452.5	580	1.28	25
3-1		465	600	1.29	25
3-2	16	460	600	1.30	25
Average value		462.5	600	1.295	25

TABLE 3: Mechanical property of high-performance mortar.

Test item	Time	Measured value
Compressive strength (MPa)	1 d	24.96
	28 d	93.52
Rupture strength (MPa)	1 d	5.29
	28 d	10.44

consists of a load control procedure first and a displacement control procedure then. Moreover, four steel supports are employed on both sides of the wall symmetrically to keep the lateral stability of the specimen during the testing process. The lateral displacements of the wall are monitored by seven displacement transducers. The testing system is shown in Figure 12.

5.3. Crack Pattern and Failure Mode. For the RHC-1 specimen, the first crack observed at 210 kN was horizontal flexural cracks when the specimen was pulled, which occurred near the bottom of the wall. The crack on the top interface of rabet was generated at 240 kN when the specimen was pushed. However, for the RHC-2 specimen, the first crack was observed at 270 kN when the specimen was pushed, which occurred near the bottom of the wall. The crack on the top interface of



(a)



(b)

FIGURE 12: Test setup: (a) schematic and (b) photograph.

rabet was generated at 300 kN when the specimen was pushed.

The yield state was defined as when bonded reinforcement segments in the confined end-zone yielded, the specimen yielded. The increase of the applied load resulted in the propagation of cracks and initiation of new flexural cracks along the specimen. Further load increase extended the existing flexural cracks into flexure shear cracks and caused initiation of vertical cracks. In addition, the cracks in the center of the test specimen propagated to the compressed zone, and the crack width and the displacement increased. Finally, when the lateral resistance degenerated to 85% of the peak load, defined as the failure of the specimen, the failure mode was a typical flexural failure for each specimen, which was controlled by crushing concrete at the plastic region near the bottom of the wall. The final crack pattern and failure mode are shown in Figure 13.

From Figure 13(b), it was noted that the failure mode was not symmetrical. The reason was that the push force and pull force of hydraulic actuator during test were not symmetrical, but had little effect.



FIGURE 13: Final crack pattern and failure mode of (a) RHC-1 specimen and (b) RHC-2 specimen.

5.4. Load-Displacement Relationship. The lateral load versus top displacement curves of the two specimens is shown in Figure 14.

It is observed in Figure 14 that the number of hysteresis loop is greater and the curve is plumper in the RHC-1 specimen than in the RHC-2 specimen. The bearing capacity of the specimen is decreased by reducing the axial compression ratio, whereas the yield displacement and ultimate displacement are increased at the same time.

5.5. Bearing Capacity and Deformation. From the tests, we obtain the crack load F_{cr} , crack displacement Δ_{cr} , yield load F_y , yield displacement Δ_y , peak load F_m , peak displacement Δ_m , ultimate load F_u , and ultimate displacement Δ_u of two specimens, as shown in Table 4.

Table 4 shows that F_{cr} , F_y , F_m , and F_u increase, whereas Δ_{cr} , Δ_y , Δ_m , and Δ_u decrease with increase of the axial compression ratio.

5.6. Verification. Applying (13) and (15), the yield displacement can be expressed as

$$\Delta_y = \varphi_y \frac{H^2}{3} + \frac{\varepsilon_y l_s H}{h_w/2 - x_y \pm e}. \quad (17)$$

Applying (14) and (16), the ultimate displacement can be expressed as

$$\Delta_u = \varphi_y \frac{H^2}{3} + (\varphi_u - \varphi_y) \frac{2Hl_p - l_p^2}{2} + \frac{\delta_{gt} l_s H}{h_w/2 - x_u \pm e}. \quad (18)$$

From (17) and (18), the yield displacement and ultimate displacement can be calculated, which are compared with test values (Table 5).

Table 5 shows that theoretical values are a little smaller than test values. There are two reasons. One is that the elongation of bonded segment is ignored when calculating Δ_{y2} and Δ_{u2} , which leads to the theoretical values smaller. Another reason is that there exist some errors and virtual

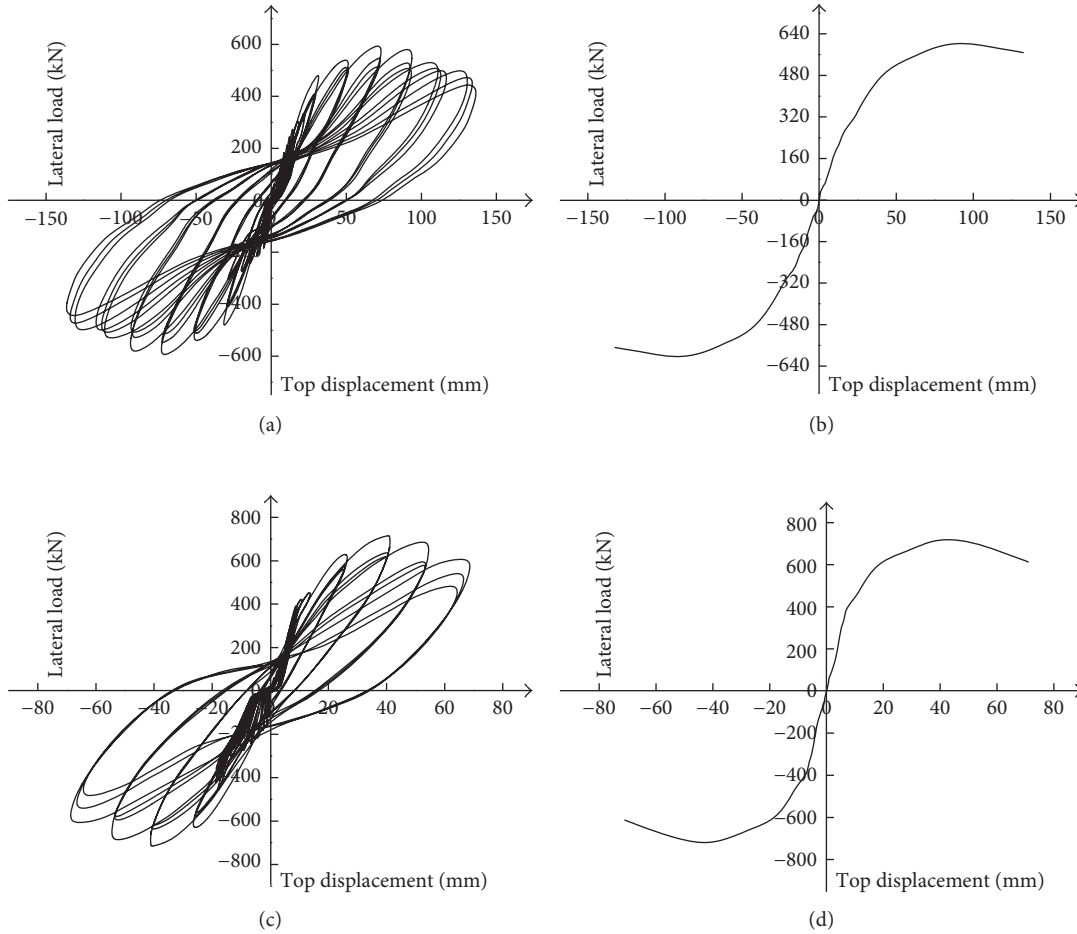


FIGURE 14: Hysteresis curves and skeleton curves of RHC-1 and RHC-2. (a) Hysteresis curve of RHC-1. (b) Skeleton curve of RHC-1. (c) Hysteresis curve of RHC-2. (d) Skeleton curve of RHC-2.

TABLE 4: Test results of two specimens.

Specimen	F_{cr} (kN)	Δ_{cr} (mm)	F_y (kN)	Δ_y (mm)	F_m (kN)	Δ_m (mm)	F_u (kN)	Δ_u (mm)
RHC-1	210	12.28	330	18.30	610	85.44	518.50	137.70
RHC-2	270	11.74	420	13.60	718	46.49	610.30	75.50

TABLE 5: Comparison of theoretical and test values of displacement ductility.

Specimens	Yield displacement (mm)		Ultimate displacement (mm)		Displacement ductility		
	Theoretical	Test	Theoretical	Test	Theoretical	Test	Theoretical/test
RHC-1	15.23	18.30	133.57	137.70	8.77	7.52	1.16
RHC-2	11.74	13.60	68.52	75.50	5.83	5.60	1.04

displacements in test inevitably, which leads to the test values larger. However, on the whole, both are in good agreement.

6. Effect of Unbonded Reinforcement on Yield Displacement and Ultimate Displacement

In order to study the effect of unbonded reinforcement on yield displacement and ultimate displacement, set RHC-2 as

example, Table 6 lists the effect of unbonded reinforcement on yield displacement and ultimate displacement.

Table 6 shows that the effect of unbonded reinforcement on ultimate displacement is more pronounced than that of yield displacement. The reason is that in the yield state, deformation of unbonded reinforcement is small which leads to small effect; however, in the ultimate

TABLE 6: Effect of unbonded reinforcement on yield displacement and ultimate displacement.

Yield displacement (mm)				Ultimate displacement (mm)			
Δ_{y1}	Δ_{y1}/Δ_y	Δ_{y2}	Δ_{y2}/Δ_y	Δ_{u1}	Δ_{u1}/Δ_u	Δ_{u2}	Δ_{u2}/Δ_u
9.22	78.53%	2.52	21.47%	21.06	30.74%	47.46	69.26%

state, unbonded reinforcement yields and its deformation are large which leads to large effect.

7. Conclusions and Suggestions

7.1. *Conclusions.* In this paper, the curvature and displacement of RHC shear wall are analyzed, and the following conclusions can be drawn:

- (1) Considering the effect of confined end-zone and unbonded reinforcement on curvature, yield curvature and ultimate curvature are calculated.
- (2) In calculating displacement, assume that the displacement consists of two parts approximately: one part is that the wall generates resisting external force when all reinforcements are bonded, and assume the wall is not a rigid body and another part is that elongation of unbonded reinforcements leads the wall to generate when the wall is RHC shear wall, and assume the wall is a rigid body. Overlay the two parts linearly, and obtain the calculation equation of yield displacement and ultimate displacement. The theoretical and test values are compared. Also, the result shows that theoretical values are slightly smaller than test values, but both are in good agreement on the whole.
- (3) According to the theoretical equation, effects of unbonded reinforcement on yield displacement and ultimate displacement are studied. The result shows that the effect of unbonded reinforcement on ultimate displacement is more pronounced than that of yield displacement.

7.2. *Suggestions.* Only two specimens were applied to verify the displacement ductility in the paper, which was inadequate to convince. Numerous tests considering different parameters should be performed to verify the displacement ductility.

Conflicts of Interest

The authors declare that there are no conflicts of interest regarding the publication of this paper.

Acknowledgments

This work was financially supported by the Green Subway Construction Innovation Team of Jinan, National Natural Science Foundation for Young Scientists of China (Grant No. 51708260), the University Natural Science Foundation funded by the Jiangsu Province Government (Grant No. 2016TM045J).

References

- [1] W. B. Hu, X. M. Zhai, and H. B. Jiang, "Study on seismic performance and construction measures optimization of precast fabricated RC integration shear wall," *Journal of Building Structures*, vol. 37, no. 8, pp. 1–10, 2016.
- [2] B. J. Smith, Y. C. Kurama, and M. J. McGinnis, "Perforated hybrid precast shear walls for seismic regions," *ACI Structural Journal*, vol. 112, no. 3, pp. 359–370, 2015.
- [3] J. A. Abdalla, E. I. Saqan, and R. A. Hawileh, "Optimum seismic design of unbonded post-tensioned precast concrete walls using ANN," *Computers and Concrete*, vol. 13, no. 4, pp. 547–567, 2014.
- [4] E. I. Saqan and R. A. Hawileh, "Nondimensional design charts for unbonded, posttensioned, split precast concrete walls," *PCI Journal*, vol. 55, no. 4, pp. 78–99, 2010.
- [5] R. A. Hawileh, E. I. Saqan, and J. A. Abdalla, "Simplified optimum design procedure for special unbonded post-tensioned split precast shear walls," *Journal of Structural Engineering*, vol. 139, no. 2, pp. 294–299, 2013.
- [6] B. J. Smith, Y. C. Kurama, and M. J. McGinnis, "Behavior of precast concrete shear walls for seismic regions: comparison of hybrid and emulative specimens," *Journal of Structural Engineering*, vol. 139, no. 11, pp. 1917–1927, 2013.
- [7] F. J. Perez, P. Stephen, and S. Richard, "Experimental lateral load response of unbonded post-tensioned precast concrete walls," *ACI Structural Journal*, vol. 110, no. 6, pp. 1045–1055, 2013.
- [8] S. M. Kang, O. J. Kim, and H. G. Park, "Cyclic loading test for emulative precast concrete walls with partially reduced rebar section," *Engineering Structures*, vol. 56, pp. 1645–1657, 2013.
- [9] A. Solak, Y. S. Tama, S. Yilmaz, and H. Kaplan, "Experimental study on behavior of anchored external shear wall panel connections," *Bulletin of Earthquake Engineering*, vol. 13, no. 10, pp. 3065–3081, 2015.
- [10] S. T. Liang, C. F. Sun, X. J. Zhu, and X. F. Jin, "A precast shear wall horizontal connection node," China Patent 201410269148.5, 2016.
- [11] L. J. Si, G. Q. Li, and F. F. Sun, "Calculation method for predicting ductility of reinforced concrete shear walls," *Journal of Hebei University of Science and Technology*, vol. 27, no. 1, pp. 8–11, 2010.
- [12] H. G. Park, S. M. Kang, L. Chung, and D. Lee, "Moment-curvature relationship of flexure-dominated walls with partially confined end-zones," *Engineering Structures*, vol. 29, no. 1, pp. 33–45, 2007.
- [13] X. W. Liang, H. J. Zhao, and M. K. Deng, "Moment-curvature relationship analysis of high-strength concrete shear wall with partially confined end-zone," *Journal of Building Structures*, no. 2, supplement 2, pp. 62–67, 2009.
- [14] Y. G. Chen, *Research on Evaluation of Seismic Performance and Design Method about Horizontal Joints in Precast Concrete Shear Wall Structure*, Ph.D. thesis, Southeast University, Nanjing, China, 2013.
- [15] Q. L. Wang, Y. L. Chi, and D. T. Niu, "Simulation test and analysis of unbonded reinforced concrete beam after corrosion," *Building Structure*, vol. 31, no. 4, pp. 51–53, 2001.
- [16] X. L. Zhang, *Research on Reinforced Concrete Beams with Localized Unbonding*, M.D. thesis, Shanghai Jiao Tong University, Shanghai, China 2006.
- [17] J. H. Mun and K. H. Yang, "Displacement ductility ratio-based flexural design approach of reinforced concrete slender shear walls," *Magazine of Concrete Research*, vol. 68, no. 8, pp. 409–422, 2016.

Research Article

Novel Crashworthy Device for Pier Protection from Barge Impact

W. Wang  and G. Morgenthal

Modeling and Simulation of Structures, Bauhaus University Weimar, Marienstrasse 13, 99423 Weimar, Germany

Correspondence should be addressed to W. Wang; dwsjzri@gmail.com

Received 22 August 2017; Revised 30 December 2017; Accepted 10 January 2018; Published 2 April 2018

Academic Editor: Chiara Bedon

Copyright © 2018 W. Wang and G. Morgenthal. This is an open access article distributed under the Creative Commons Attribution License, which permits unrestricted use, distribution, and reproduction in any medium, provided the original work is properly cited.

Barge impact is a potential hazard for bridge piers located in navigation waterways. Protective structures of different types, for example, dolphin structures, artificial islands, and guiding structures, have been widely used in bridge designs against barge impact. However, such structures often imply high cost and suffer from difficulties in installation as well as maintenance challenges. This paper aims to devise and investigate a new type of crashworthy device which is comprised of vertically supported impact cap connected to the bridge pier using a series of steel beams in a frame-type arrangement. This sacrificial steel structure is designed to form plastic hinges for energy dissipation whilst limiting the force transmitted to the protected pier. The dynamic analysis of the proposed crashworthy device subjected to barge impact is conducted using a simplified impact model previously developed by the authors. The parametric studies in this paper show that the proposed device has a large energy dissipation capacity and that the magnitude of impact force transmitted to the bridge pier can be dramatically reduced. In addition, an optimization model is proposed in this paper to achieve the cost-optimized design of the crashworthy device for a given impact scenario with constraints as per the prescribed design requirements.

1. Introduction

Bridge piers located in navigation waterways are often threatened by vessel impact due to the increment of vessel transportation volume. It was pointed out by Manen and Frandsen [1] and Larsen [2] previously that at least one major vessel-bridge collision accident of serious consequences occurred each year on average in the past. Barge collisions upon bridge structures were also frequently reported. Such collisions can often lead to catastrophic consequences including human casualties and economic losses; thus substantial investigations regarding the quantification of barge impact loading and dynamic structural responses have been conducted in recent years [3–8].

Different protection measures are being employed to protect bridge piers from vessel impact loading or reduce the damage of bridge piers during impact. As one of these protection measures, independent protective structures such as dolphin structures are frequently used in bridge designs. Such structures were, for example, adopted and installed for long-span bridges such as the Rosario-Victoria Bridge in Argentina [9], the Rhine Bridge in Kehl, Germany [10], and

the American Sunshine Bridge [11]. The advantage of such independent protective structures is that they can absorb high impact energy and protect bridge piers from direct contact with the vessels. However, such independent protective structures require high cost and suffer from durability problems and challenges regarding installation and maintenance. In addition, reconstruction of such independent protective structures after being damaged by vessel impact is often expensive, if at all possible. Other protective structures, for example, artificial islands [12] or guiding structures [13], are also frequently used. However, these structures suffer from problems as those mentioned above.

The problems related to the above mentioned protective structures have led to the investigation of bridge protections from impact by strengthening the bridge piers themselves, for example, with carbon fibre-reinforced polymers (CFRPs) [6, 14]. Such strengthening techniques can improve the pier resistance; that is, the pier undergoes less damage during impact. However, such technique cannot reduce the maximum impact force; therefore, it is effective for pier protection but not for barge protection [6]. In addition, the studies by Sha and Hao [6] indicate that the effectiveness of

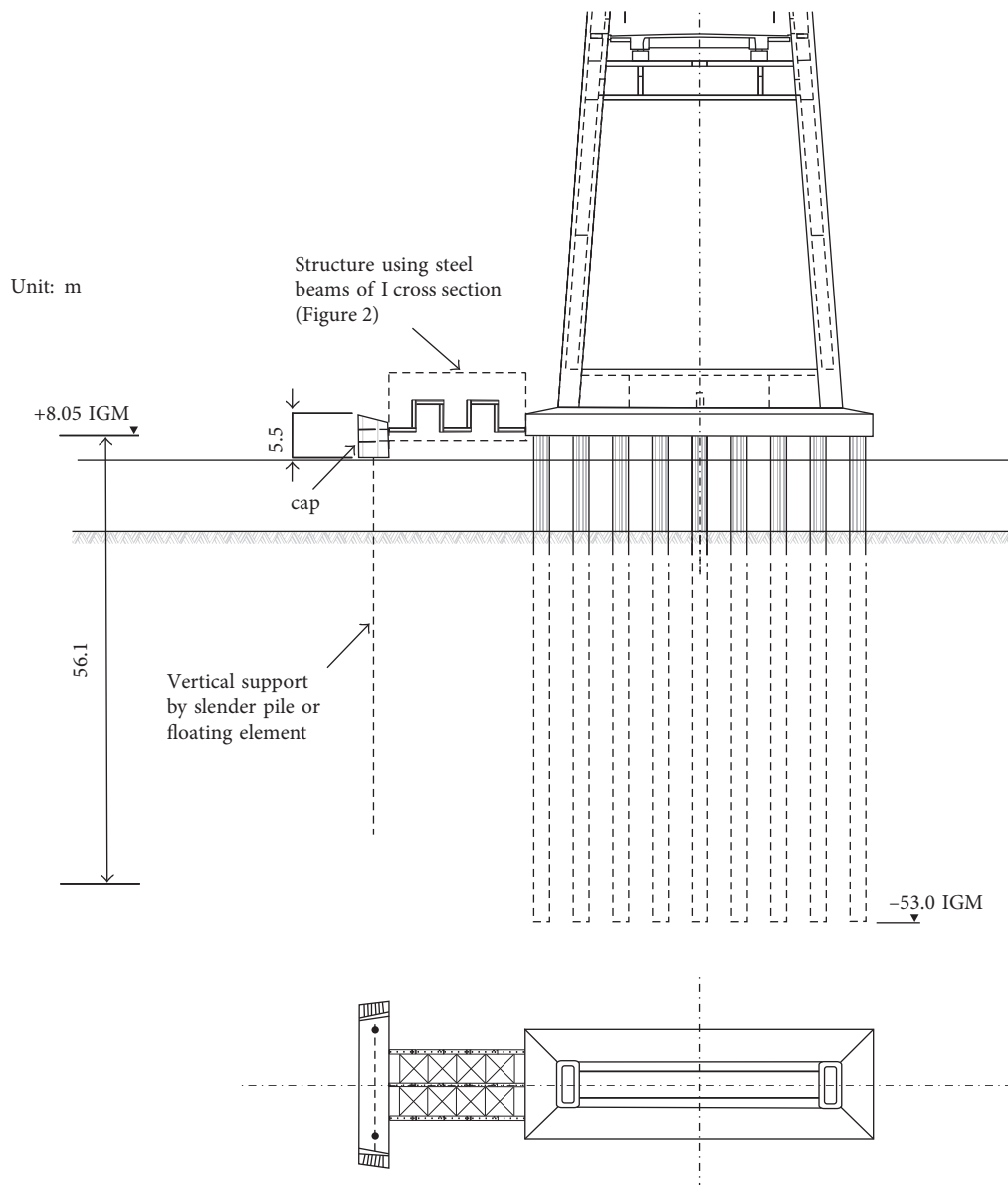


FIGURE 1: The structure connecting the cap and the bridge pier using steel beams of I cross section for a sample bridge pylon foundation.

the CFRP strengthening technique is very limited regarding the maximum pier displacement.

This paper aims to devise a novel crashworthy device which is comprised of a supported or floated cap connected to the pier using steel beams arranged in a frame-type manner. During a high-energy barge impact, many plastic hinges form in the proposed device, enabling it to absorb large amounts of impact energy through plastic deformations. Such crashworthy device is easy to install, maintain, and restore after an impact event. Through the choice of configuration, plastic moments, and postyield hardening, the maximum force transmitted to the main pier can be designed to not exceed an allowable force that is acceptable by the main pier.

To investigate the effectiveness of the proposed crashworthy device for barge impact, the simplified impact model previously developed by the authors is employed in this

paper to conduct dynamic analysis of the device subjected to barge impact. The simplified impact model transforms the highly nonlinear full barge impact model (FBIM) into a coupled multi-degree-of-freedom model (CMM). The accuracy and efficiency of CMM were thoroughly assessed for different impact scenarios [8]. This paper employs such simplified impact model to investigate the energy dissipation capacity of the proposed device and the magnitude of impact force transmitted to the bridge pier by the steel beams during impact for different structural configurations. The parametric studies in this paper indicate that the proposed device has a large energy dissipation capacity for barge impact and can significantly reduce the maximum impact force transmitted to the bridge pier during impact. To achieve cost-optimized design of such device for a given impact scenario, a mathematical optimization model is proposed in this

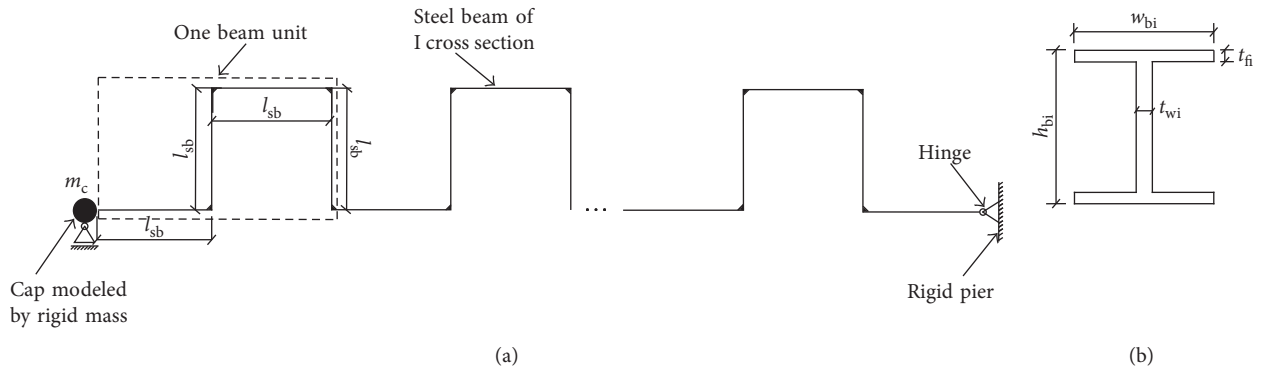


FIGURE 2: Configuration of (a) the cap steel beam structure and (b) I cross section of steel beams. N_{bu} : number of beam units in one plane; l_{sb} : length of each single steel beam; m_c : cap mass.

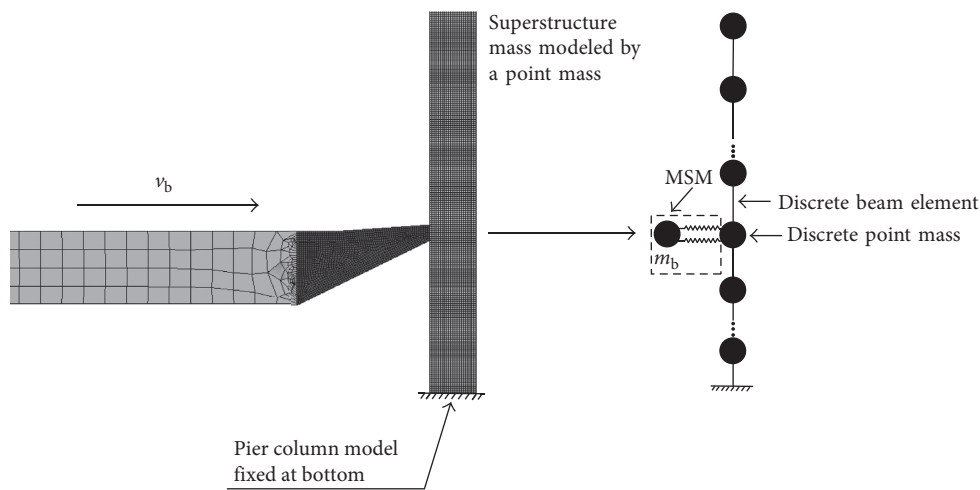


FIGURE 3: Transformation of FBIM (left) into CMM (right).

paper with constraints as per the prescribed design requirements. Examples presented in this paper show that the optimum configuration of the device can be obtained for different impact scenarios using the proposed optimization model.

2. Configuration of the Device

During a barge impact, a portion of the impact energy is transformed into the residual kinetic energy of the barge while the rest of the impact energy is dissipated through the plastic deformations of the barge and the impacted structure. In order to protect both the bridge pier and the barge, it is necessary to devise a crashworthy device which is easy to install, maintain and restore and can absorb large portions of the impact energy through plastic deformations. In this way, the energy absorbed by the barge and the pier during impact would be low, and consequently, both the barge and the pier can remain in the linear range, that is, elastic (undamaged), through the limitation of the force transmitted.

The configuration of the proposed crashworthy device is depicted in Figure 1 for a sample bridge pylon foundation to

be protected. The cap structure is designed to collect the local impact forces and is vertically supported for its self-weight by a structure that does not provide a significant lateral restraint, for example, a flexible pile system or a floating structure. The cap is connected to the pylon foundation using a series of steel beams of I cross section arranged in multiple frames. The individual steel beam legs are connected bending stiff, for example, through welds, such that a force applied to the cap generates bending moments in the steel structure. Several planes of beam units can be installed to provide the energy dissipation capacity and the elastic and plastic deformation behavior desired. In Figure 1, three planes are shown, which can be braced against each other to avoid out-of-plane stability failure.

For simplification purposes, several assumptions are adopted herein: (1) the lateral resistance of the cap's supporting structure is ignored, (2) the pylon foundation is assumed to be rigid, and (3) the cap is assumed to be rigid and is modeled using a lumped mass. Based on these assumptions, the structure shown in Figure 1 can be simplified into the cap steel beam structure, as shown in Figure 2. The cap can move freely in the horizontal direction whilst its vertical movement is constrained.

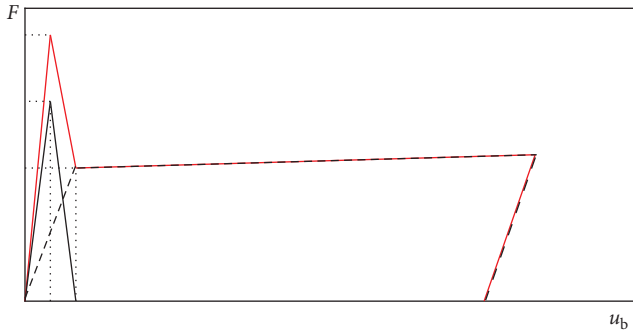


FIGURE 4: General shape of barge bow force-deformation curve. —, curve 1; —, curve 2; - -, curve 3.

3. Overview of CMM

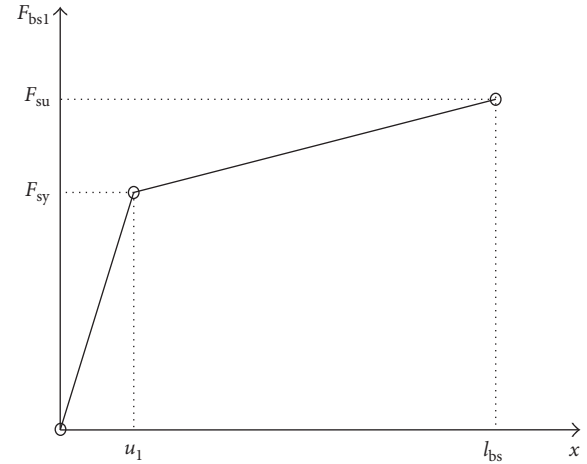
The CMM previously developed by the authors simplifies the complex finite-element barge model into a nonlinear mass-spring model (MSM) and models the pier column using discrete masses and fibre beam elements [8], as shown in Figure 3, where m_b is the lumped barge mass and v_b is the impact velocity.

As per previous studies [3, 4, 7], the force-deformation curve of the barge bow during impact (curve 1) generally includes a linear increase of impact force until the force peak is followed by an abrupt decrease when the barge bow yields, as shown in Figure 4, where u_b is the barge bow deformation and F is the impact force. Then the impact force roughly reaches a plateau until the unloading stage. The shape of curve 1 can be regarded as the superposition of two curves—a triangular curve (curve 2) and a bilinear curve (curve 3), as shown in Figure 4. Two nonlinear springs which act in parallel are thus introduced to represent the barge bow resistance. The force-deformation curves of the two nonlinear springs are taken to be bilinear and triangular, respectively, as shown in Figure 5, where u_1 and u_2 are the yielding deformations of two springs, respectively; F_{sy} is the yielding force of the first spring; F_{sp} is the peak force of the second spring; and x is the spring deformation. By coupling MSM with the column at the impact position, the CMM is developed to predict the dynamic barge impact process efficiently, as shown in Figure 3. The MSM parameters are determined by an optimization model which minimizes the integration error of impact force time histories determined by CMM and FBIM, respectively.

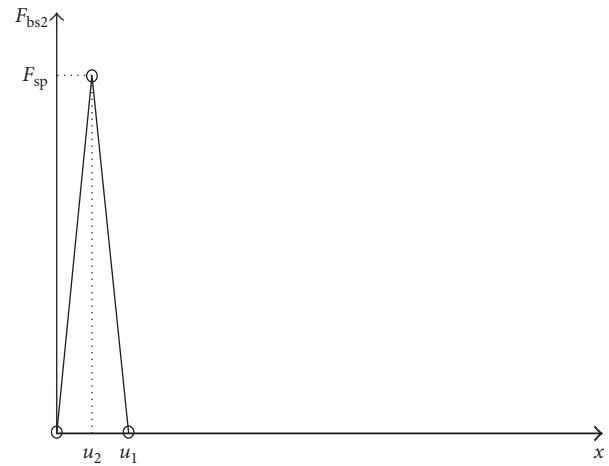
The quality of CMM regarding the prediction of impact force time history and dynamic pier responses was assessed in large detail for different impact scenarios in [8] by using FBIM as the benchmark model. The validated CMM is thus used for the studies herein.

4. Simplified Impact Model Based on CMM

In this section, the simplified impact model is developed based on CMM for dynamic analysis of the proposed crashworthy device subjected to barge impact. As shown in Figure 6, the steel beams are modeled using discrete masses and fibre beam elements. The MSM is coupled with the cap which is expected to contact with the barge when impact occurs. It is assumed in



(a)



(b)

FIGURE 5: Bilinear spring model (a) and triangular spring model (b) used in MSM [8].

this study that the beam elements undergo no shear deformations or torsional deformations. The stress-strain curve of the beam steel is bilinear in this study.

The MATLAB code was written with the fibre method for solving the numerical model illustrated in Figure 6. The code was previously verified by detailed finite-element simulation results from LS-DYNA [8]. Geometric nonlinearity of beam elements is analyzed using the corotational approach for problems of large displacements and small strains. The basic idea is to decompose the motion of the element into rigid body part and pure deformational part. A local coordinate system, which moves and rotates with the element's overall rigid body motion, is defined, and the deformational part is measured under this local coordinate system [15].

5. Parametric Studies

The effectiveness of the proposed device is investigated in this section by parametric studies using the simplified impact model. The cap surface which contacts with the barge is flat and is 3.0 m in width. The bridge pier is flat and 6.0 m in

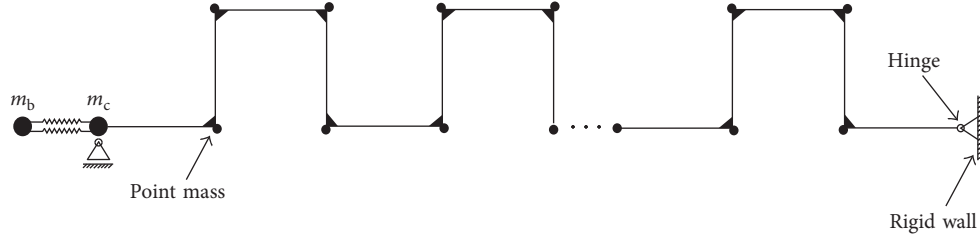
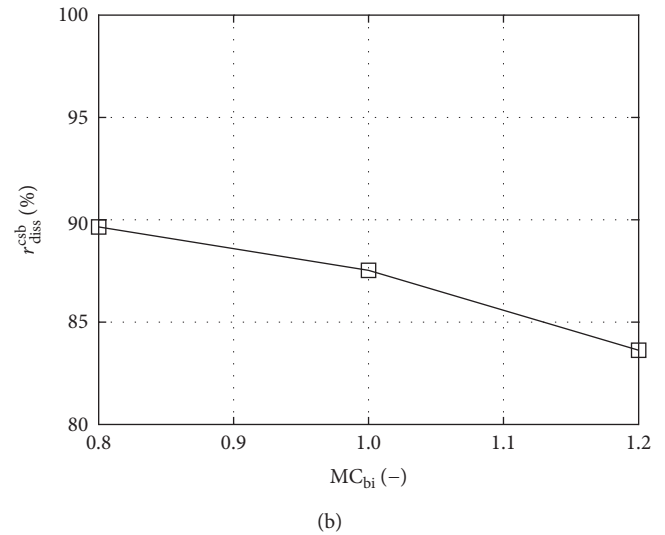
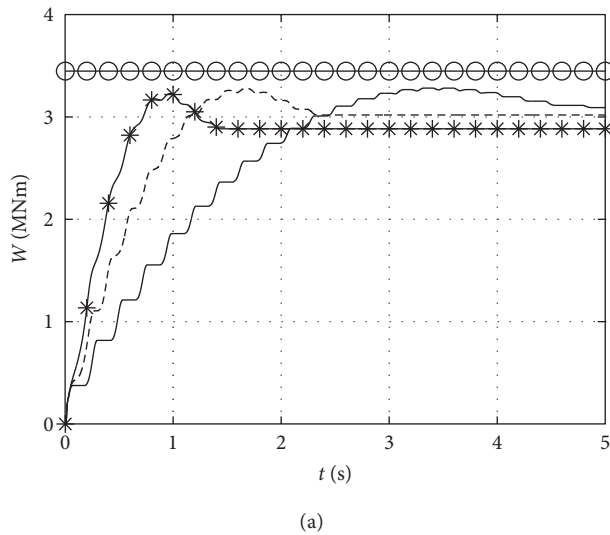


FIGURE 6: Simplified impact model based on CMM for dynamic analysis of the proposed device subjected to barge impact.

TABLE 1: Prespecified parameters for parametric studies of the device.

Member	Parameter	Value
Barge	m_b = barge mass	1723.7 ton
	v_b = impact velocity	2.0 m/s
Cap	w_c = cap width	3.0 m
	m_c = cap mass	100.0 ton
	N_{pl} = number of planes of beam units	1
Steel beams	l_{csb} = total length of beam units in one plane	15.0 m
	ρ_{bs} = mass density of beam steel	8020.0 kg/m ³
	E_{bs} = elastic modulus of beam steel	200.0 GPa
	E_t^{bs} = tangent modulus of beam steel	1.5 GPa
	ϵ_u^{bs} = failure strain of beam steel	0.25
Pier	w_p = pier width	6.0 m

FIGURE 7: Time histories of energy absorbed by the device (a) corresponding to different beam cross-section dimensions and the ratio of energy absorbed by the device after impact to the total impact energy, respectively, versus MC_{bi} (b). —, W_{diss}^{csb} ($MC_{bi} = 0.8$); ---, W_{diss}^{csb} ($MC_{bi} = 1.0$); -*- , W_{diss}^{csb} ($MC_{bi} = 1.2$); -○-, W_{total} ; □, the ratio of energy absorbed by the device after impact to the total impact energy.

width. The cap mass (m_c) is taken to be 100.0 ton. The total length of the beam units in one plane (l_{csb}) is taken to be 15.0 m. The number of planes of beam units (N_{pl}) is taken to be one in this study. The information of the prespecified parameters regarding the device is tabulated in Table 1.

Three parameters, that is, beam cross-section dimension, yielding strength of beam steel (f_y^{bs}), and number of beam units in one plane (N_{bu}), are considered for the parametric studies herein. For comparison purposes, the following baseline simulation is conducted: beam cross-section dimension as follows: $h_{bi} = 0.75$ m, $w_{bi} = 0.50$ m, $t_{fi} = 0.05$ m, and $t_{wi} = 0.03$ m; beam steel yielding strength of 350.0 MPa; and beam unit

number of two in one plane. The parameter MC_{bi} , which means the ratio of the studied beam cross-section dimensional parameters, that is, h_{bi} , w_{bi} , t_{fi} , and t_{wi} , to the respective beam cross-section dimensional parameters used for the baseline simulation, is denoted herein.

5.1. Beam Cross-Section Dimension. Three beam cross-section dimensions corresponding to MC_{bi} of 0.8, 1.0, and 1.2, respectively, are considered herein. The energy absorbed by the device (W_{diss}^{csb}) during impact corresponding to each beam cross-section dimension is shown in Figure 7, where the total impact energy (W_{total}) and the ratio (r_{diss}^{csb}) of energy

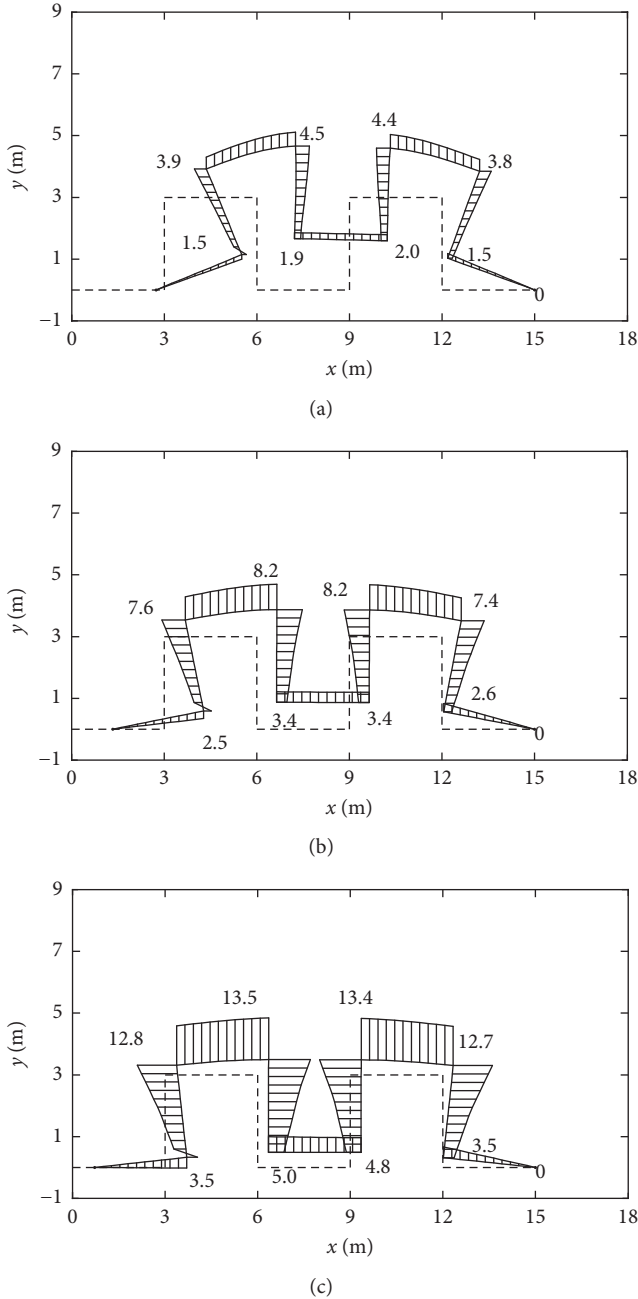


FIGURE 8: Maximum bending moment diagrams of the structures during impact and deflections of the structures after impact corresponding to different beam cross-section dimensions (unit: MNm). —, original shape of the device; —, deformed shape of the device. (a) $MC_{bi} = 0.8$; (b) $MC_{bi} = 1.0$; (c) $MC_{bi} = 1.2$.

absorbed by the device after impact to the total impact energy are also presented. Figure 7 shows that a large portion of the impact energy is absorbed by the device and that the increase of beam cross-section dimension reduces the energy absorbed by the device due to the decrease of structure deformation caused by the increase of structure stiffness, as shown in Figure 8, where the maximum bending moment diagram of the structure during impact and the structure deflection after impact corresponding to each beam cross-section dimension are presented.

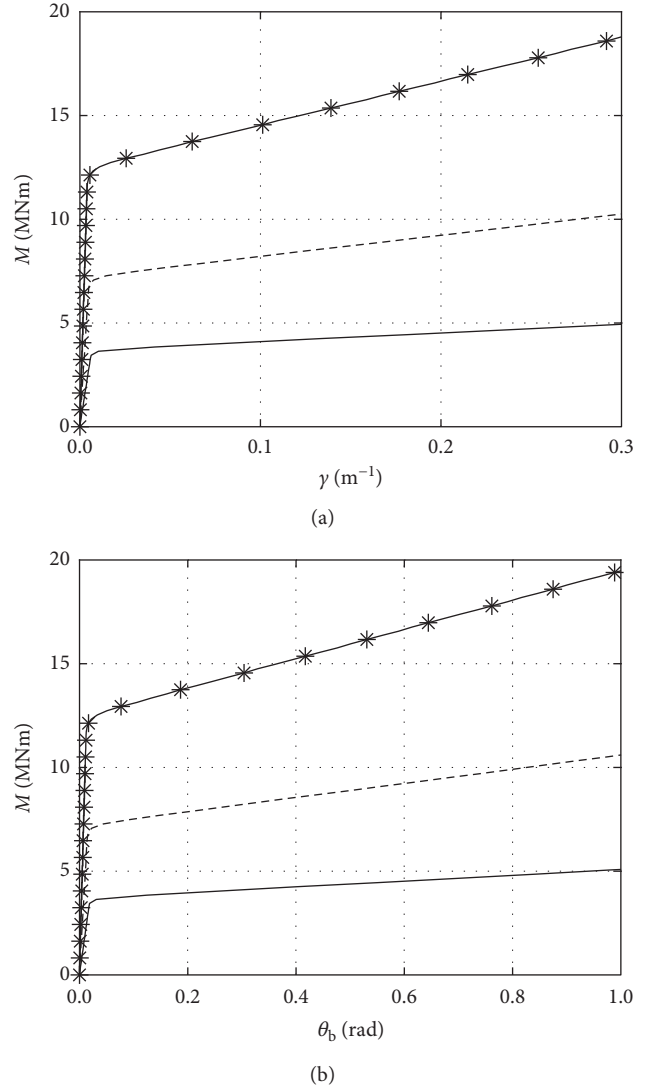


FIGURE 9: Moment-curvature relationships of the I cross sections (a) and moment-rotation relationships of single steel beams (b) corresponding to different beam cross-section dimensions. —, $MC_{bi} = 0.8$; - - -, $MC_{bi} = 1.0$; —*, $MC_{bi} = 1.2$.

The moment-curvature relationship of each beam cross section and the moment-rotation relationship of a single steel beam corresponding to each beam cross-section dimension are shown in Figure 9, where γ is the curvature of beam cross section and θ_b is the relative rotation angle of two boundary sections of a single steel beam. Figures 8 and 9 show that the plastic hinges which form during impact are located at the upper part of the structure, that is, the horizontal beams at the top and the upper part of the vertical beams, where the maximum bending moment exceeds the corresponding yielding moment of beam cross section. The formation of plastic hinges enables the device to absorb a large portion of energy during impact, as shown in Figure 7. The lower part of the structure, that is, the horizontal beams at the bottom and the lower part of the vertical beams, undergoes only elastic deformations, as Figure 8 shows.

The time histories of impact force on the pier with the device corresponding to each beam cross-section dimension and without the device, respectively, together with the reduction ratio (r_f) of maximum impact force when the device is used, are shown in Figure 10, which shows that the maximum impact force can be significantly reduced when the device is used. The increase of beam cross section would increase the magnitude of impact force due to the increase of cross-section fibres.

5.2. Yielding Strength of Beam Steel. Three steel yielding strengths of 250.0 MPa, 350.0 MPa, and 450.0 MPa, respectively, are considered herein. The energy absorbed by the device (W_{diss}^{csb}) during impact corresponding to each steel yielding strength is shown in Figure 11, where the total impact energy (W_{total}) and the ratio (r_{diss}^{csb}) of energy absorbed by the device after impact to the total impact energy are also presented. Figure 11 shows that the increase of steel yielding strength reduces the energy absorbed by the device during impact. This is because the structure resistance increases with the increase of steel yielding strength and consequently the structure undergoes smaller deformations, as shown in Figure 12.

The time histories of impact force on the bridge pier with the device corresponding to each steel yielding strength and without the device, respectively, together with the reduction ratio of maximum impact force when the device is used, are shown in Figure 13, which shows that the increase of steel yielding strength would increase the magnitude of impact force on the pier due to the increase of structure resistance.

5.3. Number of Beam Units. The devices of one beam unit, two beam units, and three beam units, respectively, are considered herein. The energy absorbed by the device (W_{diss}^{csb}) during impact corresponding to each beam unit number is shown in Figure 14, where the total impact energy (W_{total}) and the ratio (r_{diss}^{csb}) of energy absorbed by the device after impact to the total impact energy are also presented. Figure 14 shows that the increase of beam unit number slightly reduces the energy absorbed by the device. This is because the structure becomes stiffer when more beam units are used, as indicated in Figures 15 and 16 which show that the structure undergoes smaller deflections and smaller deformations during impact when more beam unit number is used.

The time histories of impact force on the pier with the device corresponding to each beam unit number and without the device, respectively, together with the reduction ratio (r_f) of maximum impact force when the device is used, are shown in Figure 17, which shows that the magnitude of impact force on the pier increases when beam unit number increases due to the increase of structure stiffness.

6. Cost-Optimized Design of the Device

The studies in the previous section have shown the great potentiality of the proposed crashworthy device for pier protection from barge impact due to its large energy dissipation capacity during impact. In order to achieve cost-optimized

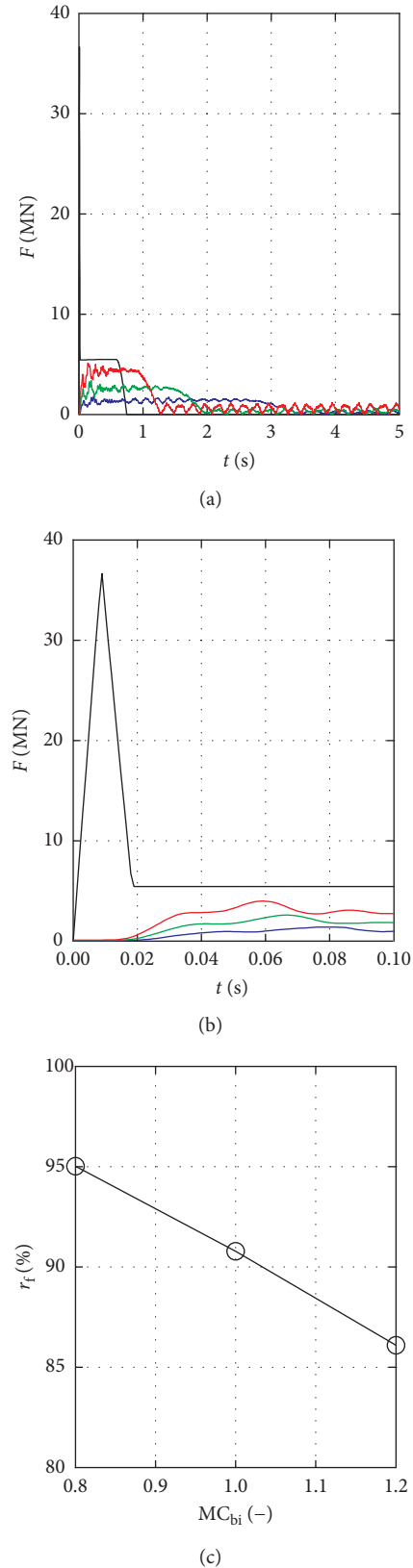


FIGURE 10: Impact force time histories on the bridge pier for the whole impact process (a), for the first 0.10 s of impact process (b) corresponding to different beam cross-section dimensions, and the reduction ratio of maximum impact force versus MC_{bi} (c). —, without the device; —, $MC_{bi} = 0.8$; —, $MC_{bi} = 1.0$; —, $MC_{bi} = 1.2$.

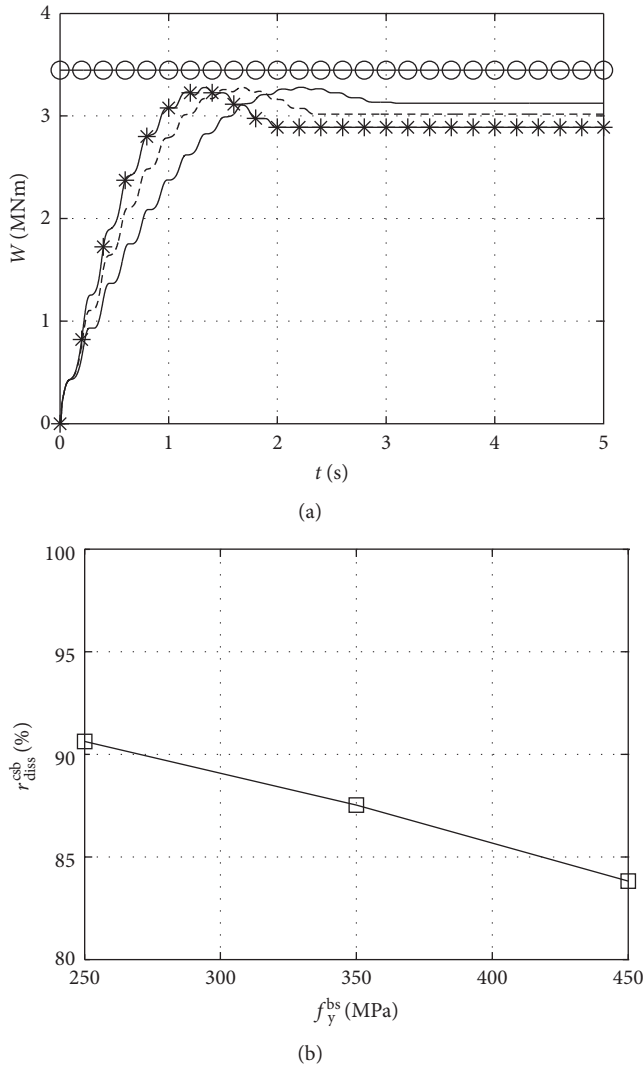


FIGURE 11: Time histories of energy absorbed by the device (a) corresponding to different yielding strengths of beam steel and the ratio of energy absorbed by the device after impact to the total impact energy, respectively, versus yielding strength of beam steel (b). —, W_{diss}^{csb} ($f_y^{bs} = 250.0$ MPa); ---, W_{diss}^{csb} ($f_y^{bs} = 350.0$ MPa); -·-, W_{diss}^{csb} ($f_y^{bs} = 450.0$ MPa); -○-, W_{total} ; □, the ratio of energy absorbed by the device after impact to the total impact energy.

design of such device for a given impact scenario, a mathematical optimization model is proposed in this section with constraints as per the prescribed design requirements.

6.1. Mathematical Optimization Model. For a given barge mass (m_b) and impact velocity (v_b), when the number of planes of beam units (N_{pl}), the yielding strength of beam steel (f_y^{bs}), and the maximum allowable impact force F_{max}^{allow} on the bridge pier are specified, the device can be designed in such a way that the design requirements are satisfied and the required cost is minimized by using minimum amount of steel. The design of the device can thus be transformed into an optimization problem where the number of beam units in one plane (N_{bu}), the four dimensional parameters of the I cross section, that is, h_{bi} , w_{bi} , t_{fi} , and t_{wi} , and the length of each

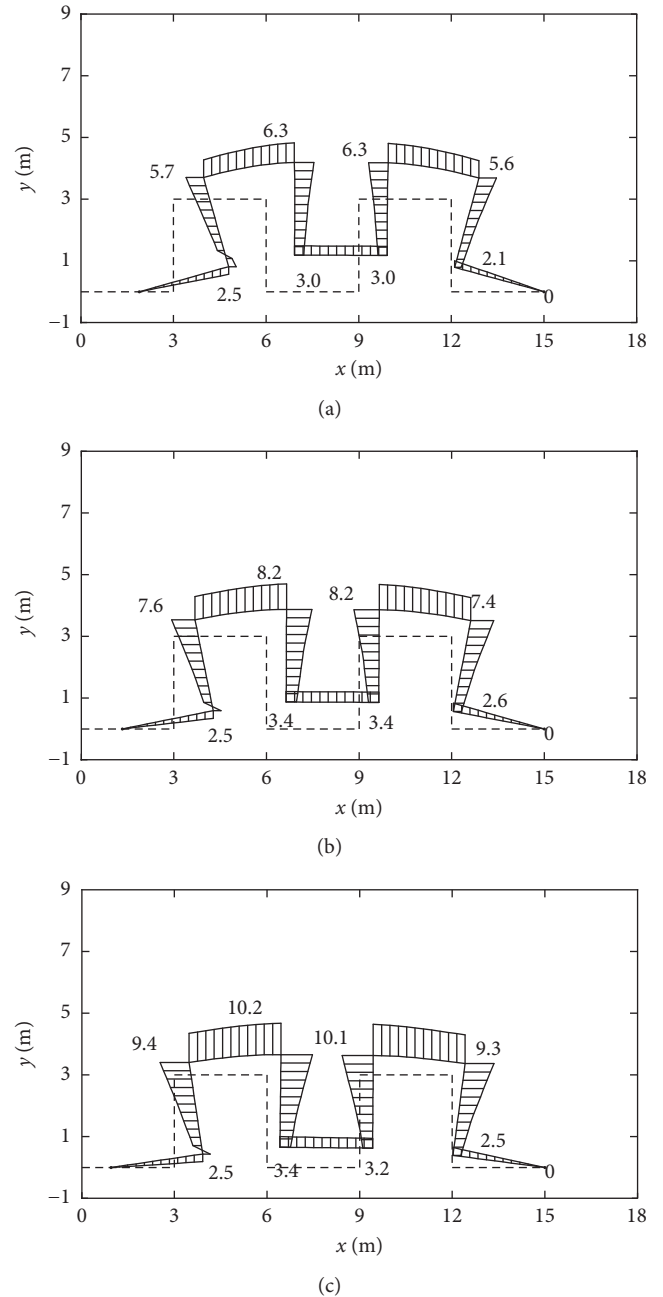


FIGURE 12: Maximum bending moment diagrams of the structures during impact and deflections of the structures after impact corresponding to different yielding strengths of beam steel (unit: MNm). —, original shape of the device; —, deformed shape of the device. (a) $f_y^{bs} = 250.0$ MPa; (b) $f_y^{bs} = 350.0$ MPa; (c) $f_y^{bs} = 450.0$ MPa.

single steel beam l_{sb} are optimized. For simplification purposes, the four dimensional parameters of the I cross section are assumed to satisfy the relationships as tabulated in Table 2.

The optimization model and the corresponding constraints are described as follows:

minimize:

$$m_{sb} = (4N_{bu} + 1)l_{sb}A_1N_{pl}\rho_{bs}, \quad (1)$$

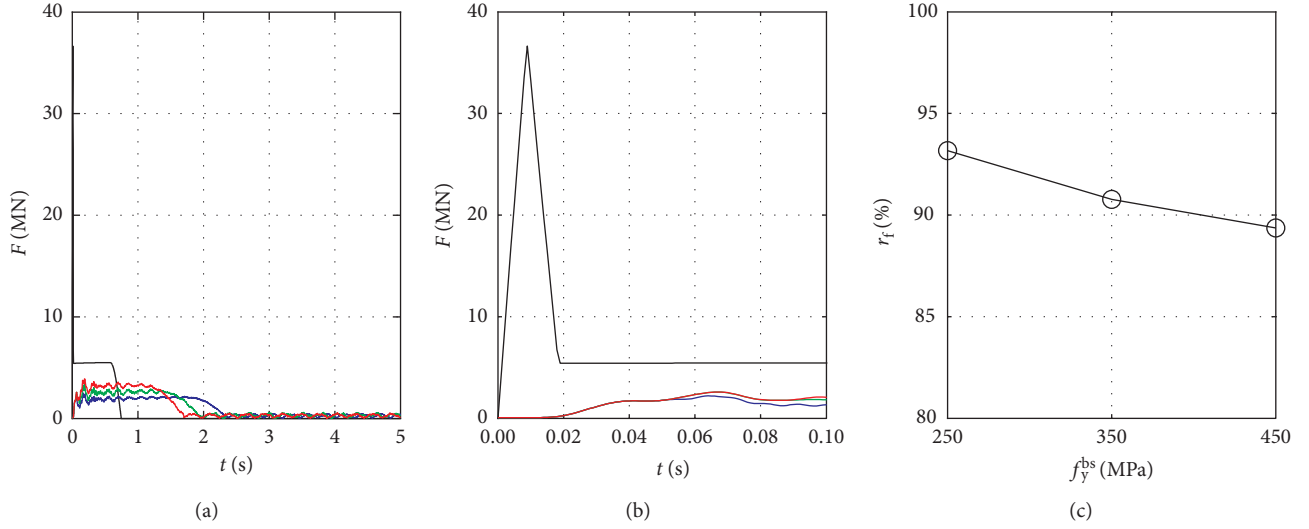


FIGURE 13: Impact force time histories on the bridge pier for the whole impact process (a), for the first 0.10 s of impact process (b) corresponding to different yielding strengths of beam steel and the reduction ratio of maximum impact force versus yielding strength of beam steel f_y^{bs} (c). —, without the device; —, $f_y^{bs} = 250.0$ MPa; —, $f_y^{bs} = 350.0$ MPa; —, $f_y^{bs} = 450.0$ MPa.

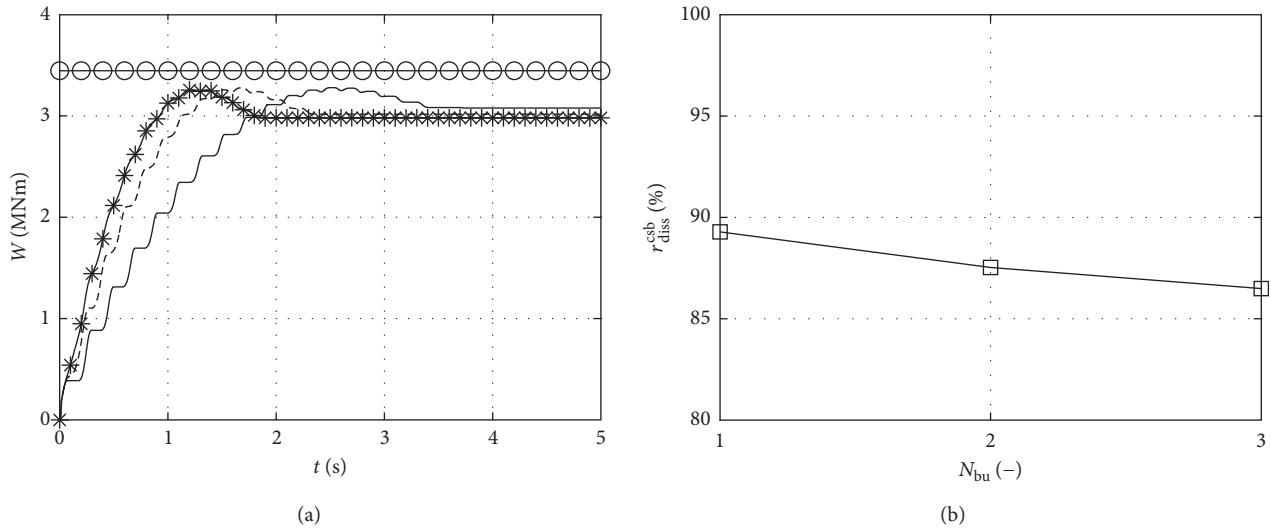


FIGURE 14: Time histories of energy absorbed by the device (a) corresponding to different beam unit numbers and the ratio of energy absorbed by the device after impact to the total impact energy, respectively, versus beam unit number in one plane N_{bu} (b). —, W_{diss}^{csb} ($N_{bu} = 1$); - - -, W_{diss}^{csb} ($N_{bu} = 2$); - * -, W_{diss}^{csb} ($N_{bu} = 3$); -○-, W_{total} ; □, the ratio of energy absorbed by the device after impact to the total impact energy.

subject to:

$$5h_{bi} \leq l_{sb}, \quad (2)$$

$$N_{bu}^l \leq N_{bu} \leq N_{bu}^u, \quad (3)$$

$$h_{bi}^l \leq h_{bi} \leq h_{bi}^u, \quad (4)$$

$$l_{sb}^l \leq l_{sb} \leq l_{sb}^u, \quad (5)$$

$$F_{max} \leq F_{max}^{allow}, \quad (6)$$

$$D_{cap}^{max} \leq D_{max}^{allow} = N_{bu} l_{sb}, \quad (7)$$

where m_{sb} is the total mass of steel beams (ton), A_I is the area of the I cross section (m^2), ρ_{bs} is the mass density of beam steel (ton/m^3), N_{bu}^l and N_{bu}^u are the lower bound and upper bound of the number of beam units in one plane (-), respectively, h_{bi}^l and h_{bi}^u are the lower bound and upper bound of the depth of the I cross section (m), respectively, l_{sb}^l and l_{sb}^u are the lower bound and upper bound of beam length (m), respectively, F_{max} is the maximum impact force on the bridge pier during impact (MN), D_{cap}^{max} is the maximum cap displacement during impact (m), and D_{max}^{allow} is the maximum allowable cap displacement (m). The value of D_{max}^{allow} is taken to be $N_{bu} l_{sb}$ to avoid the contact of adjacent vertical beams during impact.

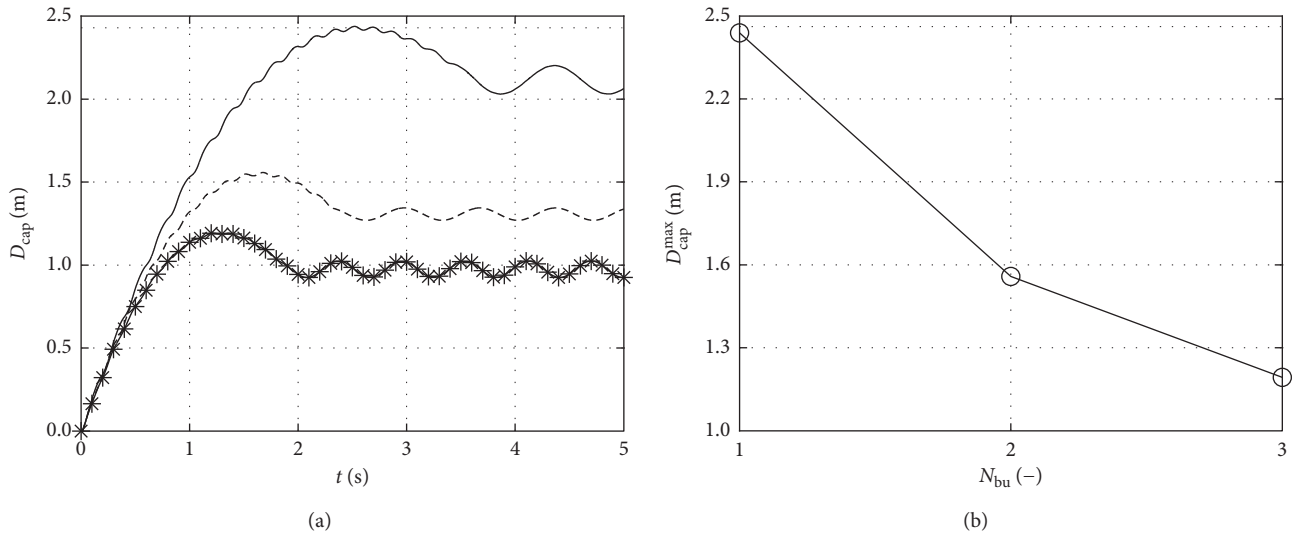


FIGURE 15: Time histories of cap displacement corresponding to different beam unit numbers (a) and maximum cap displacement D_{cap}^{max} versus beam unit number in one plane N_{bu} (b). —, $N_{bu} = 1$; ---, $N_{bu} = 2$; -*-, $N_{bu} = 3$.

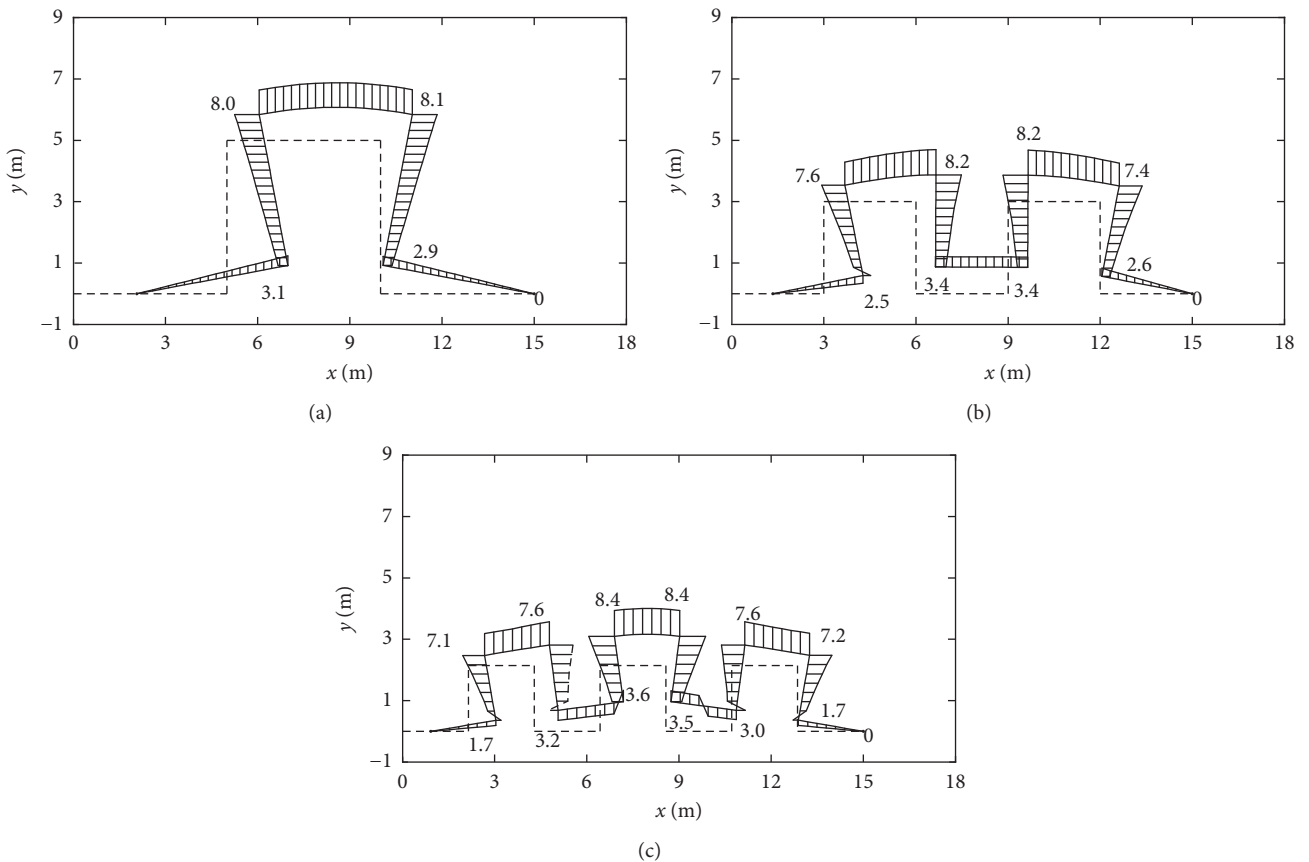


FIGURE 16: Maximum bending moment diagrams of the structures during impact and deflections of the structures after impact corresponding to different beam unit numbers (unit: MNm). —, original shape of the device; —, deformed shape of the device. (a) $N_{bu} = 1$; (b) $N_{bu} = 2$; (c) $N_{bu} = 3$.

Three variables, that is, N_{bu} , h_{bi} , and l_{sb} , are included in the optimization process. The sequential quadratic programming (SQP) [16] is used for solving the proposed constrained optimization problem.

6.2. *Application Example.* In this section, the optimum configurations of the devices corresponding to several different impact scenarios are obtained using the proposed optimization model. The combinations of three barge

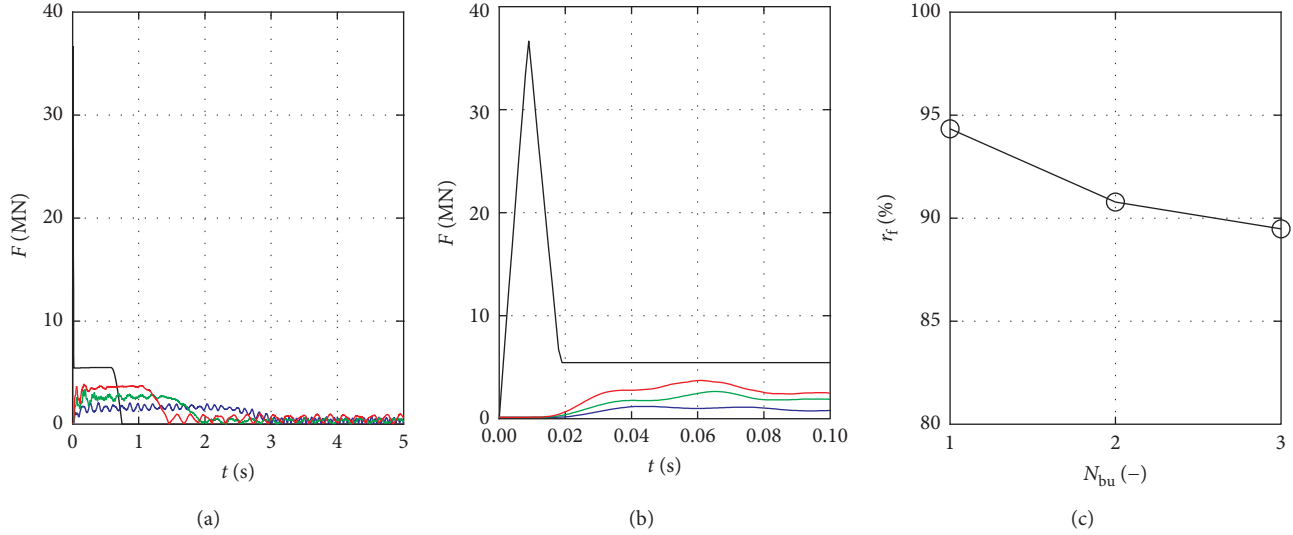


FIGURE 17: Impact force time histories on the bridge pier for the whole impact process (a), for the first 0.10 s of impact process (b) corresponding to different beam unit numbers, and the reduction ratio of maximum impact force versus beam unit number N_{bu} (c). —, without the device; —, $N_{bu} = 1$; —, $N_{bu} = 2$; —, $N_{bu} = 3$.

TABLE 2: Relationships of I cross-section dimensional parameters.

Ratio	Value (-)
w_{bi}/h_{bi}	1.0
t_{fi}/h_{bi}	0.05
t_{wi}/h_{bi}	0.03

masses, that is, 181.4 ton (empty barge), 952.6 ton (half loaded barge), and 1723.7 ton (fully loaded barge), and three impact velocities, that is, 1.0 m/s, 3.0 m/s, and 5.0 m/s, are considered herein. Each impact scenario is labeled as IS_{ij} , where i denotes the number index of barge mass varying from 1 to 3 and j denotes the number index of impact velocity varying from 1 to 3, as tabulated in Table 3. The cap surface which contacts with the barge is flat and is 3.0 m in width. The cap mass (m_c) is taken to be 100.0 ton. The number of planes of beam units (N_{pl}) is taken to be two. The yielding strength of beam steel (f_y^{bs}) is taken to be 350.0 MPa, and the maximum allowable impact force (F_{max}^{allow}) on the bridge pier is taken to be 5.0 MN. The information of the prespecified parameters regarding the structure is tabulated in Table 4.

The optimum parameters generated by the proposed optimization model, the total masses of beam steel, and the configurations of optimum devices corresponding to different impact scenarios are tabulated in Table 5. The total number of beam units ($N_{bu}^{total} = N_{bu} \times N_{pl}$) and the total mass of beam steel (m_{sb}) used by the optimum device plotted against total barge impact energy (W_{total}) are shown in Figure 18, which shows that N_{bu}^{total} increases to four, corresponding to two beam units in one plane, when W_{total} reaches around 5.0 MNm. This is because the maximum cap displacement (D_{cap}^{max}) increases with the increase of W_{total} , as shown in Figure 19. When W_{total} reaches around 5.0 MNm, D_{cap}^{max} increases to such a level that two beam units in one plane are needed to increase the maximum allowable cap displacement

TABLE 3: Impact scenarios considered for structure optimization.

Impact scenario	m_b (ton)	v_b (m/s)
IS ₁₁	181.4	1.0
IS ₁₂	181.4	3.0
IS ₁₃	181.4	5.0
IS ₂₁	952.6	1.0
IS ₂₂	952.6	3.0
IS ₂₃	952.6	5.0
IS ₃₁	1723.7	1.0
IS ₃₂	1723.7	3.0
IS ₃₃	1723.7	5.0

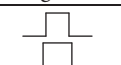
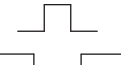
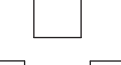
(D_{max}^{allow}) based on (7), enabling D_{cap}^{max} to be lower than D_{max}^{allow} to satisfy the design requirement. It is also shown in Figure 18 that m_{sb} approximately shows linear dependency on W_{total} , indicating that m_{sb} is approximately directly proportional to barge mass while an increase of impact velocity could lead to a roughly quadratic increase of m_{sb} .

The maximum cap displacements (D_{cap}^{max}) and maximum impact forces (F_{max}) on the pier corresponding to different impact scenarios are tabulated in Table 6, which shows that for each impact scenario, D_{cap}^{max} is smaller than D_{max}^{allow} and F_{max} is smaller than F_{max}^{allow} (5.0 MN); thus the design requirements can be satisfied for all impact scenarios. The maximum impact forces (F_{max}^{unprot}) on the pier for different impact scenarios without using the optimum devices are also tabulated in Table 6 along with the reduction ratio (r_f) of maximum impact forces when the optimum devices are used. It is shown in Table 6 that the optimum device can significantly reduce the maximum impact force on the pier by more than 90.0% for different impact scenarios. Table 6 indicates that for a given impact velocity, F_{max}^{unprot} is not strongly influenced by barge mass. This phenomenon has been explained in detail in [8]. It is also indicated from Table 6 that D_{cap}^{max} is often close to or

TABLE 4: Prespecified parameters for structure optimization.

Member	Parameter	Value
Barge	m_b = barge mass	181.4 ton ~ 1723.7 ton
	v_b = impact velocity	1.0 m/s ~ 5.0 m/s
Cap	w_c = cap width	3.0 m
	m_c = cap mass	100.0 ton
	N_{pl} = number of planes of beam units	2
Steel beams	ρ_{bs} = mass density of beam steel	8020.0 kg/m ³
	E_{bs} = elastic modulus of beam steel	200.0 GPa
	E_t^{bs} = tangent modulus of beam steel	1.5 GPa
	f_y^{bs} = yielding strength of beam steel	350.0 MPa
	ϵ_u^{bs} = failure strain of beam steel	0.25
	N_{bu}^l = lower bound of N_{bu}	1
	N_{bu}^u = upper bound of N_{bu}	10
Design requirements	h_{bi}^l = lower bound of h_{bi}	0.2 m
	h_{bi}^u = upper bound of h_{bi}	1.0 m
	l_{sb}^l = lower bound of l_{sb}	1.0 m
	l_{sb}^u = upper bound of l_{sb}	5.0 m
	F_{max}^{allow} = maximum allowable force on pier	5.0 MN

TABLE 5: Optimum parameters, total masses of beam steel, and configurations of optimum devices corresponding to different impact scenarios.

Impact scenario	N_{bu} (-)	h_{bi} (m)	l_{sb} (m)	m_{sb} (ton)	Optimum structure configuration
IS ₁₁	1	0.20	1.00	0.41	
IS ₁₂	1	0.25	1.26	0.82	
IS ₁₃	1	0.35	1.76	2.22	
IS ₂₁	1	0.23	1.16	0.64	
IS ₂₂	2	0.41	2.04	6.23	
IS ₂₃	2	0.57	2.83	16.62	
IS ₃₁	1	0.29	1.43	1.19	
IS ₃₂	2	0.50	2.51	11.60	
IS ₃₃	2	0.70	3.48	30.77	

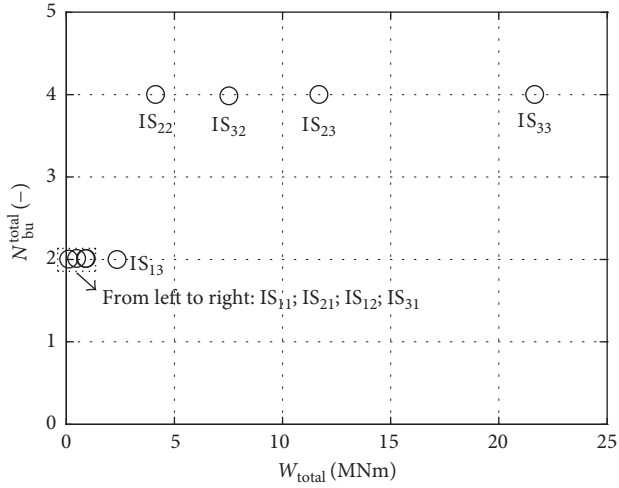
equal to D_{max}^{allow} . This is because for a given impact scenario, decreasing the amount of beam steel would reduce the structure stiffness and consequently lead to the increase of D_{cap}^{max} until the point where D_{cap}^{max} approximately reaches D_{max}^{allow} and the optimum solution is attained.

The maximum bending moment diagrams and deflections of the optimum devices corresponding to impact scenarios IS₃₁, IS₃₂, and IS₃₃ are shown in Figure 20, which shows that the horizontal beams at the top and two vertical beams in the middle experience apparent plastic deformations after impact, enabling the devices to absorb high energy during impact, as shown in Figure 21.

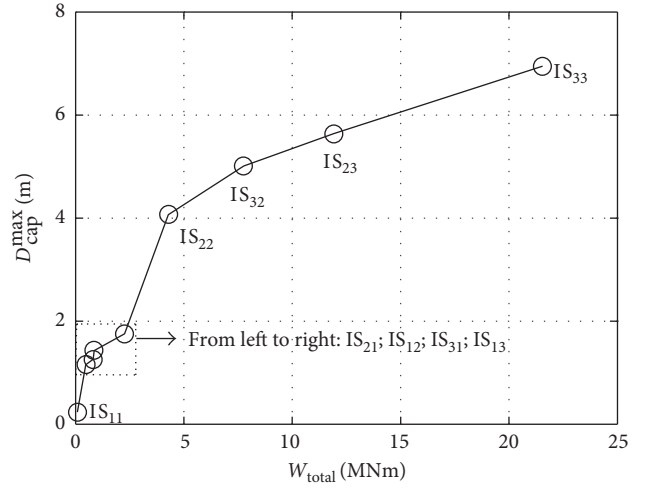
7. Summary

This paper devised a novel crashworthy device for pier protection from barge impact and conducted parametric studies to investigate the effectiveness of the proposed device using the simplified impact model. A mathematical optimization model was developed with constraints as per the prescribed design requirements to achieve cost-optimized design of the device for a given impact scenario.

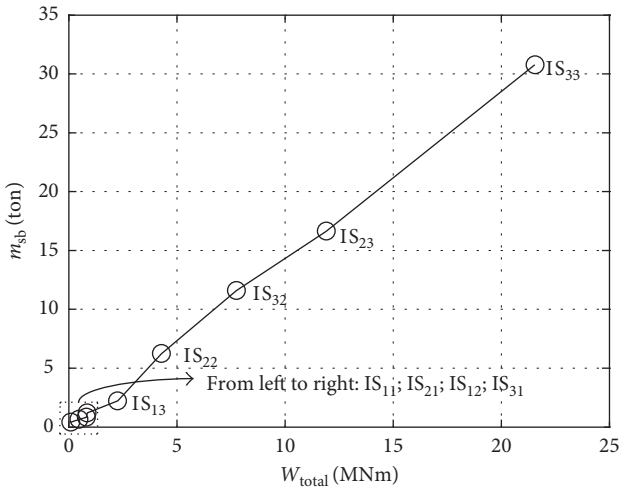
The studies indicate that the proposed crashworthy device has a large energy dissipation capacity due to the



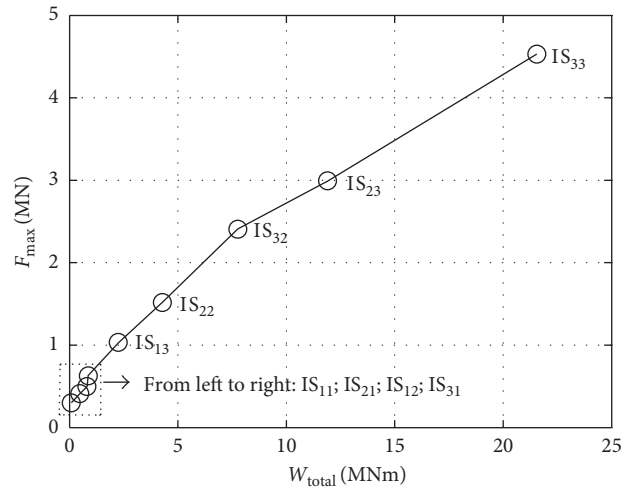
(a)



(a)



(b)



(b)

FIGURE 18: The total number of beam units N_{bu}^{total} and the total mass of beam steel m_{sb} used by the optimum device versus barge impact energy W_{total} ($N_{pl} = 2$).

FIGURE 19: Maximum cap displacement D_{cap}^{max} (a) and maximum impact force on the bridge pier F_{max} (b) versus barge impact energy W_{total} using the optimum device.

TABLE 6: Maximum cap displacements and maximum impact forces on the pier using or without using optimum devices corresponding to different impact scenarios.

Impact scenario	D_{cap}^{max} (m)	D_{max}^{allow} (m)	F_{max} (MN)	F_{max}^{unprot} (MN)	$r_f = 100 \times (F_{max}^{unprot} - F_{max}) / F_{max}^{unprot}$ (%)
IS ₁₁	0.23	1.00	0.30	16.24	98.15
IS ₁₂	1.26	1.26	0.50	39.90	98.75
IS ₁₃	1.75	1.76	1.03	47.57	97.83
IS ₂₁	1.16	1.16	0.41	27.24	98.50
IS ₂₂	4.07	4.08	1.52	39.68	96.17
IS ₂₃	5.64	5.66	2.99	48.53	93.84
IS ₃₁	1.43	1.43	0.63	27.18	97.68
IS ₃₂	5.01	5.02	2.41	39.45	93.89
IS ₃₃	6.95	6.95	4.56	48.63	90.62

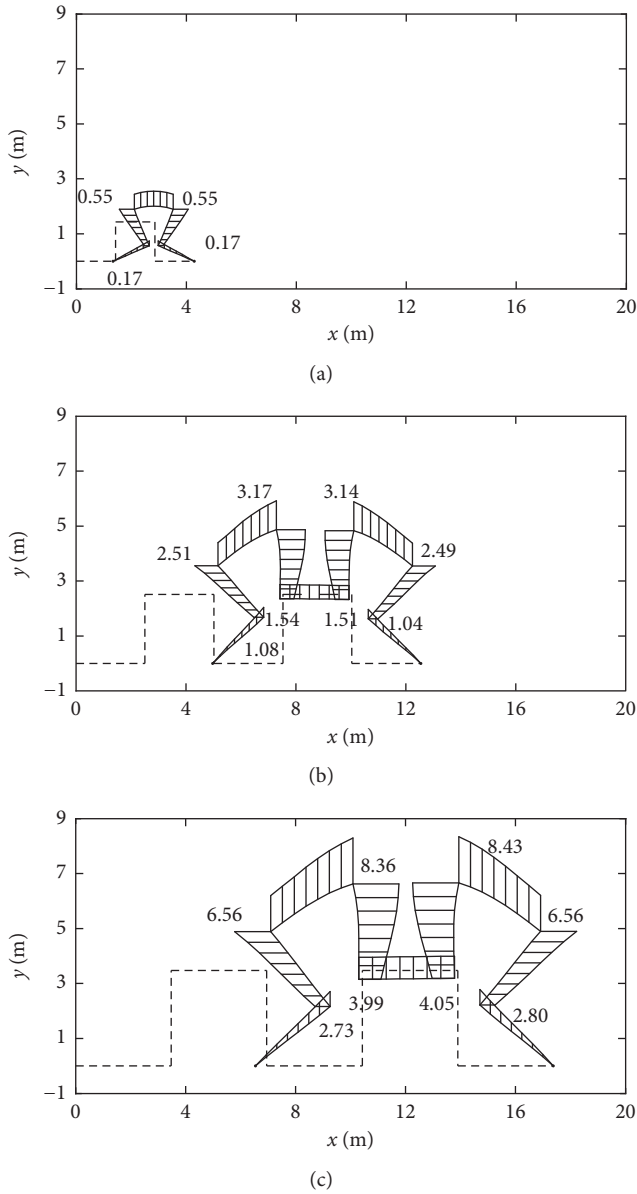


FIGURE 20: Maximum bending moment diagrams of the optimum devices during impact and deflections of the structures after the impact corresponding to the impact scenarios (a) IS₃₁, (b) IS₃₂, and (c) IS₃₃ (unit: MNm). —, original shape of the device; —, deformed shape of the device.

formation of plastic hinges in the structure during impact. These number and location of plastic hinges, and consequently the energy that can be absorbed, is determined by the design of the frame-like steel beam arrangement. The studies show that the magnitude of the impact force transmitted to the main bridge pier can be dramatically reduced when the device is properly designed and installed and that the maximum force transmitted can be chosen as part of the device design. A mathematical optimization model proposed in this paper can be used for obtaining the optimum

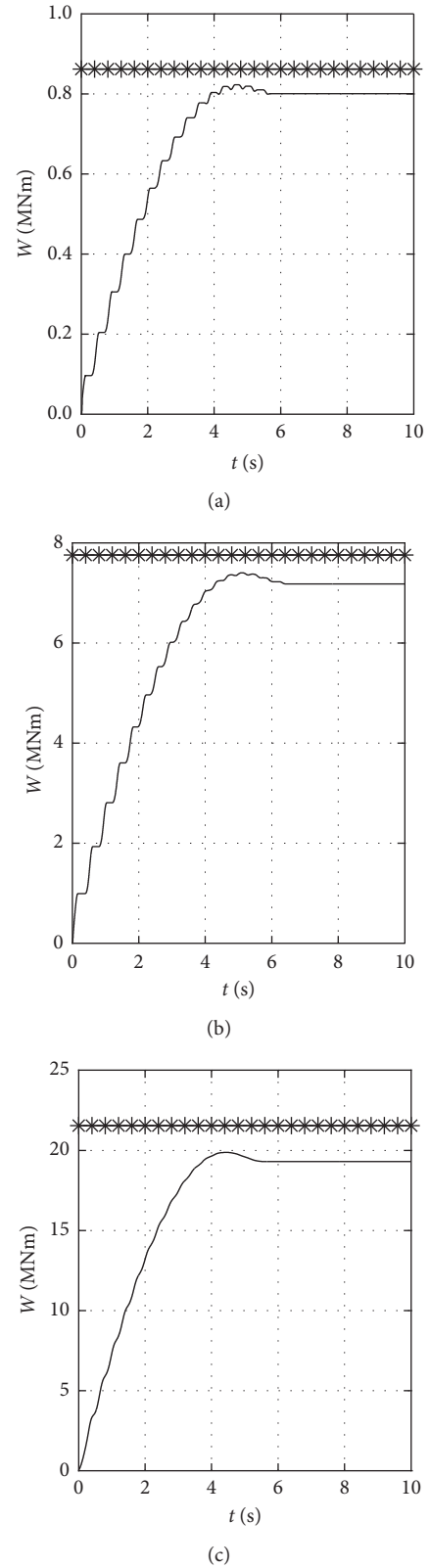


FIGURE 21: Energy absorbed by the optimum device (—) and the total impact energy (—*) during impact corresponding to the impact scenarios (a) IS₃₁, (b) IS₃₂, and (c) IS₃₃.

configuration of the device which satisfies the design requirements for a given impact scenario.

The concept proposed here can be extended further to other configurations, for example, symmetrical or entwined arrangements which avoid vertical displacements or reduce the device's overall dimensions, respectively.

The device concept presented and the analysis model adopted have the potential to rationalize ship impact protection and thus to provide cost-effective future protection solutions.

Conflicts of Interest

The authors declare that there are no conflicts of interest regarding the publication of this paper.

Acknowledgments

The authors wish to thank the China Scholarship Council for providing scholarship to W. Wang for conducting the study.

References

- [1] S. E. Manen and A. G. Frandsen, "Ship collision with bridges, review of accidents," in *Ship Collision Analysis*, H. Gluwer and D. Olsen, Eds., pp. 3–11, Balkema, Rotterdam, Netherlands, 1998.
- [2] O. D. Larsen, *Ship Collision with Bridges, the Interaction between Vessel Traffic and Bridge Structures*, IABSE, Zuerich, Switzerland, 1993.
- [3] P. Yuan, *Modeling, Simulation, and Analysis of Multi-Barge Flotillas Impacting Bridge Piers*, Ph.D. thesis, Department of Civil Engineering, University of Kentucky, Lexington, Kentucky, 2005.
- [4] C. H. Cao, *Simplified Static and Dynamic Analysis for Barge-Bridge Collision*, M.S. thesis, Department of Bridge Engineering, Tongji University, Shanghai, China, 2010, in Chinese.
- [5] Y. Y. Sha and H. Hao, "Laboratory tests and numerical simulations of barge impact on circular reinforced concrete piers," *Engineering Structures*, vol. 46, pp. 593–605, 2013.
- [6] Y. Y. Sha and H. Hao, "Laboratory tests and numerical simulations of CFRP strengthened RC pier subjected to barge impact load," *International Journal of Structural Stability and Dynamics*, vol. 15, no. 2, p. 1450037, 2015.
- [7] Y. Y. Sha and H. Hao, "Nonlinear finite element analysis of barge collision with a single bridge pier," *Engineering Structures*, vol. 41, pp. 63–76, 2012.
- [8] W. Wang and G. Morgenthal, "Dynamic analyses of square RC pier column subjected to barge impact using efficient models," *Engineering Structures*, vol. 151, pp. 20–32, 2017.
- [9] R. Saul, K. Humpf, and A. Patsch, "The Rosario-Victoria cable-stayed bridge across the river Paran ; in Argentina and its ship impact protection system," in *Proceedings of the First International Conference on Steel and Composite Structures*, pp. 1011–1018, Pusan, South Korea, June 2001.
- [10] G. Morgenthal and R. Saul, "Die Geh- und Radwegbruecke Kehl–Strasbourg," *Stahlbau*, vol. 74, no. 2, pp. 121–125, 2005, in German.
- [11] M. Knott, "Pier protection system for the sunshine skyway bridge replacement," in *Proceedings at 3rd Annual International Bridge*, pp. 56–61, Pittsburgh, PA, USA, 1986.
- [12] B. C. Simonsen and N. Ottesen-Hansen, "Protection of marine structures by artificial islands," in *Proceedings of the International Symposium on Advances in Ship Collision Analysis*, Balkema Publishers, pp. 201–215, Copenhagen, Denmark, May 1998.
- [13] H. Svensson, "Protection of bridge piers against ship collision," *Steel Construction*, vol. 2, no. 1, pp. 21–32, 2009.
- [14] R. Pinzelli and K. Chang, "Reinforcement of bridge piers with FRP sheets to resist vehicle impact: tests on large concrete columns reinforced with aramid sheets," in *Proceedings of the International Conference on FRP Composites in Civil Engineering*, pp. 12–15, Hong Kong, China, December 2001.
- [15] T. N. Le, J. M. Battini, and M. Hjjaj, "Corotational dynamic formulation for 2d beams," in *ECCOMAS Thematic Conference on Computational Methods in Structural Dynamics and Earthquake Engineering*, Corfu, Greece, May 2011.
- [16] W. Hock and K. Schittkowski, "A comparative performance evaluation of 27 nonlinear programming codes," *Computing*, vol. 30, no. 4, pp. 335–358, 1983.

Research Article

Dynamic Response of Steel Box Girder under Internal Blast Loading

Shujian Yao ^{1,2}, Nan Zhao,^{1,3} Zhigang Jiang,⁴ Duo Zhang,² and Fangyun Lu²

¹School of Traffic and Transportation Engineering, Central South University, Changsha, Hunan 410075, China

²College of Science, National University of Defense Technology, Changsha, Hunan 410073, China

³PowerChina, Zhongnan Engineering Corporation Limited, Changsha, Hunan 410072, China

⁴College of Basic Education, National University of Defense Technology, Changsha, Hunan 410072, China

Correspondence should be addressed to Shujian Yao; yaoshujian@gmail.com

Received 16 August 2017; Revised 6 November 2017; Accepted 5 December 2017; Published 29 March 2018

Academic Editor: Michel Arrigoni

Copyright © 2018 Shujian Yao et al. This is an open access article distributed under the Creative Commons Attribution License, which permits unrestricted use, distribution, and reproduction in any medium, provided the original work is properly cited.

This paper aims at investigating the dynamic response of the steel box girder under internal blast loads through experiments and numerical study. Two blast experiments of steel box models under internal explosion were conducted, and then, the numerical methods are introduced and validated. The dynamic response process and propagation of the internal shock wave of a steel box girder under internal blast loading were investigated. The results show that the propagation of the internal shock wave is very complicated. A multi-impact effect is observed since the shock waves are restricted by the box. In addition, the failure modes and the influence of blast position as well as explosive mass were discussed. The holistic failure mode is observed as local failure, and there are two failure modes for the steel box girder's components, large plastic deformation and rupture. The damage features are closely related to the explosive position, and the enhanced shock wave in the corner of the girder will cause severe damage. With the increasing TNT mass, the crack diameter and the deformation degree are all increased. The longitudinal stiffeners restrict the damage to develop in the transverse direction while increase the crack diameter along the stiffener direction.

1. Introduction

Since the 9–11 attacks by terrorists, there has been increasing public concern about the threat of bomb attacks on infrastructure such as bridges and tunnels as well as buildings. Major and monumental bridges might be targeted by terrorists because collapse of these structures can cause economic disaster, a large number of casualties, and great public panic. Therefore, protection of major bridges against blast load has been attached great importance by the international bridge community [1–3].

Many scholars studied the responses of concrete bridge structural components under blast loadings by using simplified theory method, such as Timoshenko beam theory [4] and analysis of equivalent single degree of freedom (SDOF) system [5–8]. These simplified methods are very efficient, but it is difficult to give reliable predictions of localized damages. However, with the advancement in computer technology

and computational mechanics techniques, the numerical simulation method had been widely used in investigations of blast effect on structures, and these simulations are proved yielding to reliable structural response predictions [9, 10].

Large span cable-supported bridge is under great risk of terrorist bomb attacks; many scholars processed numbers of numerical simulation studies on it. Through numerical simulations, Deng et al. [11] analyzed the impact damage of continuous steel truss single tower cable-stayed bridge under blast loads, and Son [12] and Son and Lee [13] analyzed the explosion impact response of the deck and the tower structure of cable-supported bridge. Tang and Hao [14] and Hao and Tang [15] studied the localized destruction of the bridge towers, piers, and deck structure as well as the overall collapse of a long span cable-stayed bridge under car bomb blast loading through numerical simulations with the nonlinear finite element software LS-DYNA.

Steel box girder has many advantages, such as much lighter, easy shaped, and can save construction time, and is now become the most common type of the main beam of large span cable-supported bridge. The response of orthotropic steel decks and steel box girders under terror blast loading was investigated with ANSYS/LS-DYNA by Jiang et al. [16], and the breach process and failure mechanism of the deck had been analyzed deeply.

Researches in [17–20] had shown that interaction mechanism of internal blast is more complex, and the destructive effect is more strongly than free air explosion, so the study of internal explosion of steel box girder is necessary and imperative.

The ALE fluid-structure coupling algorithm can consider the influence of the structure's response to the propagation of shock wave and is approved of accuracy [21–24]. In the current study, the numerical methods are validated through comparison of experimental and numerical results. Then, finite element models of the steel box girder are established and numerical simulations are carried out with ANSYS/LS-DYNA using the ALE algorithm. The dynamic response process and propagation of internal shock wave inside the steel box girder are analyzed. The failure mode and the influence of blast position as well as explosive mass are also discussed.

The results obtained in this study give information for owners of similar type of structures on the probable responses when subjected to internal blast loads and can assist engineers to choose the most effective retrofit measures to bring in better resistance against internal blast loads.

2. Validation of the Numerical Method

2.1. Experimental Setup. To validate the effectiveness of the numerical method for the box-shaped steel structure under internal blast, two steel box models with the same dimension were designed and manufactured to conduct internal blast experiments. The box model is made up of 2 mm thickness Q235 mild steel plates with Young's modulus of 200 GPa. The yield strength and ultimate strength of Q235 steel are 370 MPa and 485 MPa, respectively, which are obtained through tensile test with MTS.

The steel box specimen is shown in Figure 1. The side length of all side plates is 300 mm, and an extra length of 60 mm is welded to every box side plate for the purpose of simulating the constraint condition. A hole is reserved in the center of the top plate for the purpose of placing the explosive. The final dimension of the specimens is 420 mm × 420 mm × 420 mm. Two different explosive masses of 12.8 g and 40.2 g are selected with the purpose of examining different damage degrees.

2.2. Numerical Model. Finite element models with the same dimension of experiments were built by ANSYS/LS-DYNA; the box model is shown in Figure 2(a). The explosive is defined in the central region of air as shown in Figure 2(b). The explosive and air are meshed with the eight-node element SOLID164, while the box is meshed with four-node

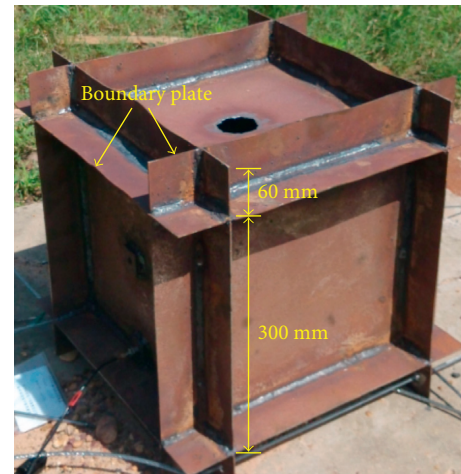


FIGURE 1: Steel box specimen.

element SHELL163. The fluid-structure interaction algorithm is adopted to model the impacts of blast wave to structure. The mesh size of structure and air are 5 mm and 4 mm, respectively. The total element numbers for the shell and solid are 42,820 and 1520,875, respectively.

In these numerical models, *MAT_HIGH_EXPLOSIVE_BURN is used for high explosives (TNT), and the JWL equation of state is adopted to model the pressure generated from blast [25]. The Johnson–Cook material model together with the Gruneisen state equation is used to model the dynamic behavior of the steel box [26, 27].

2.3. Comparisons of Numerical and Experimental Results. Figure 3 shows the comparison of damage features obtained from both blast tests and numerical simulations. Outward bulging of the whole plate is observed in all sides of all tests, and in-plane buckling produces in the central area of the boundary plates. These damage features are all observed in numerical results as shown in the right-side pictures of Figure 3 which indicate that the numerical model can simulate the damage features well.

The side plate center deflection-time curves obtained through numerical simulations of both tests are shown in Figure 4. The ultimate plate center deflections of experiments were measured by using an electronic digital display depth caliper, and the ultimate deflections for 12.8 g and 40.2 g TNT tests are 14.9 mm and 34.4 mm, respectively. The ultimate deflections of simulation results cannot be obtained directly since the calculating time is limited. However, the deflection data after the first extreme value present a phenomenon of oscillation around a specific value as shown in Figure 4. Hence, the ultimate deflections could be estimated through analyzing the corresponding deflection-time curves. The estimated ultimate deflections for 12.8 g and 40.2 g TNT simulations are 15.5 mm and 35.5 mm, respectively. It shows that the maximum error of 4% occurs in the FEM calculated to caliper measured of experiments.

The above analyses indicate that the deformation features and deflection data obtained through finite element

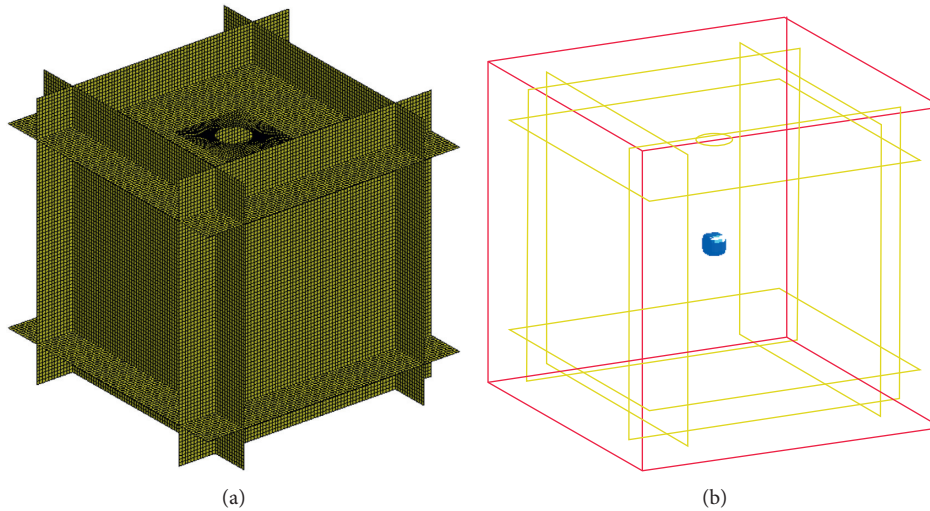


FIGURE 2: Finite element model. (a) Box model. (b) Air and explosive.

method are in good agreement with the experimental results, and hence the numerical method is validated.

3. Finite Element Models of Steel Box Girder under Internal Blast Loading

Considering the localized effect of blast load and the calculated efficiency, a segment of the steel box girder has been selected as the analytical model in this paper. Figure 5 shows the girder's cross section and four typical explosive positions; the bombs in positions 2 and 3 have only one-side contact to the soleplate, while positions 1 and 4 have two or three sides contact to soleplate and diaphragms, named multisides contact. The position 4 located next to the joint of four boxes, 1.96 m away from position 1. The length of the girder segment (along the direction of bridge) is 12.0 m; the distance of two transverse diaphragms is 4.0 m; the thickness of the diaphragm is 12 mm; the width of the roof (along the transverse direction of bridge) is 20.12 m and thickness is 14 mm, while the bottom plate is 17 m and thickness is 10 mm; the thickness of longitudinal diaphragm is 9 mm and U-shaped stiffener is 6 mm [17, 28]. The calculation model is shown in Figure 6: situation of positions 1~3 is longitudinal symmetry, and a 1/2 segment model is given, while position 4 is unsymmetrical, a 2/3 segment model is selected which includes 3 transverse diaphragms (as shown in Figure 6(b)). 8-node solid element type (SOLID164) is used for modeling air and TNT; SHELL163 element type is selected for the steel box in these simulations. The automatic single surface contact type (*Contact_Automatic_Single_Surface) is defined to consider the contact and collision of different plates or fragments. The mesh size for the girder is 5 cm, and the mesh size for air is in proportion to the explosive distance (the mesh size for the central zone of explosive position is smaller than 2 cm).

With the purpose of investigating the influence of blast position and explosive mass, two sets of simulations are designed. The first set is for the blast position, in which four typical blast positions (Figure 5) are selected with an

explosive mass of 23 kg TNT (typical suitcase bomb). The other set is for explosive mass where four different TNT masses ranging from 10 kg to 50 kg are detonated in position 2 (as shown in Figure 5).

4. Response Process and the Propagation of Internal Shock Waves

4.1. One-Side Contact Explosion Situation. The response process of the bomb exploded in positions 2 and 3 is similar because they both belong to the type of one-side contact which leads to serve destruction only in the TNT-concluded box while the neighboring box is less influenced. The position 2 is taken as an example to study the response process for position 2 located next to the chamber center which is more typical. In Figure 7, some pressure fringe plots at typical time are given, and the pressure unit in these plots is Pa. Figure 8 shows the positions of 4 elements and their ID in the four corners of the right box chamber as well as their pressure-time curves.

The response progresses are as follows: $t \approx 0.14$ ms, the bottom plate has generated local large deformation; $t \approx 0.78$ ms, the shock wave has reached the roof first time; thereafter, the shock wave reflects back from the roof. When the shock wave arrives the diaphragm and longitudinal clashboard, deformation is caused immediately, and then the shock waves reflect back again to the center of the roof from both sides of the diaphragms at $t \approx 4.4$ ms which causes a secondary impact; $t \approx 8.8$ ms, shock waves convergence occur at the four corners of the box, at which larger over-pressure produces (as shown in Figure 8), and the shock waves converge in the ">" shaped corner (constituted by the right-inclined web and roof) and was much more stronger which led to a severer impact on the roof (as shown in Figure 9); shock waves reach the joint of the longitudinal clashboard and bottom plate again at $t \approx 16.74$ ms causing secondary impacts (element B position and pressure-time curves are shown in Figure 8); after that, multiple reflections take place while the shock wave intensity gradually decreases.

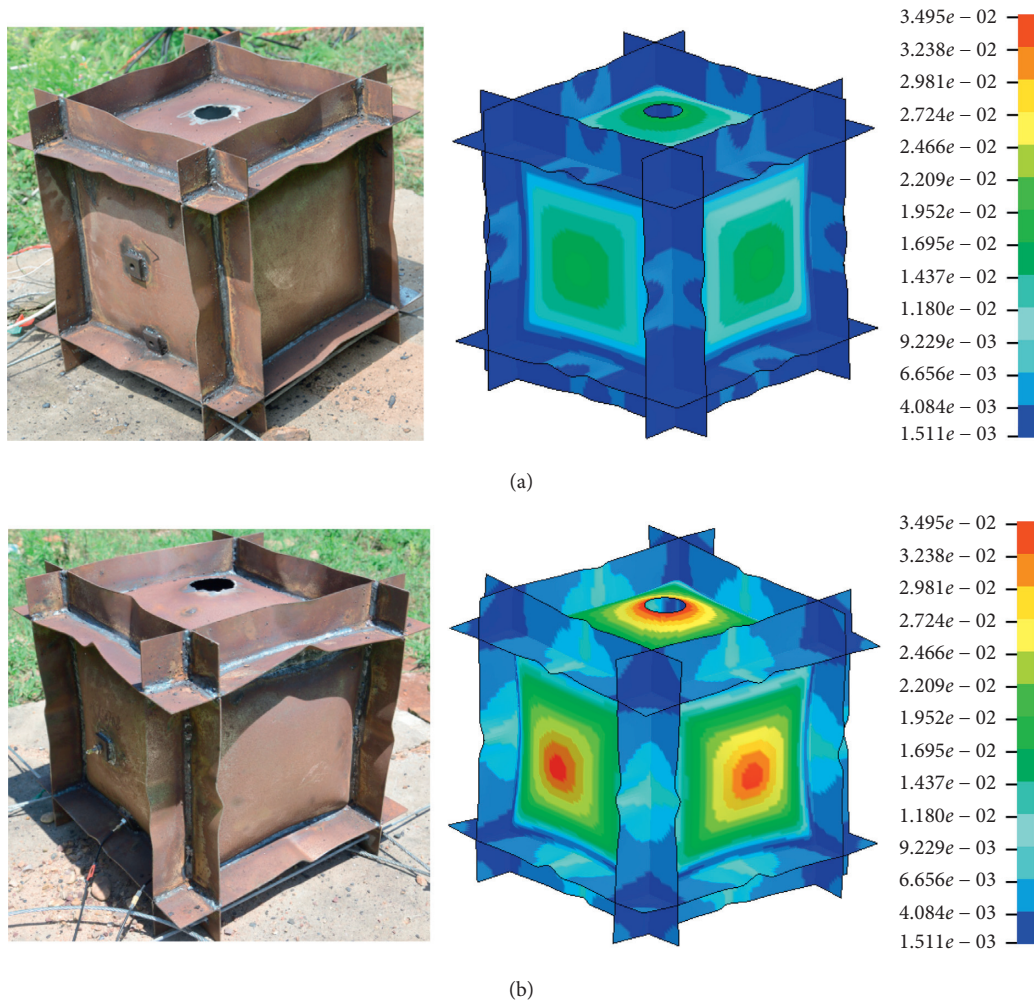


FIGURE 3: Deformation comparison between experimental result and numerical result (the left picture is the experimental result and the right is numerical). (a) 12.8 g TNT. (b) 40.2 g TNT.

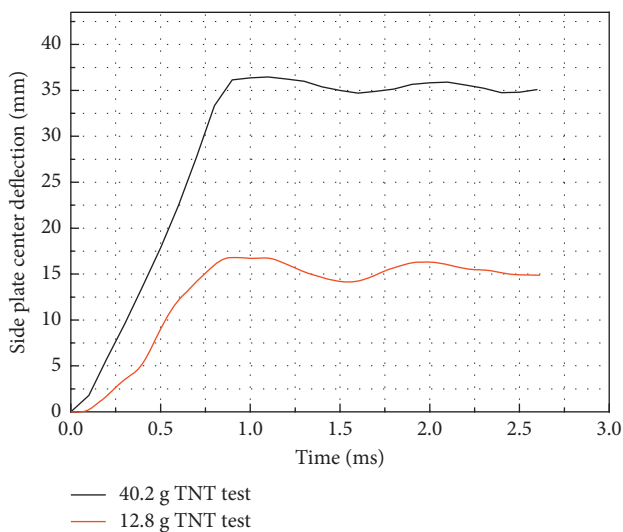


FIGURE 4: The side plate center deflection-time curves obtained through numerical simulations.

From Figure 8, elements B and D reach the first peak pressure at $t \approx 8.76$ ms, and the magnitude of unit B is up to 0.82 MPa; $t \approx 14$ ms, unit A reaches the second peak pressure 0.3 MPa, and at $t \approx 17$ ms, element B reaches a second peak pressure of 0.36 MPa, the second impact peak pressure can reach more than one-third of the first peak pressure, and it seems that the second impact effect cannot be neglected; and then series of reflection peak pressure were also observed though the pressure magnitude attenuated.

In Figure 9, the fringe plot of displacement and the elements' position of the deck is shown; the element of the deck (element 1218 to 23,658) in order from left to right is counted as A~D. Figure 10 shows the deflection-time curves (positive upward) of the elements A~D. From Figures 9 and 10, the positions close to elements C and D have maximum deformation, where element C was under direct impact by the shock wave, while the explosive distance of element D is farther but located at the corner where the shock wave aggregation effect strengthened in, so big deflection of about 0.093 m appeared in those two areas.

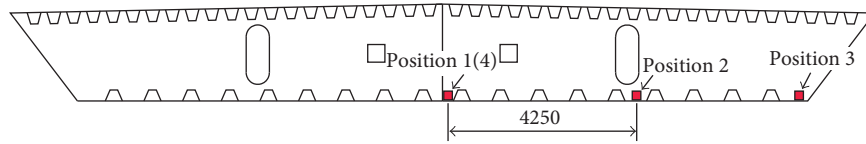


FIGURE 5: Cross section and explosive positions (unit: mm).

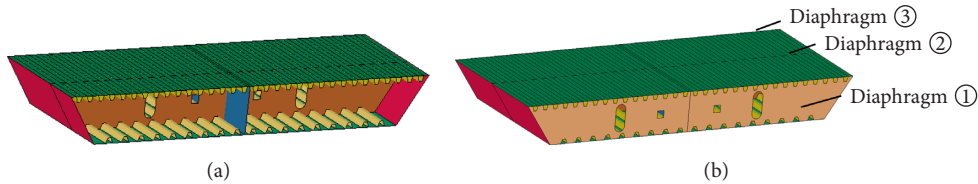


FIGURE 6: Finite element models. (a) 1/2 girder. (b) 2/3 girder.

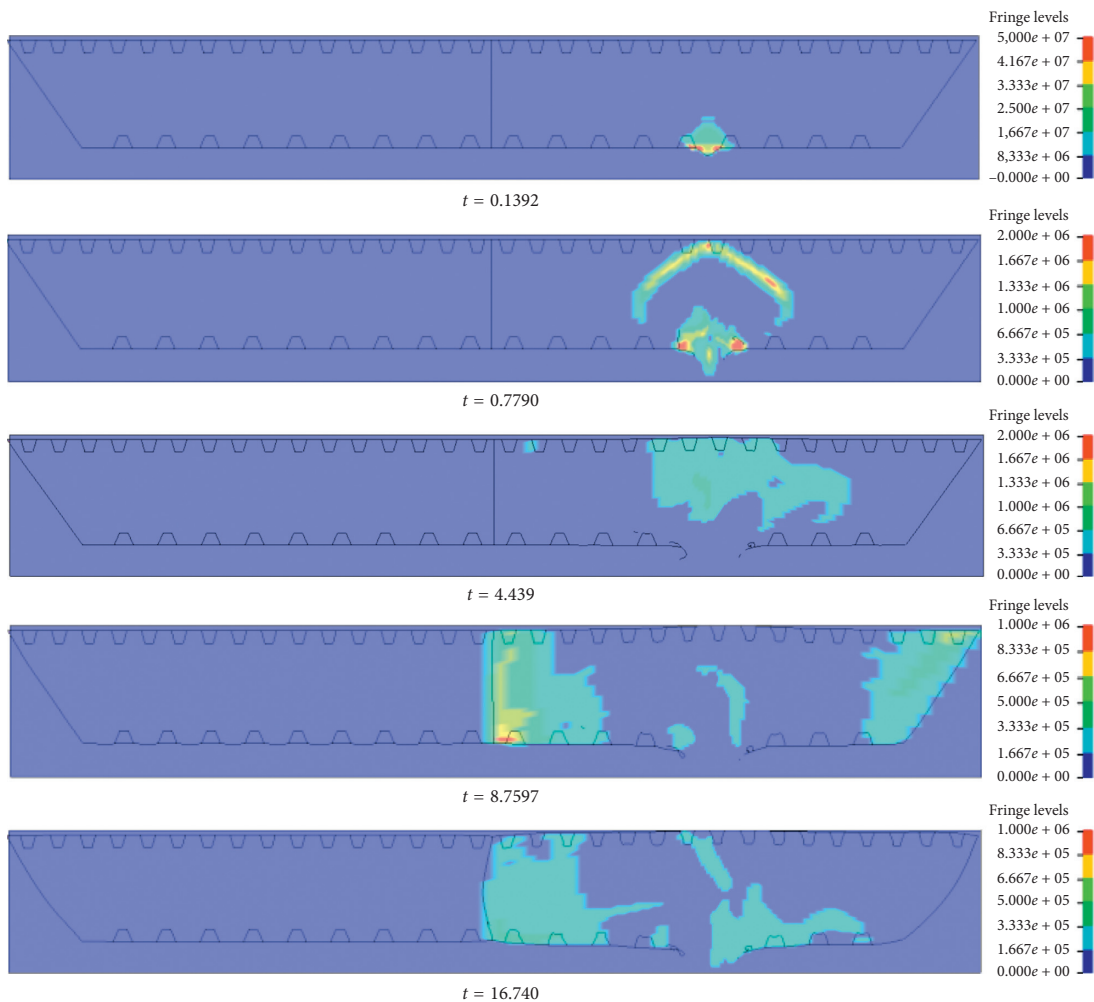


FIGURE 7: Pressure evolutions of explosion in position 2 (middle cross section, time unit: ms).

4.2. *Multiside Contact Explosion Situation.* Blasts in position 1 and position 4 belong to multiside contact explosion, especially position 4 close to three plates; the blast wave was constrained seriously by 3 sides, and the adjacent four box chamber was greatly influenced. For this reason, the position 4 explosion was selected to analyze the response

process and damage effects. Figure 11 shows some pressure fringe plots at typical time, and the pressure unit in these plots is Pa.

The response processes are $t \approx 0.1$ ms, the bottom plate and longitudinal, transverse diaphragm had already produced local large deformation and cracks, and the bottom

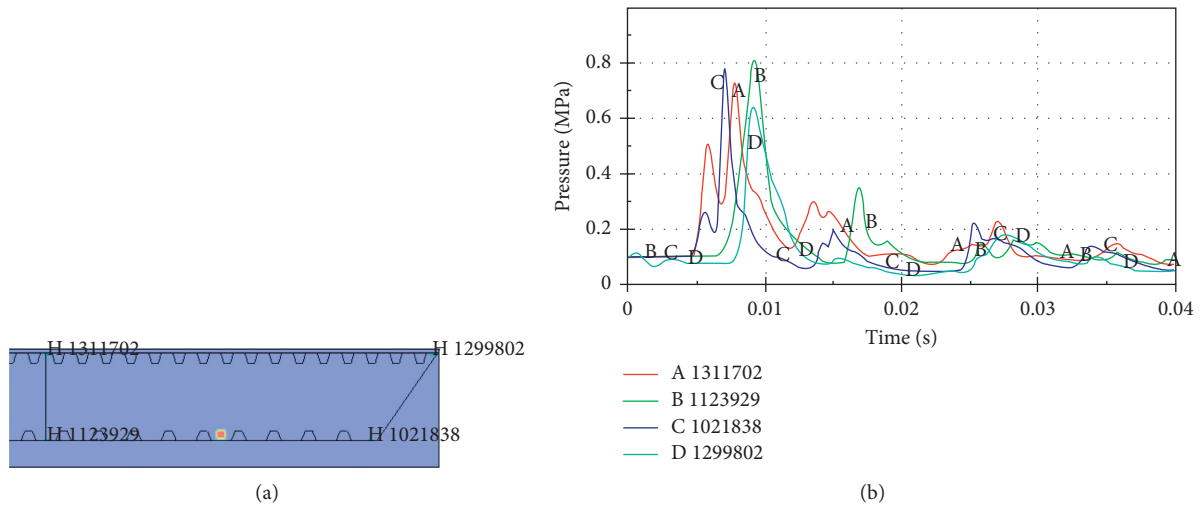


FIGURE 8: (a) The elements' position and (b) pressure-time curves.

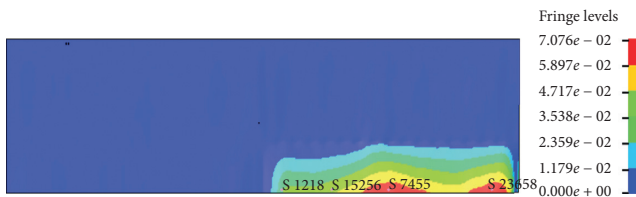


FIGURE 9: Fringe plot of displacement and the elements' position of the deck (top view, unit: m).

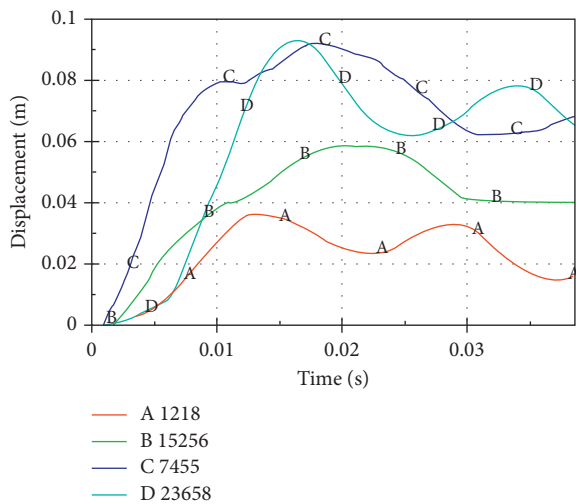


FIGURE 10: Deflection-time curves of the deck.

plate and diaphragm plate ② has fragments produced; $t \approx 0.8$ ms, the shock wave reaches the roof, and the roof begins to deform; $t \approx 1.5$ ms, the shock wave reaches diaphragm plate ①; $t \approx 2.8$ ms, the shock waves are encountered in the top right-hand corner of the right-hand box chamber, and at the same time, the shock wave crosses the hole in diaphragm plate ② and traverses the left box chamber and reaches diaphragm plate ③; $t \approx 5.2$ ms, the shock waves in the left box chamber are converged in the

upper-left corner; at the same time, the roof diaphragm plate ① in the right box room has produced great deformation; $t \approx 9.8$ ms, the shock waves in the right box reflect back again and encounter at the place just below the roof and above the explosive directly; element B reaches the extreme values for the first time; since then, multiple reflections take place in each box chamber while the shock wave intensity rapidly reduces.

5. Discussions

5.1. Damage Mode Analysis. The fringe plots of final displacement of different whole models, bottom plate, and roof are given in Figures 12–14. The longitudinal and transverse diaphragms have been destroyed seriously when the bomb is exploded in position 1 and position 4; a diameter of larger than 1 m breaches is observed in the longitudinal diaphragm in both positions 1 and 4; the damage degree in position 2 is much lighter, which may be because of the bomb in position 2 only in contact with one side (the bottom plate), which means constraint effect is not obvious. In position 3, the deformation of the roof is the largest, which may be caused by the impact of the shock wave converged in the top right corner. The damage degree is the most serious in position 4 as shown in Figures 13 and 14.

The three transverse diaphragms' deformation and the final damage shape of explosion in position 4 are shown in Figures 15 and 16. The diaphragm ② is cracked, and the crevasse size is $0.91 \text{ m} \times 0.75 \text{ m}$, and the diaphragms ① and ③ undergo great deformation, and the deformation is in opposite directions, which are caused by shock waves in different chambers. The final shape of damage shows that the local failure is serious, and the tearing break phenomenon at the weld zone is obvious.

On the whole, the failure mode of the steel box girder includes two levels; one is the holistic failure mode of the steel box, and the other is the failure mode of plates. The holistic failure mode presented local failure obviously in the

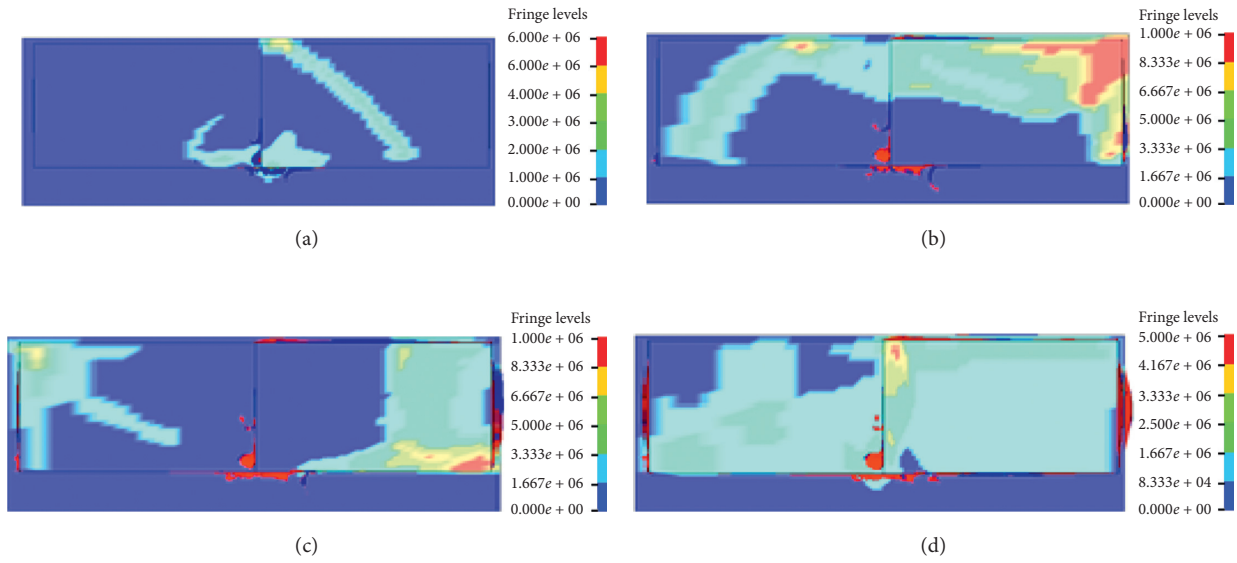


FIGURE 11: Response process of explosion in position 4 (the axial longitudinal section, time unit: ms). (a) $t = 0.7994$. (b) $t = 2.7986$. (c) $t = 5.1991$. (d) $t = 9.7986$.

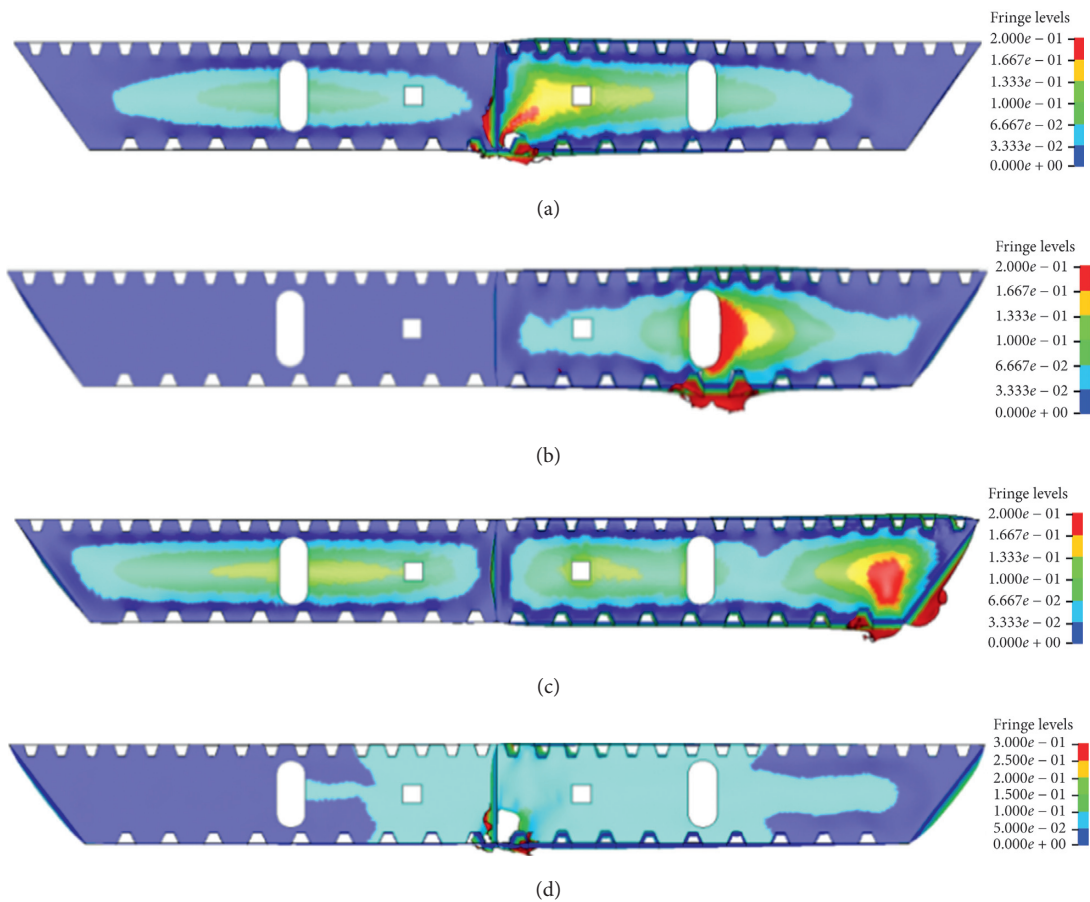


FIGURE 12: Fringe plot of the final displacement of the box girder (unit: m). (a) Position 1. (b) Position 2. (c) Position 3. (d) Position 4.

current study under four explosive positions: the plates close to the blast occurred crevasse and serve deformation (the bottom plate is cracked; nearby U-shaped ribs are destroyed), and the plate in the distance produced large plastic deformation

caused by shock wave in which the pressure magnitude is much lower compared to that of the nearby blast wave.

The plates' failure mode can be divided into two kinds as follows: namely, inelastic large deformation and

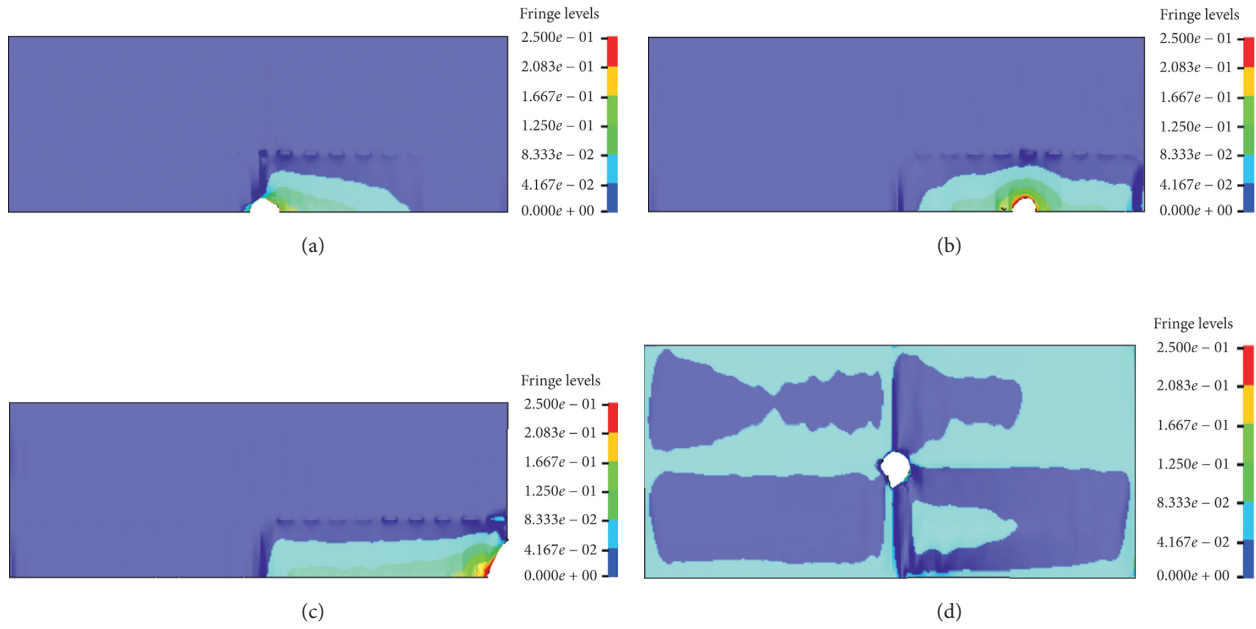


FIGURE 13: Fringe plot of the final displacement of the bottom plate (top view, unit: m). (a) Position 1. (b) Position 2. (c) Position 3. (d) Position 4.

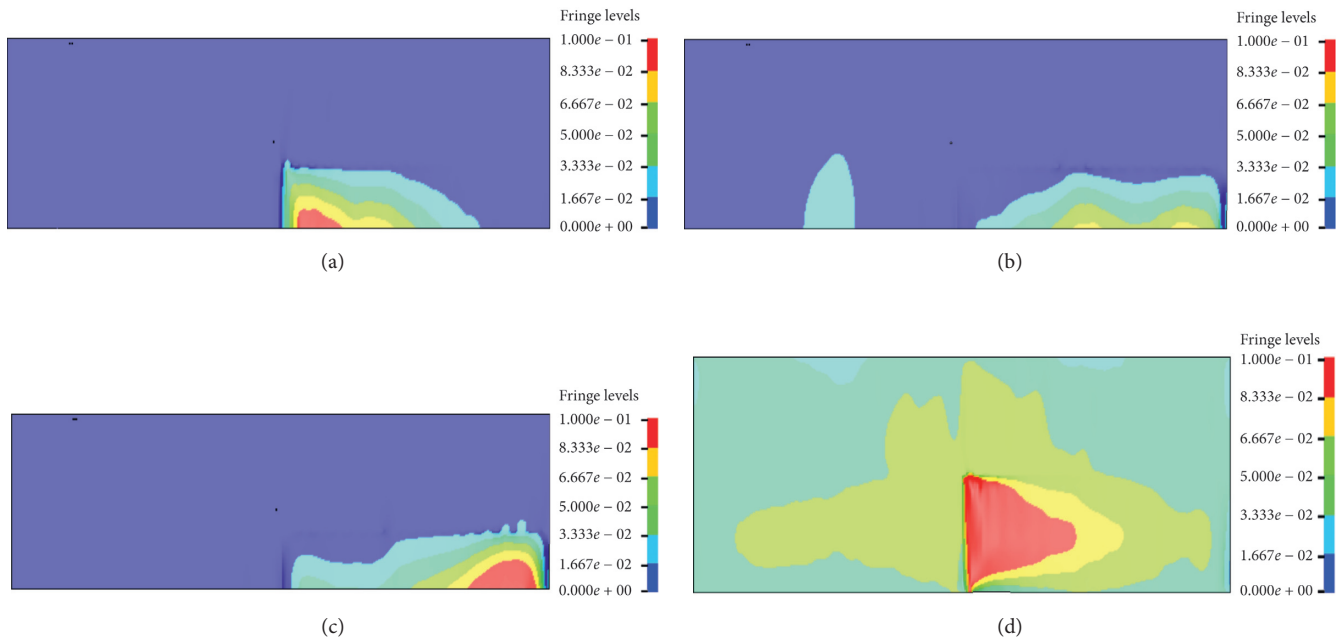


FIGURE 14: Fringe plot of the final displacement of the deck (top view, unit: m). (a) Position 1. (b) Position 2. (c) Position 3. (d) Position 4.

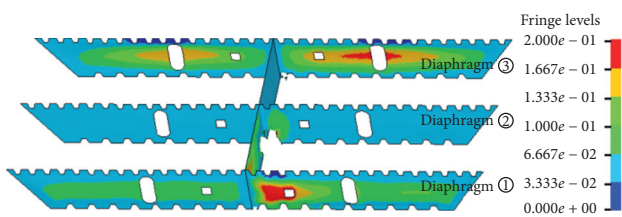


FIGURE 15: Fringe plot of diaphragm's displacement (unit: m).

crevasse. The plates near the bomb all undergo cracking and breach (such as the bottom plate), while most plates in distance suffered air shock wave-produced plastic deformation, mainly manifested bulking in the plate center.

5.2. Analysis of Blast Position. The main damage parameters of the girder are given in Figures 17 and 18.

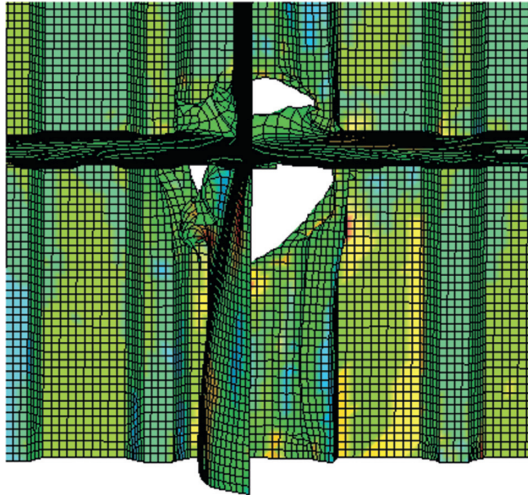


FIGURE 16: Final damage shape of explosion in position 4 (time unit: ms).

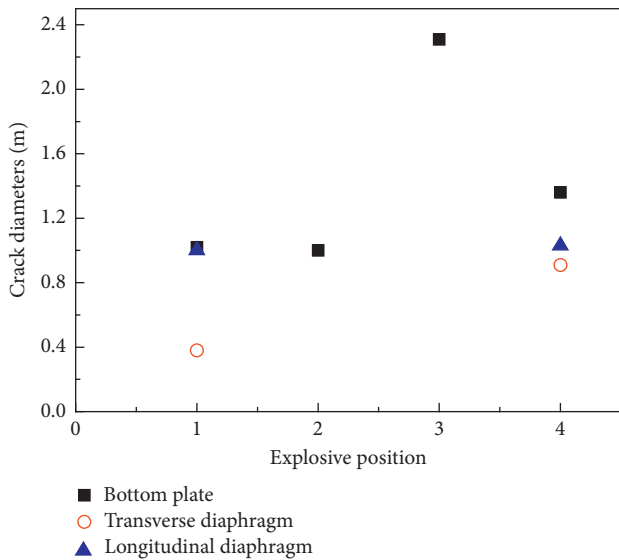


FIGURE 17: Crevasse diameter of plates in different explosive positions.

- (1) To the bottom plate, 1 m diameter’s breach is produced when blast starts off in positions 1, 2, and 4, while in position 3, a crack up to 2.31 m is emerged which may be caused by the split effect along the weld line between the inclined web and bottom plate. It can also be found out that the crevasse dimensions along the longitudinal direction are bigger than that along the transverse direction, which is because the U-shaped rib limited the development of crevasse along the transverse direction. A diameter range of 3 meters around positions 1~3 has experienced plastic deformation, while in position 4, the range of plastic deformation is far less due to the constraint effect of longitudinal and transverse diaphragm.

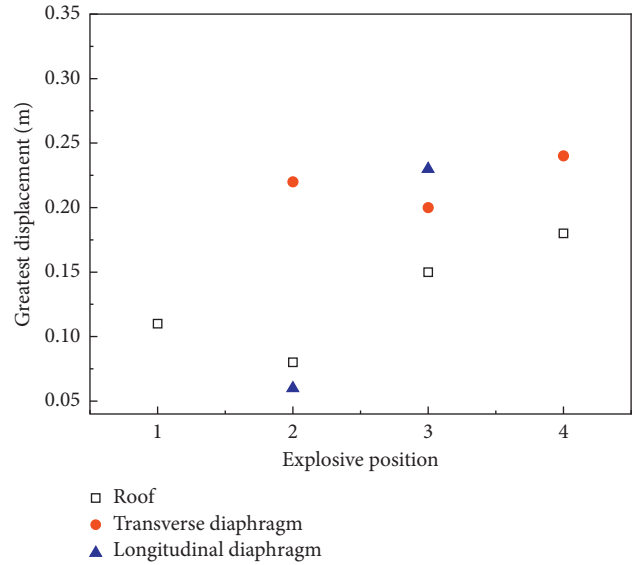


FIGURE 18: Greatest displacement of plates in different explosive positions.

- (2) To the roof, great upward deflection is generated, especially in position 4 in which the shock wave is constrained and converged in the up-right corner of the box girder. And a range of 4.35-meter longitudinal plastic deformation is produced because of the same reason.
- (3) To the diaphragm plate, the crevasse is only observed in position 1 and position 4; the crevasse reason in position 1 is that the shock wave was reflected and converged by the bottom plate and longitudinal diaphragm, in position 4 is the small blast standoff distance.
- (4) To the longitudinal diaphragm, breaches only produce in close-in explosion (position 1 and position 4); the damage parameters of inclined web are not given here because only one crevasse up to 2.3 m produced in the right-inclined web (the same as the bottom plate).

To sum up, the explosive position has great influence on the damage degree. Explosion in position 4 creates the severest damage which may be caused by the three sides’ constraint condition of explosive. And vice versa, in position 2, the damage degree is relatively light; only the bottom plate produced a breach; the roof’s displacement and plastic district range are minimums. To mitigate the damage degree and reduce the damage parameter of the steel box girder, some measures can be taken as follows: (1) improve the weld strength, to reduce split failure along the joint of plates; (2) increase the explosion-proof distance in the box corner, to prevent multichamber damage; and (3) set up transverse stiffener, to limit the development of the longitudinal crack.

5.3. Analysis of Explosive Mass. The damage features of different explosive masses exploded in position 2 are shown

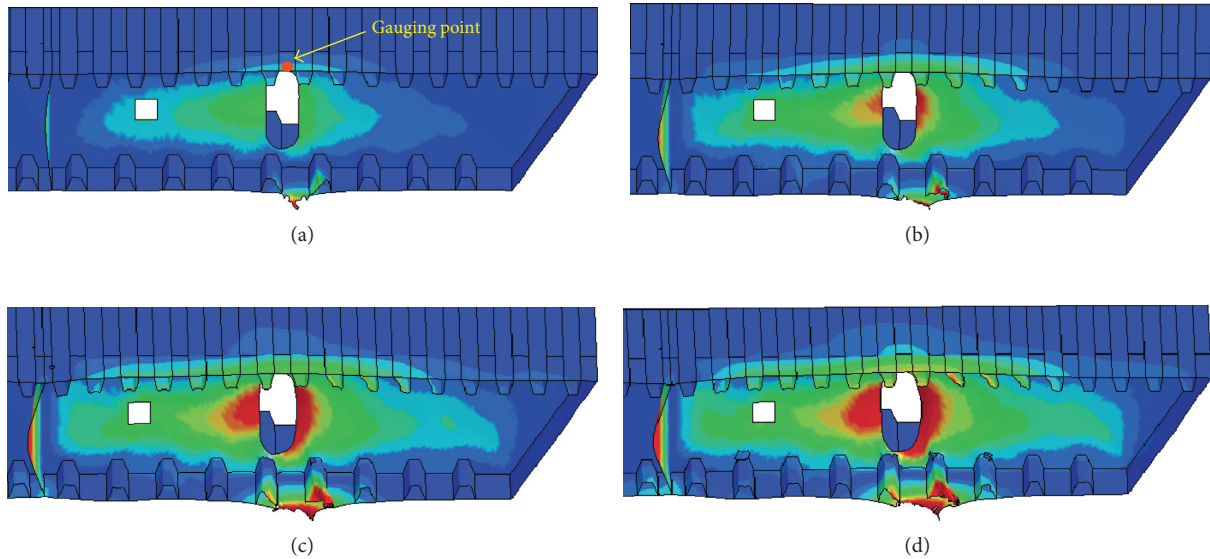


FIGURE 19: Damage features of different explosive masses in position 2. (a) 10 kg TNT. (b) 23 kg TNT. (c) 36 kg TNT. (d) 50 kg TNT.

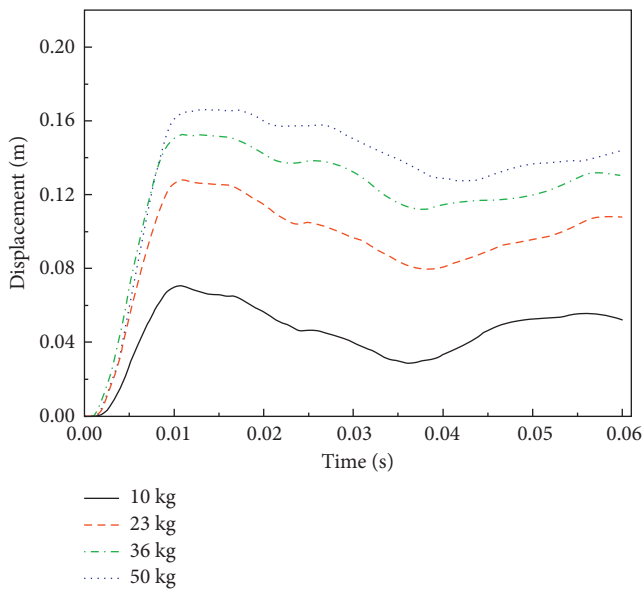


FIGURE 20: Displacement-time curves of the roof.

in Figure 19. With the increasing of TNT mass, the crack diameter in the bottom deck, the deformation degree of the roof, and the transverse and longitudinal diaphragm are all increased. Figure 20 shows the displacement-time curves of the gauging point in the roof (Figure 19(a)). The maximum deflections occur at about $t=0.01$ s with the magnitudes of 0.07 m in 10 kg TNT case and 0.162 m in 50 kg TNT case. Figure 21 shows the crack diameter of the bottom plate of both transverse and longitudinal directions. The results show that the longitudinal crack is bigger than that of the transverse crack in all cases, and the longitudinal crack increases sharply with the TNT mounting up while the transverse crack increases gently. These phenomena result from the constrain effects of the longitudinal “n”-shaped stiffener. In addition,

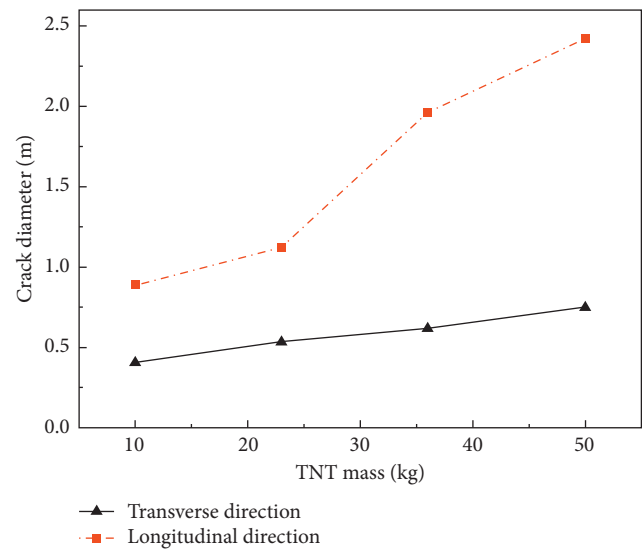


FIGURE 21: Crack diameter of the bottom plate.

due to the tearing that happens along the longitudinal stiffener, the longitudinal crack in 36 kg TNT case extremely increased comparing to 23 kg case. The results indicated that the one-way stiffener can restrict the damage to develop in the perpendicular direction of stiffener while increase the crack diameter along the stiffener direction. Hence, two-way orthogonally welded stiffeners should be designed to enhance the antiblast capability.

6. Concluding Remarks

Aiming at the problem of large span cable-supported steel bridges suffering the threat of terrorist blast attack, the dynamic response process and propagation of internal shock wave of the steel box girder under internal blast loading were investigated in the current research with nonlinear finite

element software LS-DYNA and the fluid-solid coupling arithmetic method of ALE multimaterial formulations. The failure mode and the influence of blast position as well as explosive mass were discussed.

The results show that the response process of the steel box girder under internal blast loading is different from that of the external explosion for a multi-impact effect is observed which is caused by the reflection of the shock wave, and the second impact effect seems cannot be ignored. When the internal shock waves propagated to the weld area of two plates and the corner of box, they converged and will be intensified, and the enhanced shock wave has much bigger load effects.

The holistic failure mode of the girder is observed as local failure, and there are two failure modes for the steel box girder's components, large plastic deformation and rupture. Explosive position has strong effect on the box's destruction, for a multibox destruction will be caused if the explosion takes place at the juncture of two boxes. The constraint effects of the box also have great influence on the damage degree. With the increasing of TNT mass, the crack diameter in the bottom deck, the deformation degree of the roof, and the transverse and longitudinal diaphragm are all increased. The longitudinal stiffeners restrict the damage to develop in the transverse direction while increase the crack diameter along the stiffener direction.

Some measures can be taken to enhance the antiblast capability of a steel box girder by improving the weld strength, increasing the explosion-proof distance in the box corner, setting up two-way orthogonally welded stiffeners, and increasing the venting area to decrease the effect of confined explosion. Numerical results presented in the current study may help structure or bridge engineers to determine appropriate protection measures for bridges and structures against possible explosion loads.

Conflicts of Interest

The authors declare that they have no conflicts of interest.

References

- [1] The Blue Ribbon Panel on Bridge and Tunnel Security, *Recommendations for Bridge and Tunnel Security*, FHWA, Washington, DC, USA, 2003.
- [2] Transport Canada, "Terrorist Attack Methodology and Tactics Against Bridges and Tunnels: January 2002–December 2008," Intelligence Report, IR#92–2009, 2009.
- [3] H. Lin and A. R. Chen, "Study of performance-based anti-terrorism design for bridges," *Journal of Tongji University (Natural Science)*, vol. 37, no. 8, pp. 999–1002, 2009.
- [4] T. Krauthammer, A. Assadi-Lamouki, and H. M. Shanaa, "Analysis of impulsively loaded reinforced concrete structural elements," *Computers & Structures*, vol. 48, no. 5, pp. 851–860, 1993.
- [5] H. Y. Low and H. Hao, "Reliability analysis of direct shear and flexural failure modes of RC slabs under explosive loading," *Engineering Structures*, vol. 24, no. 2, pp. 189–198, 2002.
- [6] T. Ngo, P. Mendis, A. Gupta, and J. Ramsay, *Blast Loading and Blast Effects on Structure—An Review*, Electronic Journal of Structural Engineering Special Issue, 2007.
- [7] D. G. Winget, K. A. Marchand, and E. B. Williamson, "Analysis and design of critical bridges subjected to blast loads," *ASCE Journal of Structural Engineering*, vol. 131, no. 8, pp. 1243–1255, 2005.
- [8] S. Fujikura, M. Bruneau, and D. Lopez-Garcia, "Experimental investigation of multi-hazard resistant bridge piers having concrete-filled steel tube under blast loading," *Journal of Bridge Engineering*, vol. 13, no. 6, pp. 586–594, 2008.
- [9] X. Q. Zhou, V. A. Kuznetsov, H. Hao, and A. Waschl, "Numerical prediction of concrete slab response to blast loading," *International Journal of Impact Engineering*, vol. 35, no. 10, pp. 186–200, 2008.
- [10] W. Riedel, C. Mayrhofer, K. Thoma, and A. Stolz, "Engineering and numerical tools for explosion protection of reinforced concrete," *International Journal of Protective Structures*, vol. 1, no. 1, pp. 85–101, 2010.
- [11] R. B. Deng, X. L. Jin, X. D. Chen, and Z. Li, "Numerical simulation for the damage effect of bridge subjected to blast wave," *Journal of Shanghai Jiaotong University*, vol. 42, no. 11, pp. 1927–1930, 2008.
- [12] J. Son, "Performance of cable supported bridge decks subjected to blast loads," Ph.D. thesis, University of California, Berkeley, CA, USA, 2008.
- [13] J. Son and H. J. Lee, "Performance of cable-stayed bridge pylons subjected to blast loading," *Engineering Structures*, vol. 33, no. 4, pp. 1133–1148, 2011.
- [14] E. K. C. Tang and H. Hao, "Numerical simulation of a cable-stayed bridge response to blast loads, Part I: model development and response calculations," *Engineering Structures*, vol. 32, no. 10, pp. 3180–3192, 2010.
- [15] H. Hao and E. K. C. Tang, "Numerical simulation of a cable-stayed bridge response to blast loads, Part II: damage prediction and FRP strengthening," *Engineering Structures*, vol. 32, no. 10, pp. 3193–3205, 2010.
- [16] Z. G. Jiang, X. M. Zhu, B. Yan, and S. J. Yao, "Numerical simulation on local failure of steel box girders under blast loading," *Journal of Vibration and Shock*, vol. 32, no. 13, pp. 159–164, 2013.
- [17] S. J. Yao, F. Y. Lu, Z. G. Jiang et al., "Research on the shock wave and failure modes of steel box subjected to internal blast loading," *Acta Armamentarii*, vol. 34, pp. 314–320, 2013.
- [18] W. E. Baker, *Explosion Hazards and Evaluation*, New York Elsevier Publishing Company, New York, NY, USA, 1983.
- [19] Y. Lu and K. Xu, "Prediction of debris bunch velocity of vented concrete structure under internal blast," *International Journal of Impact Engineering*, vol. 34, no. 11, pp. 1753–1767, 2007.
- [20] S. J. Yao, D. Zhan, X. G. Chen, F. Y. Lu, and P. D. Zhao, "A combined experimental and numerical investigation on the scaling laws for steel box structures subjected to internal blast loading," *International Journal of Impact Engineering*, vol. 102, pp. 36–46, 2017.
- [21] M. S. Gadala and J. Wang, "ALE formulation and its application in solid mechanics," *Computer Methods in Applied Mechanics and Engineering*, vol. 167, no. 1–2, pp. 33–35, 1998.
- [22] N. Aquelet, M. Souli, and L. Olovsson, "Euler–Lagrange coupling with damping effects: application to slamming problems," *Computer Methods in Applied Mechanics and Engineering*, vol. 195, no. 1–3, pp. 110–132, 2006.
- [23] M. Souli, N. Aquelet, E. Al-Bahkali, and M. Moatamedi, "A mapping method for shock waves using ALE formulation," *Computer Modeling in Engineering and Sciences (CMES)*, vol. 91, no. 2, pp. 119–133, 2013.
- [24] A. Alia and M. Souli, "High explosive simulation using multi-material formulations," *Applied Thermal Engineering*, vol. 26, no. 10, pp. 1032–1042, 2006.

- [25] LSTC, *LS-DYNA Keyword User's Manual*, Livermore Software Technology Corporation, Livermore, CA, USA, 2007.
- [26] G. R. Johnson and W. H. Cook, "A constitutive model and data for metals subjected to large strains, high strain rate and high temperatures," in *Proceedings of the 7th International Symposium on Ballistics*, The Hague, Netherlands, 1983.
- [27] S. Dey, T. Børvik, O. S. Hopperstad, and M. Langseth, "On the influence of constitutive relation in projectile impact of steel plates," *International Journal of Impact Engineering*, vol. 34, no. 3, pp. 464–486, 2007.
- [28] T. S. Huang, "The introduction of the steel box girder of Dadao-Bridge," *Bridges Abroad*, vol. 2, pp. 93–101, 1994.

Research Article

Seismic Response Analysis of Fully Base-Isolated Adjacent Buildings with Segregated Foundations

Khaled Ghaedi , **Zainah Ibrahim** , **Mohammed Jameel** , **Ahad Javanmardi**, and **Hamed Khatibi** 

Department of Civil Engineering, University of Malaya, 50603 Kuala Lumpur, Malaysia

Correspondence should be addressed to Khaled Ghaedi; khaledghaedi@yahoo.com and Zainah Ibrahim; zainah@um.edu.my

Received 27 August 2017; Accepted 26 November 2017; Published 12 March 2018

Academic Editor: Chiara Bedon

Copyright © 2018 Khaled Ghaedi et al. This is an open access article distributed under the Creative Commons Attribution License, which permits unrestricted use, distribution, and reproduction in any medium, provided the original work is properly cited.

In populous cities, construction of multistorey buildings close to each other due to space limitation and increased land cost is a dire need. Such construction methods arise several problems during earthquake excitation. The aim of this study is to investigate the bidirectional seismic responses of fully base-isolated (FBI) adjacent buildings having different heights and segregated foundations. Therefore, two scenarios, namely, (a) investigation of the responses of FBI adjacent buildings compared to those with fixed base (FFB) and (b) the effects of separation distance on FBI adjacent buildings, were studied. Based on these investigations, the results showed that isolation system significantly enhances the overall responses of the BI buildings. Spectacularly, the base isolation system was further efficient to decrease displacement rather than the acceleration. In addition, increase of the seismic gap changed the acceleration, pounding, base shear, base moment, and storey drift, as well as the force-deformation performance of the isolators. Therefore, it seems a need to focus on the effect of the separation distances for the design of base isolators for FBI adjacent buildings in future works.

1. Introduction

Adjacent buildings are constructed without any structural link connected to surrounding buildings. However, in few cases, they are rarely connected at the foundation level. As a matter of fact, engineers have taken serious concerns about structural damages caused by devastating earthquakes [1–3]. Therefore, the structural pounding phenomenon will usually occur in adjacent buildings during earthquake excitations [4]. Consequently, the buildings with inadequate seismic gap suffer from damages due to the pounding force. Mexico City, 1985, and Northern California, 1989, are good examples to signify the importance of seismic gap between adjacent buildings. It is good enough to flashback both events where pounding effect has been seen by 132 demolished adjacent buildings in the Mexico City and 200 collapsed buildings in Northern California [5, 6]. In this regard, many researchers have studied the structural responses of either the base-isolated (BI) building in adjacent with a conventional fixed supported building [7–9], FFB adjacent buildings, or

adjacent building equipped with other dissipative devices [6, 10–18].

Structural responses of adjacent buildings have been investigated by means of nonlinear techniques which demonstrated that collapse of structures has a significant influence on the performance of light and flexibility of buildings mainly in the pounding direction [11, 19–22]. Penzien [23] used the complete quadratic mode combination (CQC) approach, whilst Kasai et al. [24] used the spectral difference (SPD) method to calculate the required gap between two FB adjacent buildings. Both techniques were able to predict the structural responses concerning building vibration. Moreover, the square root of the sum of the squares (SRSS) approach has been governed by the international buildings codes (IBC), and consequently, the required distances between buildings were provided [25]. Shrestha [26] offered a minimum required gap for buildings to prevent pounding by means of double difference combination (DDC) and SRSS techniques. The obtained results exhibited that the DDC method assessed the required

separation gap to hold pounding up. Furthermore, structural responses of FFB adjacent buildings have been numerically analyzed [26, 27]. Khatiwada et al. [28] proposed the Hunt–Crossley model. The precise calculation of damping constant was presented in that model. The efficiency of Hunt–Crossley model in linear and nonlinear analysis for pounding simulation of concrete structures was compared with nonlinear viscoelastic, linear viscoelastic, and modified linear viscoelastic models. The nonlinear Hunt–Crossley model was capable to predict the contact force between FB adjacent buildings.

From the literature review, it was found that the seismic responses of FBI adjacent buildings have not been studied thoroughly. In this paper, an attempt was thoroughly made by dividing the scenarios into two cases comprising (i) investigate the seismic response characteristics of FBI adjacent building comparing to FFB buildings (Scenario 1) and (ii) investigate the gap size effect on seismic pounding of FBI adjacent buildings (Scenario 2) having different heights. For this aim, lead rubber bearings (LRB) were designed based on the NEHRP provisions [29]. Afterwards, a comparative analysis of two FFB and BI adjacent buildings under bi-directional seismic excitations was carried out.

2. Methodology

2.1. Nonlinear Dynamic Analysis. In the present study, nonlinear dynamic analysis was done using a typical bi-directional seismic recorded and a finite element (FE) analysis package. That is, SAP2000 was selected as an appropriate tool for aiding the purpose. The main equations of motion were taken deliberating equilibrium of forces at each DOF. The motion equations for superstructure and base isolation were written as

$$[M]\{\ddot{y}_b + \dot{y}\} + [C]\{\dot{y}\} + [K]\{y\} = -[M][T_g][\ddot{y}_g], \quad (1)$$

in which $[M]$ is the mass matrix, $[C]$ and $[K]$ are damping and stiffness matrix of the superstructure, respectively, and $\{y\}$ is the superstructure displacement. Displacement and acceleration corresponding to the ground are nominated by $\{y_b\}$ and $\{\ddot{y}_g\}$. The earthquake effect coefficient matrix is given by $[T_g]$.

All nonlinearities are only restricted to the elements of the base isolator. In the above dynamic equilibrium equation, the base isolator and superstructure are considered as nonlinear and elastic, respectively. Therefore, (1) is written as

$$M\ddot{y}(t) + C\dot{y}(t) + K_L y(t) + r_N(t) = r(t), \quad (2)$$

where K_L is the stiffness matrix for superstructure as the linear elastic and r_N is the force vectors due to nonlinear degrees of freedom related to isolator elements. The displacement, velocity, and acceleration corresponding to ground is determined by y , \dot{y} , and \ddot{y} , respectively; and the vector of imposed loads is defined by r . At nonlinear DOF, the effective stiffness is arbitrary, but it changes between zero and the utmost stiffness of that DOF. The equation of equilibrium could be rewritten as

$$[M][\ddot{y}(t)] + [C][\dot{y}(t)] + [K_L][y(t)] + r_N(t) = r(t) - [r_N(t) - K_N y(t)], \quad (3)$$

in which

$$K = K_L + K_N, \quad (4)$$

where K_N is the stiffness matrix for all nonlinear DOFs.

2.2. Gap Elements. The gap distance between the buildings was represented by the link element in SAP2000. It is remarkable that the gap (link) element is active only in a compression state. The function of the link element (gap element) is to transfer pounding force through itself only at the moment of the impact of buildings. The force-deformation correlation in nonlinearity form was expressed as follows:

$$f = \begin{cases} k(d - \text{open}), & \text{if } d - \text{open} < 0, \\ 0, & \text{otherwise,} \end{cases} \quad (5)$$

in which k is the constant of spring, d represents the displacement, and the initial gap opening (has to be zero or positive) is defined by open. For gap element in nonlinear analysis cases, its stiffness was defined as one to two orders stiffer than surrounding columns and beams in each level. The gap element stiffness was selected to be 10^2 times larger than the stiffness of adjacent attached element. Hence, in this study, the stiffness of the gap elements was determined as

$$K = \left(\frac{EA}{L}\right) \times 100,$$

$$K = \frac{\text{Young's modulus of concrete} \times \text{contact surface area}}{\text{element length of contact surface}} \times 100, \quad (6)$$

in which A is the cross-sectional area of the element, E is Young's modulus of the element, and L is the element length in perpendicular direction to the contact surface. Furthermore, dissipating energy during collision can be determined by damping. The linear effective stiffness effect and damping were included in the gap element to achieve favourable contact behaviour.

2.3. Nonlinear Time History Analysis. The finite element software SAP2000 was implemented to investigate the response of adjacent buildings under different seismic loads by modelling two adjacent ordinary moment-resisting concrete frame (OMRCF) buildings considering FFB adjacent buildings and FBI adjacent buildings subjected to bidirectional earthquake excitations. Nonlinear dynamic time history analysis was carried out through bilateral seismic recorded of Cape (PGA 2.85 m/s²), Los Angeles Century City, LACC-North (PGA 3.85 m/s²), Santa Monica (PGA 1.20 m/s²), and El-Centro (PGA 3.20 m/s²), as shown in Figure 1.

Fast nonlinear analysis procedure proposed by Wilson has been weighed to solve the equilibrium equations [30]. The approach was exceedingly effective for structural systems that are initially linear elastic [2]. In the present study, material

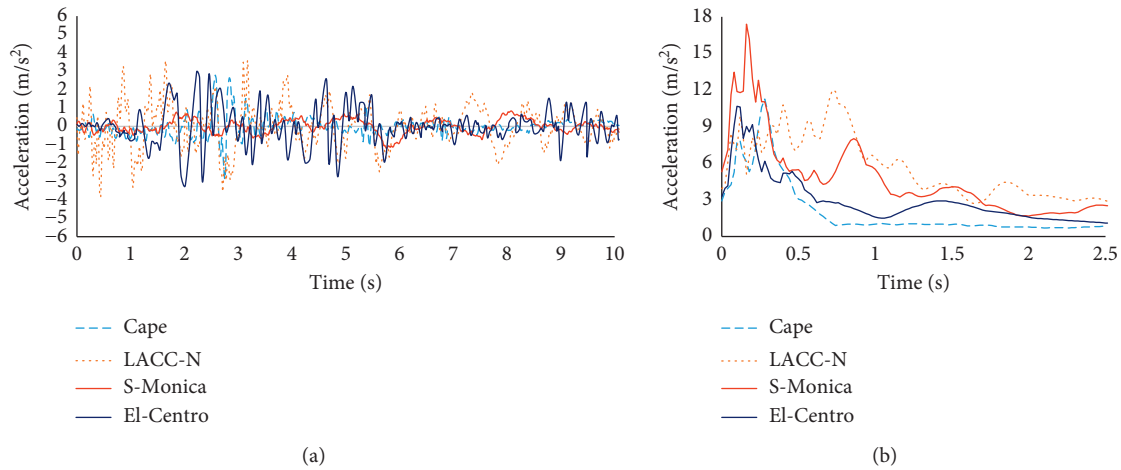


FIGURE 1: (a) Time histories and (b) spectral accelerations (5% damping) of the applied earthquakes.

and link nonlinearities were also considered and direct integration was performed by the alpha method. All nonlinearities were restricted to the link (gap) elements. The detailed time history loading was imposed quasistatically through high damping. The fast nonlinear analysis method deliberates a ramp-form time history which rises in a linear trend from zero to one over a time period. Thus, the nonlinear equations were iteratively solved in every time step. Eventually, the iterations were accomplished until the result converges.

2.4. Base Isolator Design. Base isolator (herein LRB) device is shaped by placing a lead plug into a prepared orifice in the scant damping elastomeric bearing. The lead plug is deformed in shear due to enforcing of steel plates. LRB performance is preserved during repetition of severe ground motions with good reliability and durability. LRB generates the required damping and sophisticated initial stiffness. The LRB behaviour is affected by the horizontal elastomer stiffness, horizontal lead plug stiffness, and the yield strength of the lead plug.

The LRB isolator was designed as suggested by Kelly [31], Kelly et al. [32], and Naeim [33]. In this study, ISODNG09 (a computer code) has been made to design the isolator iteratively. The dimensions, total seismic weight, number of bearings layers, and their thickness were taken into account as the initial input. The parameters such as high initial stiffness, post-elastic stiffness, yield strength, effective damping, and post-yield stiffness ratio were calculated by means of the aforesaid code. The parameters were then assigned into SAP2000 software package. The bearings were connected at the bottom of the columns. In general, a lead core with 60 mm diameter and two 25 mm thick steel plates were used to attach both sides of the bearing. The IRHD (International Rubber Hardness Degrees) 50 was used for rubber material with shear modulus, Young’s modulus, modified factor (k), maximum shear strain (γ_{max}), and ultimate elongation of 0.64 MPa, 2.2 MPa, 0.73, 50%, and 650%, respectively. Stiffness of nonlinear unloading was set to 10.57 kN/mm, whereas the yield strength was 249.25 kN. The earthquake forces on the bearing taken from the

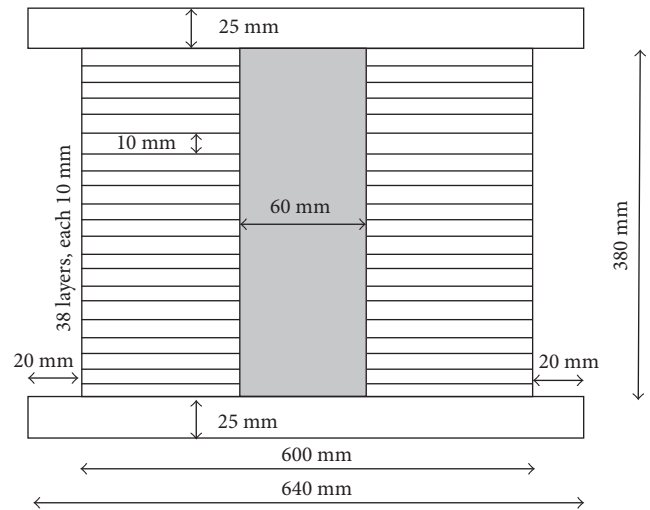


FIGURE 2: LRB details used in this study.

dynamic analysis of BI building were utilized to control the roll-out state of the base isolators. The designed height and diameter of the steel shim plates and rubbers were 380 mm and 600 mm, respectively. Figure 2 demonstrates the LRB details used in the present study. The importance coefficient and response modification factor of isolated buildings were taken as $I = 1.0$ and $RI = 2.0$, respectively [31]. Configuration of damping system was analyzed for 10 s durational earthquake. The used time step for numerical solution was selected as 0.002 s. The flowchart procedure for the design of isolators is illustrated in Figure 3.

2.5. Static Analysis. Analysis of linear static, the easiest of all, was carried out as the lowest level of complication. Seismic lateral force was defined by taking the R and Z factors, soil profile, importance factor, etc. Equations for earthquake analysis has been derived from Building and Housing Research Center (BHRC) of Iran [34]. The summation of the horizontal earthquake loads or the minimum base shear in each direction was expressed from

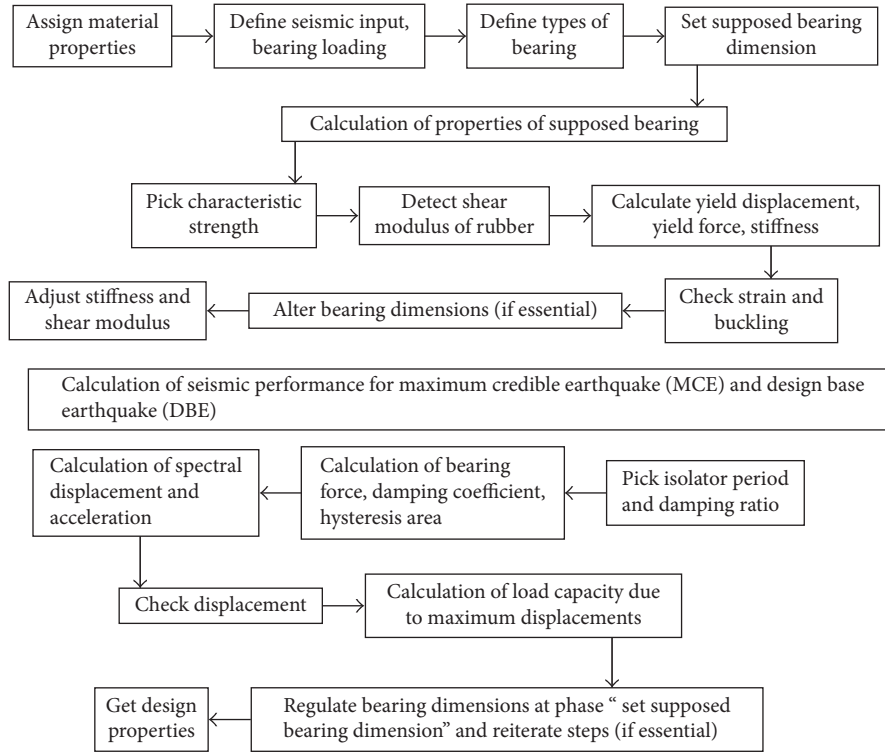


FIGURE 3: Typical design procedure of base isolators.

$$V = CW, \quad (7)$$

in which V is the shear force in the base level. The base level is determined as the level where the building does not have any movement with respect to the base ground during a seismic excitation, W is the total weight of the structure, that is, the total dead load and a percentage of other loads, and C is the seismic coefficient which was obtained from the following equation:

$$C = \frac{ABI}{R}, \quad (8)$$

where A is the design base acceleration (g) and B is the building response coefficient taken from the design response spectrum which was specified based on the below equation:

$$B = 2 \left(\frac{T}{T_0} \right)^{2/3}, \quad (9)$$

in which T is the fundamental natural period and T_0 was specified based on the soil classification and for this study was defined as 0.3 for soil type I . I is the importance factor, and R is the building behaviour coefficient.

According to the BHRC, the design base shear must not be less than $V = 0.1AIW$ and the C value must be greater than 10% of the A .

2.6. Required Lateral Force for Superstructures. To calculate the required lateral force for superstructures, we need to compute the minimum and then the maximum effective stiffness of the base isolators. In this regard, the equations are calculated as follows:

$$K_{Dmin} = \frac{4\pi^2}{g} \left(\frac{W}{T_D^2} \right), \quad (10)$$

$$K_{Dmax} = (1.3)(K_{Dmin}),$$

in which the ground acceleration (g), weight of the structure (W), and the effective period (T_D) are 9.81 m/s^2 , 3405198 kg , and 3 seconds, respectively. Substituting these values in (10) gives the minimum and maximum effective stiffness, i.e., 15210.73 kN/m and 19773.95 kN/m , respectively. Therefore, the required lateral force for superstructures, V_s , can be computed as below:

$$V_s = \frac{V_b}{R_I}, \quad (11)$$

in which V_b is the required lateral force for the isolation system. $R_I = (3/8)R$ which is the numerical coefficient regarding the type of lateral force resisting system above the base isolation system as given in Table 13.3.4.2 of NEHRP provision for seismically isolated structures. R is the response modification coefficient as given in Table 5.2.2 of that provision and it is taken as 3 in this study. Hence, R_I goes to be 1.125. The above expression sets V_s for 2590.878 kN .

2.7. Numerical Study. In this study, two adjacent buildings having different heights (4- and 8-storey buildings) were considered for the evaluation of structural pounding. The plan and elevation views of the buildings are shown in Figure 4. The place of seismic gaps (30 mm) for both the FFB and FBI adjacent buildings is illustrated in Figure 5.

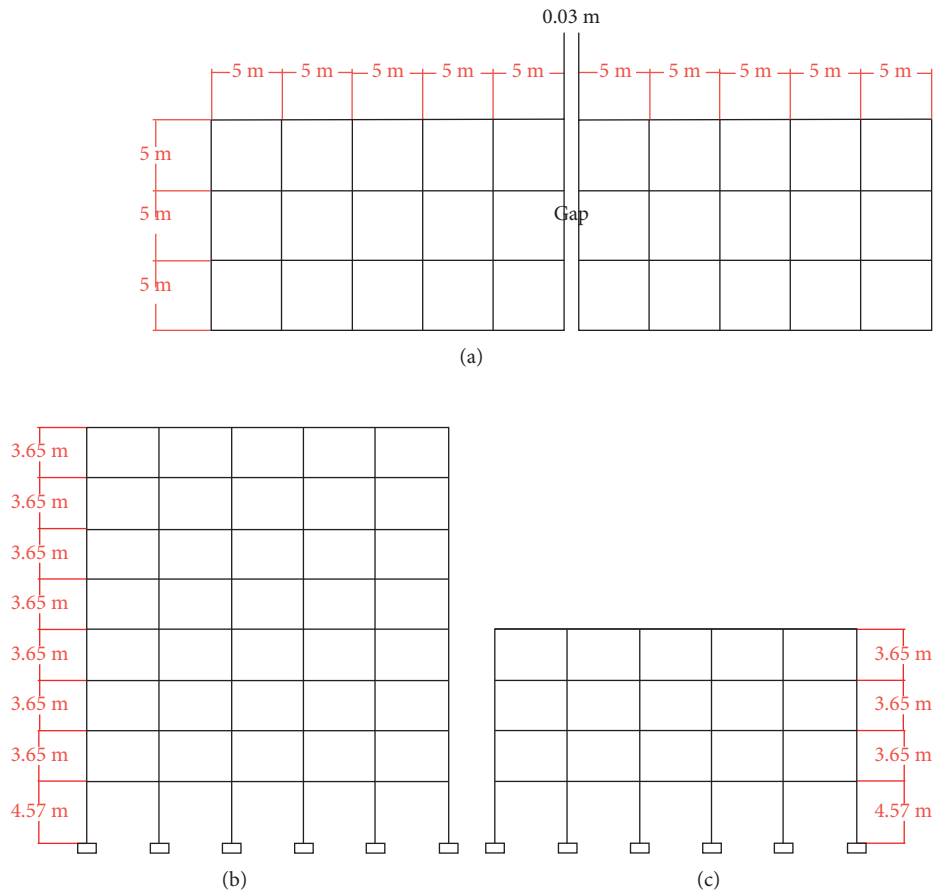


FIGURE 4: Plan and elevation views of buildings having segregated foundations. (a) Plan view; (b) 8-storey-level elevation view; (c) 4-storey-level elevation view.

As Figure 4 shows, the total height of the 8-storey and 4-storey OMRCF buildings is 30.12 m and 15.52 m, respectively. The frame section of columns and beams detailing for floor levels is described in Table 1. The gap elements between adjacent buildings were located at 4 joints (Figures 5(a) and 5(b)). Young's modulus and shear modulus of concrete were taken as $E = 2.168 \times 10^7 \text{ kN/m}^2$ and $G = 0.834 \times 10^7 \text{ kN/m}^2$, respectively.

3. Results and Discussions

The comparative results of the present study are divided into two parts, in which each part provides a comprehensive study on the objective:

- (1) Responses of FBI adjacent buildings compared to the FFB adjacent buildings (Scenario 1).
- (2) Gap size influence on the responses of the FBI adjacent buildings (Scenario 2).

3.1. Seismic Responses of Fully BI Adjacent Buildings (Scenario 1)

3.1.1. Free Vibration Analysis. It has ascertained that the input frequency generates the pounding force. In other words, the pounding force is a function of the frequency [35, 36]. Moreover, the modes with large impressive masses

are normally a substantial contributor to the response of the structures [37, 38]. Table 2 presents the natural frequency of the FFB and FBI adjacent buildings considering the most participated mass ratio for the four effective modes in the longitudinal (pounding) direction. It can be seen from the table that the governor modes were changed from 1, 4, 7, and 11 in the FFB system to 1, 3, 7, and 10 in the FBI system. Furthermore, by comparing the common modes (1st and 7th), it can be concluded that the base isolation system decreases the structure stiffness, therefore reducing the natural frequency. In such a circumstance, the superstructure part, as a rigid unit, will react to earthquake vibrations in lieu of resonating with imposed vibration. The obtained results from Table 2 confirmed that the isolation system reduced the natural frequency of the buildings by 28%–43% for the governor modes. It is obvious that, by decreasing the natural frequency, the time period will be lengthened which results to have a smooth vibration. Also, from the participating mass ratio analysis, it can be observed that the mass participation for the FBI buildings is greater than the FFB buildings in the first mode of vibration with a time delay.

For better understanding, the first modal vibration of the buildings for both FFB and FBI adjacent buildings is illustrated in Figure 6. In FFB condition, the adjacent buildings experienced a contact in the first mode. On the contrary, in the FBI condition, the taller building deflected

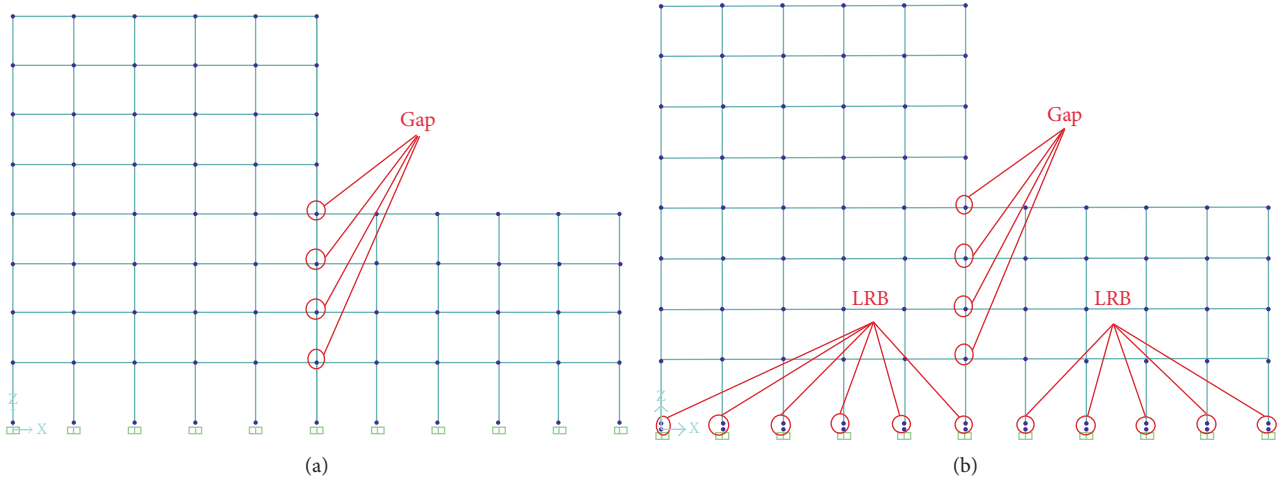


FIGURE 5: Location of gap elements and LRB devices in FFB and FBI buildings. (a) FFB adjacent buildings. (b) FBI adjacent buildings.

TABLE 1: Structural members of OMRCF adjacent buildings.

Column section	Short building	Tall building	Beam section	Short building	Tall building
55 × 55	1	1	40 × 60	2	2
50 × 50	2	2	40 × 50	2	4
45 × 45	1	2	30 × 40	—	3
40 × 40	—	3	—	—	—

TABLE 2: Natural frequency of FFB and FBI systems considering the governor modes.

Mode	FB			Mode	BI		
	T (s)	ω (Hz)	Mass part. ratio		T (s)	ω (Hz)	Mass part. ratio
1	2.000	0.500	0.470	1	3.524	0.284	0.628
4	0.962	1.039	0.301	3	2.435	0.411	0.357
7	0.795	1.258	0.100	7	1.110	0.900	0.012
11	0.440	2.271	0.043	10	0.558	1.791	0.001

toward the left direction because of the effect of the base isolation system.

3.1.2. Displacement Response. The envelope displacement values for each floor level of the taller FB and BI buildings subjected to applied earthquakes are presented in Figure 7. As shown in the figure, the maximum displacements occurred at the top level (8th floor level) and the maximum displacements of the buildings in both positive and negative directions are shown for both FB and BI adjacent buildings. However, the top level displacements of the FBI buildings were generally greater than the FFB building, but by considering the base displacements for both systems, the relative displacement can be calculated. It can be seen from the figure that the relative displacement of the FBI building in both positive and negative directions was smaller than the relative displacement of the FFB building. To clarify the statement, the below expression is written for the system considering El-Centro motions:

Positive relative displacement of the FBI building:
 $21.2 \text{ cm} - 10 \text{ cm} = 11.2 \text{ cm} < 12 \text{ cm}$ for the FFB building

(6.7% reduction). Negative relative displacement of the FBI building: $(-18.1) - (-11.4) \text{ cm} = -6.7 \text{ cm} < -12.1$ for the FFB building (44.7% reduction).

Furthermore, the distortion of FFB building under applied motions is not desirable such that the building deformations are not controlled unlike the FBI building which has a smooth deformation under the earthquakes as illustrated in the figure. Overall, taking an average calculation for the relative displacement of the buildings under different applied motions shows that the BI system is capable to reduce displacement responses up to 46% in the pounding (longitudinal) direction. The values are indicated in Table 3.

For a shorter building, it can be seen from Figure 8 that the relative displacement responses of the FBI building is less than the FFB building. The displacement values of the pounding floor (4th floor level) are illustrated in the figure for both the FFB and FBI buildings in both positive and negative directions. Similar to the taller building and with subtraction of the top displacement from the base displacement, the relative displacement can be computed.

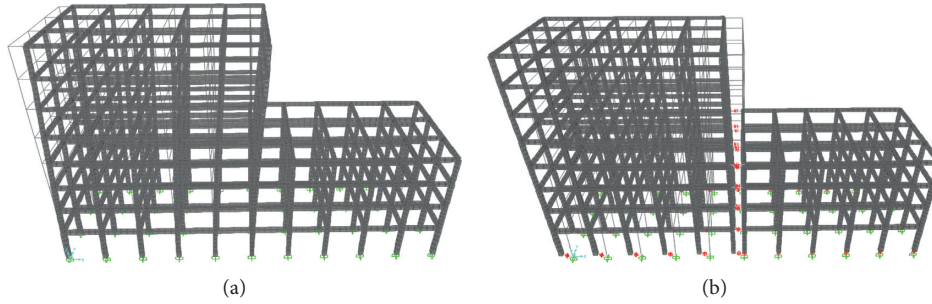


FIGURE 6: First modal response of the adjacent structures. (a) FFB adjacent buildings. (b) FBI adjacent buildings.

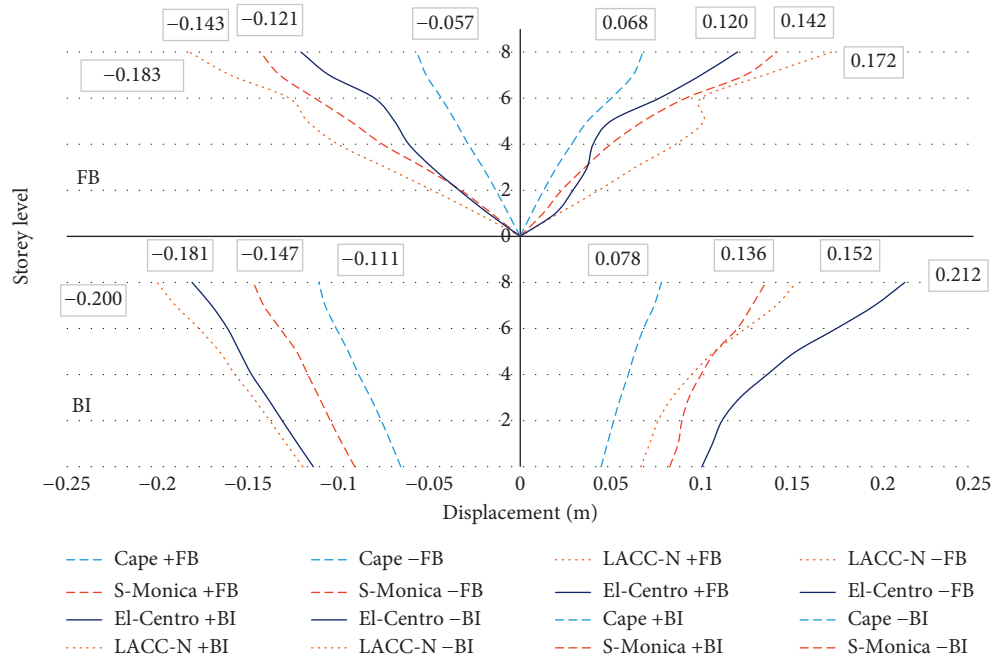


FIGURE 7: Envelope displacements of the taller buildings in different floors under seismic loads.

Herein, an example is given for the building subjected to the El-Centro motion:

Positive relative displacement of the BI building: $13.09 - 11.3 = 1.8 \text{ cm} < 7.1 \text{ cm}$ for the FB building (74.6% reduction). Negative relative displacement of the BI building: $(-9.3) - (-8) = -1.3 \text{ cm} < -5.7 \text{ cm}$ for the FB building (77.2% reduction).

Overall, taking an average calculation for the relative displacement of the shorter building under different applied motions shows that the BI system is capable to reduce displacement responses up to 77.5% in the pounding (longitudinal) direction. The values are indicated in Table 4.

Figures 9 and 10 show the displacement time history response of the taller and shorter buildings at the pounding level subjected to the ground motions. In view of the nonlinear displacement responses, it could be concluded that the displacement interval of the FBI buildings has a significant lower oscillation. In other words, the base isolators increased the vibration period of the structures

TABLE 3: Relative displacement of the taller FFB and FBI buildings under considered motions.

Earthquake	FFB taller building disp. (cm)		FBI taller building disp. (cm)		Reduction (%)	
	Pos.	Neg.	Pos.	Neg.	Pos.	Neg.
Cape	6.8	-5.7	3.34	-4.5	51	21
LACC-N	17.2	-18.3	8.6	-8	50	56
S-Monica	14.2	-14.3	5.4	-5.6	62	61
El-Centro	12	-12.1	11.2	-6.7	7	45
				Ave.	42.5	46

which led the structures to experience lesser collision during the excitations (Figure 11). In contrary, the adjacent FFB buildings with smaller vibration periods are more prone to high risk of collision. This can increase the damage possibility of the FFB buildings more than FBI buildings during seismic excitations.

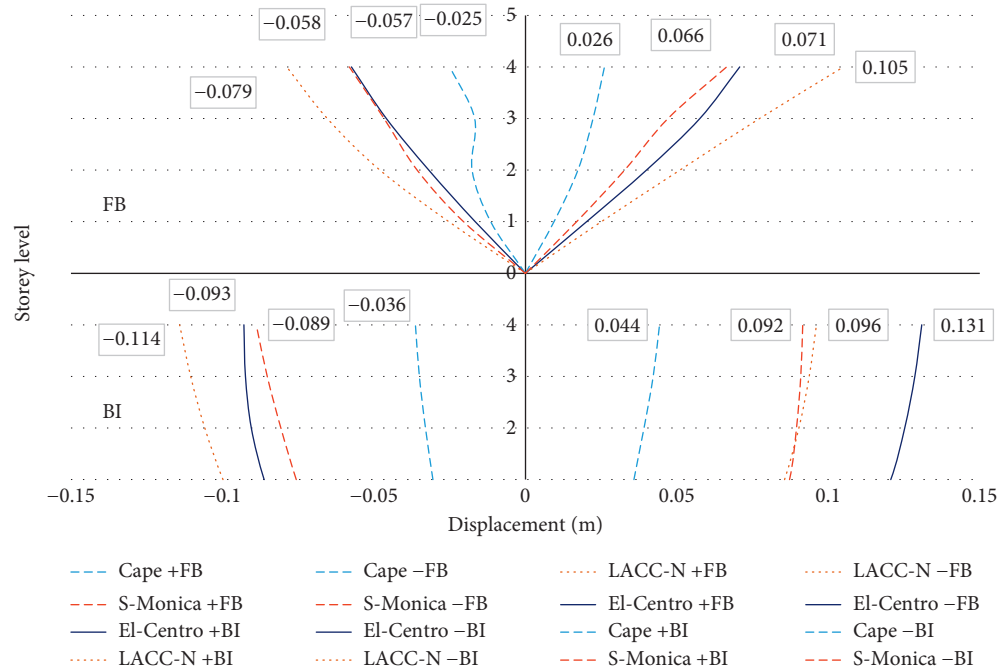


FIGURE 8: Envelope displacements of the shorter buildings in different floors under seismic loads.

TABLE 4: Relative displacement of the shorter FFB and FBI buildings under considered motions.

Earthquake	FFB shorter building disp. (cm)		FBI shorter building disp. (cm)		Reduction (%)	
	Pos.	Neg.	Pos.	Neg.	Pos.	Neg.
Cape	2.6	-2.5	1.1	-0.8	58	68
LACC-N	10.5	-7.9	1.7	-2.2	84	72
S-Monica	6.6	-5.8	1	-1.9	85	67
El-Centro	7.1	-5.7	1.8	-1.3	75	77
				Ave.	75.5	71

3.1.3. Acceleration Response. Stopping the displacement in a moment results a rapid and enormous pulse of acceleration at the pounding level in the opposite side. During earthquake excitations, large accelerations will be produced owing to the energetic ground motions. These accelerations may intensify several times once structural pounding happens. Figure 12 illustrates the maximum acceleration response of the buildings for each floor level independently. As it is shown in the figure, the acceleration response of FBI buildings was smaller than those with FB support. However, the first three floors of the FBI adjacent building attracted more accelerations compared to the FFB adjacent buildings under S-Monica excitations. It is because of the structure movement (especially the taller one) at their base level due to the presence of the base isolators. For the taller building, at its first floor, this phenomenon is observed under all earthquakes except LACC-N. As a result of colliding, the adjacent buildings bounce. For this reason, regardless of support systems, the acceleration response of taller buildings is tended in the negative direction and for smaller building is in the positive direction. The maximum accelerations for the taller

and shorter FFB adjacent buildings at 4th (pounding), at the contact moment, are depicted in Figure 12. Comparing the values showed that using base isolation system resulted in a significant reduction of acceleration response at the pounding level for both adjacent buildings. Moreover, the absorbed acceleration by the top floor of the taller building also confirmed the effectiveness of the BI system in mitigation of the input acceleration imposed to the buildings. Table 5 indicates the average reduction of acceleration response of the buildings subjected to the motions. From the table, it can be concluded that using BI system mitigates the absorbed acceleration by the adjacent buildings up to 41% for the taller building and 35% for the shorter one.

3.1.4. Pounding Force. The greater pounding force increases the collapse risk of buildings during ground motions; therefore, it is much favourable to reduce the pounding force between structures. In addition, pounding is too less important in the transverse direction compared to the perpendicular (principal or longitudinal) direction. An investigation

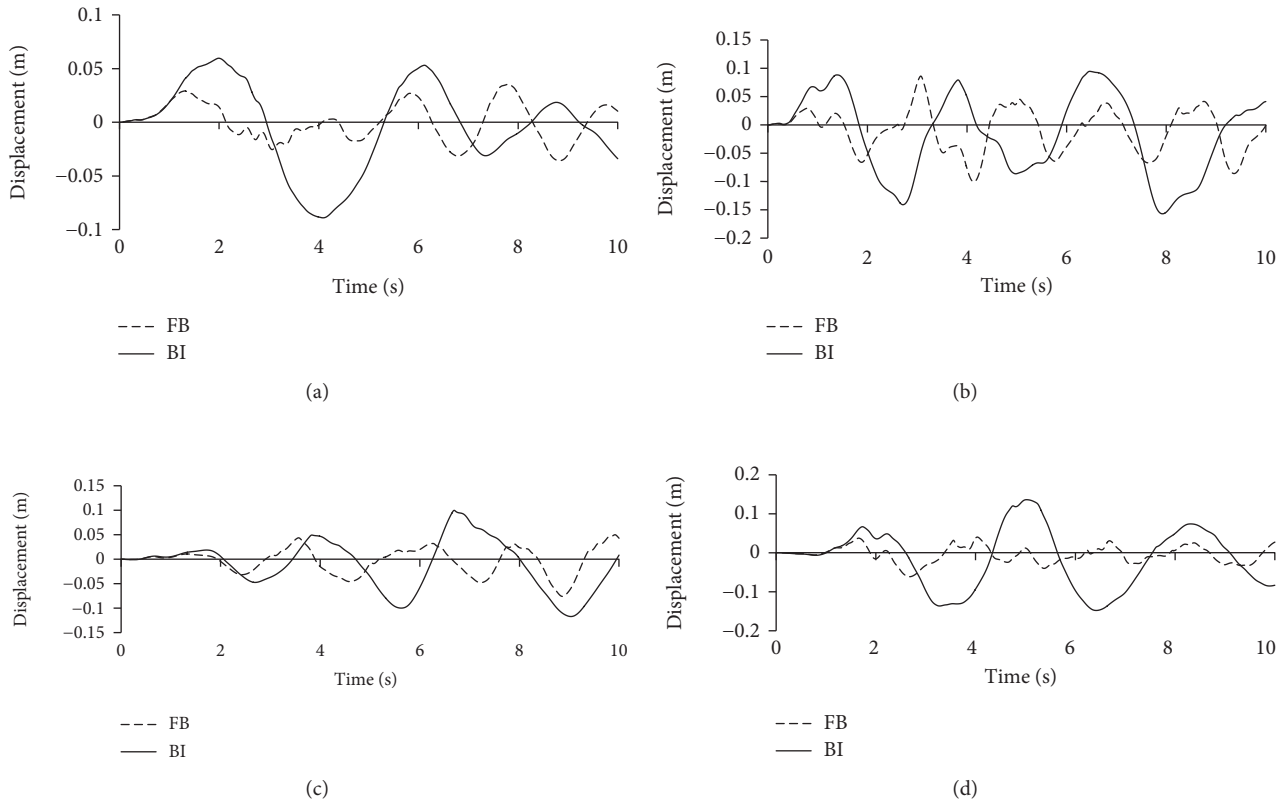


FIGURE 9: Displacement time history response of the taller building at the pounding level under the motions. (a) Cape. (b) LACC-N. (c) S-Monica. (d) El-Centro.

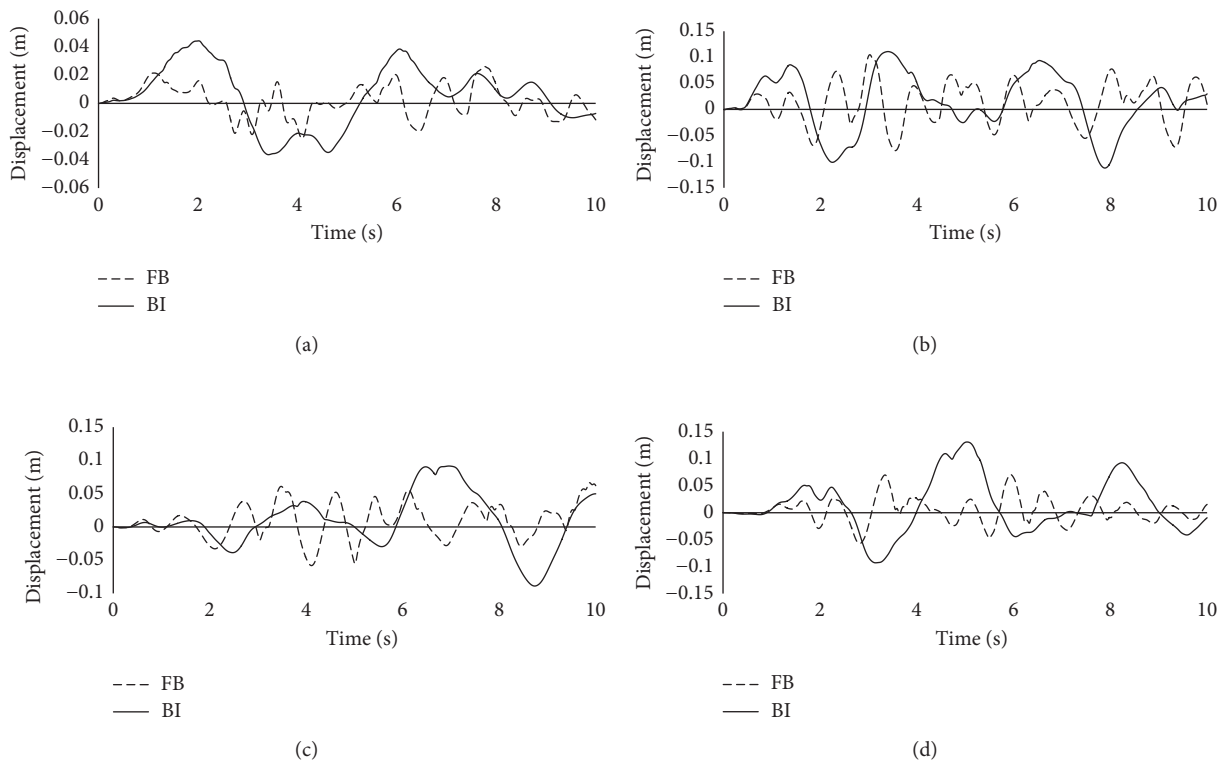


FIGURE 10: Displacement time history response of the shorter building at the pounding level under the motions. (a) Cape. (b) LACC-N. (c) S-Monica. (d) El-Centro.

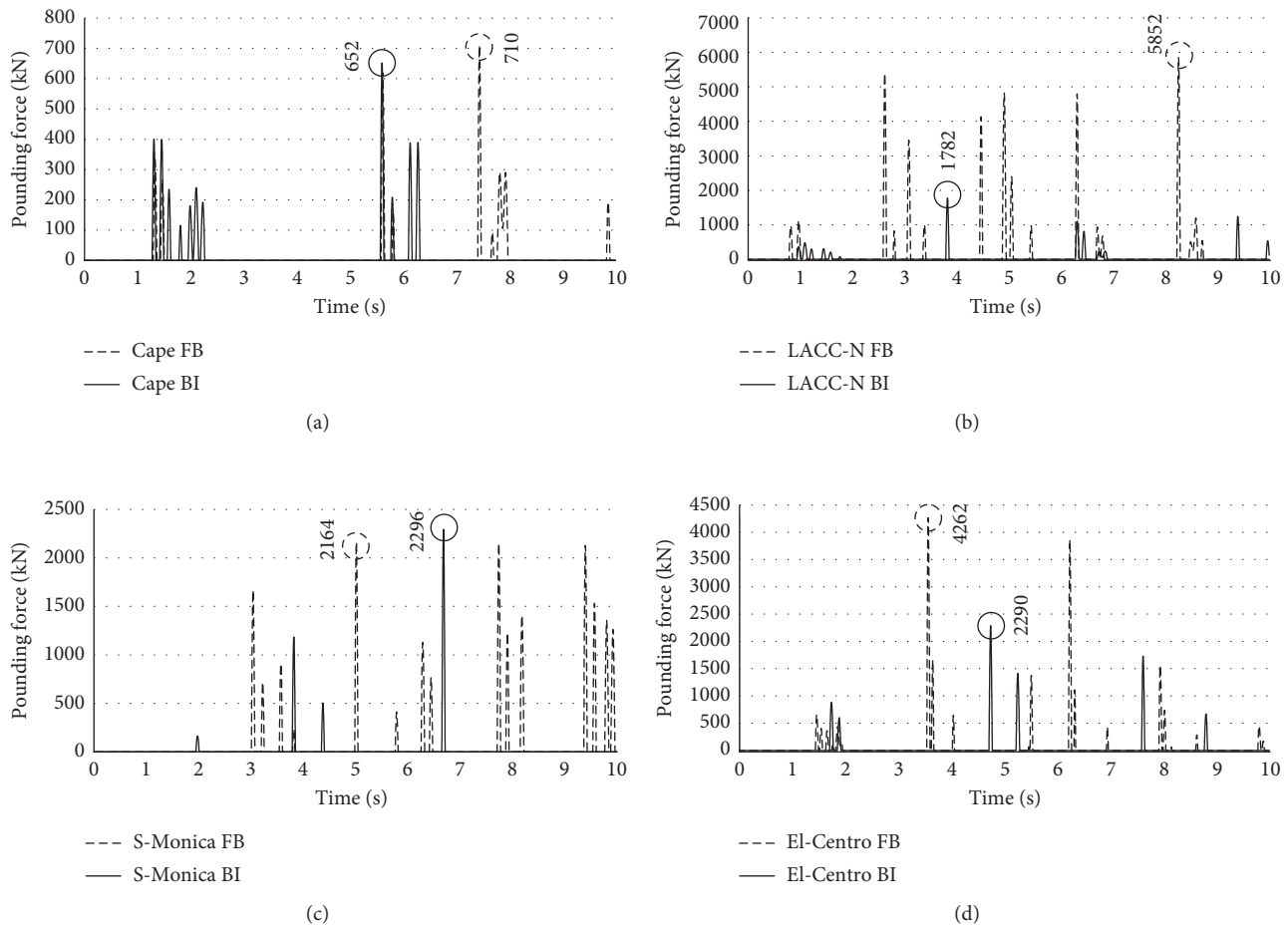


FIGURE 11: Pounding force at the pounding level of FFB and FBI adjacent buildings. (a) Cape. (b) LACC-N. (c) S-Monica. (d) El-Centro.

of structural pounding between stairway tower and main building revealed that the main structure with considerable stiffness and large mass would respond for independent vibration and pounding in the transverse direction [35]. This is because, the contact between two adjacent buildings is mostly occurred at the pounding (longitudinal) direction. In the transverse direction, buildings only carry the friction forces. Herein, the time history of pounding force for both FFB and FBI adjacent buildings at the 4th level in the longitudinal direction is presented in Figure 11. Under the different considered earthquakes, the maximum pounding force of FFB buildings was remarkably greater than the pounding force between FBI adjacent buildings. Indeed, uncontrolled movement and oscillation along with short period of vibration in the FFB system lead the buildings to have such pounding. Such great pounding forces result a wide and undesirable movement in adjacent buildings. In addition to this, from the figure, it can be seen that the number of collisions of the FFB adjacent due to the aforementioned reasons is much more compared to the collisions of the FBI buildings.

3.1.5. Time History Base Shear and Base Moment Analysis. One of the significant issues in seismic design of structures is controlling or reducing base shear and base moment response of structures. Figure 13 depicts the base

shear time history analysis in the longitudinal (X) and transverse (Y) direction for FFB and FBI adjacent buildings. The maximum shear force in both directions was decreased using LRB devices. It can also be observed from the time history analysis that the absorbed shear in the FBI buildings has very smooth trend, whilst this trend for the FFB adjacent buildings is very harsh. Taking a look at the values presented in Table 6 confirmed that the FBI buildings undertake smaller base shear in the X and Y directions averagely by 52% and 60%, respectively, as compared to the FFB building. Figure 14 also indicates an example of the reduction of absolute base shear in FBI buildings in comparison to FFB buildings during El-Centro excitations at each one second interval.

The base moment response has direct relationship to the base shear of the structure. Thus, it is predicted that the reduction in values of base moment for the FBI buildings be lesser than that of the FFB buildings in both directions. From Figure 15, it can be concluded that implementation of the LRBs reduced the base moment averagely by 52% and 61% (Table 7) in both the longitudinal and transverse directions compared to the base moments in the FFB adjacent buildings. As predicted, the average base moment reduction values are similar to those values obtained for the base shear. It should be noted that because of using LRBs and reduction in the natural frequencies (increased time period) in the BI buildings, the

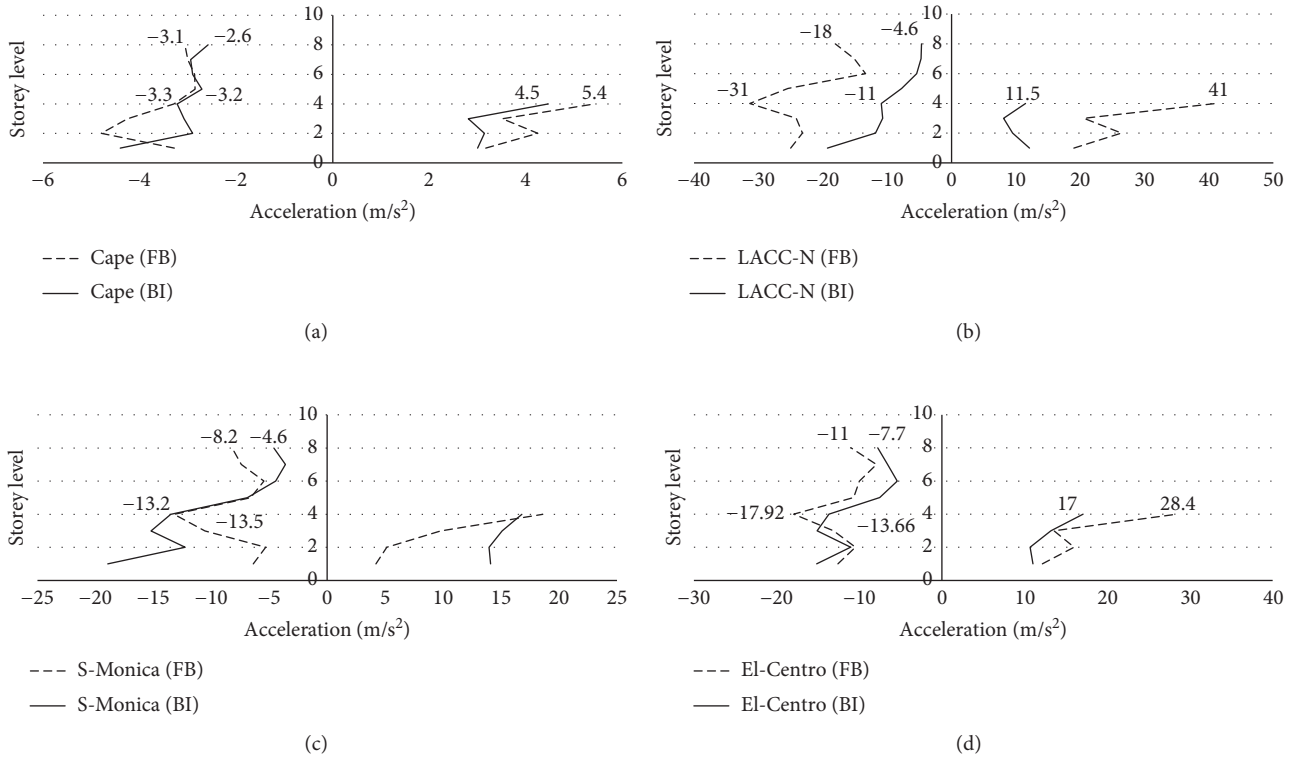


FIGURE 12: Maximum accelerations of the floor levels of the adjacent buildings under the earthquakes. (a) Cape. (b) LACC-N. (c) S-Monica. (d) El-Centro.

TABLE 5: Acceleration response of the shorter FFB and FBI buildings under considered motions.

Earthquake	FFB taller building acc. (m/s^2)		FBI taller building acc. (m/s^2)		Reduction (%)	
	8th floor	4th floor	8th floor	4th floor	8th	4th
Cape	-3.1	-3.3	-2.6	-3.2	16	3
LACC-N	-18	-31	-4.6	-11	74	65
S-Monica	-8.2	-13.2	-4.6	-13.5	44	2
El-Centro	-11	-17.92	-7.7	-13.66	30	24
Ave.					41	22.5

Earthquake	FFB shorter building acc. (m/s^2)	FBI shorter building acc. (m/s^2)	Reduction (%)
	4th floor	4th floor	
Cape	5.4	4.5	17
LACC-N	41	11.5	72
S-Monica	18.6	16.8	10
El-Centro	28.4	17	40
Ave.			35

base moment reaction is occurred in a smooth way similar to the base shear, acceleration, and displacement responses as presented earlier. Figure 16 also illustrates an example of the absolute base moment reduction owing to the use of LRBs in each one second interval during El-Centro excitation.

3.1.6. Storey Drift. Structural pounding of buildings demonstrated that the transverse direction has insignificant effect in storey drift [35]. As a result, it can be concluded that the storey drift in the longitudinal (pounding) direction is

more perilous. Furthermore, it is commonly accepted that the storey drift of a structure takes changes along its height. In the present study, therefore, the storey drifts of the taller building in the pounding direction considering both systems subjected to the ground motions were investigated as illustrated in Figure 17. Based on the figure, using base isolators not only markedly controls the drift ratio of the building in a better pattern but it also reduces the drift values. In other words, the pattern of the storey drift and the overall structural movement for the taller FBI building

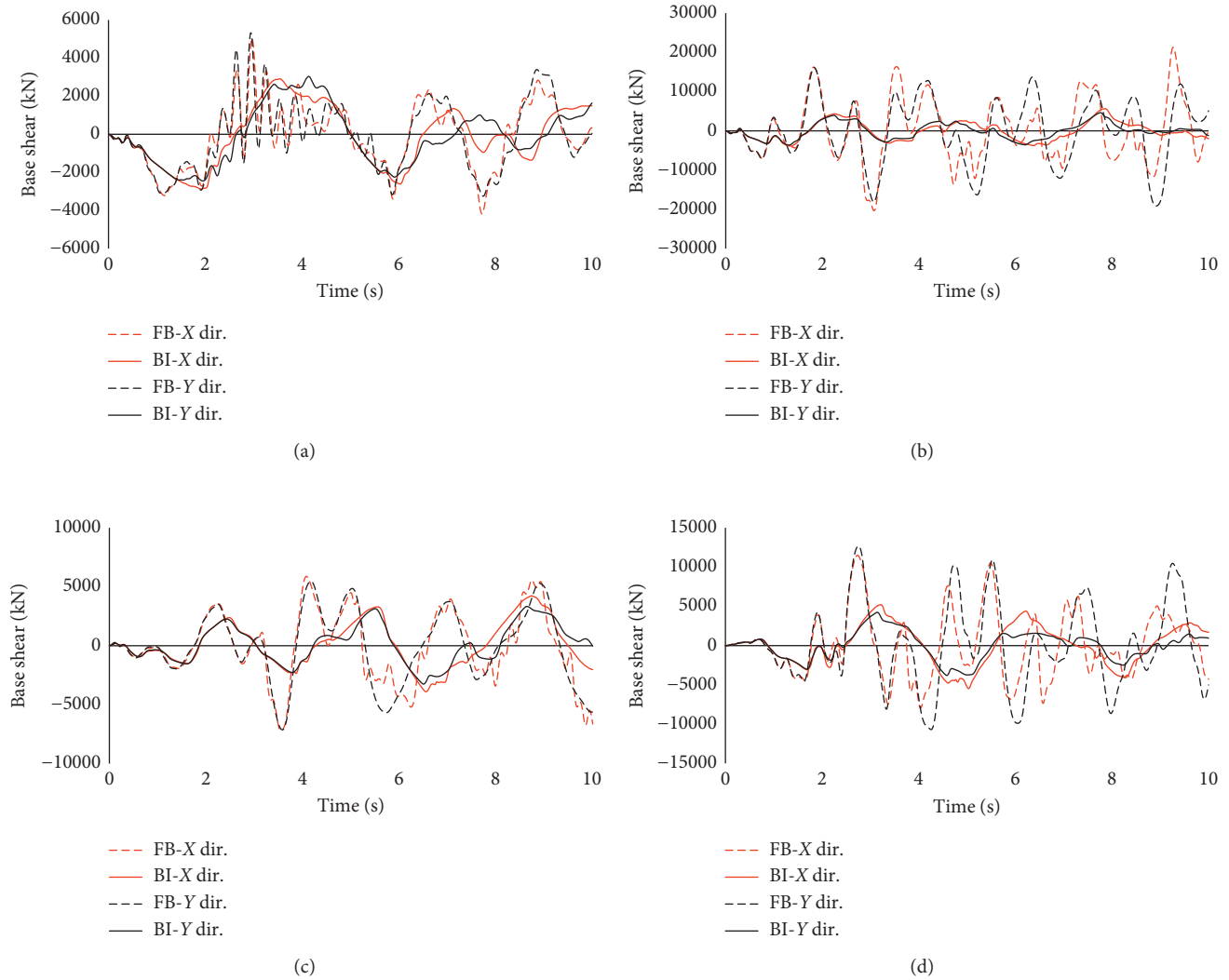


FIGURE 13: Base shear for FFB and FBI adjacent buildings under applied earthquakes. (a) Cape. (b) LACC-N. (c) S-Monica. (d) El-Centro.

TABLE 6: Absolute base shear (kN) of the adjacent buildings under applied earthquakes.

Earthquake	FFB system		FBI system		Reduction (%)	
	X	Y	X	Y	X	Y
Cape	5043	5330	2910	3036	42	43
LACC-N	21,298	19,159	5646	4629	73	76
S-Monica	7163	7137	4223	3331	41	53
El-Centro	11,495	12,679	5472	4246	52	67
Ave.					52	60

shows how the drift of the building was modified. It is because of the existence of LRB devices placed under columns which led the buildings to have a smooth movement during the ground motion.

3.1.7. Storey Shear Force. The variation of shear force for both the FFB and FBI adjacent buildings along the storey levels was compared through Figure 18. Unlike the FFB adjacent buildings, the shear forces in all floors of both taller

and shorter FBI buildings were reduced after the implementation of LRBs. As it can be seen from the figure, the shear forces near to the pounding level (4th level) is enlarged due to the collision of both investigated systems of the adjacent buildings. This phenomenon reveals the importance of the design adjacent buildings (particularly structural frames exposed to possible colliding). As a result, the sizes of designed members can remarkably be reduced when base isolation systems are used, leading to more cost-effective and operative system.

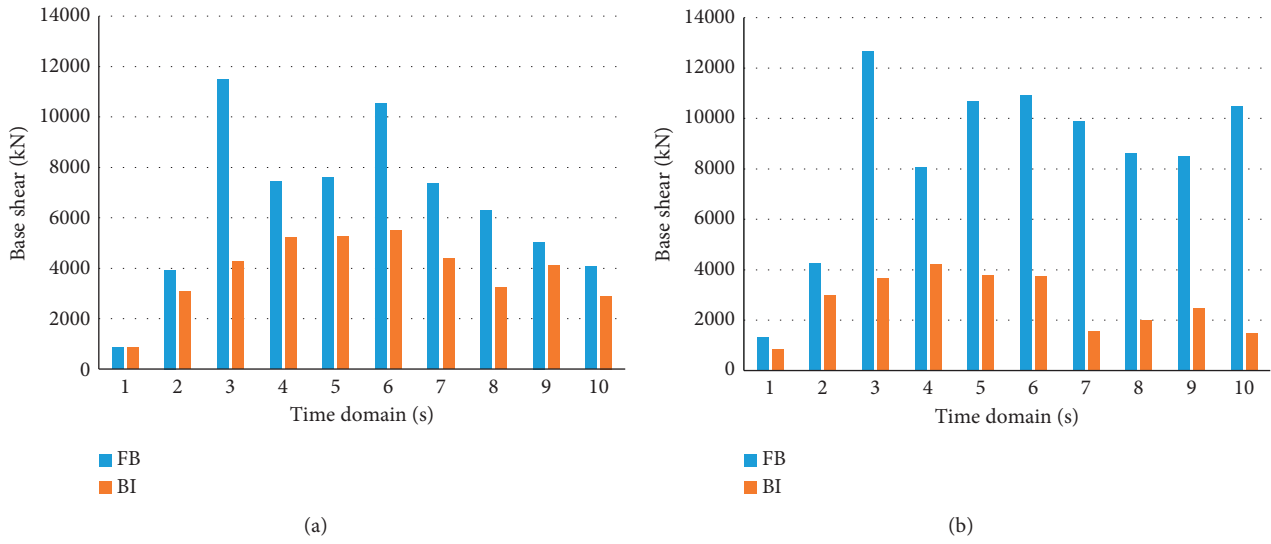


FIGURE 14: Absolute base shear reduction in FBI adjacent buildings. (a) Longitudinal direction. (b) Transverse direction.

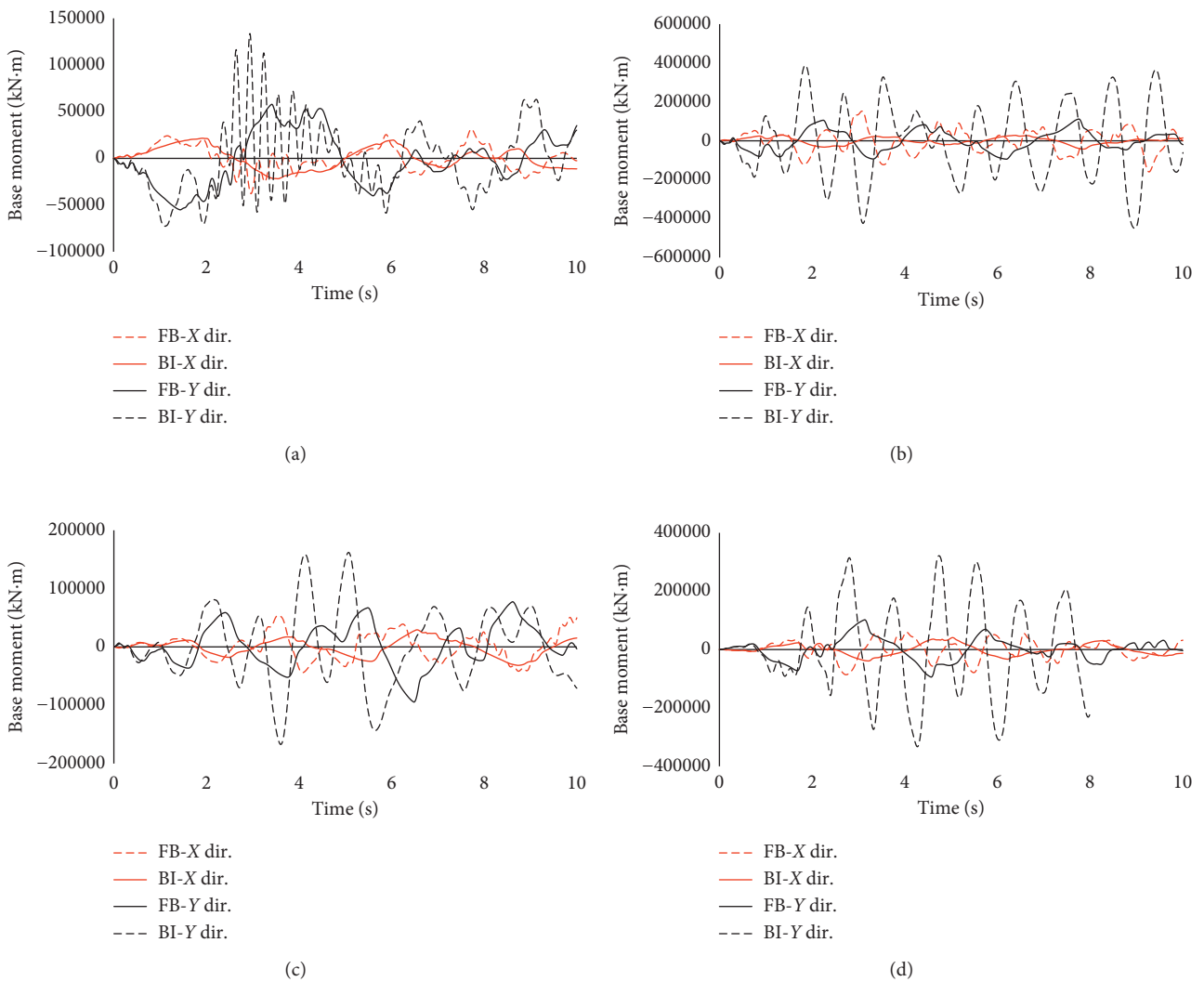


FIGURE 15: Base moment for FFB and FBI adjacent buildings under applied earthquakes. (a) Cape. (b) LACC-N. (c) S-Monica. (d) El-Centro.

TABLE 7: Absolute base moment (kN-m) of the adjacent buildings under applied earthquakes.

Earthquake	FFB shorter building disp. (cm)		FBI shorter building disp. (cm)		Reduction (%)	
	X	Y	X	Y	X	Y
Cape	37,819	133,587	21,826	57,920	42	57
LACC-N	159,732	450,658	42,346	112,108	73	75
S-Monica	53,719	167,263	31,674	94,593	41	43
El-Centro	86,210	332,957	41,036	102,045	52	69
Ave.					52	61

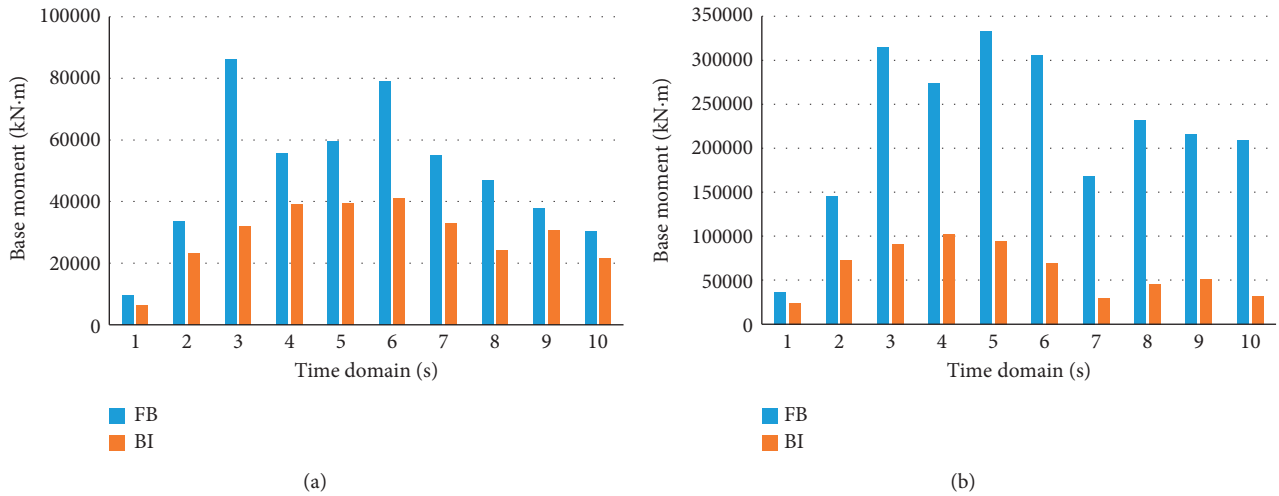


FIGURE 16: Absolute base moment in FFB and FBI adjacent buildings. (a) Longitudinal direction. (b) Transverse direction.

3.2. *Effects of Separation Gap on FBI Adjacent Buildings (Scenario 2).* According to previous results, significant reductions were observed for relative displacements, accelerations, pounding forces, base shear, and base moment responses of FBI adjacent buildings. In this section, the FBI adjacent buildings studied above (Figure 5(b)) were chosen to investigate the effects of separation gap on them. To aid the aim, three seismic gaps were modelled as follows:

- (1) 30 mm (Case A)
- (2) 170 mm (Case B)
- (3) 300 mm (Case C)

3.2.1. *Displacement Responses.* By considering the displacement response of the FBI adjacent building, the taller building had more movement; thus, the authors decided to investigate the displacement responses of the taller building. The displacement response along the floor levels is indicated in Figure 19. As figure shows, the peak displacement for three cases occurred at the roof level of buildings at both positive and negative directions. Toward the positive direction, the maximum displacements were 21.21 cm, 21.33 cm, and 21.14 cm for Case A, B, and C, respectively. Although the displacement values were approximately the same, the motion pattern of the buildings at each floor level for different size of gaps was not similar. The displacement pattern along the floor levels once the seismic gap was 30 mm and 170 mm has

high-pitched slope in the positive direction, particularly above level 4 (pounding level). This was due to the collision of the shorter building to the taller one at that level. Insofar that the inconsistency of displacement at floors was almost removed in the positive direction for the building with 300 mm gap size as demonstrated in the figure.

3.2.2. *Acceleration Responses.* Figure 20 displays the acceleration response of the taller building for different cases along the building height. The building with a 30 mm separation gap had the peak accelerations along its floors in both positive and negative directions compared to the other two cases. By increasing separation distances between buildings, the acceleration response of each floor reduced. In the positive direction, the maximum accelerations took place with 5.16 m/s^2 at the third floor for 30 mm gap and 4.912 m/s^2 at the roof level for both 170 mm and 300 mm gaps. In contrast, for the negative direction, the peak accelerations with -15.14 m/s^2 and -11.27 m/s^2 occurred at the first floor for 30 mm and 170 mm gaps, respectively. The above explanations illustrated 4.8% reduction in acceleration response of the building for Case B and C compared to Case A, in the positive direction. On the other hand, in the negative direction, there was 30.35% and 48.2% acceleration reduction in values which could be seen when the separation gap increased from 30 mm to 170 mm and 300 mm, respectively.

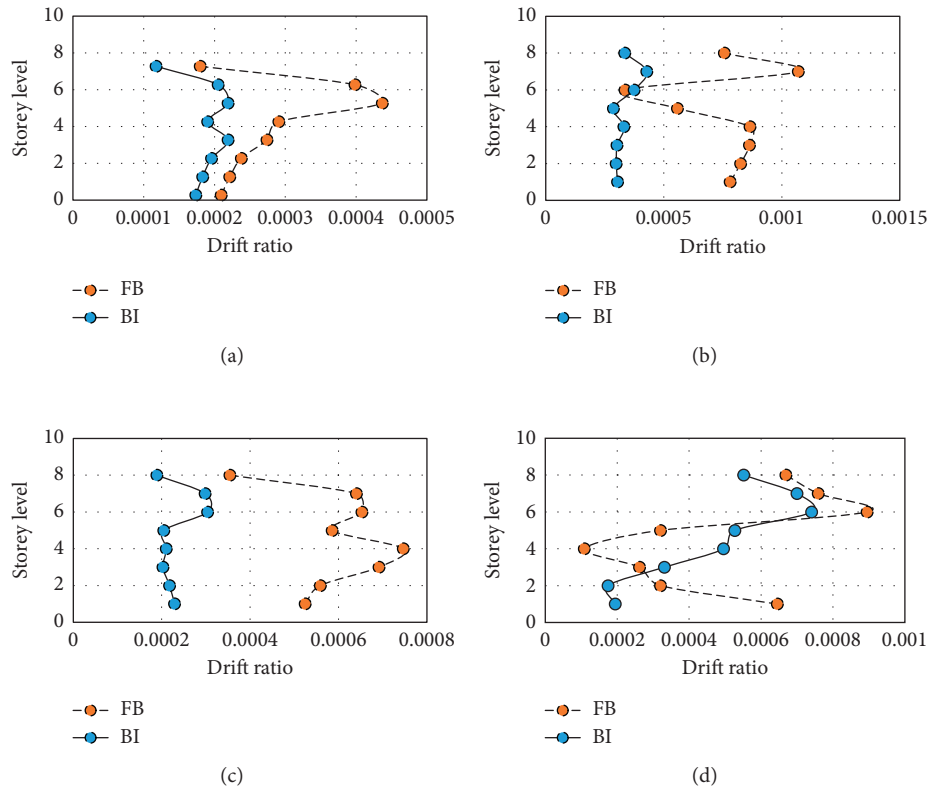


FIGURE 17: Storey drift for FFB and FBI buildings. (a) Cape. (b) LACC-N. (c) S-Monica. (d) El-Centro.

3.2.3. Pounding Force. From Table 8, it can be observed that the pounding force was decreased as seismic gaps were increased. The pounding force was 2289.81 kN, 1920.70 kN, and 1366.15 kN for 30 mm, 170 mm, and 300 mm gaps, respectively. It showed a reduction of 16.12% and 40.3% for Case B and Case C compared to Case A. Moreover, there was a 28.9% decrease for Case C (300 mm) in comparison to Case B (170 mm). This consequence demonstrated that a sufficient separation distance between structures would profoundly reduce the pounding damage not only for FBI adjacent buildings but for FFB adjacent buildings as well. Consequently, the damages and collapse of structures reduce when the pounding forces become smaller. In addition to these, Figure 21 depicts the peak pounding forces occurred at 4.74 seconds, 4.93 seconds, and 5.24 seconds for structure with 30 mm, 170 mm, and 300 mm gaps, respectively. This comparison showed that the increase in the separation gap between buildings reduced the collision chance during earthquake excitations. Also, it could be observed that when the gap was only 30 mm, over fifteen times the structures contacted each other, whilst for 170 mm and 300 mm seismic gaps, they collided ten and seven times, respectively.

3.2.4. Base Shear and Base Moment. Figure 22 shows the effect of gap distance on the FBI adjacent building in terms of base shear and base moment in both longitudinal and transverse directions. Based on the figure, closer gap resulted higher base shear and base moment in the longitudinal

(pounding) direction, although in the transverse direction there was no much difference to carry the shear and moment. This was because in the transverse direction there was no effect of the pounding except a bit frictional force which was reported as a negligible matter [35]. Accordingly, the base shear in the longitudinal direction for Case A was 5471.6 kN and for both cases of B and C was 4351.6 kN. In the transverse direction, the base shear for all cases was 4246 kN. In addition, the base moment in the longitudinal direction for Case A was 41037 kN·m and for both cases of B and C was 30567 kN·m. In the transverse direction, the base moment for Case A, B, and C was recorded as 102044 kN·m, 102319 kN·m, and 102573 kN·m, respectively. These small changes in base moment response was due to the existence of that friction force mentioned above.

3.2.5. Storey Drift. The storey drift in Cases A and B had approximately the same tendency; however, it had different trends in Case C as shown in Figure 23. It was because of the pounding effect in the principal direction. Increase of the seismic gap led the building to experience less pounding force and then having more moderate behaviour. In particular, the maximum drift occurred for the buildings with 30 mm and 170 mm gap distance at the 6th floor level with 0.000741 and 0.000535, respectively. For the building with 300 mm gap distance, the peak drift happened in the 4th floor level with 0.000428. It is concluded that, by increasing the seismic gap between FBI adjacent buildings, the storey drift was reduced and the trend of movement became better.

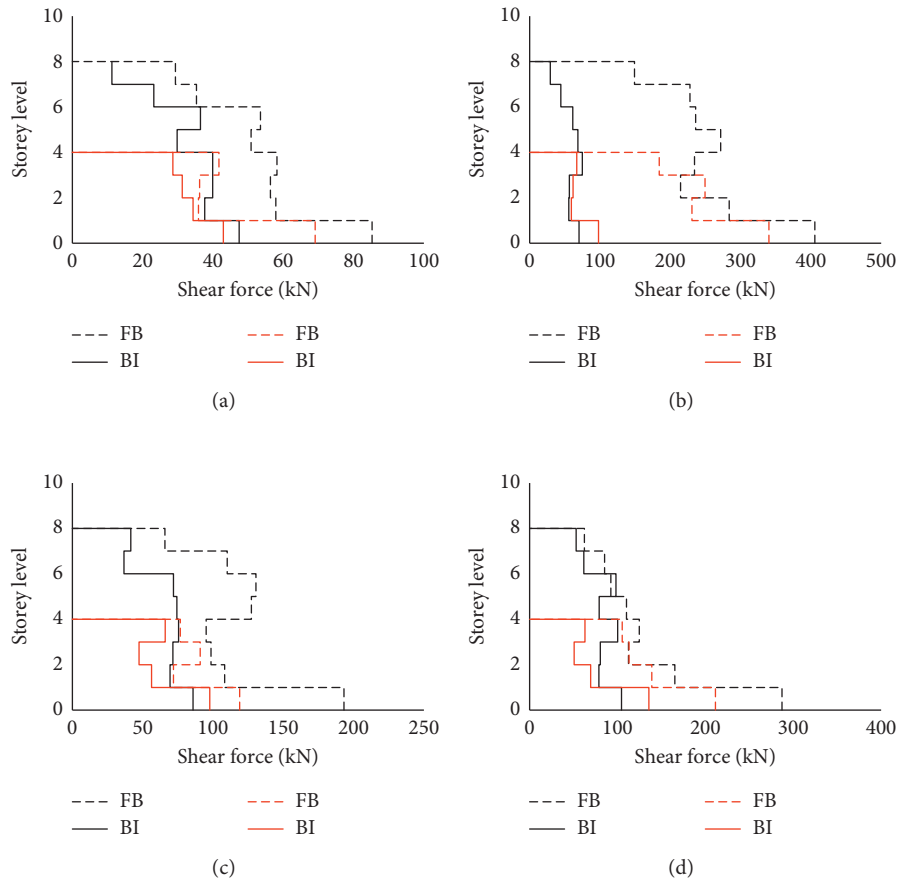


FIGURE 18: Storey shear force in the adjacent buildings subjected to the different ground motions.

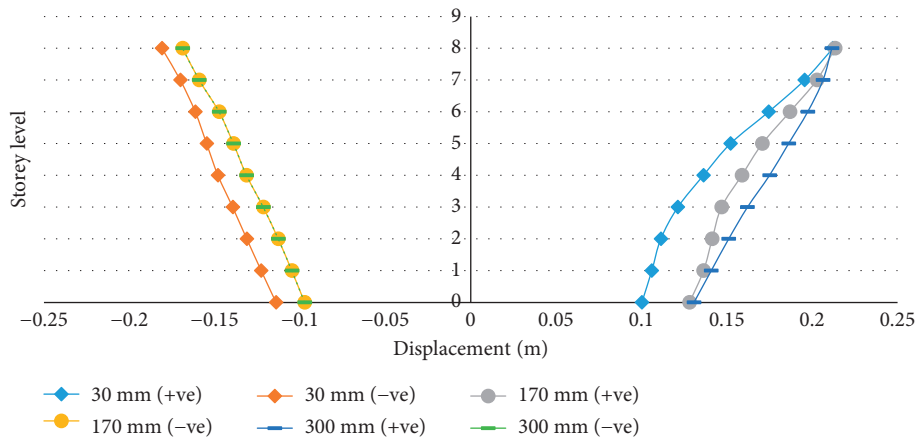


FIGURE 19: Envelope displacement response of the tall BI buildings considering different seismic gaps.

3.2.6. *Hysteresis Behaviour.* The hysteresis response of the base isolators used in the current study under longitudinal component of the El-Centro earthquake is shown in Figure 24. As illustrated in the figure, the forces and deformations in the longitudinal direction (principal direction) were changed considering the effect of different gaps between FBI adjacent buildings.

In the shorter building, the force-deformation (F-D) carried by the isolators was 130 kN-11 mm in Case A. For

both 170 mm and 300 mm separation distance, the F-D was similarly 91 kN-7 mm.

In the taller building, the F-D for Case A was 119 kN-10 mm, and for both Case B and C the F-D was 145 kN-13 mm and 147 kN-13 mm, respectively. The behavioural fluctuations of the F-D of isolators were noticeable, spectacularly, for the shorter building, the values of the F-D were decreased as the gap distance between buildings was increased. In contrary, for the taller building, the values of the

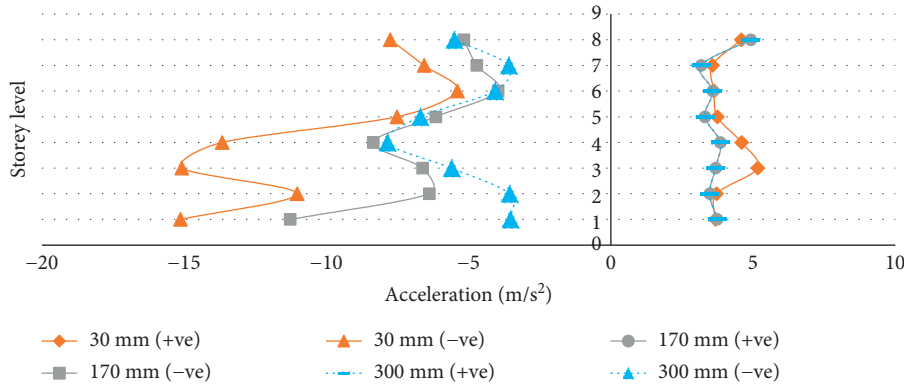


FIGURE 20: Acceleration response of BI buildings considering different seismic gaps.

TABLE 8: Effect of different seismic gaps on the pounding force at the pounding level.

Storey level	Separation distance (mm)	Pounding force (kN)	Time (s)
4th	30	2289.81	4.74
4th	170	1920.70	4.93
4th	300	1366.15	5.24

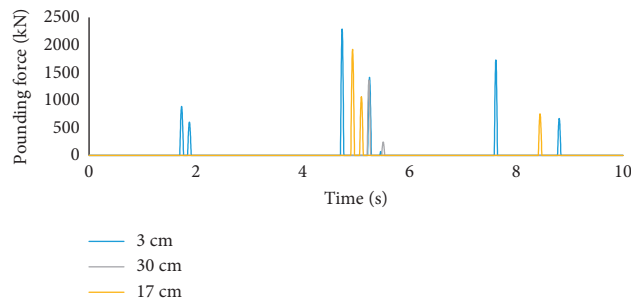


FIGURE 21: Pounding force considering different seismic gaps.

F-D were increased as the gap distance was increased. Based on these consequences, in design of base isolators for FBI adjacent buildings, it is felt to take the effect of seismic gaps between buildings into consideration.

The overall seismic responses of FBI adjacent buildings considering the effect of different separation gaps are summarized in Table 9. From the table, it can be concluded that to perform a BI building in vicinity of other BI buildings, it is a vital need to consider the effect of structural gaps, particularly for those regions with high risk potential of seismic excitations.

4. Conclusions

The present study has been divided into two scenarios. In the first scenario, the nonlinear time history responses of the FFB and FBI adjacent buildings under bilateral excitations have been carried out. To study the effect of the base isolation system on seismic response of the FBI adjacent buildings, their performance has been compared to those with FFB

support. In the second scenario, three different seismic gaps have been modelled for the FBI adjacent buildings to investigate the effect of separation gaps on response of the FBI adjacent buildings subjected to earthquake load. From both the scenarios and comparative results of the free vibration and time history analyses, the following conclusions can be drawn:

- (1) The most impressive option in the study showed that the base isolators resulted in a lower frequency which led the FBI adjacent buildings to have a lower acceleration.
- (2) All the displacement, storey drift, acceleration, base shear, and base moment responses of the superstructure of the FBI buildings were much less sensitive, whilst these responses for FFB buildings were increased significantly.
- (3) From the relative displacement analysis and acceleration responses of FBI adjacent buildings, it could be concluded that the base isolation system was

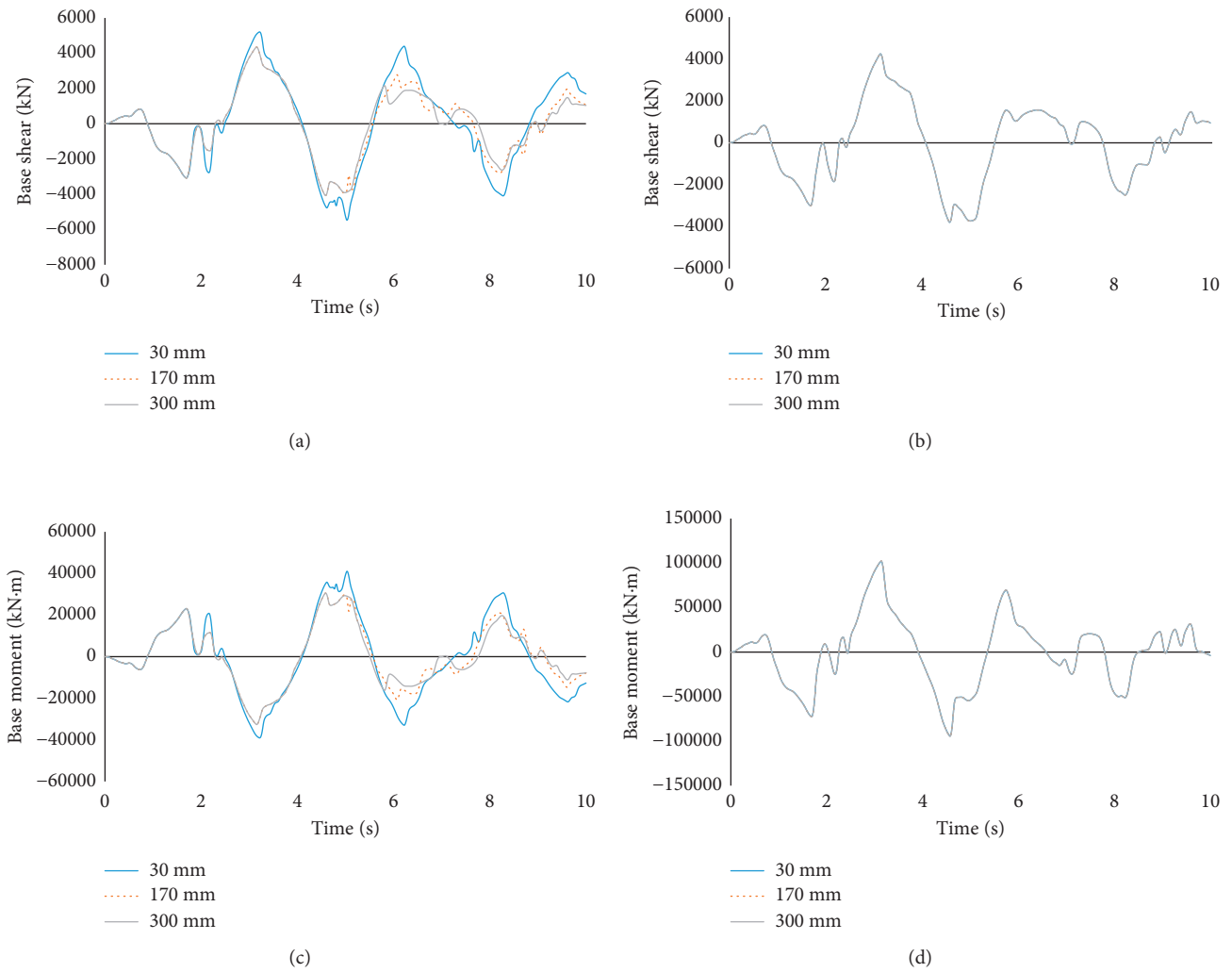


FIGURE 22: Effect of seismic gaps on base shear and base moment. (a) Longitudinal direction. (b) Transverse direction. (c) Longitudinal direction. (d) Transverse direction.

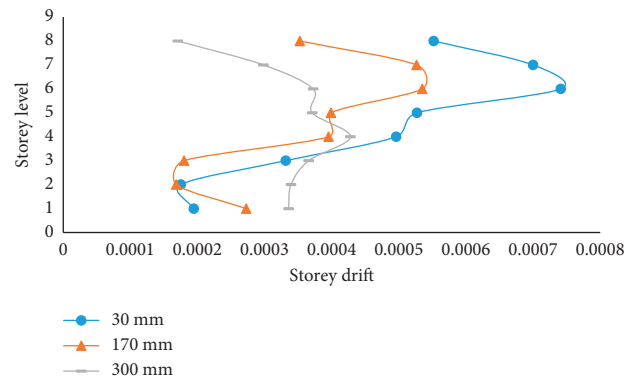


FIGURE 23: Storey drift in each floor level for different separation distances.

further efficient to decrease displacement compared to acceleration.

(4) Shear force in the vertical members and maximum base shear of FBI buildings were reduced significantly.

So, it anticipates fine to save a number of structures as well as supplies economic aid.

(5) Reduction of overturning moment in FBI adjacent buildings makes the buildings more stable in

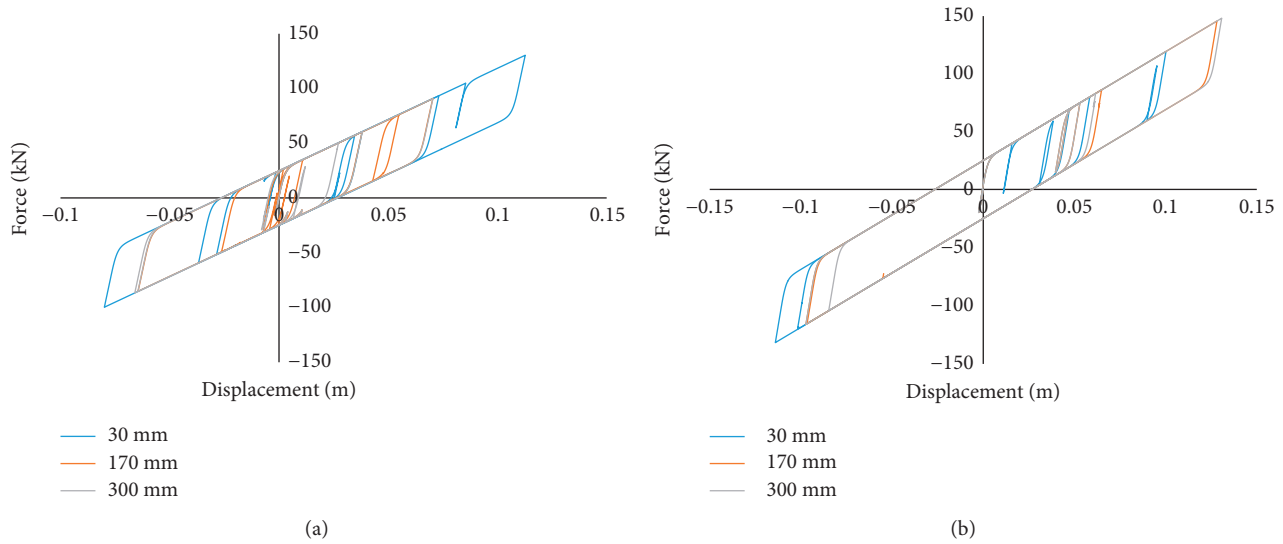


FIGURE 24: Hysteresis behaviour of LRB devices considering different seismic gaps. (a) Shorter building. (b) Taller building.

TABLE 9: Summarized responses of fully BI adjacent buildings considering seismic gaps.

Response	Gap distance (mm)		
	30	170	300
Pounding force (kN)	2289.81	1920.70	1366.15
Dis. ^(taller building-) top floor (cm)	21.21	21.33	21.14
Dis. ^(taller building+) top floor (cm)	-18.09	-16.88	-16.88
Acc. ^(taller building-) (m/s ²)	-15.14	-11.27	-7.85
Acc. ^(taller building+) (m/s ²)	5.16	4.192	4.192
Base shear _(x) (kN)	5471.6	4351.6	4351.6
Base shear _(y) (kN)	4246	4246	4246
Base moment _(x) (kN·m)	41,037	30,567	30,567
Base moment _(y) (kN·m)	102,044	102,319	102,573
Storey drift ratio	0.000741	0.000535	0.000428
F-D of base isolators ^(taller building) (kN·mm)	119-10	145-13	147-13
F-D of base isolators ^(shorter building) (kN·mm)	130-11	91-7	91-7

-: negative direction; +: positive direction.

comparison to the FFB adjacent buildings. This leads the buildings to experience less contact in both the transverse and longitudinal directions. Allowance of transitional displacement of support suddenly mutates the trend of entire building deformation.

- (6) Closer gap resulted in undesired movements for the middle floors for FBI adjacent buildings. Moreover, closer seismic gap resulted in higher base shear and base moment in the FBI adjacent buildings in the longitudinal (pounding) direction.
- (7) As seismic gap increases in FBI adjacent buildings, the number of collisions decreases because of time delay in pounding.
- (8) As base isolators affected the displacement pattern of substructure of buildings, the storey drift of the taller BI adjacent building comes into a favourable trend.

- (9) The values of the F-D of the base isolators were changed as the seismic gap between buildings was altered. Thus, it is a need to focus on the effect of the seismic gaps on the design of base isolators in future studies.

Conflicts of Interest

The authors have no conflicts of interest regarding preparation, contribution, and authorship of the present manuscript.

Acknowledgments

The authors gratefully acknowledge the support given by Fundamental Research Grant Scheme, Ministry of Education, Malaysia (FRGS project no. FP004-2014B), Postgraduate Research Grant (PPP project no. PG177-2016A),

and University of Malaya Research Grant (UMRG project no. RP004A-13AET).

References

- [1] K. Ghaedi, Z. Ibrahim, H. Adeli, and A. Javanmardi, "Invited review: recent developments in vibration control of building and bridge structures," *Journal of Vibroengineering*, vol. 19, no. 5, pp. 3564–3580, 2017.
- [2] A. Javanmardi, Z. Ibrahim, K. Ghaedi, M. Jameel, H. Khatibi, and M. Suhatri, "Seismic response characteristics of a base isolated cable-stayed bridge under moderate and strong ground motions," *Archives of Civil and Mechanical Engineering*, vol. 17, no. 2, pp. 419–432, 2017.
- [3] M. Gordan, H. A. Razak, Z. Ismail, and K. Ghaedi, "Recent developments in damage identification of structures using data mining," *Latin American Journal of Solids and Structures*, vol. 14, no. 13, pp. 2373–2401, 2017.
- [4] K. Ghaedi and Z. Ibrahim, "Earthquake prediction," in *Earthquakes - Tectonics, Hazard and Risk Mitigation*, pp. 205–227, InTechOpen, London, UK, 2017.
- [5] K. Kasai and B. F. Maison, "Building pounding damage during the 1989 Loma Prieta earthquake," *Engineering Structures*, vol. 19, no. 3, pp. 195–207, 1997.
- [6] E. Rosenblueth and R. Meli, "The 1985 earthquake: causes and effects in Mexico City," *Concrete International*, vol. 8, pp. 23–24, 1986.
- [7] P. Komodromos, P. C. Polycarpou, L. Papaloizou, and M. C. Phocas, "Response of seismically isolated buildings considering poundings," *Earthquake Engineering and Structural Dynamics*, vol. 36, no. 12, pp. 1605–1622, 2007.
- [8] S. Mahmoud and R. Jankowski, "Pounding-involved response of isolated and non-isolated buildings under earthquake excitation," *Earthquakes and Structures*, vol. 1, no. 3, pp. 231–252, 2010.
- [9] P. C. Polycarpou and P. Komodromos, "Earthquake-induced poundings of a seismically isolated building with adjacent structures," *Earthquake Engineering and Structural Dynamics*, vol. 39, no. 8, pp. 933–940, 2010.
- [10] M. Jameel, A. B. M. S. Islama, R. R. Hussain, S. D. Hasan, and M. Khaleel, "Non-linear FEM analysis of seismic induced pounding between neighbouring multi-storey structures," *Latin American Journal of Solids and Structures*, vol. 10, no. 5, pp. 921–939, 2013.
- [11] R. Jankowski, "Earthquake-induced pounding between equal height buildings with substantially different dynamic properties," *Engineering Structures*, vol. 30, no. 10, pp. 2818–2829, 2008.
- [12] S. E. Abdel Raheem, "Mitigation measures for earthquake induced pounding effects on seismic performance of adjacent buildings," *Bulletin of Earthquake Engineering*, vol. 12, no. 4, pp. 1705–1724, 2014.
- [13] A. V. Bhaskararao and R. S. Jangid, "Seismic response of adjacent buildings connected with friction dampers," *Bulletin of Earthquake Engineering*, vol. 4, pp. 43–64, 2006.
- [14] V. Jeng and W. Tzeng, "Assessment of seismic pounding hazard for Taipei City," *Engineering Structures*, vol. 22, no. 5, pp. 459–471, 2000.
- [15] J. H. Lin and C. C. Weng, "Spectral analysis on pounding probability of adjacent buildings," *Engineering Structures*, vol. 23, no. 7, pp. 768–778, 2001.
- [16] B. Madani, F. Behnamfar, and H. Tajmir Riahi, "Dynamic response of structures subjected to pounding and structure–soil–structure interaction," *Soil Dynamics and Earthquake Engineering*, vol. 78, pp. 46–60, 2015.
- [17] K.-S. Park and S.-Y. Ok, "Hybrid control approach for seismic coupling of two similar adjacent structures," *Journal of Sound and Vibration*, vol. 349, pp. 1–17, 2015.
- [18] Y. L. Xu, S. Zhan, J. M. Ko, and W. S. Zhang, "Experimental investigation of adjacent buildings connected by fluid damper," *Earthquake Engineering and Structural Dynamics*, vol. 28, pp. 609–631, 1999.
- [19] A. B. M. Islam, M. Jameel, S. I. Ahmad, and M. Z. Jumaat, "Study on corollary of seismic base isolation system on buildings with soft storey," *International Journal of Physical Science*, vol. 6, no. 11, pp. 2654–2661, 2011.
- [20] A. B. M. Islam, M. Jameel, and M. Z. Jumaat, "Seismic isolation in buildings to be a practical reality: behavior of structure and installation technique," *Journal of Engineering and Technology Research*, vol. 3, no. 4, pp. 97–117, 2011.
- [21] A. B. M. S. Islam, R. Rizwan, M. Jameel, and M. Zamin, "Non-linear time domain analysis of base isolated multi-storey building under site specific bi-directional seismic loading," *Automation in Construction*, vol. 22, no. 22, pp. 554–566, 2012.
- [22] Z. Ren, C. J. Anumba, G. Augenbroe, and T. M. Hassan, "A functional architecture for an e-Engineering hub," *Automation in Construction*, vol. 17, no. 8, pp. 930–939, 2008.
- [23] J. Penzien, "Evaluation of building separation distance required to prevent pounding during strong earthquakes," *Earthquake Engineering and Structure Dynamics*, vol. 26, no. 8, pp. 849–858, 1997.
- [24] K. Kasai, A. Jagiasi, and V. Jeng, "Inelastic vibration phase theory for seismic pounding mitigation," *Structural Engineering*, vol. 122, no. 10, pp. 1136–1146, 1996.
- [25] H. Hao and S. R. Zhang, "Spatial ground motion effect on relative displacement of adjacent building structures," *Earthquake Engineering and Structural Dynamics*, vol. 28, no. 4, pp. 333–349, 1999.
- [26] B. Shrestha, "Effects of separation distance and nonlinearity on pounding response of adjacent structures," *International Journal of Civil Engineering and Structural Engineering*, vol. 3, no. 3, pp. 603–612, 2013.
- [27] V. K. Agarwal, J. M. Niedzwecki, and J. W. van de Lindt, "Earthquake induced pounding in friction varying base isolated buildings," *Engineering Structures*, vol. 29, no. 11, pp. 2825–2832, 2007.
- [28] S. Khatiwada, N. Chouw, and J. W. Butterworth, "A generic structural pounding model using numerically exact displacement proportional damping," *Engineering Structures*, vol. 62–63, pp. 33–41, 2014.
- [29] Building Seismic Safety Council for the Federal Emergency Management Agency, "NEHRP recommended provisions for seismic regulations for new buildings and other structures," Rep. No. Fema 368, Building Seismic Safety Council, Washington, DC, USA, 2001.
- [30] E. L. Wilson, *Three-Dimensional Static and Dynamic Analysis of Structures*, Computers and Structures, Inc., Berkeley, CA, USA, 2002.
- [31] T. E. Kelly, *Base Isolation of Structures: Design Guidelines*, Holmes Consulting Group Ltd, Auckland, New Zealand, 2001.
- [32] T. E. Kelly, W. H. Robinson, and R. I. Skinner, *Seismic Isolation for Designers and Structural Engineers*, Robinson seismic Ltd., Wellington, New Zealand, 2006.
- [33] F. Naeim and J. Kelly, *Design of Seismic Isolated Structures: From Theory to Practice*, Wiley, Hoboken, NJ, USA, 1999.

- [34] Building and Housing Research Center, *Iranian Code of Practice for Seismic Resistant Design of Buildings (Standard No. 2800)*, Building and Housing Research Center, Tehran, Iran, 3rd edition, 2007.
- [35] R. Jankowski, "Non-linear FEM analysis of earthquake-induced pounding between the main building and the stairway tower of the Olive View Hospital," *Engineering Structures*, vol. 31, no. 8, pp. 1851–1864, 2009.
- [36] R. Jankowski, "Non-linear viscoelastic modelling of earthquake-induced structural pounding," *Earthquake Engineering and Structural Dynamics*, vol. 34, no. 6, pp. 595–611, 2005.
- [37] M. U. Hanif, Z. Ibrahim, M. Jameel, K. Ghaedi, and M. Aslam, "A new approach to estimate damage in concrete beams using non-linearity," *Construction and Building Materials*, vol. 124, no. 11, pp. 1081–1089, 2016.
- [38] K. Ghaedi, F. Hejazi, Z. Ibrahim, and P. Khanezaei, "Flexible foundation effect on seismic analysis of Roller Compacted Concrete (RCC) dams using finite element method," *KSCE Journal of Civil Engineering*, pp. 1–13, 2017.

Research Article

A Designer's Approach for Estimation of Nuclear-Air-Blast-Induced Ground Motion

Shashank Pathak  and **G. V. Ramana**

Department of Civil Engineering, Indian Institute of Technology Delhi, New Delhi, India

Correspondence should be addressed to Shashank Pathak; shashankpathaks@gmail.com

Received 19 August 2017; Accepted 5 December 2017; Published 8 March 2018

Academic Editor: Chiara Bedon

Copyright © 2018 Shashank Pathak and G. V. Ramana. This is an open access article distributed under the Creative Commons Attribution License, which permits unrestricted use, distribution, and reproduction in any medium, provided the original work is properly cited.

A reliable estimate of free-field ground displacement induced by nuclear-air-blast is required for design of underground strategic structures. A generalized pseudostatic formulation is proposed to estimate nuclear-air-blast-induced ground displacement that takes into account nonlinear stress-strain behaviour of geomaterials, stress-dependent wave propagation velocity, and stress wave attenuation. This proposed formulation is utilized to develop a closed-form solution for linearly decaying blast load applied on a layered ground medium with bilinear hysteretic behaviour. Parametric studies of closed-form solution indicated that selection of appropriate constrained modulus consistent with the overpressure is necessary for an accurate estimation of peak ground displacement. Stress wave attenuation affects the computed displacement under low overpressure, and stress-dependent wave velocity affects mainly the occurrence time of peak displacement and not its magnitude. Further, peak displacements are estimated using the proposed model as well as the UFC manual and compared against the field data of atmospheric nuclear test carried out at Nevada test site. It is found that the proposed model is in good agreement with field data, whereas the UFC manual significantly underestimates the peak ground displacements under higher overpressures.

1. Introduction

Underground siting of strategic structures [1] is an option to enhance the safety against nuclear-air-blast [2]. Nuclear explosions generate rapidly moving air-overpressures capable of producing significant ground displacements [3]. Most severe loading occurs within a close vicinity around the ground zero (GZ) known as superseismic zone. This zone is subjected to significantly high overpressures. The velocity of moving air-overpressure fronts is also more than the P-wave velocity of the ground [3–6]. Hence, a reliable estimate of nuclear-air-blast-induced ground displacement is required for design in superseismic zone [5, 7, 8]. Several studies using numerical approaches that account for realistic stress-strain behaviour and boundary conditions are reported for calculating the free-field response [9–16]. Such studies require specialized expertise in numerical tools and are unattractive to practicing engineers. Before the advent of computational tools, Wilson and Sibley [17] conceptualized a one-dimensional pseudostatic approach to estimate air-blast-induced ground displacement.

Whitman [4] and Baron et al. [18] have also shown that air-blast-induced ground motion is predominantly one-dimensional and vertical in superseismic zone. In the present work, a generalized one-dimensional pseudostatic formulation is developed to estimate nuclear-air-blast-induced vertical ground displacement that accounts for (i) nonlinear stress-strain behaviour [e.g., 19, 20], (ii) stress-dependent wave propagation velocity, and (iii) stress wave attenuation. Using the proposed formulation, a closed-form solution is developed for linearly decaying blast load with negligible rise-time applied on a layered ground medium with bilinear hysteretic stress-strain behaviour. The proposed model is validated against the field data of an atmospheric nuclear test conducted at Nevada test site [21], and various parametric studies are carried out. In addition, performance of the closed-form solution is also compared with the model given in UFC [22].

2. Generalized Formulation

The developed formulation is explained in detail below.

2.1. Determination of Overstress Distribution (due to Air-Blast) in the Ground. Air-overpressure generated due to nuclear-air-blast consists of an initial rising portion followed by a decaying portion (Figure 1). Overpressure time-history can be visualized as consisting of multiple overpressure fronts. These overpressure fronts are transferred to the ground as P-waves. On arrival of an air-shock front at the point of interest, an initial pulse travels with seismic P-wave velocity and reaches a depth Z_{0i} at time t_i . Subsequently, other fronts arrive and penetrate into the ground. If the location of peak overpressure front at time t_i is given as Z_{pi} , then, the ground above the depth Z_{pi} experiences compressive stresses lower than those caused by the peak overpressure front at that depth. Therefore, the depths above Z_{pi} are referred to as “unloading zone.” However, the peak overpressure front is yet to reach at locations deeper than Z_{pi} , and therefore, the zone lying beneath the depth Z_{pi} is denoted as “loading zone” (Figure 1). It is noted that “unloading zone” corresponds to the “decay portion” of overpressure, whereas “loading zone” corresponds to the “rising portion.” Therefore, at times earlier than the rise-time, there does not exist any unloading zone as overpressure fronts from the decay portion do not arrive before the end of rise-time.

To determine the stress distribution in the ground at time t_i , contribution from all stress fronts arrived before time t_i is considered. If the k th overpressure front arrives at the point of interest on ground surface at time t_k such that $t_k \leq t_i$, then the k th overpressure front reaches at depth Z_{ki} at time t_i . Stress fronts propagating through ground are affected by attenuation (caused by hysteresis losses, viscosity of ground materials, and dispersion of energy in 3-dimensional space) and interference with reflected wave fronts (generated due to impedance variation with depth). In the present study, stress wave attenuation is taken into account through a geometrical attenuation parameter, whereas interference of incident and reflected stress waves is ignored. If the attenuation coefficient at depth Z_{ki} is given as

$$f_{kz} = \begin{cases} (f_{rz} - 1) \frac{P(t_k)}{P_0} + 1 \approx (f_{rz} - 1) \frac{t_k}{t_r} + 1, & 0 \leq t_k \leq t_r : \text{rising portion} \\ f_{rz}, & t_r \leq t_k \leq t_p : \text{decay portion,} \end{cases} \quad (3)$$

where subscript “z” represents the depth coordinate. Using the average loading rate as P_0/t_r , $P(t_k)/P_0$ can be approximated as t_k/t_r (3). As wave propagation velocity through ground media is proportional to the square root of the tangential modulus [24], f_{rz} is given by the following equation:

$$f_{rz} = \sqrt{\frac{(\partial\sigma_z/\partial\varepsilon_z)|_{\sigma=0}}{(\partial\sigma_z/\partial\varepsilon_z)|_{\sigma_{rz}}}}, \quad (4)$$

where $(\partial\sigma_z/\partial\varepsilon_z)|_{\sigma=0}$ is the tangential modulus at initial stress level at depth “z” and $(\partial\sigma_z/\partial\varepsilon_z)|_{\sigma_{rz}}$ is the tangential modulus at peak stress level at depth “z.”

$\alpha(Z_{ki})$, then the stress generated at depth Z_{ki} can be written as $\alpha(Z_{ki}) \times P(t_k)$, where $P(t_k)$ is the magnitude of the k th overpressure front. Depth of the penetration Z_{ki} depends upon wave propagation velocity of the stress front, which in turn depends upon the tangential modulus of the geo-material at the stress level at the depth of interest. If wave velocity of the k th stress front is denoted as V_{kz} (a function of depth “z”), then (1) can be solved to obtain Z_{ki} as a function of t_i , t_k , and V_{kz} (2),

$$\int_0^{Z_{ki}} \frac{dz}{V_{kz}} = t_i - t_k, \quad (1)$$

$$Z_{ki} = g(t_i - t_k, V_{kz}) = \varphi(t_k), \quad (2)$$

where g is the function obtained by solving (1). It is noted that for a given t_i , Z_{ki} is effectively a function (φ) of t_k only because V_{kz} is also a function of t_k . As soon as the air-blast slaps the ground surface, ground deforms elastically and an elastic wave is generated which propagates with seismic P-wave velocity. Upon subsequent arrival of higher overpressure fronts, inelastic waves propagate at velocities smaller than P-wave velocity. If the ratio of P-wave velocity to wave velocity corresponding to the k th overpressure front at depth “z” is denoted as $f_{kz} = (V_{pz}/V_{kz})$, then at initial stress levels f_{kz} is equal to one. With increasing stress level, V_{kz} decreases [17, 23]; hence, it is logical to assume that f_{kz} increases with increasing stress level and the maximum value is attained at a peak stress level corresponding to the peak overpressure front. Therefore, a simplest choice is to assume a linearly increasing f_{kz} in direct proportion to overpressure (3). Overpressure fronts from the decay portion propagate through the media which is already stressed in a nonlinear range due to passage of the peak overpressure front. Therefore, it is assumed that wave velocity of overpressure fronts in the decay portion is the same as the peak overpressure front, and hence f_{kz} is the same as f_{rz} :

It should be noted that the ground is in equilibrium under geostatic stresses and at rest before nuclear explosion and only the overstresses caused by nuclear-air-blast causes the ground displacement.

2.2. Determination of Strain Distribution in Ground. Strain distribution with depth (ε_{iz}) can be determined using stress distribution (σ_{iz}) and an appropriate stress-strain relationship [e.g., 25–27] as given in the following equation:

$$\varepsilon_{iz} = \begin{cases} f_L(z, \sigma_{iz}) : \text{loading} \\ f_U(z, \sigma_{iz}) : \text{unloading,} \end{cases} \quad (5)$$

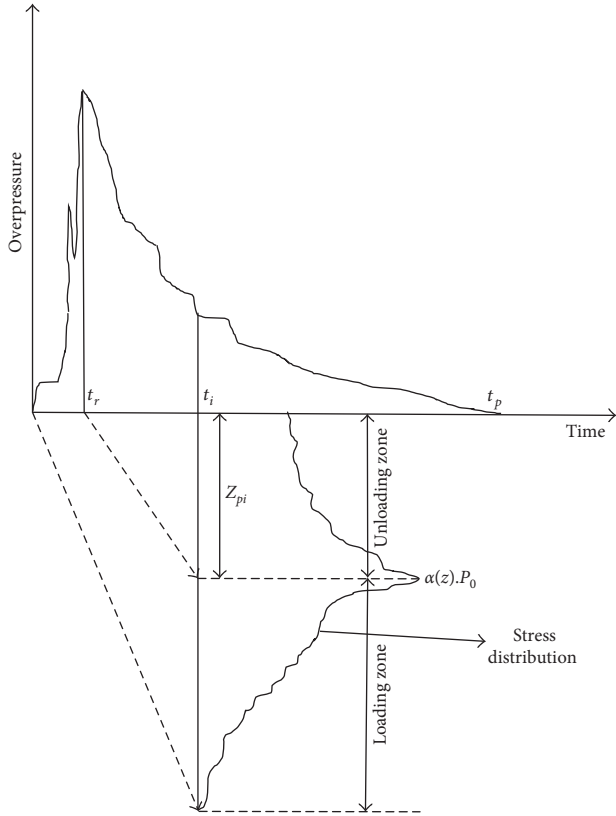


FIGURE 1: Schematic representation of dilatational stress distribution in ground at time t_i .

where functions f_L and f_U denote the loading and unloading branches of the stress-strain curve, respectively (Figure 2).

2.3. *Integration of Strains.* To obtain the vertical ground displacement u_i at time instant t_i , the strain distribution is

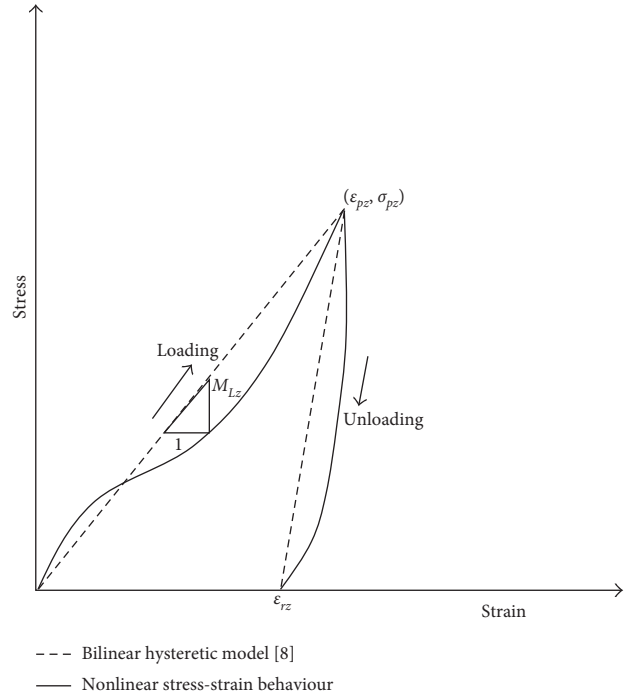


FIGURE 2: Schematic diagram for stress-strain relation at a depth “z.”

integrated (6) from the ground surface to the penetrated wavelength in the ground up to time $t_i (Z_{0i})$,

$$u_i = \int_0^{Z_{0i}} \epsilon_{iz} dz = \int_0^{Z_{ri}} f_U(z, \sigma) dz + \int_{Z_{ri}}^{Z_{0i}} f_L(z, \sigma) dz. \quad (6)$$

Substituting $Z = \varphi(t_k)$ in (6) leads to the following equation:

$$u_i = \begin{cases} \int_{t_i}^0 f_L(\varphi(t_k), \sigma(\varphi(t_k))) \times \varphi'(t_k) dt_k, & 0 \leq t_i \leq t_r : \text{loading} \\ \int_{t_r}^0 f_L(\varphi(t_k), \sigma(\varphi(t_k))) \times \varphi'(t_k) dt_k + \int_{t_i}^{t_r} f_U(\varphi(t_k), \sigma(\varphi(t_k))) \times \varphi'(t_k) dt_k, & t_r \leq t_i \leq t_p : \text{unloading.} \end{cases} \quad (7)$$

Thus, the displacement time-history can be estimated using (7).

3. Closed-Form Solution

Using (7), closed-form solutions can be obtained for several simplified cases [28]. In this article, a closed-form approximation is developed for the following simplifications:

- (a) Linearly decaying overpressure time-history with zero rise-time (Figure 3, (8)),

$$P(t_k) = P_o \left(1 - \frac{t_k}{t_{eq}} \right), \quad (8)$$

where P_o and t_{eq} are peak overpressure and equivalent positive phase duration, respectively.

The reason behind choosing the special case with zero rise-time is the popularity of approximating the actual decay of the incidental pressure by an equivalent triangular pressure pulse among practicing engineers [8, 22]. It is to mention that design charts and empirical relations between the weapon yield, peak overpressure, and the equivalent positive phase durations are also available for equivalent triangular pulses with zero rise-time [5, 8, 29]. Thus, for practicing engineers, a linear decay model with zero rise-time is more useful.

- (b) Bilinear hysteretic stress-strain model [8] with the loading secant modulus (M_L) and strain recovery ratio (r) as parameters (Figure 2).

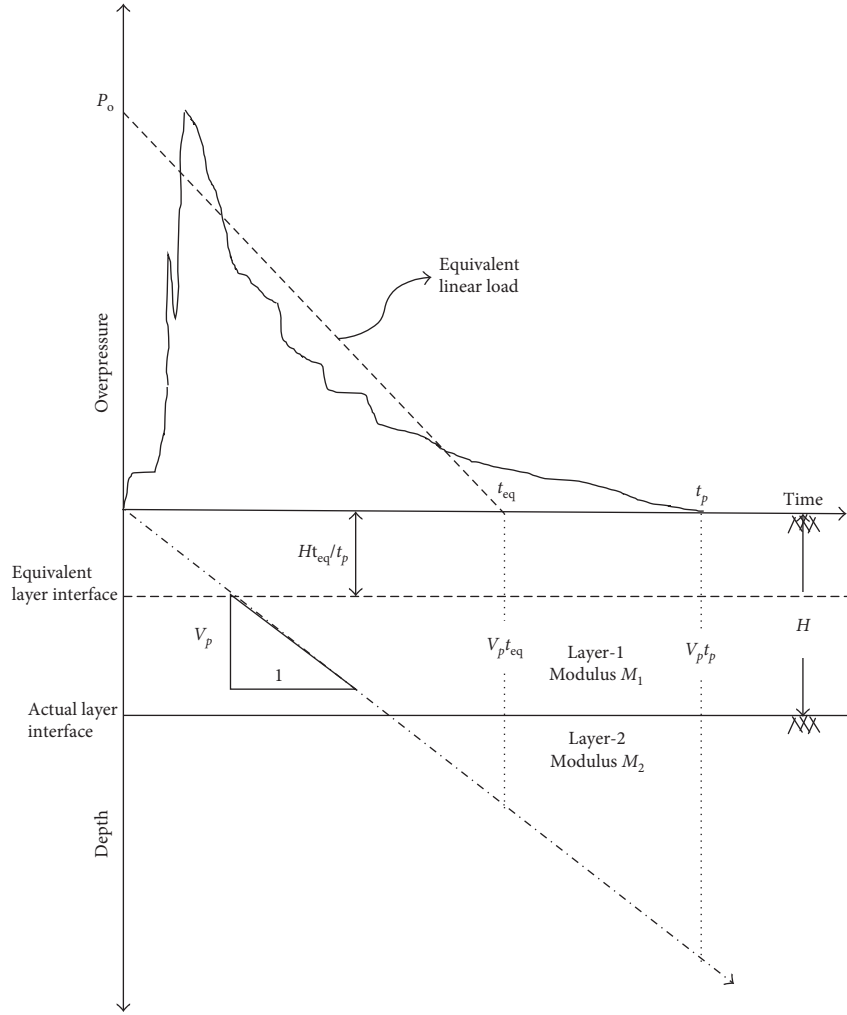


FIGURE 3: Scaling of equivalent ground media.

- (c) Attenuation coefficient (α) is given by the following equation [8, 30]:

$$\alpha = \left(1 + \frac{z}{L_w} \right)^{-1}, \quad (9)$$

where $L_w = 0.971 \times W^{1/3} \times P_o^{-1/2} \times V_L$,

where W is the yield of the explosion in kiloton and V_L is the wave propagation velocity of the peak overpressure front.

- (d) Using (4), f_{rz} is determined as 1 for the bilinear stress-strain model. However, due to nonlinear stress-

strain behaviour, f_{rz} is usually greater than 1. Wilson and Sibley [17] and Batdorf [23] recommended a range of 1.5 to 2. Hereafter, f_{rz} is denoted as f and assumed to be constant with depth.

- (e) A constant but representative P-wave velocity V_p of ground media is assumed.

Using assumptions (a)–(e), integral for loading fronts in (7) (with $t_r \rightarrow 0$) between general time instants t_x and t_{x+1} is written as $\text{Lim}_{t_r \rightarrow 0} \left[\int_{t_x}^{t_{x+1}} f_L(\varphi(t_k), \sigma(\varphi(t_k))) \times \varphi'(t_k) dt_k \right] = P_o / M_L \times \text{Lim}_{t_r \rightarrow 0} L(t_x \rightarrow t_{x+1})$, where $L(t_x \rightarrow t_{x+1})$ can be shown to be given by the following equation:

$$L(t_x \rightarrow t_{x+1}) = \frac{(f-1)t_i + t_r}{(f-1)L_w - t_r V_p} \times \left[\frac{L_w V_p}{(f-1)} \ln \left(\frac{(f-1)t_{x+1} + t_r}{(f-1)t_x + t_r} \right) + \frac{L_w(L_w + V_p t_i)}{(t_r + f t_i - t_i)} \right. \\ \left. \times \ln \left(\frac{(f L_w - L_w - t_r V_p)t_{x+1} + t_r(L_w + V_p t_i)}{(f L_w - L_w - t_r V_p)t_x + t_r(L_w + V_p t_i)} \times \frac{(f-1)t_x + t_r}{(f-1)t_{x+1} + t_r} \right) \right]. \quad (10)$$

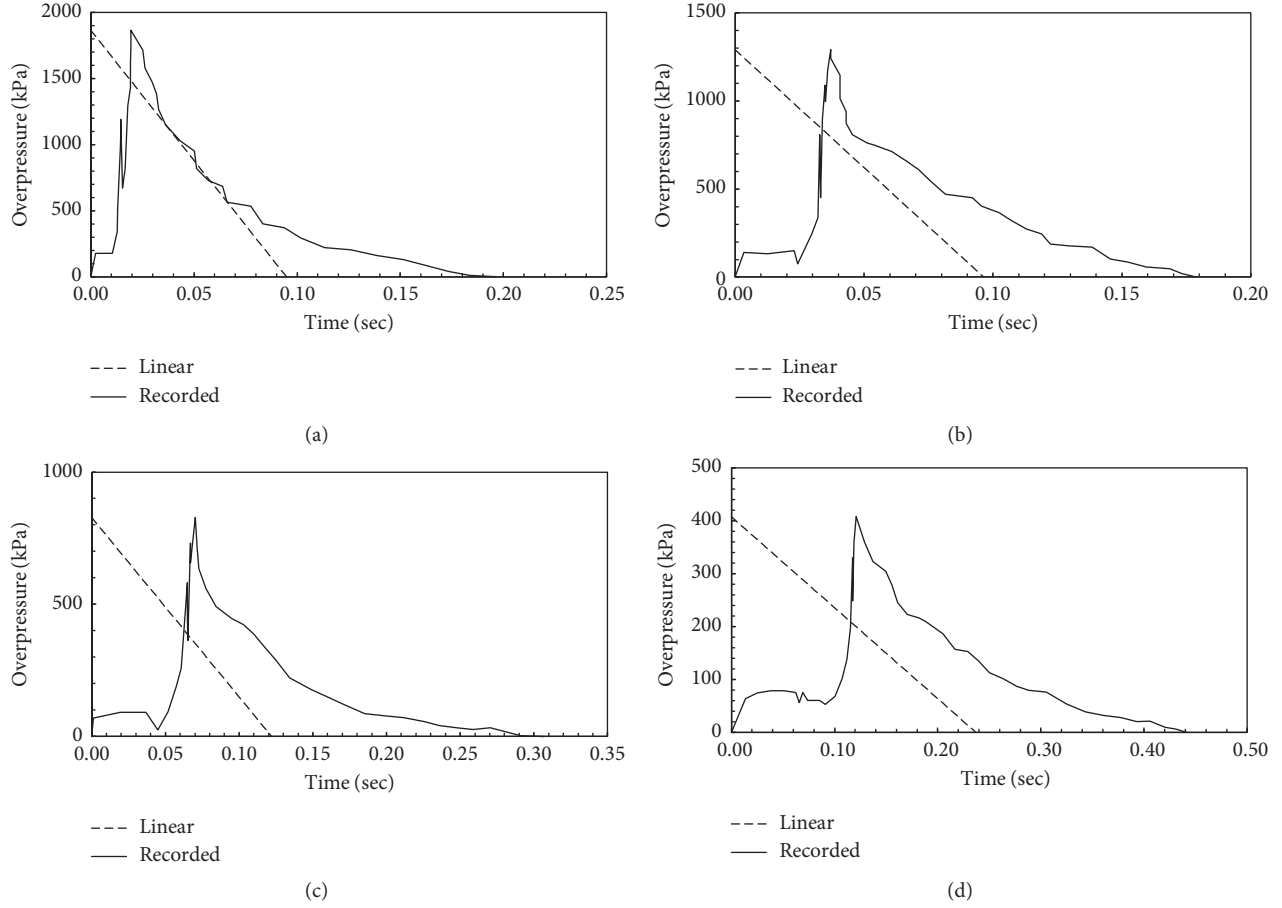


FIGURE 4: Measured and equivalent (linear) overpressure time-histories for shot Priscilla at stations (a) P1, (b) P2, (c) P3, and (d) P4 (measured overpressure time-histories [21]).

It is to clarify that the overpressure time-history defined by the piecewise function $P(t_k)$ such that $P(t_k) = P_o t_k / t_r$ for $t_k \leq t_r$ and $P(t_k) = P_o (1 - (t_k - t_r)) / (t_{eq} - t_r)$ for $t_r \leq t_k \leq t_{eq}$ converges to (8) in the limiting case when $t_r \rightarrow 0$. Therefore, the expression $L(t_x \rightarrow t_{x+1})$ in (10) is first obtained for a case of finite t_r and then it is evaluated for the case when $t_r \rightarrow 0$ to determine the solution for overpressure time-history of (8). Similarly, the integral for unloading fronts in (7) (with $t_r \rightarrow 0$) between general time instants t_x and t_{x+1} can be written as $\int_{t_x}^{t_{x+1}} f_U(\varphi(t_k), \sigma(\varphi(t_k))) \times \varphi'(t_k) dt_k = (P_o / M_L) \times U(t_x \rightarrow t_{x+1})$, where $U(t_x \rightarrow t_{x+1})$ can be shown to be given by the following equation:

$$U(t_x \rightarrow t_{x+1}) = L_w \left[1 - \frac{r f L_w}{t_p V_p} - \frac{r t_i}{t_p} \right] \ln \left(\frac{f L_w + V_p t_i - V_p t_x}{f L_w + V_p t_i - V_p t_{x+1}} \right) + \frac{r L_w (t_{x+1} - t_x)}{t_p} \quad (11)$$

By setting the appropriate values of t_x and t_{x+1} in (10) and (11), the closed-form integrals between desired time

instants can easily be evaluated. Thus, the closed-form solution is given by the following equation:

$$u_i = \frac{P_o}{M_L} \lim_{t_r \rightarrow 0} [L(0 \rightarrow t_r) + U(t_r \rightarrow t_i)] \quad (12)$$

The closed-form solution is further extended to accommodate multiple ground layers. This requires the determination of time instants t_x and t_{x+1} during which the wave fronts pass through a particular layer. For illustration, a layered ground medium with an interface at depth H with the modulus of top layer as M_1 and modulus of bottom layer as M_2 is considered as shown in Figure 3. This leads to the three cases (Table 1) and corresponding displacement solutions (shown in Table 1).

4. Validation

The proposed closed-form solution is validated against the field data from an atmospheric nuclear test conducted at Frenchman Flat (Nevada). Perret [21] presented the measured overpressure time-histories (Figure 4) along with corresponding peak ground displacements at different distances from GZ (Table 2) for a 37 kt nuclear explosion at

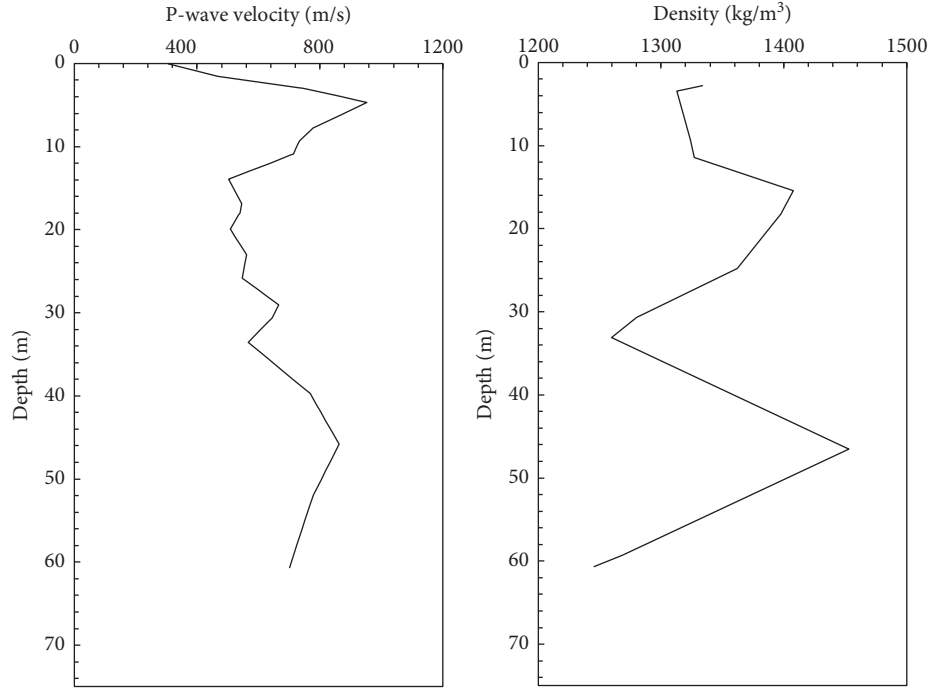


FIGURE 5: P-wave velocity and geomaterial density profile at Frenchman Flat, NTS [21].

a height of 214 m. Model input parameters for above mentioned nuclear test are determined as follows.

The recorded overpressure time-histories are converted to equivalent linearly decaying overpressure time-histories (Figure 4). Equivalent overpressure time-histories are given by (8) such that the peak overpressure (P_o) is equal to the recorded peak overpressure, and equivalent positive phase duration t_{eq} is given by the following equation:

$$t_{eq} = \frac{2I_p}{P_o}, \quad (13)$$

where I_p is the positive phase impulse (area under the recorded overpressure time-history). It is worth mentioning, though the rise-time is taken to be zero in the equivalent overpressure time-history in (8), that the effect of non-zero rising time has been accounted for by considering the total positive phase impulse (in (13)) which includes the area under the rising and decaying portions of actual overpressure time-history. Therefore, it is expected that setting the rise-time as zero in (8) would have a negligible impact on the magnitude of peak displacement. Furthermore, the ratios of length of rise-time to total positive phase duration for the four cases (P1, P2, P3, and P4) are 0.10, 0.21, 0.23, and 0.27, respectively. This indicates that rise-time is reasonably small near ground zero; however, the relative length of rise-time increases with increasing distance from ground zero. Thus, it is expected that the errors (if any) due to setting rise-time to zero would be more pronounced only at distances far away from ground zero. Even in such cases, a closed-form solution can be developed using (7) by setting a finite rise-time. However, it is worth noting that at far away

distances (from ground zero), other important factors related to outrunning ground motion would start governing [31].

The initial pulse moving at seismic P-wave velocity (V_p) penetrates to a depth of $V_p t_{eq}$ for equivalent case, whereas for actual case, it penetrates to a depth of $V_p t_p$. It is noted that the depth of the stressed zone in the equivalent case is smaller compared to the actual case as equivalent duration (t_{eq}) is smaller than the actual positive phase duration (t_p) (Figure 4). Thus, all depth-dependent parameters are scaled by a factor $SF = t_p/t_{eq}$, such that the total depth of the stressed zone becomes $SF \times V_p t_{eq} = V_p t_p$ with the depth of the top layer being H/SF , and with a characteristic attenuation length of L_w/SF . Based on the variation of P-wave velocity with depth at Frenchman Flat (Figure 5), the average P-wave velocity (V_p) is estimated as 658.69 m/s. Whitman [4] presented the representative constrained modulus for Frenchman Flat interpreted from different experimental techniques (Table 3). Whitman [4] also emphasized that all aspects of stress-strain behaviour of geomaterials under blast loading are not captured by a single test and advocated to choose the modulus judiciously. The stress attenuation coefficient is calculated using (9) with scaled L_w (Table 4). Using the closed-form solution (shown in Table 1), parametric variations are studied (Table 5) and peak displacements (Table 6) are estimated.

The parametric studies (Table 5) highlight that the proposed model is most sensitive to the constrained modulus compared to other parameters and choice of the modulus is also subjective for engineers. However, based on the parametric studies, the last column "Recommended Value" of Table 5 provides some guidelines to select the constrained modulus. With increasing

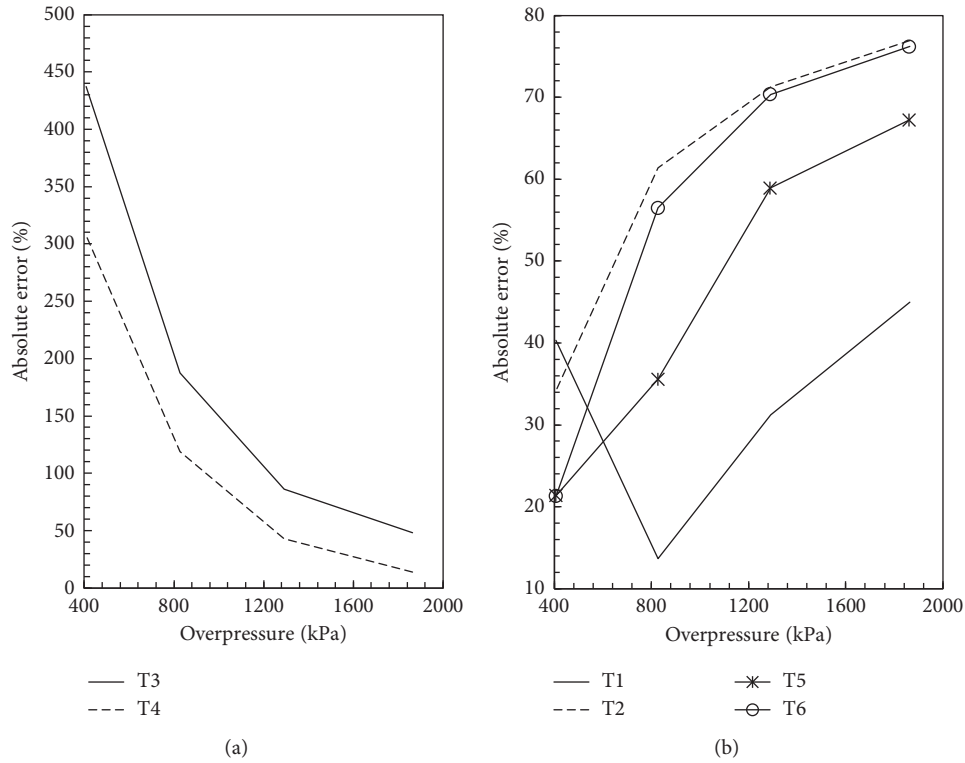


FIGURE 6: Variation of error in estimated peak displacement using constrained modulus determined from different experimental techniques: (a) T3 and T4 and (b) T1, T2, T5, and T6. T1: deduced from observed ground motion; T2: calculated from seismic velocity; T3: triaxial tests: initial loading; T4: dynamic 1-D compression test: initial loading; T5: triaxial tests: reloading; T6: resonant column test.

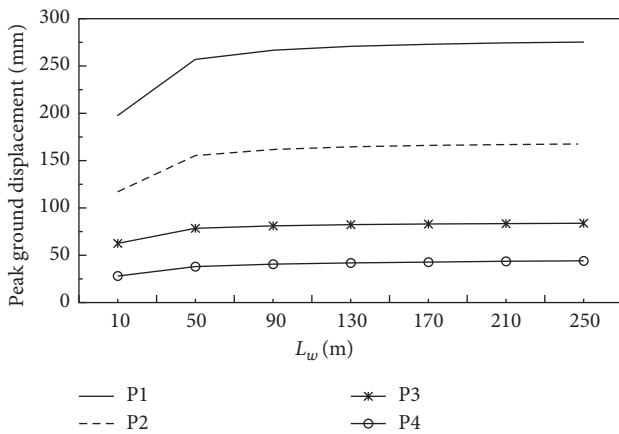


FIGURE 7: Variation of peak ground displacement with attenuation characteristic length L_w .

availability of similar case studies, these guidelines can further be refined.

5. Comparison with UFC Model

The UFC manual [22] provides an expression for air-blast-induced peak vertical displacement based on one-dimensional elastic wave propagation:

$$u_i|_{\max} = \frac{I_p}{\rho V_p} \tag{14}$$

where ρ is the bulk density of geomaterials. To estimate peak displacements using (14), positive phase impulse (I_p) is taken from Table 2. Representative P-wave velocity (V_p) and density (ρ) are taken as 658.69 m/s and 1331 kg/m³, respectively, taking into account the variation with depth (Figure 5). Computed peak displacements using the proposed model and UFC model are shown in Figure 9 along with the measured field values. It can be clearly seen that the predicted values of the proposed model are in good agreement with the measured values and the UFC model significantly underestimates the peak displacements under high overpressures (with increasing war head capacity).

6. Conclusions

A closed-form expression is developed to estimate nuclear-air-blast-induced free-field ground displacement that takes into account peak overpressure, positive phase impulse, depth of layer interface, representative constrained modulus of each layer, strain recovery, stress attenuation, P-wave velocity, and velocity ratio. The solution is validated against a nuclear test conducted at Frenchman Flat (Nevada) and the following conclusions are arrived at:

- (i) Peak ground displacement estimates are quite sensitive to the constrained modulus, and a judicious

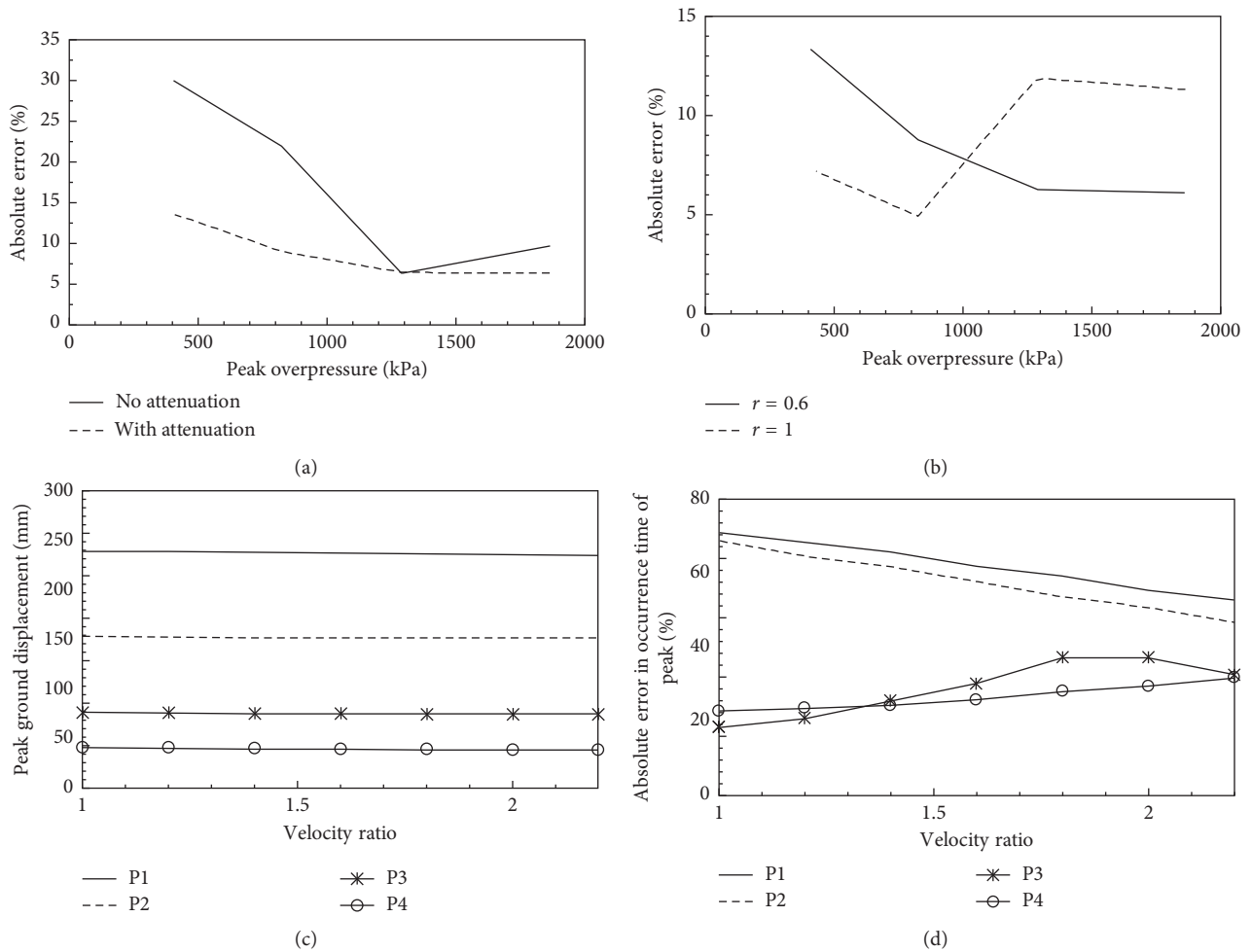


FIGURE 8: Effect of (a) attenuation; (b) strain recovery ratio; (c) velocity ratio on estimated ground displacement; (d) velocity ratio on time of occurrence of peak displacement.

selection of appropriate constrained modulus based on the magnitude of applied overpressure is recommended.

- (ii) Based on the presented case study, two guidelines are recommended to select the appropriate modulus: (a) shallow ground layers are likely to have modulus values determined by unconfined or triaxial compression test and deep ground layers are likely to have modulus values computed from seismic velocity test, and (b) constrained modulus increases with decreasing ratio of applied stress to overburden.
- (iii) Effect of attenuation should be accounted for low overpressures and may be neglected at higher overpressures (or high war head capacities).
- (iv) The velocity ratio affects mainly the time of occurrence of peak ground displacement and not the

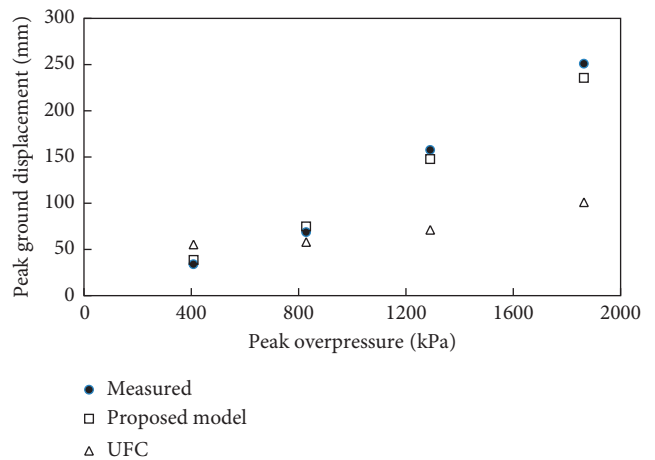


FIGURE 9: Comparison between measured and estimated peak ground displacements.

TABLE 1: Displacement solutions for the double-layered media.

Case	Explanation	Displacement equation
1	When all loading and unloading fronts are in layer-1 ($t_i \leq H/V_p$).	$u_i = P_o \text{Lim}_{t_r \rightarrow 0} \left[\frac{L(0 \rightarrow t_r)}{M_1} + \frac{U(t_r \rightarrow t_i)}{M_1} \right]$
2	When some loading fronts have crossed layer-1 and remaining loading fronts along with all unloading fronts are in layer-1 ($H/V_p < t_i \leq fH/V_p$). Here, the first task is to determine those loading fronts which have crossed layer-1. This can be obtained by equating loading front velocity multiplied with travel time with the depth of layer. The loading front velocity of the k th front can be written using (3) as $V_p/\{(f-1)(t_k/t_r) + 1\}$, and travel time is $(t_i - t_k)$. Thus, the last loading front to reach at depth H by the time t_i would be given by $t_{kH} = t_r(V_p t_i - H)/\{H(f-1) + V_p t_r\}$.	$u_i = P_o \text{Lim}_{t_r \rightarrow 0} \left[\frac{L(0 \rightarrow t_{kH})}{M_2} + \frac{L(t_{kH} \rightarrow t_r)}{M_1} + \frac{U(t_r \rightarrow t_i)}{M_1} \right]$
3	When all loading fronts are in layer-2 and some unloading fronts have crossed layer-1 ($fH/V_p < t_i$). Similar to case 2, the last unloading front to reach at depth H by the time t_i would be given by $t_{kH} = t_i - fH/V_p$.	$u_i = P_o \text{Lim}_{t_r \rightarrow 0} \left[\frac{L(0 \rightarrow t_r)}{M_2} + \frac{U(t_r \rightarrow t_i - fH/V_p)}{M_2} + \frac{U(t_i - fH/V_p \rightarrow t_i)}{M_1} \right]$

TABLE 2: Details of recording stations.

Station designation	Range (m)	Peak overpressure (kPa)	Positive phase duration (sec)	Positive phase impulse (kPa-sec)	Equivalent duration (sec)	Scale factor (SF)
P1	198	1863	0.196	88.32	0.0948	2.07
P2	259	1290	0.179	62.18	0.0964	1.86
P3	320	828	0.307	50.54	0.1221	2.51
P4	411	408	0.442	48.34	0.2371	1.86

TABLE 3: Constrained modulus of playa silt at Frenchman Flat [4].

Method	Notation	Constrained modulus (MPa)	
		For depths less than 18 m	For depths more than 18 m
Deduced from observed ground motion	T1	96.6	552
Calculated from seismic velocity	T2	242	1035
Triaxial tests: initial loading	T3	55.2	103.5
Dynamic 1-D compression test: initial loading	T4	69	138
Triaxial tests: reloading	T5	276	448.5
Resonant column test	T6	276	759

TABLE 4: Scaling of attenuation characteristic length (L_w).

Station designation	W (kt)	P_o (kPa)	V_p (m/s)	L_w (m)	Scaled L_w (m)
P1	37	1863	658.69	48.58	23.47
P2		1290	658.69	58.38	31.44
P3		828	658.69	72.88	28.98
P4		408	658.69	103.84	55.70

magnitude under higher overpressures. Therefore, the velocity ratio becomes important when design calculations utilize the complete displacement time-history such as in case of shock spectra.

(v) A complete strain recovery is a better representation of actual conditions under low overpressure zones, and under higher overpressures, a partial strain recovery is recommended.

TABLE 5: Parametric studies carried out on the proposed closed-form solution.

Parameter	Parametric study	Observation	Recommended value
M_1 and M_2	Parameters M_1 and M_2 based on six different methods are adopted from Table 3.	Peak ground displacements are very sensitive to the constrained modulus value.	Observed results are consistent with the observations of Wilson and Sibley [17]. (1) Shallow ground layers are likely to have modulus values determined by unconfined or triaxial compression test, and deep ground layers are likely to have modulus values computed from seismic velocity test or resonant column test. The justification to this variation in selection of modulus values can be attributed to the small strains associated with deeper layers and higher strains at shallow depths.
	Other parameters kept constant at $r=0.6$; $f=2$; L_w adopted from Table 4.	Average coefficient of variation in peak displacement estimates = 83%.	(2) Constrained modulus increases with decreasing ratio of applied stress to overburden. For higher overpressures, the overstress ratio would be higher and therefore modulus value will be lower compared to lower overpressures. An optimal choice of constrained modulus values is adopted as shown in Table 6. The computed displacements are found to be in good agreement with measured displacements (Table 6).
	Variation of absolute percentage errors in estimated peak ground displacements is plotted against peak overpressures in Figures 6(a) and 6(b).	Estimates are close to measured values if higher modulus values are used for smaller overpressures.	
L_w	L_w is varied from 10 m to 250 m. Other parameters kept fixed at M_1 and M_2 adopted from Table 6; $f=2$; $r=0.6$. Estimated peak displacements are plotted against L_w as shown in Figure 7. Errors in estimated peak displacements for the attenuating medium and non-attenuating medium are also plotted against peak overpressure in Figure 8(a).	As L_w increases (or α decreases), peak displacement increases. Beyond L_w of 250 m, the peak ground displacement does not increase, and $L_w \geq 250$ is considered as the non-attenuating medium.	Attenuation has to be taken into account under low overpressures, and it can be ignored under high overpressures.
	Two cases are considered: (i) full strain recovery $r=1$ and (ii) partial strain recovery $r=0.6$. Other parameters fixed at M_1 and M_2 adopted from Table 6; $f=2$; L_w adopted from Table 4. Errors in estimated peak displacement for the two cases are plotted as shown in Figure 8(b).	Assumption of full strain recovery gives less errors as compared to partial strain recovery under low overpressures.	Under low overpressure, ground is not stressed beyond its elastic limit, and hence full strain recovery is a better representation of actual conditions in low overpressure zones. A lower strain recovery causes higher permanent deformations and increases peak ground displacement compared to elastic case (i.e., unit strain recovery ratio). Under higher overpressures, the ground is stressed beyond its elastic limit and the assumption of partial strain recovery is recommended.
f	f is varied from 1.0 to 2.2.	Under high overpressure (P1 and P2), error in occurrence time of peak displacement reduces significantly with increasing f .	f has insignificant effect on magnitude of estimated peak displacements. However, as the velocity ratio increases, the rise-time of overstress pulse with depth also increases and affects the occurrence time of the peak displacement.
	Other parameters fixed at M_1 and M_2 adopted from Table 6; $r=0.6$; L_w adopted from Table 4. Estimated peak displacements are plotted against f (Figure 8(c)). Error in occurrence time of peak displacement are also plotted against f (Figure 8(d)).	Error increases marginally under lower overpressures as the velocity ratio is close to 1 under lower stress (in (3) when $t_k \rightarrow 0$).	

TABLE 6: Suggested combination of modulus values and corresponding estimated peak displacements.

Station designation	M_1 (MPa) (depths less than 18 m)	M_2 (MPa) (depths more than 18 m)	Estimated peak displacement (mm)	Experimental records (mm)	% error
P1	55.2 triaxial tests: initial loading	552 deduced from observed ground motion	235.59	250.95	6.12
P2	69 dynamic 1-D compression test: initial loading	759 resonant column test	147.68	157.56	6.27
P3	69 dynamic 1-D compression test: initial loading	759 resonant column test	74.79	68.75	8.79
P4	96.6 deduced from observed ground motion	1035 calculated from seismic velocity	38.49	33.95	13.37

(vi) The proposed model closely estimates the experimental values at all overpressures, whereas the UFC model significantly underestimates the peak ground displacements at high overpressures.

Notations

$\alpha(Z_{ki})$:	Attenuation coefficient at depth Z_{ki}
ε_{iz} :	Strain at time t_i at depth “z”
ε_{pz} :	Peak strain level in geomaterial at depth “z”
ε_{rz} :	Residual strain level in geomaterial at depth “z”
f :	Representative velocity ratio (between P-wave velocity and peak stress velocity) of ground media
f_{kz} :	Ratio of P-wave velocity to wave velocity corresponding to the k th overpressure front at depth “z”
f_L :	Functional form for the loading branch of the stress-strain curve
f_{rz} :	Ratio of P-wave velocity to wave velocity corresponding to the peak overpressure front at depth “z”
f_U :	Functional form for the unloading branch of the stress-strain curve
H :	Depth of the top ground layer
I_p :	Positive phase impulse of overpressure time-history
L_w :	Characteristic attenuation length
M_L :	Loading secant modulus
M_2 :	Modulus of bottom layer
M_1 :	Modulus of top layer
P_o :	Peak overpressure
$P(t_k)$:	Pressure magnitude of the k th overpressure front
r :	Strain recovery ratio
ρ :	Bulk-density of geomaterials
SF:	Scale factor
σ_{pz} :	Peak stress level in geomaterial at depth “z”
t_{eq} :	Equivalent positive phase duration of linearly decaying overpressure time-history
t_k :	Time when the k th overpressure front arrives at the point of interest on ground surface

t_{kH} :	Time of arrival of the last loading front to reach at depth H (by the time t_i)
t_p :	Positive phase duration of overpressure time-history
t_r :	Rise-time to peak overpressure in overpressure time-history
u_i :	Vertical ground displacement at time t_i
V_p :	Representative P-wave velocity of ground media
V_L :	Representative wave propagation velocity of the peak overpressure front in ground
V_{kz} :	Wave velocity of the k th stress front at depth “z”
W :	Yield of the explosion
Z_{ki} :	Depth penetrated by the k th overpressure front at time t_i
σ_{iz} :	Stress at time t_i at depth “z”
Z_{0i} :	Depth penetrated by initial pulse at time t_i
Z_{pi} :	Depth penetrated by the peak overpressure front at time t_i
$(\partial\sigma_z/\partial\varepsilon_z) _{\sigma=0}$:	Tangential modulus at initial stress level at depth “z”
$(\partial\sigma_z/\partial\varepsilon_z) _{\sigma_{rz}}$:	Tangential modulus at peak stress level at depth “z.”

Conflicts of Interest

The authors declare that there are no conflicts of interest regarding the publication of this paper.

References

- [1] S. Pinto, “Underground construction of nuclear power reactors,” *Nuclear Engineering and Design*, vol. 61, no. 3, pp. 441–458, 1980.
- [2] C. V. Chester and G. P. Zimmerman, “Civil defense shelters: a state-of-the-art assessment,” *Tunnelling and Underground Space Technology*, vol. 2, no. 4, pp. 401–428, 1987.
- [3] S. Glasstone and P. J. Dolan, *The Effects of Nuclear Weapons*, Castle House Publications, London, UK, 1980.
- [4] R. V. Whitman, *The Response of Soils to Dynamic Loadings; Report 26, Final Report*, Massachusetts Institute of Technology, Cambridge, MA, USA, 1970.

- [5] R. E. Crawford, C. J. Higgins, and E. H. Bultmann, *The Air Force Manual for Design and Analysis of Hardened Structures, Final Report Jun 71-May 74 (No. AD-B-004152/5)*, Civil Nuclear Systems Corporation, Albuquerque, NM, USA, 1974.
- [6] B. M. Das, *Fundamentals of Soil-Dynamics*, Chapter 4, Elsevier, Amsterdam, Netherlands, 1983.
- [7] H. L. Brode, *A Review of Nuclear Explosion Phenomena Pertinent to Protective Construction, R 425 PR*, The Rand Corporation, Santa Monica, CA, USA, 1964.
- [8] M. S. Agbalian, *Design of Structures to Resist Nuclear Weapon Effects, ASCE Manual on Engineering Practice*, Vol. 42, ASCE, Reston, VA, USA, 1985.
- [9] J. H. Prevost, *DYNAFLOW: A Nonlinear Transient Finite Element Analysis Program*, Princeton University, Princeton, NJ, USA, 1981.
- [10] F. Rischbieter and K. Michelmann, *Bodenwelle bei Gasexplosionen. Beitrag der induzierten Bodenwelle zur Belastung von KKW-Strukturen*, Batelle-Institut, Frankfurt, Germany, 1984.
- [11] K. J. Kim and S. E. Blouin, *Response of Saturated Porous Nonlinear Materials to Dynamic Loadings*, Applied Research Associates Inc., South Royalton, VT, USA, 1984.
- [12] H. Werkle and G. Waas, "Analysis of ground motion caused by propagating air pressure waves," *Soil Dynamics and Earthquake Engineering*, vol. 6, no. 4, pp. 194–202, 1987.
- [13] Z. Yang, "Finite element simulation of response of buried shelters to blast loadings," *Finite Elements in Analysis and Design*, vol. 24, no. 3, pp. 113–132, 1997.
- [14] Z. Wang, H. Hao, and Y. Lu, "A three-phase soil model for simulating stress wave propagation due to blast loading," *International Journal for Numerical and Analytical Methods in Geomechanics*, vol. 28, no. 1, pp. 33–56, 2004.
- [15] Y. Lu and Z. Wang, "Characterization of structural effects from above-ground explosion using coupled numerical simulation," *Computers & Structures*, vol. 84, no. 28, pp. 1729–1742, 2006.
- [16] T. Bierer and C. Bode, "A semi-analytical model in time domain for moving loads," *Soil Dynamics and Earthquake Engineering*, vol. 27, no. 12, pp. 1073–1081, 2007.
- [17] S. D. Wilson and E. A. Sibley, "Ground displacements from air-blast loading," *Journal of the Soil Mechanics and Foundations Division*, vol. 88, no. 6, pp. 1–32, 1962.
- [18] M. L. Baron, I. Nelson, and I. Sandler, *Investigation of Air Induced Ground Shock Effect Resulting from Various Explosive Sources. Report 2, Influence of Constitutive Models on Ground Motion Predictions*, Weidlinger Associates, New York, NY, USA, 1971.
- [19] Z. Wang and Y. Lu, "Numerical analysis on dynamic deformation mechanism of soils under blast loading," *Soil Dynamics and Earthquake Engineering*, vol. 23, no. 8, pp. 705–714, 2003.
- [20] S. Wang, L. Shen, F. Maggi, A. El-Zein, and G. D. Nguyen, "Uniaxial compressive behavior of partially saturated granular media under high strain rates," *International Journal of Impact Engineering*, vol. 102, pp. 156–168, 2017.
- [21] W. R. Perret, *Ground Motion Studies at High Incident Overpressure*, Sandia Corporation, Albuquerque, NM, USA, 1960.
- [22] UFC Manual, *Structures to Resist the Effects of Accidental Explosions*, US DoD, Washington, DC, USA, UFC 3-340-02, 2008.
- [23] S. B. Batdorf, "Air-induced ground shock: a one-dimensional theory," in *Proceedings of International Symposium on Wave Propagation and Dynamic Properties of Earth Materials, Albuquerque, NM, USA, August 1967*, G. Triandafilidis, Ed., pp. 423–432, Aerospace Corp., San Bernardino, CA, USA, 1969.
- [24] S. L. Kramer, *Geotechnical Earthquake Engineering*, Pearson Education, Delhi, India, 1996.
- [25] X. Tong and C. Tuan, "Viscoplastic cap model for soils under high strain rate loading," *Journal of Geotechnical and Geoenvironmental Engineering*, vol. 2, no. 206, pp. 206–214, 2007.
- [26] J. An, C. Y. Tuan, B. A. Cheeseman, and G. A. Gazonas, "Simulation of soil behavior under blast loading," *International Journal of Geomechanics*, vol. 11, no. 4, pp. 323–334, 2011.
- [27] P. Y. Hicher and J. F. Shao, *Constitutive Modeling of Soils and Rocks*, John Wiley & Sons, Hoboken, NJ, USA, 2013.
- [28] S. Pathak and G. V. Ramana, "Air-blast induced ground displacement," *Procedia Engineering*, vol. 173, pp. 555–562, 2017.
- [29] N. M. Newmark and J. D. Haltiwanger, *Air Force Design Manual, Principles and Practices for Design of Hardened Structures*, University of Illinois at Urbana–Champaign, Champaign, IL, USA, 1962.
- [30] A. J. Hendron Jr. and H. E. Auld, "Effect of soil properties on the attenuation of airblast-induced ground motions," in *Proceedings of International Symposium on Wave Propagation and Dynamic Properties of Earth Materials, Albuquerque, NM, USA, August 1967*, G. Triandafilidis, Ed., pp. 29–47, University of Illinois, Urbana, IL, USA, 1969.
- [31] I. Nelson and G. Y. Baladi, "Outrunning ground shock computed with different models," *Journal of the Engineering Mechanics Division*, vol. 103, no. 3, pp. 377–393, 1977.

Research Article

Temperature Effect on Lime Powder-Added Geopolymer Concrete

Sandeep L. Hake ¹, R. M. Damgir,² and S. V. Patankar³

¹Dr. V. V. P. College of Engineering, Ahmednagar, Maharashtra, India

²Civil Engineering Department, Government College of Engineering, Aurangabad, India

³S.R.E.S. College of Engineering, Kopargaon, Ahmednagar, Maharashtra, India

Correspondence should be addressed to Sandeep L. Hake; drsandeephake@gmail.com

Received 8 August 2017; Revised 3 January 2018; Accepted 9 January 2018; Published 28 February 2018

Academic Editor: Arnaud Perrot

Copyright © 2018 Sandeep L. Hake et al. This is an open access article distributed under the Creative Commons Attribution License, which permits unrestricted use, distribution, and reproduction in any medium, provided the original work is properly cited.

The need for concrete increases with rapid development in the field of infrastructure because of the increased use of cementing material of concrete. The production of concrete is unsafe to the earth. Consequently, there is a need to discover new binding material with cementing properties. Fly ash debris is wastage of thermal power plants and acquires hectares of land for the dumping reason. This paper concentrates on development of alternative binding material in the field of construction. The fly ash-based geopolymer concrete is a better option, but it needs heat curing for the polymerization. The use of lime powder in the geopolymer concrete gives better result without heat curing. The experiment depends on the characteristics of daylight curing and impact of temperature in controlled oven curing. The M30 grade geopolymer concrete plans with the addition of lime powder. The addition of lime powder is changed by 0%, 5%, 10%, 15%, 20%, and 25%. The compressive strength increases with addition of lime powder, but in the cases of 20% and 25%, the workability gets hamper. The study also deals with temperature variations when oven cured for 35°C, 40°C, 50°C, and 60°C hence assessed.

1. Introduction

Concrete, as a noteworthy development material, is being utilized at a regularly expanding rate all around the globe. The cement is right now used in ordinary Portland concrete, which brings about a gigantic worldwide bond industry. Consistently, the creation of OPC is expanding with the expanding interest of development. Hence, the carbon dioxide discharge rate increases step by step into the air. One ton of carbon dioxide is transmitted into the air with the generation of one ton of Portland cement. The ozone-depleting substance emanation from the creation of Portland concrete is around 1.35 billion tons yearly, which is around 7% of the aggregate ozone-depleting substance outflow [1] (Patanekar 2013). On the other way, fly ash is the waste material of coal-based thermal power plants, available abundantly, but creates a disposal problem. Several hectares of agricultural land are acquired by the thermal power plant for the disposal of fly ash. As it is light in weight and flies easily, it creates health problems like asthma and bronchitis.

Now, the challenge amongst the researchers is to find an appropriate alternative for eliminating the environmental hazards caused by the production of cement. A very prominent research by Davidovits in 1978 was the invention of geopolymer concrete which was a cement-free concrete. This attracted a lot of attention where fly ash is replaced by cement for 100%. It had its own identity and left remarkable impressions in the research studies. Geopolymer exhibits similar properties to that of conventional concrete; the only difference is that it is being 100% cement free. But challenging human tendency of having blind faith for years over cement for its strength and durability is an uprising challenge. Building this faith and trust for the use of geopolymer concrete over conventional concrete is a huge task and requires testing of geopolymer concrete against conventional concrete. Not only can the elimination of CO₂ emission be avoided, but also there are lot many reasons for geopolymer concrete to be eco-friendly. The most prolific reason for use of fly ash is its dumping issue and its minimum use. Previous investigation made on geopolymer

concrete reveals that good strength is achieved when curing is done at elevated temperature limiting its application on site. With an addition and replacement of optimum percentage of lime and cement, respectively, an additional amount of heat will be produced; when mixed with water, the reaction being exothermic can be used as an alternative for the elevated curing temperatures, thereby achieving the desired strength at normal room temperature and by wet curing giving it a wide scope and various practical applications and uses.

2. Literature Review

Dutta and Ghosh [2] studied that the pore sizes get a reduction after addition of limestone dust into the geopolymer paste sample. This phenomenon influences water absorption and compressive strength. Incorporation of limestone dust up to 15% increases the compressive strength of paste specimens about 44%. The reduction in compressive strength due to lower curing temperature may be compensated by incorporation of calcium compound which can accelerate the rate of polymerization even at low temperature. Hake et al. [3] reported that the cement production generated carbon dioxide, which pollutes the atmosphere. The thermal industry produces a waste called fly ash which is simply dumped on the earth, which occupies larger areas. The waste water from the chemical industries is discharged into the ground which contaminates ground water. By producing geopolymer concrete, all the above-mentioned issues shall be solved by rearranging them. Waste fly ash from thermal industry + waste water from chemical refineries = geopolymer concrete. Further, the use of fly ash as a value-added material as in the case of geopolymer concrete reduces the consumption of cement. Reduction of cement usage will reduce the production of cement which in turn cut the CO₂ emissions. Many researchers have worked on the development of geopolymer cement and concrete for the past ten years. The present work deals with the result of the experimental investigation carried out on geopolymer concrete using processed and unprocessed fly ash with sodium silicate and sodium hydroxide. The study analyses the effect of processed and unprocessed fly ash on compressive strength and split tensile strength for different temperatures. To study the effect of different types of processed and unprocessed fly ash, we use processed fly ash such as P60, P80, and P100 from Dirk India Pvt. Ltd. and unprocessed fly ash from different cities such as Bhusawal, Nashik, and Beed. In this paper, the effect of the alkaline solution on different fly ash is investigated. Namagga and Atadero [4] investigated that the replacement of high-lime fly ash in concrete generally increases the ultimate strength of concrete. It is probable that even higher percentile replacements of cement would still be able to provide the same compressive strength as no fly ash concrete. Replacement of cement with high-lime fly ash reduces the rate of strength development/gain beyond the optimal limits obtained for 25–35% fly ash mixes. More air entrained admixture is required for increasing amounts of fly ash used. Vijaya Rangan [5] stated that the elastic properties of hardened geopolymer concrete and the behavior and strength of reinforced geopolymer concrete structural members are

TABLE 1: Chemical composition of materials.

Chemical composition	Fly ash (%)	Lime (%)
SiO ₂	57.30	3.92
Al ₂ O ₃	27.13	2.74
Fe ₂ O ₃	8.06	0.38
MgO	2.13	0.28
SO ₃	1.06	—
Na ₂ O	0.73	—
CaO	0.03	51.01
LOI	1.60	41.56
K ₂ O	—	0.04
TiO ₂	—	0.09

similar to those observed in the case of Portland cement concrete. Heat-cured low-calcium fly ash-based geopolymer concrete also shows excellent resistance to sulfate attack and fire, good acid resistance, low creep, and suffers very little drying shrinkage. Geopolymer concrete has several economic benefits. Bondar [6] investigated that geopolymer concrete can be produced with the same cost of OPC concrete and comparable properties. Geopolymer concrete develops moderate to high mechanical strength with a high modulus of elasticity and shrinkage much lower than that of OPC. Geopolymer concrete manufacture is liable to reduce CO₂ emission as compared to OPC production. Vora and Dave [7] investigated that the compressive strength of the geopolymer concrete increases with the increase of concentration in terms of molarity of sodium hydroxide. The ratio of alkaline liquid to fly ash by mass does not affect the compressive strength of the geopolymer concrete. The sodium silicate to sodium hydroxide ratio by mass equal to 2 has resulted into the higher compressive strength as compared to the ratio of 2.5 for the geopolymer concrete. The workability of the geopolymer concrete in the fresh state increases with the increase of extra water added to the mix. The compressive strength of the geopolymer concrete decreases with the increase in the ratio of water to geopolymer solids by mass. The increase in the curing temperature in the range of 60°C–90°C also increases the compressive strength of the geopolymer concrete.

3. Materials Used

3.1. Fly Ash. Fly ash used in this study is low-calcium class F-processed fly ash from Dirk India Private Limited under the name of the product POZZOCONCRETE 60. The chemical compositions of the fly ash used along with the specifications are given in Table 1. The specific gravity of the fly ash used is 2.26. The residue of fly ash retained on 45 μm IS sieve was reported as 16.84%. The fineness of the fly ash by Blen's method is 360 m²/kg.

3.2. Alkaline Solution. The alkaline liquid used was a combination of sodium hydroxide and sodium silicate solution. Sodium hydroxide (NaOH) in flakes form with 98% purity purchased from the local chemical supplier was used, and

sodium silicate solution ($\text{NaO} = 16.84\%$, $\text{SiO}_2 = 35.01\%$, and water = 46.37% by mass) was used as the alkaline liquid. Sodium hydroxide solution is prepared by dissolving the flakes in water. Tap water available in the laboratory was used to prepare NaOH solution. The activator solution was prepared at least one day prior to its use. Molarity of the solution was 16 M.

3.3. Aggregates. Locally available 12.5 mm and 20 mm crushed aggregates are used as coarse aggregates having specific gravity 2.65. Locally available river sand is used as fine aggregate in the concrete mixes having specific gravity 2.5 and of Zone-I conforming IS specifications.

3.4. Lime. The limestone dust is a solid composite having a specific gravity of 2.7 and a bulk density of 1425 kg/m^3 . It has an average particle size of 25 microns while particle size varies between 10μ and 70μ . Chemical compositions of the fly ash used along with the specifications are given in Table 1.

4. Experimental Work

The concrete cubes of size $150 \times 150 \times 150 \text{ mm}$ were cast for trial mixes M30 grade for checking the workability slump cone test performed. In the geopolymer concrete, the alkaline activators such as sodium hydroxide and sodium silicate were used. The proportionate ratio of the alkaline solution is taken as 2.5. The experimental work evaluation of the optimum percentage of lime addition has to be worked out. For the same, cubes are to be cast for 5%, 10%, 15%, 20%, and 25% of lime addition, whereas lime percentage is by weight to that of fly ash. Initially, temperature and testing age are kept constant, and curing hours are varied such as 06 hrs, 12 hrs, 18 hrs, and 24 hrs. In this case, the optimized curing hours were acquired; by using this, the degree of heating ranging from 40°C to 120°C at an interval of 10°C for oven curing was obtained. The concrete cubes were cast and cured at normal room temperature to know their characteristic strength as well. After evaluating the optimum curing hours, rest period and temperature beams and cylinders were cast for the evaluation of flexural and split tensile strength of lime-added fly ash-based geopolymer concrete.

4.1. Percentage of Lime Addition (M30). The specimens were cast of size $150 \text{ mm} \times 150 \text{ mm} \times 150 \text{ mm}$ of grade M30 having alkaline solution ratio as 2.5. The concrete cubes were cured at 90°C in an oven for 24 hrs with addition of varied lime percentages by weight of fly ash. After the completion of the defined curing time, the specimens were kept at normal room temperature with a rest period of 07 days. The specimens were tested for compression on a compression testing machine of capacity 2000 KN to know the optimum percentage of lime addition and to study its effect on the strength of geopolymer concrete.

Figure 1 represents the variation in the strength of geopolymer concrete of grade M30 with the addition of lime percentage cured for 24 hours at a temperature of 90°C .

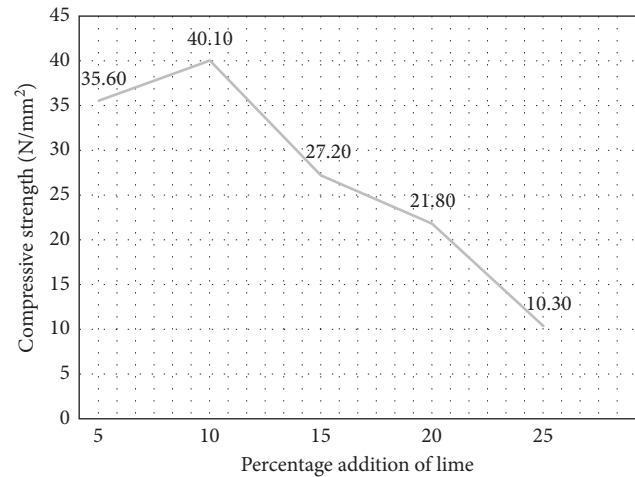


FIGURE 1: Percentage addition of lime powder in GPC oven cured at 90°C .

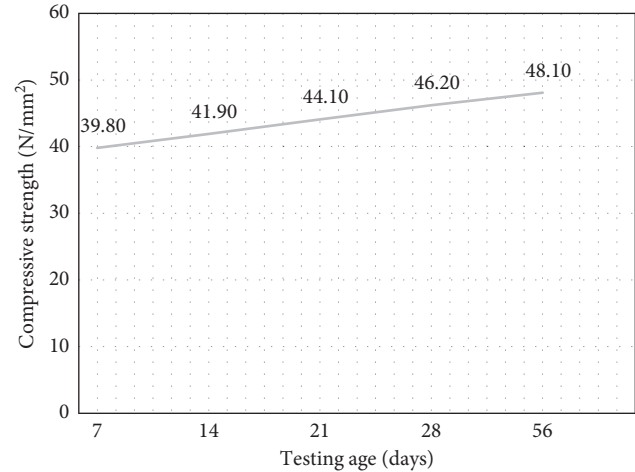


FIGURE 2: Effect of testing age on geopolymer concrete with oven curing.

The rest period for the cured specimens was 07 days. The maximum compressive strength was achieved with an addition of 10% of lime. Thus, the optimum percentage of lime addition observed here is 10%.

4.2. Effect of Rest Period. The specimens were cast of size $150 \text{ mm} \times 150 \text{ mm} \times 150 \text{ mm}$ of grade M30 having alkaline solution ratio as 2.5 and were cured at 90°C in an oven for 24 hrs with the addition of optimized lime percentages (10%). The lime percentages were calculated in accordance with the weight of fly ash. After the completion of the defined curing time, these specimens were kept at normal room temperature with a rest period or testing age of 07, 14, 21, 28, and 56 days. The specimens were tested after testing age to know the effect of the rest period on the strength of GPC with lime addition into geopolymer concrete.

Figure 2 represents the increase in the strength of geopolymer concrete of grade M30 with the increase in the rest period at a temperature of 90°C . The maximum compressive

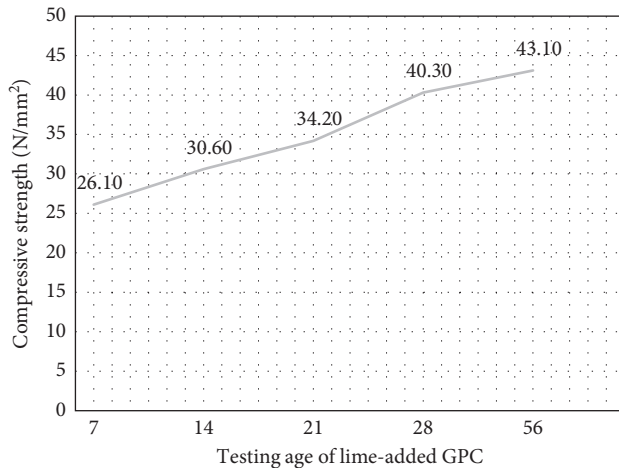


FIGURE 3: Cube cured at natural room temperature.

strength was achieved in 28 days. But, at 7th day, the strength achieved was more than the designed strength. Thus, the optimum rest period observed here is 7 days for the project work being time bound.

4.3. GPC (M30) with 10% Lime Addition Cured at Normal Room Temperature. The specimens were cast of size 150 mm × 150 mm × 150 mm of grade M30 having alkaline solution ratio as 2.5 and were cured at normal room temperature with an addition of 10% lime. These specimens were kept at normal room temperature for a rest period of 07, 14, 21, and 28 days after which the specimens were tested for compressive strength. The readings were recorded and listed, to know the effect on strength of GPC cured at normal room temperature.

Figure 3 represents the increase in the strength of geopolymer concrete of grade M30 + 10% with the increase in the rest period at normal room temperature. The normal room temperature on an average was recorded as 28°C (temperature in the morning was recorded as 27°C, and in the evening, it was recorded as 29°C). The strength observed during the rest period of 7 days was achieved more than 70%, unlike conventional cement concrete. The maximum compressive strength was achieved at 28th day which is more than the designed strength. Thus, geopolymer concrete of grade M30 with 10% lime addition by weight of fly ash does achieve strength more than desired at normal room temperature.

4.4. Effect of Varied Curing Temperature of GPC (M30) with 10% Lime Addition. The specimens were cast of size 150 mm × 150 mm × 150 mm of grade M30 with addition of 10% of lime. The concrete cubes were cured at different elevated temperatures of 40°C, 50°C, 60°C, 70°C, 80°C, 90°C, 100°C, 110°C, and 120°C in an oven for 24 hours. After the completion of the defined curing time, these specimens were kept at normal room temperature for a rest period of 07 days after which the specimens were tested for compression on a compression testing machine of capacity 2000 KN. The readings were recorded and listed to study the effect of

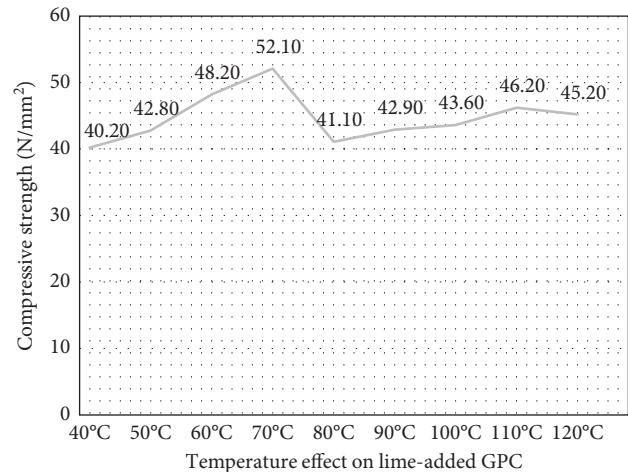


FIGURE 4: Effect of temperature on lime-based GPC.

varied curing temperature for geopolymer concrete with 10 percent of lime addition.

Figure 4 represents the variation in the strength of geopolymer concrete of grade M30 with the addition of 10% lime cured for 24 hours at varied temperatures. The rest period for the cured specimens was 07 days. The graph depicts the decrease in strength at higher temperatures. The maximum compressive strength was achieved with an addition of 10% of lime at 70°C. Thus, the optimum temperature with 10% lime addition observed here is 70°C.

5. Conclusion

- (1) The compressive strength of geopolymer concrete of grade M30 goes on increasing with the addition of 5% and 10% of lime, where maximum can be achieved by the addition of 10% of lime.
- (2) Addition of 15%, 20%, and 25% of lime in geopolymer concrete of grade M30 makes the concrete harsh which adversely affects its workability as well as its compressive strength.
- (3) The compressive strength goes on increasing for an M30 grade of geopolymer concrete with 10% lime addition, as the rest period increases, where the maximum strength is achieved at the completion of 28 days of the rest period.
- (4) The compressive strength of M30 grade of geopolymer concrete with the addition of 10% of lime goes on increasing with the increase in the curing temperature ranging from 40°C to 70°C, where maximum can be achieved at 70°C.
- (5) When 5% of fly ash was replaced by lime by weight, the mixture observed was deficient in the binder, that is, fly ash, thereby decreasing the compressive strength of the geopolymer concrete making it necessary to add lime rather than replacing lime in the preparation of geopolymer concrete.
- (6) compressive strength can also be achieved at higher curing temperatures ranging from 80°C to 120°C for

M30 grade of geopolymer concrete with the addition of 10% lime.

- (7) The compressive strength goes on increasing with the increase in the rest period of geopolymer concrete (M30) with the addition of 10% of lime when cured at normal room temperature, and the maximum compressive strength was achieved at the completion of 28 days of the rest period, thereby giving it a wide scope.
- (8) The compressive strength achieved by grade M30 of geopolymer concrete cured at normal room temperature in a rest period of 7 days is higher than the compressive strength achieved by ordinary concrete for a similar rest period.

Conflicts of Interest

The authors declare that there are no conflicts of interest regarding the publication of this paper.

References

- [1] S. V. Patankar, S. S. Jamkar, and Y. M. Ghugal, "Effect of water-to-geopolymer binder ratio on the production of fly ash based geopolymer concrete," in *Proceedings of the International Conference on Recent Trends in Engineering and Technology (ICRTET'2013)*, Nashik, India, February 2013.
- [2] D. Dutta and S. Ghosh, "Effect of lime stone dust on geopolymerisation and geopolymeric structure," *International Journal of Emerging Technology and Advanced Engineering*, vol. 2, no. 11, ISSN 2250-2459, 2012.
- [3] S. L. Hake, R. M. Damgir, and S. V. Patankar, "State of art-investigation of the method of curing on geopolymer concrete," *IOSR Journal of Mechanical and Civil Engineering*, vol. 12, no. 3, 2015.
- [4] C. Namagga and R. A. Atadero, "Optimization of fly ash in concrete: high lime fly ash as a replacement for cement and filler material," in *Proceedings of the World of Coal Ash (WOCA) Conference*, Lexington, KY, USA, May 2009.
- [5] B. Vijaya Rangan, "Geopolymer concrete for environmental protection," *Indian Concrete Journal*, vol. 88, no. 4, pp. 41-48, 2014.
- [6] D. Bondar, "Geo-polymer concrete as a new type of sustainable construction materials," in *Proceedings of the Third International Conference on Sustainable Construction Materials and Technologies*, Kyoto, Japan, August 2015.
- [7] P. R. Vora and U. V. Dave, "Parametric studies on compressive strength of geopolymer concrete," *Procedia Engineering*, vol. 51, pp. 210-219, 2013.
- [8] N. N. Jain, S. L. Hake, and M. N. Shirsath, "Geopolymer concrete with lime addition at normal room temperature," *International Journal of Research Publications in Engineering and Technology*, vol. 2, no. 8, 2016.
- [9] M. M. A. Abdullah, M. F. M. Tahir, K. Hussin et al., "Fly ash based lightweight geopolymer concrete using foaming agent technology," *Revista De Chimie*, vol. 66, no. 7, pp. 1001-1003, 2015.
- [10] A. C. Ayachit, P. B. Nikam, S. N. Pise, A. D. Shah, and V. H. Pawar, "Mix design of fly-ash based geopolymer concrete," *International Journal of Scientific and Research Publications*, vol. 6, no. 2, pp. 2250-3153, 2016, ISSN 2250-3153.
- [11] K. Ramujee, "Development of low calcium fly ash based geopolymer concrete," *IACSIT International Journal of Engineering and Technology*, vol. 6, no. 1, pp. 1-4, 2014.
- [12] S. Ramasamy, K. Hussin, M. M. A. B. Abdullah et al., "Recent dissertations on kaolin based geopolymer materials," *Reviews on Advanced Materials Science*, vol. 42, no. 1, pp. 83-91, 2015.
- [13] N. N. Jain, S. L. Hake, and M. N. Shirsath, "Percentage replacement of cement in geopolymer concrete," *International Journal of New Technologies in Science and Engineering*, vol. 3, no. 8, ISSN 2349-0780, 2016.
- [14] B. H. Shinde and K. N. Kadam, "Properties of fly ash based geopolymer mortar," *International Journal of Engineering Research & Technology*, vol. 4, no. 7, 2015.
- [15] S. S. Jamkar, Y. M. Ghugal, and S. V. Patankar, "Effect of fly ash fineness on workability and compressive strength of geopolymer concrete," *Indian Concrete Journal*, vol. 87, no. 4, pp. 57-61, 2013.
- [16] S. V. Patankar, Y. M. Ghugaland, and S. S. Jamkar, "Effect of concentration of sodium hydroxide and degree of heat curing on fly ash-based geopolymer mortar," *Indian Journal of Materials Science*, vol. 2014, Article ID 938789, 6 pages, 2014.
- [17] A. M. M. Al Bakri, H. Kamarudin, I. K. Nizar et al., "Processing and characterization of fly ash-based geopolymers for lightweight concrete application," *Revista De Chimie*, vol. 64, no. 4, pp. 382-387, 2013.
- [18] N. F. Shahedan, M. M. A. Abdullah, K. Hussin et al., "Characterization and design of alkali activated binder for coating application," *Materiale Plastice*, vol. 51, no. 3, pp. 258-262, 2014.
- [19] K. Ramujee and M. Potharaju, "Development of mix design for low calcium based geopolymer concrete in low, medium and higher grades-Indian scenario," *Journal of Civil Engineering and Technology*, vol. 1, no. 1, pp. 15-25, 2013.
- [20] M. I. Abdul Aleem and P. D. Arumairaj, "Optimum mix for the geopolymer concrete," *Indian Journal of Science and Technology*, vol. 5, no. 3, ISSN: 0974-6846, 2012.
- [21] C. K. Madheswaran, G. Gnanasundar, and N. Gopalakrishnan, "Effect of molarity in geopolymer concrete," *International Journal of Civil and Structural Engineering*, vol. 4, no. 2, 2013.
- [22] M. A. Javeed, M. Veerendra Kumar, and H. Narendra, "Studies on mix design of sustainable geopolymer concrete," *International Journal of Innovative Research in Engineering & Management*, vol. 2, no. 4, ISSN: 2350-0557, 2015.
- [23] M. A. Faris, M. M. A. Abdullah, A. V. Sandu et al., "Assessment of alkali activated geopolymer binders as an alternative of Portland cement," *Materiale Plastice*, vol. 54, no. 1, pp. 145-154, 2017.
- [24] S. Das, A. Mohapatra, and A. K. Rath, "Geopolymer concrete-green concrete for the future—a review," *International Journal of Civil Engineering Research*, vol. 5, no. 1, pp. 21-28, 2014, ISSN 2278-3652.
- [25] N. Nordin, M. M. A. Abdullah, M. F. M. Tahir, A. V. Sandu, and K. Hussin, "Utilization of fly ash waste as construction material," *International Journal of Conservation Science*, vol. 7, no. 1, pp. 161-166, 2016.

Research Article

Uniaxial Compressive Test of High Ductile Fiber-Reinforced Concrete and Damage Constitutive Model

Mingke Deng , Jiaojiao Pan , and Xingwen Liang

School of Civil Engineering, Xi'an University of Architecture and Technology, Xi'an 710055, China

Correspondence should be addressed to Mingke Deng; dengmingke@126.com

Received 5 August 2017; Revised 18 November 2017; Accepted 23 November 2017; Published 25 February 2018

Academic Editor: Chiara Bedon

Copyright © 2018 Mingke Deng et al. This is an open access article distributed under the Creative Commons Attribution License, which permits unrestricted use, distribution, and reproduction in any medium, provided the original work is properly cited.

It has been widely recognized that the constitutive model plays an essential role in engineering application of high ductile fiber-reinforced concrete (HDC). In this research, uniaxial compressive tests were conducted on nine groups of HDC specimens with different mixture ratios and one group of mortar matrix specimens as comparison, discussing the effect of fiber content, water-cement ratio, fly ash content, and sand-binder ratio. According to the characteristics of stress-strain curve of HDC under uniaxial compression, a damage constitutive model was proposed by introducing two damage threshold parameters and then was compared with other existing models. Results indicated that the damage model curves suggested in this paper were best consistent with experimental curves and substantially demonstrate the damage evolution process as well as the cracking resistance effect of fiber bridging stress.

1. Introduction

High ductile fiber-reinforced concrete (HDC) [1], just like engineered cementitious composites (ECCs) [2, 3], is also a kind of high performance fiber-reinforced cementitious composite (HPFRCC) [4, 5], which is composed primarily of cement, fine aggregate, and fiber. HDC is manufactured based on the designed theory of micromechanics and fracture mechanics and can be characterized by pseudostrain hardening and multiple cracking behaviors when subjected to tensile loading. Recently, due to its excellent durability, high toughness, and remarkable damage resistance capacity, HDC has been widely utilized in civil engineering, particularly in the flexure and shear-dominated members, such as coupling beams, low-rise walls, and beam-column joints [6–9]. Findings suggested that HDC can effectively enhance the structural performance and improve the shear strength, energy dissipation, and damage tolerance of members.

In the engineering application mentioned above, there are stringent requirements on mechanical behavior and stress-strain relationship of HDC. Therefore, many investigations have been carried out to investigate the compressive property and constitutive relationship of HDC.

Fakharifar et al. [10] statistically evaluated the effect of fiber content on compressive and flexural strengths through adequate tests and found that the first crack and failure strength as well as mechanical properties were enhanced by increasing the fiber content. Ma et al. [11] suggested that excessive amounts of fly ash tend to decrease the compressive strength though ductility improved with fly ash content. Due to the vital role of the constitutive model in the design and analysis of structure, Li and Liu [12] and Xu et al. [13], respectively, built the constitutive models based on the stress-strain curves of HDC under uniaxial compression. However, the abovementioned models neglected the microcracks and microvoids in HDC and thus cannot reflect the damage evolution of HDC under uniaxial compression. So, it is necessary to build a constitutive model considering the initial damage in HDC.

Over the past 30 years, damage mechanics has been widely employed to describe the failure process for traditional building material. The existing researches indicated that damage theory is a reasonable way to evaluate the constitutive relationship of concrete due to its powerful theoretical framework [14–20]. Furthermore, owing to its solid foundation for irreversible thermodynamics and

TABLE 1: Properties of PVA fiber.

Length (mm)	Diameter (μm)	Length-diameter ratio	Tensile strength (MPa)	Modulus of elasticity (GPa)	Elongation (%)	Density (g/cm^3)
12	39	0.31×10^3	1600	40	7	1.3

relevant consideration of physical mechanisms, continuum damage mechanics serves as an effective method to the research of the stress-strain relationships of concrete and rock in a comprehensive way [21–26]. Xue et al. [27] introduced the damage threshold parameters and established a damage constitutive model of steel fiber-reinforced concrete reflecting the linear elastic behavior under low stress. Therefore, damage mechanics can be used to derive the constitutive model of HDC. The toughness and deformability of HDC under uniaxial compression can be significantly improved for the lateral restraint effect of the fiber bridging stress inside the matrix, which has obvious difference with concrete [1]. The researchers [21–27] primarily focused on the concrete and steel fiber-reinforced concrete, both of which can be classified as a brittle material. Consequently, their models are unable to reflect the damage accumulation and constitutive relationship of HDC under the uniaxial compressive stress state.

The present research reports on uniaxial compressive tests of HDC with different mixture ratios, discussing the effect of fiber bridging stress on the failure mode. In addition, it includes an investigation into the influence laws of ingredients, such as polyvinyl alcohol (PVA) fiber volume, water-cement ratio, fly ash content, and sand-binder ratio, on the characteristic points of HDC stress-strain curves. Besides, based on the features of experimental curves, this paper established a modified damage constitutive model by introducing two damage threshold parameters γ and β and then compared this damage model with the existing models. It should be stressed that the model proposed in this paper describes the damage evolution process and provides a theoretical basis for the nonlinear analysis of components and the ductility design of the structure.

2. Experimental Program

2.1. Material. The ingredients of HDC adopted in the test are cement (PO 42.5R), fly ash, fine river sand, PVA fiber, mineral admixtures, water, and superplasticizer. Table 1 presents the mechanical properties of PVA fiber. Nine groups of HDC and one group of mortar matrix with different mix proportions were designed and three identical specimens were cast for each group. The dimension of prismatic specimens was $100 \text{ mm} \times 100 \text{ mm} \times 300 \text{ mm}$, and the mixture ratios are given in Table 2. Test parameters in this paper included PVA content (1%, 1.5%, and 2%), water-cement ratio (0.26, 0.29, and 0.32), fly ash content (40%, 50%, and 60%), and sand-binder ratio (0.24, 0.36, and 0.48).

2.2. Testing Method. Figure 1 gives the schematic diagram of test setup. To obtain the strain-stress curve of HDC under uniaxial compression, the linear variable differential

TABLE 2: Mix design for experimental program.

Code	PVA content (%)	Water-binder ratio	Fly ash content (%)	Sand-binder ratio
1	0	0.29	50	0.36
2	1.0	0.29	50	0.36
3	1.5	0.29	50	0.36
4	2.0	0.29	50	0.36
5	2.0	0.26	50	0.36
6	2.0	0.32	50	0.36
7	2.0	0.29	60	0.36
8	2.0	0.29	40	0.36
9	2.0	0.29	50	0.24
10	2.0	0.29	50	0.48

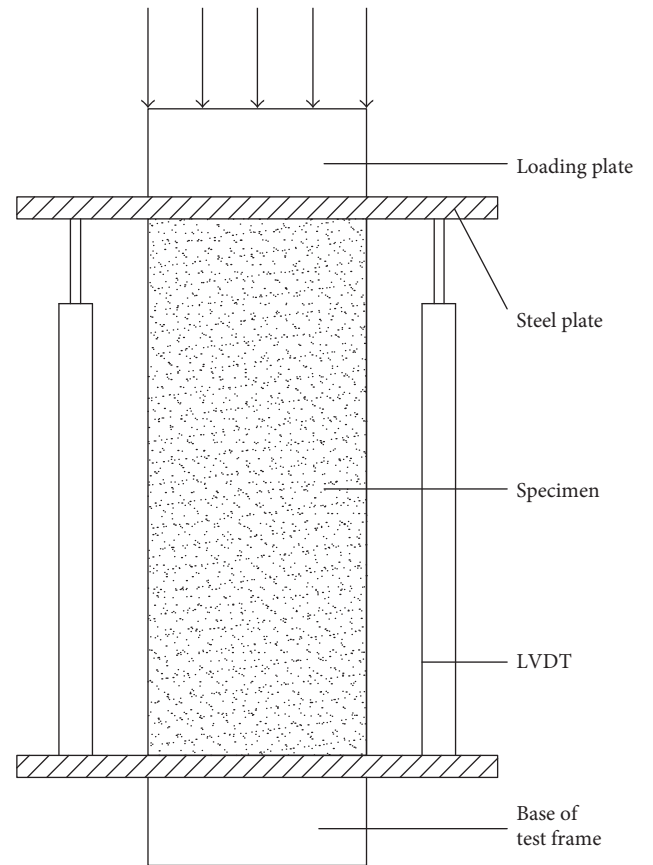


FIGURE 1: The schematic diagram of test setup.

transformers (LVDTs) were installed between both ends of the specimen and measured the whole longitudinal deformation of the specimen. The load was applied through a 500t microcomputer-controlled electrohydraulic servo

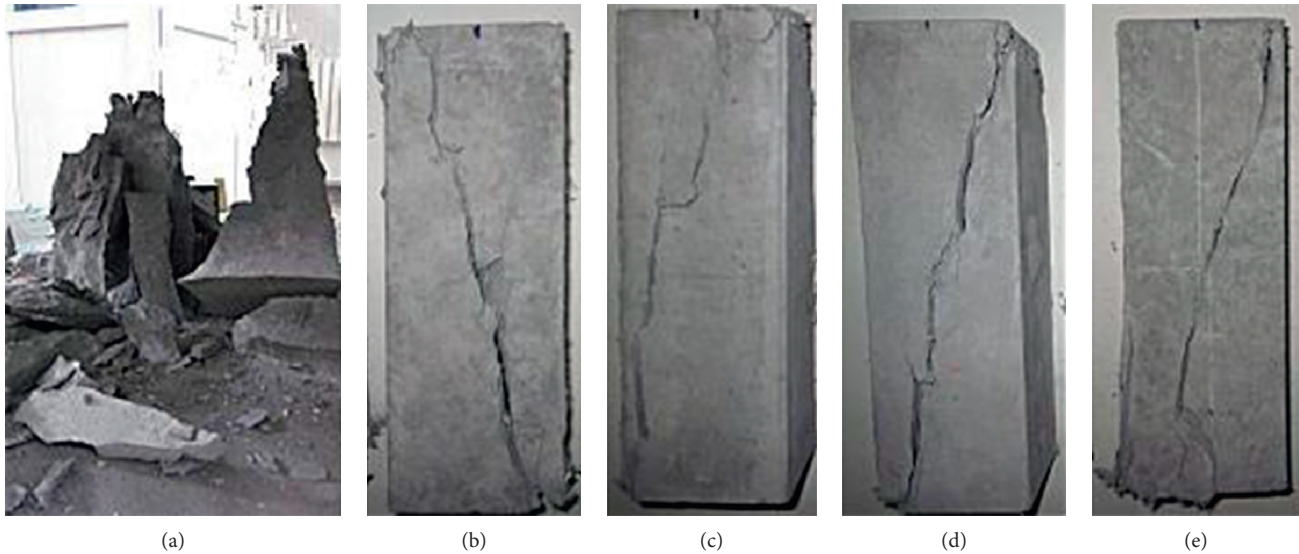


FIGURE 2: Typical failure mode of specimens. (a) Matrix, (b) HDC-2, (c) HDC-4, (d) HDC-5, and (e) HDC-6.

compressive testing machine. The loading was controlled by displacement at a rate of 0.5 mm/min, and the data were collected through the TDS602 Data Logger.

3. Results and Discussion

3.1. Failure Mode. Figure 2 shows the typical failure modes of specimens. The brittle splitting failure occurred for the matrix specimen, and the specimen was divided into several prisms at the ultimate stage (Figure 2(a)). In contrast, the HDC specimens remained intact at the softening stage, and finally a major inclined shear crack formed along the specimens (Figures 2(b)–2(e)), which agreed with the conclusions in research [28]. The shear failure mode of HDC specimens exhibited obvious ductility compared with the matrix specimen.

The fiber bridging effect can be used to explain this phenomenon. During the failure process of HDC under uniaxial compression, the fiber bridging stress effectively restrains the lateral deformation of specimens (Figure 3), and thus, the appearance and propagation of longitudinal cracks are delayed. The fibers are pulled out or pulled apart when the lateral tensile deformation exceeds the ultimate tensile strain of HDC, leading to the inefficacy of the lateral constraining force. Thus, longitudinal cracks will appear at the weakest part of specimens, which will run through the specimens from top to bottom and eventually form a major crack. During the failure process of specimens, there is obvious dislocation at both sides of the major diagonal crack. The specimens are still in good condition and have residual bearing capacity due to the fiber bridging effect even if they are damaged. Conclusions can be drawn that, due to the lateral restraint effect of fiber bridging stress, the damage and failure processes of HDC under uniaxial compression are quite different from those of concrete.

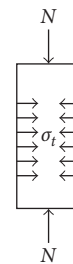


FIGURE 3: Lateral restraint effect of fiber bridging stress.

3.2. Uniaxial Compressive Stress-Strain Curves and Characteristic Points. Uniaxial compressive stress-strain curves obtained through the test are shown in Figure 4. Characteristic points of the stress-strain curves of specimens together with the corresponding values of stress and strain are given in Table 3. It can be known from Figure 4 and Table 3 that the corresponding peak strain of mortar matrix (mixture ratio 1) is 0.0021, which is quite close to that of concrete. The uniaxial compressive stress-strain curve of HDC is a unimodal curve, and the peak strain of 9 groups of HDC specimens is 2.61–3.15 times that of mortar matrix. This indicates that the deformability of HDC specimens has been significantly improved before peak load. Once over the peak load, the mortar matrix immediately loses bearing capacity. Although HDC specimen also has a sudden drop of load, there is always 10–20% residual bearing capacity in the specimen when large compressive strain appears.

3.3. Effect of Factors on the Characteristic Points of Stress-Strain Curves. According to the test results in Table 3, the effects of four factors (fiber content, water-binder ratio, fly

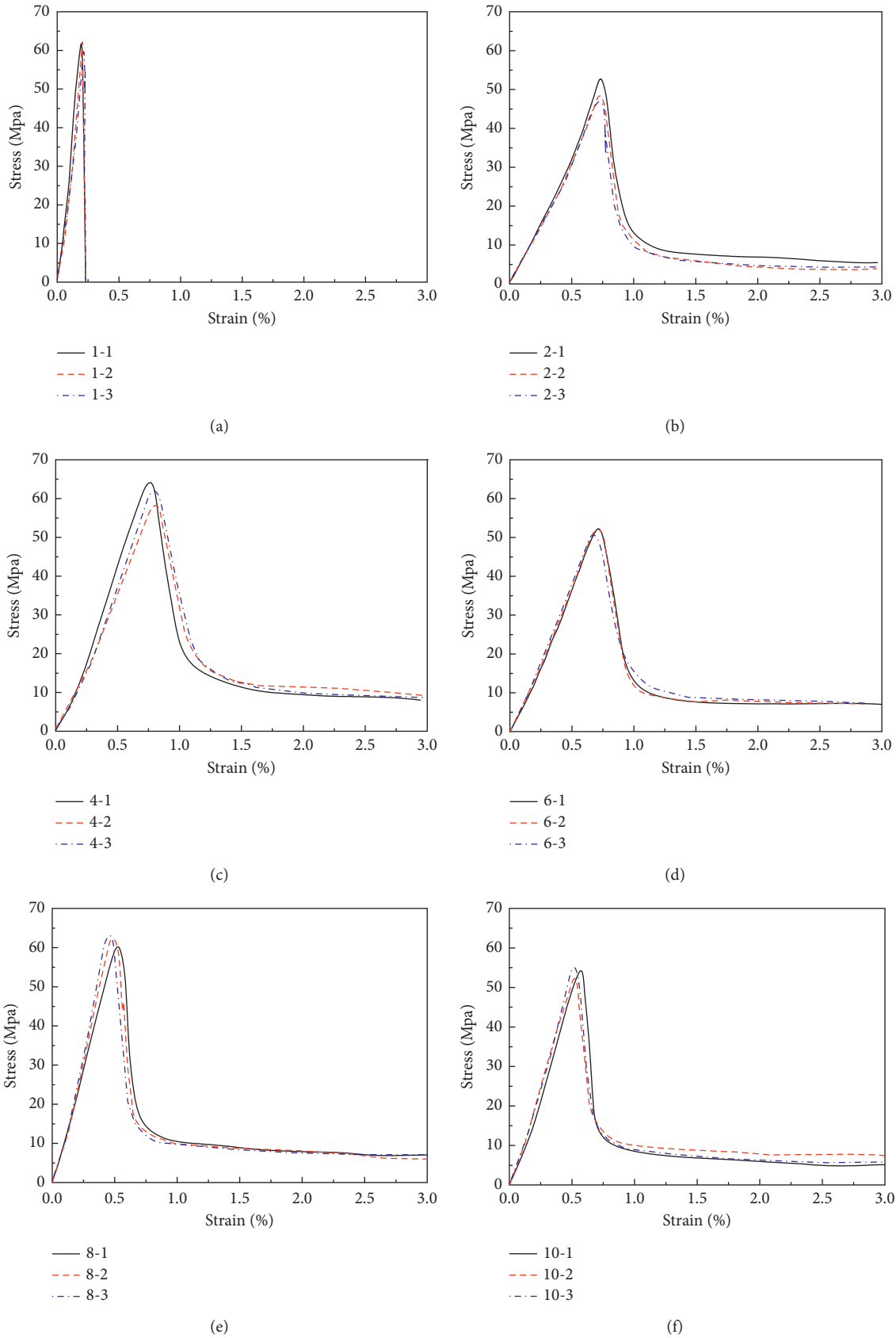


FIGURE 4: Typical uniaxial compression stress-strain curves of HDC. (a) Matrix, (b) HDC-2, (c) HDC-4, (d) HDC-6, (e) HDC-8, and (f) HDC-10.

TABLE 3: Characteristic points of HDC stress-strain curve.

Code	P_m (kN)	σ_0 (MPa)	$\sigma_{0.2}$ (MPa)	ϵ_0 (10^{-3})	$\epsilon_{0.85}$ (10^{-3})	$\epsilon_{0.5}$ (10^{-3})	$\epsilon_{0.2}$ (10^{-3})
1	630.55	63.06	—	2.13	—	—	—
2	502.78	50.28	10.06	5.69	6.02	6.67	8.64
3	568.50	56.85	11.37	6.01	6.66	6.95	11.28
4	622.52	62.25	12.45	6.72	8.01	9.32	14.07
5	560.35	56.04	11.21	6.33	7.05	7.69	11.16
6	528.38	52.84	10.57	6.52	7.88	9.52	12.76
7	536.35	53.64	10.73	6.34	7.90	9.47	13.80
8	644.32	64.43	12.89	5.61	6.41	6.94	8.87
9	519.60	51.96	10.39	6.48	8.14	9.23	13.57
10	560.05	56.01	11.20	5.56	6.05	6.66	8.10

Note: (1) P_m is peak load; σ_0 is peak stress; ϵ_0 is the strain corresponding to peak stress; (2) $\sigma_{0.2}$ is the stress value when the stress declines to 20% of peak stress; (3) $\epsilon_{0.85}$, $\epsilon_{0.5}$, and $\epsilon_{0.2}$ are the corresponding ultimate compressive strain values when the stress declines to 85%, 50%, and 20% of peak stress, respectively.

ash content, and sand-binder ratio) on the characteristic points of stress-strain curves of HDC under uniaxial compression (Figure 5) can be found out. The analyses on four influencing factors are as follows.

3.3.1. Fiber Content. As shown in Figure 5(a), the peak stress σ_0 of the HDC specimen increases with the increase in fiber content. Besides, $\epsilon_{0.85}$, $\epsilon_{0.5}$, and $\epsilon_{0.2}$ increase by 33.06%, 39.73%, and 62.85%, respectively, as fiber content increases to 2% from 1%. It can be attributed to the disordered short fibers preventing the appearance and development of microcracks. As a result, the compressive strength and deformability of HDC specimens were improved.

3.3.2. Water-Binder Ratio. From Figure 5(b), it can be seen that the ultimate strain and compressive strength of HDC specimens increase as water-binder ratio increases from 0.26 to 0.29 and then decline as the water-binder ratio increases to 0.32. It suggested that the ratio 0.29 was more effective than others in terms of enhancing the compressive behavior of HDC. This phenomenon appeared for the reason that the increased water-binder ratio improved the workability of the mixture, leading to the more uniform distribution of fibers inside the matrix. Consequently, the toughness and cracking resistance of HDC enhanced. However, the high water-binder ratio reduced the compressive strength of HDC.

3.3.3. Fly Ash Content. As shown in Figure 5(c), the peak strain of specimens demonstrates a significant rise when the fly ash content increases from 40% to 50% and a slight reduction when the fly ash content increases from 50% to 60%, together with the ultimate compressive strain. The cause is that fly ash can improve the interfacial bond properties between fibers and matrix, thus preventing excessive fiber rupture and enhancing the toughness of HDC [1]. It should also be noted that the maximum stress declines with the increase in the fly ash content. Thus, the fly ash content should be limited, considering enough compressive strength.

3.3.4. Sand-Binder Ratio. The deformation capacity of specimens improves when the sand-binder ratio rises from 0.24 to 0.36. It drops instead of rising continually when the sand-binder ratio increases to 0.48, which can be attributed to the fact that the friction force between fibers and matrix increases due to the excessive sand-binder ratio. As a result, most of the fibers are pulled apart, and the tensile deformability of the material declines, thus reducing the ultimate compressive strain of specimens. From Figure 5(d), it also can be known that the maximum stress of specimens with a sand-binder ratio of 0.36 is higher than that of specimens with sand-binder ratios of 0.24 and 0.48. Hence, the ratio 0.36 was most favorable to improving the compressive strength and strain capacity of HDC.

4. Damage Constitutive Model of HDC under Uniaxial Compression

4.1. Establishment of Damage Constitutive Model. Let A be the cross-sectional area of the material under undamaged condition and \tilde{A} be the effective bearing area decreased by the damage. Then, the damage variable D can be expressed as

$$D = \frac{A - \tilde{A}}{A} = 1 - \frac{\tilde{A}}{A} \quad (1)$$

The effective bearing area can be expressed as

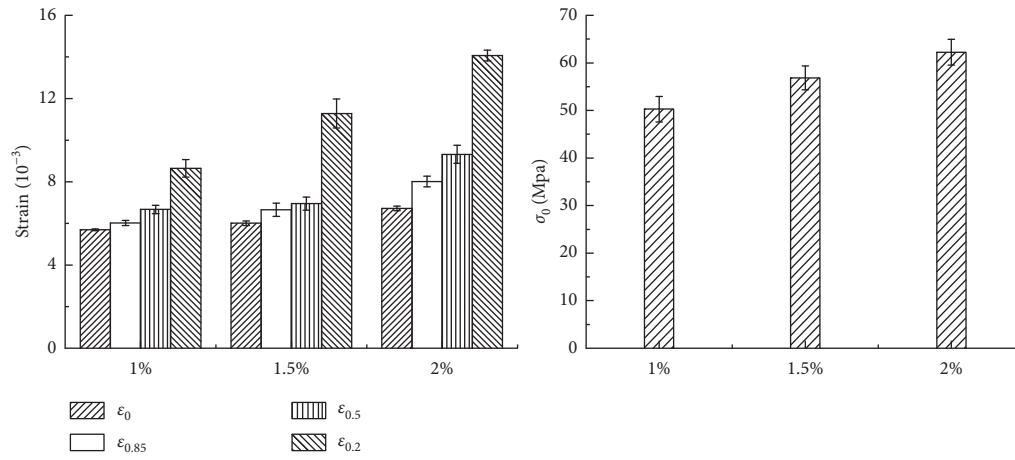
$$\tilde{A} = (1 - D)A \quad (2)$$

Let $\tilde{\sigma}$ be the ratio of external load F to the effective loading area. Then,

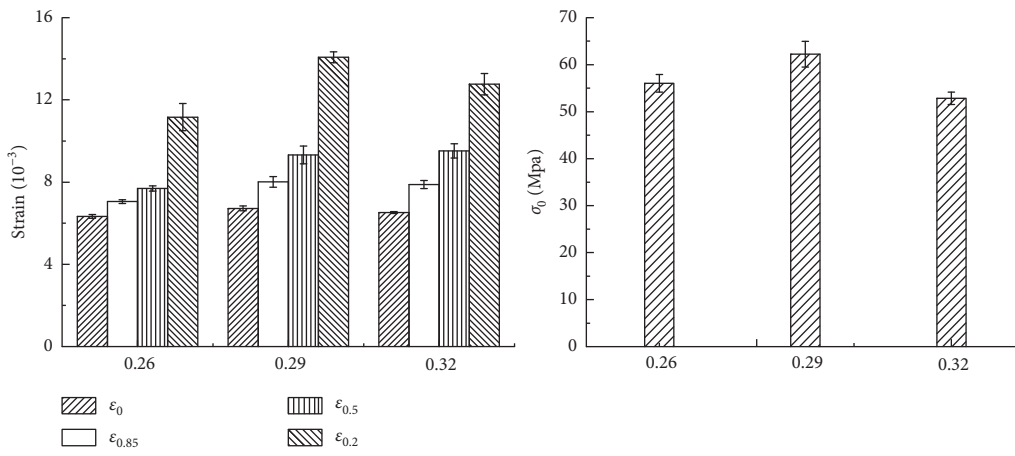
$$\tilde{\sigma} = \frac{F}{\tilde{A}} = \frac{F}{(1 - D)A} = \frac{\sigma}{(1 - D)} \quad (3)$$

where σ is the nominal stress on the cross section of components, and $\sigma = F/A$.

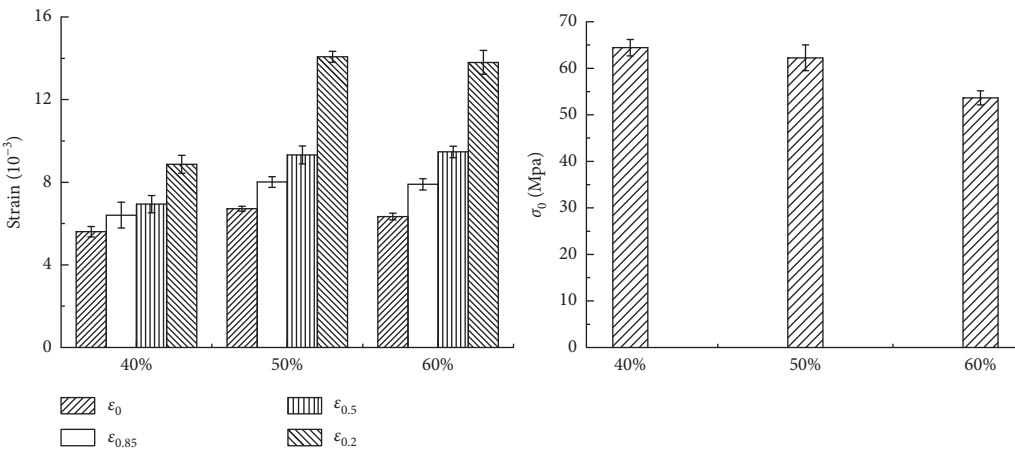
According to the equivalent strain hypothesis theory proposed by Lemaitre [29], the constitutive relation of damaged material can be derived from the constitutive equation of the nondestructive material under uniaxial stress by replacing the nominal stress of the constitutive relation of



(a)



(b)



(c)

FIGURE 5: Continued.

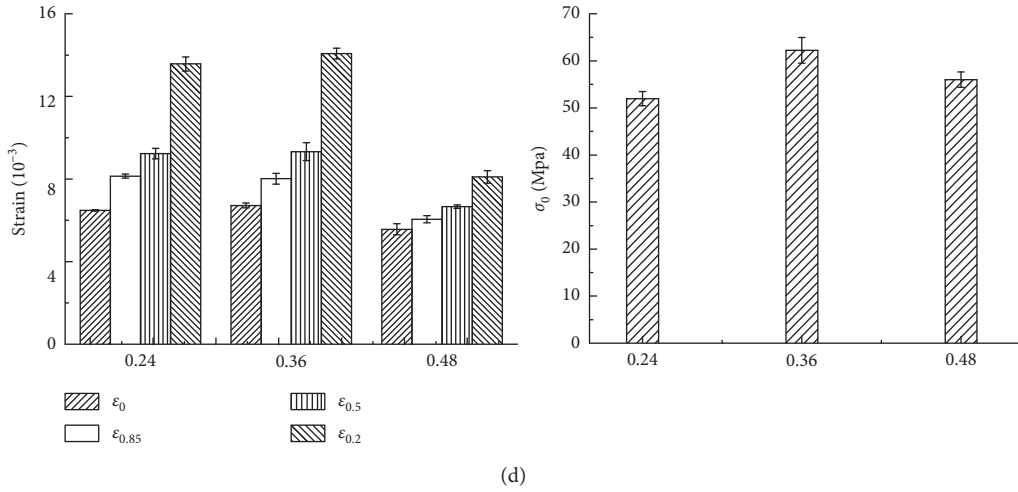


FIGURE 5: Influence of factors on the characteristic points of stress-strain curves of HDC. (a) Fiber content. (b) Water-binder ratio. (c) Fly ash content. (d) Sand-binder ratio.

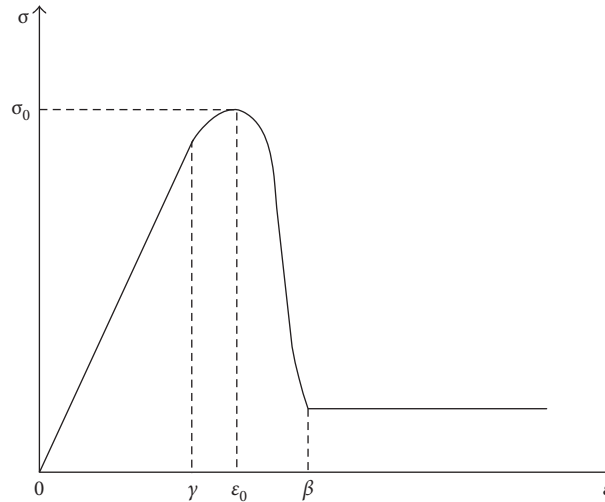


FIGURE 6: Stress-strain curve of HDC.

the undamaged material with the effective stress. Let ε be the damaged elastic strain, and then the damage constitutive relation of the material is ($\tilde{\sigma} = E\varepsilon$)

$$\sigma = E(1 - D)\varepsilon. \quad (4)$$

4.2. Derivation of Damage Evolution Equation. As for the damage fracture of rock and concrete, the literature [25, 26] suggests that the damage variable D of the material fulfills Weibull distribution. Thus,

$$D = 1 - \exp\left[-\left(\frac{\varepsilon}{\eta}\right)^m\right], \quad (5)$$

where m and η (nonnegative numbers), respectively, are the shape parameter and scale parameter.

From the stress-strain curve of the HDC specimen, it should be noted that the linear elastic stage elongates and the strain corresponding to the initial damage is enlarged. In

addition, the damage of HDC tends to be stable, and there is 10%–20% residual bearing capacity in specimens when the strain exceeds a certain value. Based on the above analysis, two damage thresholds γ and β are introduced in this paper to build the damage constitutive model of HDC. γ is the initial point at the nonlinear ascent stage, and β is the initial point at the residual stage. Then, the damage variable can be expressed as follows:

Damage variable:

$$D = \begin{cases} 0 & (\varepsilon < \gamma) \\ 1 - \exp\left[-\left(\frac{\varepsilon - \gamma}{\eta}\right)^m\right] & (\gamma \leq \varepsilon \leq \beta) \\ D_u & (\varepsilon > \beta), \end{cases} \quad (6)$$

TABLE 4: Parameters of damage constitutive model.

Code	m	$\eta (\times 10^{-3})$	γ/ε_0	β/ε_0	D		Correlation coefficient of model		
					ε_0	β	New proposal	Li	Xu
2	5.78	0.26	0.80	1.21	0.03	0.89	0.983	0.987	0.962
3	4.36	0.27	0.82	1.27	0.04	0.85	0.975	0.972	0.947
4	2.56	0.38	0.84	1.43	0.06	0.83	0.982	0.982	0.948
5	5.22	0.22	0.82	1.20	0.03	0.87	0.978	0.980	0.947
6	3.94	0.28	0.82	1.28	0.04	0.85	0.985	0.982	0.957
7	2.92	0.29	0.84	1.38	0.05	0.84	0.977	0.980	0.941
8	3.74	0.19	0.84	1.29	0.04	0.87	0.991	0.993	0.974
9	2.63	0.30	0.82	1.41	0.06	0.79	0.991	0.986	0.964
10	4.60	0.19	0.83	1.26	0.04	0.88	0.990	0.989	0.978
μ	—	—	0.83	1.30	0.05	0.85	0.984	0.983	0.958
δ	—	—	0.013	0.060	0.243	0.035	0.006	0.006	0.013

where D_u is the damage value when the strain ε is equal to β , that is, the maximum damage variable.

Damage constitutive model:

$$\sigma = \begin{cases} E\varepsilon & (\varepsilon < \gamma) \\ E(1-D)\varepsilon & (\gamma \leq \varepsilon \leq \beta) \\ (1-D_u)\sigma_0 & (\varepsilon > \beta). \end{cases} \quad (7)$$

4.3. *Determination of Model Parameter.* The shape of the stress-strain curve of HDC under uniaxial compression can be obtained (Figure 6).

As seen in Figure 6, the stress-strain curve of HDC meets the following boundary conditions:

- (1) $\varepsilon = 0, \sigma = 0$
- (2) $\varepsilon = 0, d\sigma/d\varepsilon = E$ (E is the initial elastic modulus)
- (3) $\sigma = \sigma_0, \varepsilon = \varepsilon_0$
- (4) $\sigma = \sigma_0, d\sigma/d\varepsilon = 0$

Through the features (1), (2), (3), and (4) of stress-strain curves of HDC, the parameters (m, η) can be calculated as follows:

$$m = \frac{\varepsilon_0 - \gamma}{\varepsilon_0} \frac{1}{\ln(E\varepsilon_0/\sigma_0)}, \quad (8)$$

$$\eta = \frac{\varepsilon_0 - \gamma}{(\varepsilon_0 - \gamma/m\varepsilon_0)^{1/m}}. \quad (9)$$

4.4. *Comparisons of Experimental Curves and Model Curves.* The parameters of HDC damage constitutive model under uniaxial compression was calculated, and the results of model parameters and damage variable (at point ε_0 and β) are listed in Table 4. The parameters m, η can be worked out through expressions (8) and (9). μ and δ are the average and coefficient of variation of parameters.

As shown in Table 4, the value γ/ε_0 of HDC is about 0.83. This indicates that the elastic section of HDC stress-strain curves elongates and the damage resistance ability is stronger. Let γ be $0.8\varepsilon_0$ and β be $1.3\varepsilon_0$ so as to substitute the two damage thresholds into expression (7). Then, the damage constitutive model of HDC under uniaxial compression can be worked out. Then, there is

$$\sigma = \begin{cases} E\varepsilon & (\varepsilon < 0.8\varepsilon_0) \\ E\varepsilon \exp\left[-\left(\frac{\varepsilon-\gamma}{\eta}\right)^m\right] & (0.8\varepsilon_0 \leq \varepsilon < 1.3\varepsilon_0) \\ (1-D_u)\sigma_0 & (\varepsilon \geq 1.3\varepsilon_0). \end{cases} \quad (10)$$

Li and Liu [12] and Xu et al. [13] suggested the constitutive models of this material in which the damage in HDC was not considered. The descent stage of curve adopted the same equation in these models, whereas the ascent stage used rational fraction equation and polynomial equation, respectively. Those are as follows:

The descent stage:

$$y = \frac{x}{B(x-1)^2 + x} \quad (x \geq 1). \quad (11)$$

The ascent stage:

Li's model:

$$y = \frac{Ax - x^2}{1 + (A-2)x} \quad (0 \leq x < 1). \quad (12)$$

Xu's model:

$$y = C_1 + C_2x + C_3x^2 + C_4x^3 \quad (0 \leq x < 1), \quad (13)$$

where $x = \varepsilon/\varepsilon_0$, $y = \sigma/\sigma_0$, and A, B, C_1, C_2, C_3, C_4 are the fitting coefficients.

This research, respectively, calculated the correlation coefficients of three model curves and the experimental curves as shown in Table 4. The fitting coefficients A, B, C_1, C_2, C_3, C_4 in Li's model and Xu's model were

TABLE 5: Fitting coefficients.

Code	A	B	C_1	C_2	C_3	C_4
2-1	1.034	37.134	0.0047	0.8317	-0.1147	0.2940
2-2	1.074	43.974	0.0100	0.7613	0.2643	-0.0267
2-3	1.073	43.258	0.0135	0.7258	0.2227	0.0569
3-1	1.078	27.678	0.0070	0.4882	1.0398	-0.5319
3-2	1.091	32.823	0.0059	0.3222	1.6317	-0.9484
3-3	1.080	28.726	0.0131	0.6201	0.3015	0.0776
4-1	1.109	20.536	0.0065	0.4160	1.6010	-1.0100
4-2	1.091	20.647	0.0197	0.5249	1.0022	-0.5326
4-3	1.083	16.407	0.0137	0.3248	1.4095	-0.7329
5-1	1.024	42.674	0.0029	0.6888	-0.0087	0.3471
5-2	1.032	38.564	0.0000	0.7332	-0.2785	0.5767
5-3	1.035	42.354	0.0056	0.3815	1.0399	-0.4061
6-1	1.087	20.680	0.0052	0.6321	0.7937	-0.4198
6-2	1.093	15.564	-0.0022	0.8249	0.3049	-0.1172
6-3	1.119	14.659	0.0085	0.6399	0.8406	-0.4703
7-1	1.093	12.386	-0.0009	0.6471	0.5464	-0.1774
7-2	1.103	14.471	0.0076	0.5708	0.9070	-0.4720
7-3	1.104	12.851	0.0172	0.3625	1.0927	-0.4394
8-1	1.075	35.291	0.0023	0.7590	0.6093	-0.3669
8-2	1.080	39.523	0.0062	0.5423	1.1401	-0.6759
8-3	1.073	33.200	0.0139	0.3904	1.2833	-0.6612
9-1	1.099	14.372	0.0115	0.5952	0.7945	-0.3913
9-2	1.094	15.626	0.0100	0.4324	1.4337	-0.8676
9-3	1.093	17.578	0.0028	0.6649	0.4437	-0.0906
10-1	1.055	39.618	0.0118	0.5097	0.9268	-0.4402
10-2	1.058	42.618	0.0006	0.6400	0.8168	-0.4523
10-3	1.070	35.641	0.0005	0.6940	0.4779	-0.1649

given in Table 5. Figure 7 describes the comparisons of experimental curves and constitutive model curves. The relation curves between the damage variable D and strain are shown in Figure 8, and then the damage evolution process of HDC under uniaxial compression is observed. Compared with the Li's and Xu's models, the damage model suggested in this paper had the following features:

- (1) The damage model curves are in best agreement with experimental curves reflecting the characteristic of linear elastic deformation and the residual bearing capacity of HDC which can be attributed to the restraint effect of fiber bridging stress. However, the ascent stage of Xu's model curves had great difference with the experimental curves whose correlation coefficient is smaller than those in the damage model and Li's model.
- (2) The damage model describes the damage development process and the effect of toughness and crack resistance of fiber in this period, whereas Li's and

Xu's models cannot reflect the damage evolution of HDC under uniaxial compression.

- (3) As fiber content increases, the parameter m of the damage constitutive model decreases, whereas η constantly increases. Therefore, the area enclosed by the stress-strain curve also increases gradually. It suggested that the energy dissipation capacity of HDC was improved with added fiber content.
- (4) When strain reaches the damage threshold β , the damage variable D is about 0.85 (smaller than 1.0). HDC is still not damaged completely when the deformation is large. It suggests that fibers can delay the damage propagation of concrete, just like the fact that the fiber bridging stress can delay the crack propagation.

5. Conclusions

This research dealt with the effects of ingredients on the compressive properties of HDC. The damage constitutive

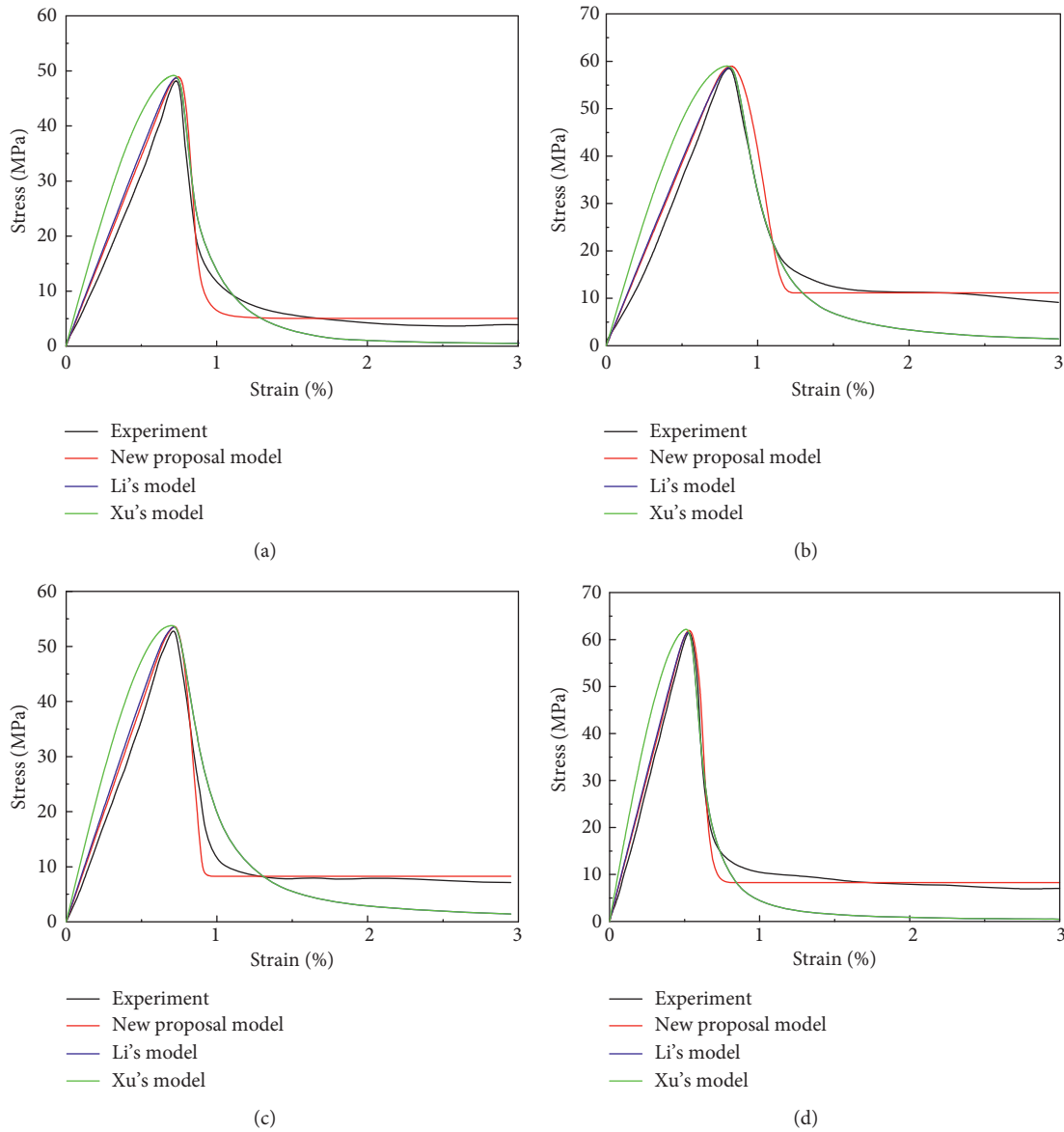


FIGURE 7: Comparisons of experimental curves and model curves. (a) HDC 2-2, (b) HDC 4-2, (c) HDC 6-2, and (d) HDC 8-1.

model was established by using two damage threshold parameters γ and β based on the stress-strain relationship attaining from uniaxial compressive tests. The following conclusions can be drawn:

- (1) The mortar matrix specimen fails in brittle split under uniaxial compression and is divided into several prisms after failure. In contrast, the ductile shear failure occurs for the HDC specimens due to the lateral confinement effect of fiber bridging stress.
- (2) The stress-strain curve of HDC under uniaxial compression is a unimodal curve, and the peak deformation is 2.61–3.15 times that of mortar matrix. Besides, the HDC specimens still remain intact and

have 10–20% residual bearing capacity at the ultimate stage.

- (3) Based on the features of stress-strain curves of HDC under uniaxial compression, two damage threshold parameters are introduced and then a damage constitutive model is built. Besides, the damage model curves fit best with the experimental curves and reflect the damage development process of HDC compared with two existing models.
- (4) As the fiber content increases, the parameter m of the damage constitutive model gradually decreases, whereas η constantly increases. It suggests that the energy dissipation capacity of HDC is improved with the added fiber content.

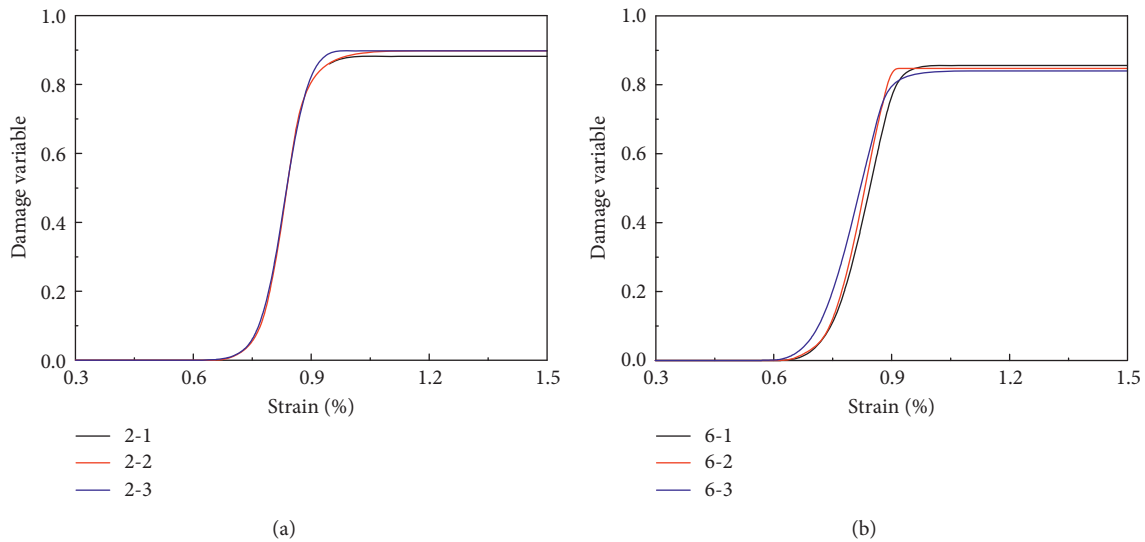


FIGURE 8: Relation curves between damage variable and strain: (a) HDC 2 and (b) HDC 6.

Conflicts of Interest

The authors declare that there are no conflicts of interest regarding the publication of this paper.

Acknowledgments

This research is funded by the Natural Science Foundation of China (No. 51578445) and Key Laboratory Project in Shaanxi Province Education Department (No. 15JS048). The authors would like to thank the laboratory teachers from the School of Civil Engineering for their help with specimen fabrication and testing.

References

- [1] M. K. Deng, J. Han, H. B. Liu, M. Qin, and X. W. Liang, "Analysis of compressive toughness and deformability of High Ductile Fiber Reinforced Concrete," *Advances in Materials Science and Engineering*, vol. 2015, Article ID 384902, 7 pages, 2015.
- [2] V. C. Li and H. C. Wu, "Conditions for pseudo strain-hardening in fiber reinforced brittle matrix composites," *Applied Mechanics Reviews*, vol. 45, no. 8, pp. 390–398, 1992.
- [3] S. Wang and V. C. Li, "High early strength Engineered Cementitious Composites," *ACI Material Journal*, vol. 103, no. 2, pp. 97–105, 2006.
- [4] K. G. Kuder and S. P. Shah, "Processing of high-performance fiber-reinforced cement-based composites," *Construction and Building Materials*, vol. 24, no. 2, pp. 181–186, 2010.
- [5] G. J. Parra-Montesinos, "High-performance fiber-reinforced cement composites: an alternative for seismic design of structures," *ACI Structure Journal*, vol. 102, no. 5, pp. 668–675, 2005.
- [6] G. Fischer and V. C. Li, "Influence of matrix ductility on tension-stiffening behavior of steel reinforced Engineered Cementitious Composites (ECC)," *ACI Structure Journal*, vol. 99, no. 1, pp. 104–111, 2002.
- [7] G. Fischer and V. C. Li, "Effect of matrix ductility on deformation behavior of steel reinforced ecc flexural members under reversed cyclic loading conditions," *ACI Structure Journal*, vol. 99, no. 6, pp. 781–790, 2011.
- [8] G. Fischer and V. C. Li, "Deformation behavior of fiber-reinforced polymer reinforced Engineered Cementitious Composite (ECC) flexural members under reversed cyclic loading conditions," *ACI Structure Journal*, vol. 100, no. 1, pp. 25–35, 2003.
- [9] S. Qian, Y. Y. Kim, and V. C. Li, "Influence of concrete material ductility on shear response of stud connections," *ACI Materials Journal*, vol. 103, no. 1, pp. 60–66, 2006.
- [10] M. Fakharifar, A. Dalvand, M. Arezoumandi, M. Sharbatdar, G. Chen, and A. Kheyroddin, "Mechanical properties of high performance fiber reinforced cementitious composites," *Construction and Building Materials*, vol. 71, pp. 510–520, 2014.
- [11] H. Ma, S. Qian, Z. Zhang, Z. Lin, and V. C. Li, "Tailoring Engineered Cementitious Composites with local ingredients," *Construction and Building Materials*, vol. 101, pp. 584–595, 2015.
- [12] Y. Li and Z. J. Liu, "Study on mechanical performance and constitutive equation of high toughness PVA-FRCC under uniaxial compression," *Journal of Building Materials*, vol. 17, no. 4, pp. 606–612, 2014, in Chinese.
- [13] S. L. Xu, X. R. Can, and Y. H. Zhang, "Experimental measurement and analysis of the axial compressive stress-strain curve of ultra high toughness cementitious composites," *Civil Engineering Journal*, vol. 42, no. 11, pp. 79–85, 2009, in Chinese.
- [14] G. Swoboda, X. P. Shen, and L. Rosas, "Damage model for jointed rock mass and its application to tunneling," *Computers and Geotechnics*, vol. 22, no. 3-4, pp. 183–203, 1998.
- [15] W. Suaris, C. Ouyang, and V. M. Fernando, "Damage model for cyclic loading of concrete," *Journal of Engineering Mechanics*, vol. 116, no. 5, pp. 1020–1035, 1990.
- [16] D. Krajcinovic and M. A. G. Silva, "Statistical aspects of the continuous damage theory," *International Journal of Solids and Structures*, vol. 18, no. 7, pp. 551–562, 1982.
- [17] C. Mazzotti and M. Savoia, "Nonlinear creep damage model for concrete under uniaxial compression," *Journal of Engineering Mechanics*, vol. 129, no. 9, pp. 1065–1075, 2003.

- [18] K. E. Loland, "Continuous damage model for load-response estimation of concrete," *Cement and Concrete Research*, vol. 10, no. 3, pp. 395–402, 1980.
- [19] D. Krajcinovic, "Constitutive equations for damaging materials," *Journal of Applied Mechanics*, vol. 50, no. 2, pp. 355–360, 1983.
- [20] J. Mazars and J. Lemaitre, *Application of Continuous Damage Mechanics to Strain and Fracture Behavior of Concrete*, pp. 375–378, Springer, Evanston, IL, USA, 1984.
- [21] M. H. Liu and Y. F. Wang, "Damage constitutive model of ash concrete under freeze-thaw cycles," *Journal of Materials in Civil Engineering*, vol. 24, no. 9, pp. 1165–1174, 2012.
- [22] H. Zhao, C. J. Shi, M. H. Zhao, and X. B. Li, "Statistical damage constitutive model for rocks considering residual strength," *International Journal of Geomechanics*, vol. 17, no. 1, p. 04016033, 2017.
- [23] T. Yu, "Statistical damage constitutive model of quasi-brittle materials," *Journal of Aerospace Engineering*, vol. 22, no. 1, pp. 95–100, 2009.
- [24] F. Leng and G. Wu, "A thermodynamics-based damage constitutive model of concrete," *European Journal of Environmental and Civil Engineering*, vol. 17, no. 1, pp. s83–s102, 2013.
- [25] Z. L. Wang, Y. S. Liu, and R. F. Shen, "Stress–strain relationship of steel fiber-reinforced concrete under dynamic compression," *Construction and Building Materials*, vol. 22, no. 5, pp. 811–819, 2008.
- [26] R. Hameed, A. Sellier, A. Turatsinze, and F. Duprat, "Damage model for concrete reinforced with sliding metallic fibers," *International Journal of Mechanics and Materials in Design*, vol. 7, no. 1, pp. 83–97, 2011.
- [27] Y. L. Xue, S. L. Li, F. Lin, and H. B. Xu, "Study of damage constitutive model of SFRC considering effect of damage threshold," *Rock and Soil Mechanics*, vol. 30, no. 7, pp. 1987–1992, 2009, in Chinese.
- [28] J. J. Zhou, J. L. Pan, and C. K. Y. Leung, "Mechanical behavior of fiber-reinforced Engineering Cementitious Composites in uniaxial compression," *Journal of Materials in Civil Engineering*, vol. 27, no. 1, p. 04014111, 2015.
- [29] J. Lemaitre, "How to use damage mechanics," *Nuclear Engineering and Design*, vol. 80, no. 2, pp. 233–245, 1984.

Research Article

Protective and Blast Resistant Design of Posttensioned Box Girders Using Computational Geometry

Majid Aleyaasin 

School of Engineering, University of Aberdeen, Fraser Noble Building, Aberdeen AB24 3UE, UK

Correspondence should be addressed to Majid Aleyaasin; eng780@abdn.ac.uk

Received 16 August 2017; Revised 21 November 2017; Accepted 6 December 2017; Published 22 February 2018

Academic Editor: Lucia Figuli

Copyright © 2018 Majid Aleyaasin. This is an open access article distributed under the Creative Commons Attribution License, which permits unrestricted use, distribution, and reproduction in any medium, provided the original work is properly cited.

The optimal tendon profile and its associated duct geometry for posttensioned box girders are investigated. A computational algorithm has been developed to determine an ideal shape for the tendon and duct. The algorithm is based on a diagonal cross point in the Magnel quadrilateral and uses computational geometry instead of graphical drawing. Thereafter, an ideal parabolic and linear tendon profiles can be calculated from which the covering duct could be shaped. To check the optimality of the results, an automatic examination of Magnel diagrams in various cross sections is incorporated in the algorithm. This enables a unique prestress level to be selected that suits all sections. Then, the midcentricity of the two crossing points with a common prestress line is chosen as a design eccentricity in each cross section. The optimal duct shape is determined based on such automatic inspections. In a numerical example, the linear, parabolic, and optimal duct geometries are compared and drawn. It is concluded that both linear and parabolic duct shapes can be very close to an optimal shape. In a numerical example, an optimal, box girder with linear open access-type tendons is designed that can withstand extra blast load when explosion occurs.

1. Introduction

Steel is used in concrete bridges as a reinforcement material. Therefore, the protection against corrosion for increasing lifetime of the bridge is an important issue and remains an active field of research [1]. Advanced methods for protection needs accessibility inside the box girder as described in [2]. A suitable open access type to the prestressed tendons is open linear duct type as shown in Figure 1 [3]. In this scheme, tendons are accessible easily and can be monitored continuously.

It is obvious that the accessibility to the steel tendon as shown in Figure 1 is superior to other types of design. This will be useful particularly when inspection for corrosion and crack protection is required. The corrosion protection in precast bridges is a formidable task as explained in [4]. Therefore, open access posttensioned segments similar to Figure 1 are corrosion and also crack protective.

Recently, protection of the bridges against explosions due to, for example, car bombs is studied seriously, and one of the damages is shown in Figure 2. The permanent deformation is caused by immediate microcracks just after explosion [5]. The

author believes that the open access design shown in Figure 1 can also be blast protective because it can be optimised to take the extra blast load as it is shown in a numerical example in this paper. Moreover, the possible cracks after explosions can be inspected much easier.

Regarding the extra blast load, the bomb power or explosive amount (equivalent TNT mass) and also the distance between the explosion centre and the bridge are required. Then, we need to find the scaled distance from the following equation:

$$Z = \frac{R}{M_{\text{TNT}}^{1/3}}. \quad (1)$$

Then, the resulting overpressure (in kPa) due to the explosion [6] is

$$p = 912.88Z^{-1.46635}. \quad (2)$$

Then, the extra blast load is $W_{\text{ex}} = pb$ (b is the width of the bridge).

This paper provides a new method that is suitable for the optimal design of an accessible linear-type, posttensioned

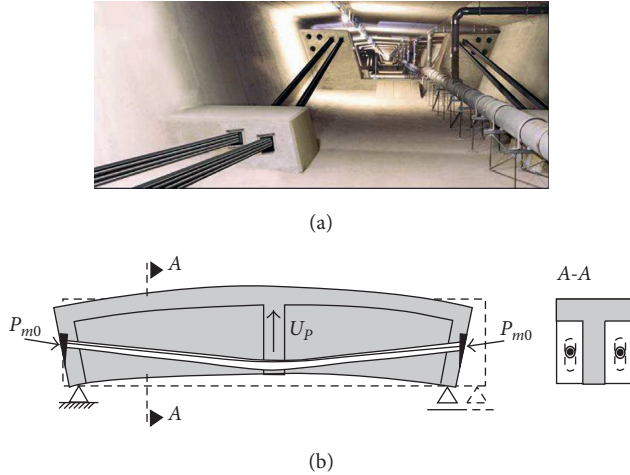


FIGURE 1: (a) Externally posttensioned: inside of box girder cross section. (b) Externally posttensioned beam: girder outside web.

tendon and its duct. The method is based on the traditional Magnel diagram [7], but its novelty is the combination with computational geometry, by which an algebraic computerised algorithm can be developed.

There are two types of prestressed concrete members. In pretensioned type, the strands are pretensioned before casting, and then it is essential that the prestress level in various cross sections should be different. In order to achieve this objective, debonding technology is adopted by which some strands are partially debonded from concrete [7]. This article is not related to pretensioned beams since the majority of box girders are built via posttensioned members.

However, in posttensioned beams and members, the prestress level in all cross sections is similar. The tensioning is planned after casting; therefore, the tendons are not straight and can be covered in a curved duct [8]. There are various methods for determination of the ideal tendon and duct profile; for example, the criteria in [8] are different from the one in [9]. In order to obtain an accurate profile, “design curves” are introduced in [10] by which in any cross section the suitable eccentricity is determined by the design curve and finally the profile could be built.

Since an ideal tendon profile determination is a design problem, it should be noted that the designers have been using a graphical design method which was developed by Magnel [11] in late forties. Since then, the Magnel design diagram has been revisited in [12], and the edges of the Magnel quadrilateral are specified as criteria for choosing an appropriate eccentricity and prestress level. Recently, Calladine [13] has used the mapping technique and converted the Magnel quadrilateral to a parallelogram by which the design procedure becomes easier. Moreover, Stanton [14] introduced a simple sign convention in order to draw the Magnel diagram by one equation only.

In this article, it is shown that the ideal tendon profile in the posttensioned beam could be determined by automated computer inspection of the Magnel diagrams, in the various cross sections without drawing any quadrilateral on paper. By using computational geometry, first the coordinates of the edges of the Magnel quadrilateral is calculated. Then, the



FIGURE 2: Permanent deformation of box girder after explosion.

coordinates of the crossing points of the two diagonals of the quadrilateral in the cross section in which maximum service bending moment occurs is determined. Similar procedure is repeated for two more cross sections, and thereby a parabolic or linear curve could be computed, knowing three eccentricities across the beam span. Further investigation is carried out to show the accuracy of this type of design.

In a numerical example for a long span box girder bridge, by examining the Magnel quadrilateral in many more cross sections and considering a prestress level that suits all the cross sections, the corresponding eccentricities are computed and a smooth curve is fitted to all the points. When comparing this optimal duct shape with the parabolic and linear ones, it does not show any significant difference.

The whole drawing process and inspection and selection are algorithmic and can be done via one computer program. It is shown that we can determine the ideal parabolic and linear duct shapes and also check their closeness to optimal duct shape, all in one algorithm. It is concluded that both parabolic and linear duct geometries introduced in this paper are simple and optimal. Therefore, we can choose an accessible and easily protectable linear tendons and duct shape which is also an optimal design. The method is based on automatic inspection of the Magnel diagram and particularly can be useful for checking the Magnel polygon in the cross section where the deviator is located and sharp changes (discontinuities) in prestress occur.

2. Magnel Design Diagram

The top fibres of a beam in transfer (before service) are in tension since the beam planned to be in hogging, and if the allowable tensile transfer stress is $f_{tt} \leq 0$, then the stress constraint would be

$$\sigma = \frac{M_T}{Z_T} + \frac{P}{A} + \frac{Pe}{Z_T} \geq f_{tt}. \quad (3)$$

In (3), $\sigma > f_{tt}$ while $|\sigma| < |f_{tt}|$ because in the transfer state, the top fibres are in tension ($-$ sign by convention) and then $f_{tt} \leq 0$ also $Z_t > 0$, $P > 0$, $M_t > 0$, and $e < 0$. Manipulating (3) leads to the following inequality:

$$\frac{1}{P} \geq \frac{e}{f_{tt}Z_t - M_t} + \frac{Z_t}{AZ_t f_{tt} - AM_t}. \quad (4)$$

The bottom fibres of a beam in transfer, when it is in hogging, are in compression, and if the allowable

compressive transfer stress is $f_{tc} \geq 0$, then the stress constraint would be

$$\sigma = \frac{M_t}{Z_b} + \frac{P}{A} + \frac{Pe}{Z_b} \leq f_{tc}. \quad (5)$$

In (5), $\sigma < f_{tc}$ while $|\sigma| < |f_{tc}|$ because in the transfer state, bottom fibres are in compression (+ sign by convention) and then $f_{tc} > 0$ also $Z_b < 0$, $P > 0$, $M_t > 0$, and $e < 0$. Manipulating (5) leads to the following inequality:

$$\frac{1}{P} \geq \frac{e}{f_{tc}Z_b - M_t} + \frac{Z_t}{AZ_b f_{tc} - AM_t}. \quad (6)$$

The top fibres of a beam in service obviously are in compression because the beam is in sagging, and if the allowable compressive service stress is $f_{sc} \geq 0$, then the stress constraint would be

$$\sigma = \frac{M_s}{Z_t} + \frac{\alpha P}{A} + \frac{\alpha Pe}{Z_t} \leq f_{sc}. \quad (7)$$

In (7), $\sigma < f_{sc}$ while $|\sigma| < |f_{sc}|$ because in the service state, top fibres are in compression (+ sign by convention); so $f_{sc} > 0$ also $Z_t > 0$, $P > 0$, $M_s > 0$, and $e < 0$. Parameter $0 \leq \alpha \leq 1$ represents the minimum conserved prestress factor in service since during service prestress level would be lost [8] and $(1 - \alpha)$ expresses this maximum loss. Now, by manipulating (7), the following inequality would be obtained:

$$\frac{1}{P} \geq \frac{\alpha e}{f_{sc}Z_t - M_s} + \frac{\alpha Z_t}{AZ_t f_{sc} - AM_s}. \quad (8)$$

The bottom fibres of a beam in service (sagging) are in tension, and if the allowable tensile service stress is $f_{st} \leq 0$, then the stress constraint would be

$$\sigma = \frac{M_s}{Z_b} + \frac{\alpha P}{A} + \frac{\alpha Pe}{Z_b} \leq f_{st}. \quad (9)$$

In (9), $0 \leq \alpha \leq 1$ appears again because of service condition. $\sigma > f_{st}$ while $|\sigma| < |f_{st}|$ because in the service state, bottom fibres are in tension (- sign by convention), so $f_{st} \leq 0$ also $Z_b < 0$, $P > 0$, $M_s > 0$, and $e < 0$. By manipulating (9), the following inequality would be obtained:

$$\frac{1}{P} \leq \frac{\alpha e}{f_{st}Z_b - M_s} + \frac{\alpha Z_b}{AZ_b f_{st} - AM_s}. \quad (10)$$

The four stress constraints (3), (5), (7), and (9) lead to the inequalities (4), (6), (8), and (10) in a coordinate system in which e is the horizontal axis and (P^{-1}) is the vertical axis. The borders of these four inequalities are designated by four lines, and when they cross each other, they form a quadrilateral in which the design parameters e and (P^{-1}) are chosen from inside of this quadrilateral. Overall design diagram was first introduced by Magnel [11] and has been used by designers ever since [7, 8]. Obviously, in various types of prestress losses and for this reason for design purposes, the minimum conservation (maximum loss) should be considered.

In Section 3, we will show that, by symbolic computation of the four edges in the Magnel quadrilateral, we can seek inside the region to find an appropriate design point for each cross section. First, parabolic and linear tendon profiles will be derived by using three cross sections. Thereafter, an algorithm for an ideal tendon profile will be explained by using several cross sections. In a numerical example, it will be shown that parabolic and linear profiles are very close to the ideal profile.

3. New Algorithm for Computation of Tendon Profile

The borderlines of the constraints for f_{tt} in (4) and f_{tc} in (6) cross each other in the edge designated by coordinates $(e)_{tt-tc}$ and $(P^{-1})_{tt-tc}$ as follows:

$$(e)_{tt-tc} = \frac{(Z_t f_{tt} - M_t)Z_b - (Z_b f_{tc} - M_t)Z_t}{(Z_b f_{tc} - M_t)A - (Z_t f_{tt} - M_t)A}, \quad (11)$$

$$(P^{-1})_{tt-tc} = \frac{(e)_{tt-tc}A - Z_t}{(Z_t f_{tt} - M_t)A}.$$

The borderlines of the constraints for f_{st} in (10) and f_{sc} in (8) cross each other in the edge designated by coordinates $(e)_{st-sc}$ and $(P^{-1})_{st-sc}$ as follows:

$$(e)_{st-sc} = \frac{(Z_b f_{st} - M_s)Z_t - (Z_t f_{sc} - M_s)Z_b}{(Z_t f_{sc} - M_s)A - (Z_b f_{st} - M_s)A}, \quad (12)$$

$$(P^{-1})_{st-sc} = \frac{((e)_{st-sc}A + Z_b)\alpha}{(Z_b f_{st} - M_s)A}.$$

The borderlines of the constraints for f_{st} in (10) and f_{tt} in (4) cross each other in the edge designated by coordinates $(e)_{st-tt}$ and $(P^{-1})_{st-tt}$ as follows:

$$(e)_{st-tt} = \frac{(Z_b f_{st} - M_s)Z_t - (Z_t f_{tt} - M_t)\alpha Z_b}{(Z_t f_{tt} - M_t)\alpha A - (Z_b f_{st} - M_s)A}, \quad (13)$$

$$(P^{-1})_{st-tt} = \frac{(e)_{st-tt}A - Z_t}{(Z_t f_{tt} - M_t)A}.$$

The borderlines of the constraints for f_{sc} in (8) and f_{tc} in (6) cross each other in the edge designated by coordinates $(e)_{sc-tc}$ and $(P^{-1})_{sc-tc}$ as follows:

$$(e)_{sc-tc} = \frac{(Z_t f_{sc} - M_s)Z_b - (Z_b f_{tc} - M_t)\alpha Z_t}{(Z_b f_{tc} - M_t)\alpha A - (Z_t f_{sc} - M_s)A}, \quad (14)$$

$$(P^{-1})_{sc-tc} = \frac{(e)_{sc-tc}A + Z_t}{(Z_b f_{tc} - M_t)A}.$$

The edge with the coordinates $(e)_{st-tt}$ and $(P^{-1})_{st-tt}$ is opposite to the edge with the coordinates $(e)_{sc-tc}$ and $(P^{-1})_{sc-tc}$. Connecting these two edges provides a diagonal with the following slope:

$$(m)_{sc-tc}^{st-tt} = \frac{(P^{-1})_{st-tt} - (P^{-1})_{sc-tc}}{(e)_{st-tt} - (e)_{sc-tc}}, \quad (15)$$

and the corresponding line can be expressed by the following equation:

$$(P^{-1}) - (P^{-1})_{st-tt} = ((e) - (e)_{st-tt})(m)_{sc-tc}^{st-tt}. \quad (16)$$

The edge with the coordinates $(e)_{tt-tc}$ and $(P^{-1})_{tt-tc}$ is opposite to the edge with the coordinates $(e)_{st-sc}$ and $(P^{-1})_{st-sc}$. Connecting these two edges provides a diagonal with the following slope:

$$(m)_{st-sc}^{tt-tc} = \frac{(P^{-1})_{tt-tc} - (P^{-1})_{st-sc}}{(e)_{tt-tc} - (e)_{st-sc}}, \quad (17)$$

and corresponding line can be expressed by the following equation:

$$(P^{-1}) - (P^{-1})_{tt-tc} = ((e) - (e)_{tt-tc})(m)_{st-sc}^{tt-tc}. \quad (18)$$

Intersection of the lines (16) and (18) represents the centre of the quadrilateral which possesses the eccentricity e_{DM} and can be calculated by

$$e_{DM} = \frac{(P^{-1})_{tt-tc} - (P^{-1})_{st-tt} + (m)_{st-tt}^{st-tt} (e)_{st-tt} - (m)_{st-sc}^{tt-tc} (e)_{tt-tc}}{(m)_{st-tt}^{st-tt} - (m)_{st-sc}^{tt-tc}}. \quad (19)$$

Similarly, we can calculate e_{DM} in two other cross sections to obtain parabolic and linear curves. For example, in a simply supported beam with span L , the maximum bending moment occurs in middle span $0.5L$, the other two cross sections could be at the supporting ends, and their corresponding eccentricity e_{DC} can be calculated from (19) by substituting $M_t = 0$ and $M_s = 0$, that is,

$$e_{DC} = e_{DM} \Big|_{M_s=M_t=0}. \quad (20)$$

Since at $x = 0.5L$, the eccentricity is $e(0.5L) = e_{DM}$ and in the supports $e(L) = e(0) = e_{DC}$, and then an ideal parabolic tendon profile could be computed by

$$e(x) = 4(e_{DM} - e_{DC}) \left(\frac{x}{L} - \frac{x^2}{L^2} \right) + e_{DC}. \quad (21)$$

And for linear tendon profile similar to Figure 1, we have

$$e(x) = 2(e_{DM} - e_{DC}) \frac{x}{L} + e_{DC}, \quad 0 \leq x \leq \frac{L}{2}, \quad (22)$$

$$e(x) = 2(e_{DM} - e_{DC}) \left(1 - \frac{x}{L} \right) + e_{DC}, \quad \frac{L}{2} \leq x \leq L. \quad (23)$$

Another ideal tendon profile can also be achieved, if the Magnel diagram would be drawn in many cross sections ($n \gg 3$), across the span. This is a formidable task for a designer, but can be programmed easily by a computer. Then, for every Magnel quadrilateral, we have a pair of diagonals with equations

$$(P^{-1}) - (P^{-1})_{st-tt} = ((e) - (e_i)_{st-tt})(m_i)_{sc-tc}^{st-tt}, \quad i = 1, 2, \dots, n, \quad (24)$$

$$(P^{-1}) - (P^{-1})_{tt-tc} = ((e) - (e_i)_{tt-tc})(m_i)_{st-sc}^{tt-tc}, \quad i = 1, 2, \dots, n. \quad (25)$$

By simple visual inspection of all diagrams in one figure, it is very easy to check which prestress level suits all the quadrilaterals in the figure. This inspection is also possible without any drawing and can be done by intelligent computer searching. When a design prestress level was selected and named $(P^{-1})_D$, by its substitution into (24) and (25), two candidates for the eccentricity in each cross section can be found via the following formulas:

$$(e_i)_{C1} = \frac{(P^{-1})_D - (P^{-1})_{st-tt}}{(m_i)_{sc-tc}^{st-tt}} + (e_i)_{st-tt}, \quad i = 1, 2, \dots, n, \quad (26)$$

$$(e_i)_{C2} = \frac{(P^{-1})_D - (P^{-1})_{tt-tc}}{(m_i)_{st-sc}^{tt-tc}} + (e_i)_{tt-tc}, \quad i = 1, 2, \dots, n. \quad (27)$$

To be on the conservative side, the average of the above could be considered as the design eccentricity for each cross section, that is,

$$(e_i)_D = 0.5((e_i)_{C1} + (e_i)_{C2}), \quad i = 1, 2, \dots, n. \quad (28)$$

4. Numerical Example

The numerical example is taken from [12]. The prestressed beam, simply supported at the ends with the cross section $A = 0.3045 \text{ m}^2$, has the span $L = 18.3 \text{ m}$, the width $b = 1.22 \text{ m}$, the height $h = 0.61 \text{ m}$, and the section modulus $Z_t = 0.0352 \text{ m}^3$ and $Z_b = -0.03869 \text{ m}^3$; the limit stresses are $f_{tt} = -1.34 \text{ MPa}$, $f_{tc} = 17.38 \text{ MPa}$, $f_{sc} = 18.6 \text{ MPa}$, and $f_{st} = -3.21 \text{ MPa}$; the dead weight is $W_t = 8.76 \text{ kN/m}$; and 500 kg of TNT exploded 200 m away from the bridge while traffic load $W_{tr} = 5.5 \text{ kN/m}$ in service condition should be considered. The prestress loss is expressed by the parameter $\alpha = 0.8$. We need to find the optimal duct shape and the eccentricities as shown in Figure 1 and displayed in [3].

The scaled distance of this explosion will be considered as a part of service load:

$$Z = \frac{R}{M_{TNT}^{1/3}} = \frac{200}{500^{1/3}} = 25.1984 \text{ m/kg}^{1/3}. \quad (29)$$

The resulting overpressure (in kPa) due to the explosion is

$$p = 912.88Z^{-1.46635} = 912.88 \times 25.1984^{-1.46635} = 8.045 \text{ kPa}. \quad (30)$$

This produces overpressure load as a result of explosion:

$$W_{ex} = pb = 8.045 \times 1.22 = 9.815 \text{ kN/m}, \quad (31)$$

$$W_a = W_{ex} + W_{tr} = (9.815 + 5.5) = 15.32 \text{ kN/m}.$$

The maximum transfer bending moment occurring at a midspan is

$$M_t = \frac{W_t L^2}{8} = \frac{8.76 \times 18.3^2}{8} = 366.1 \text{ kN} \cdot \text{m}. \quad (32)$$

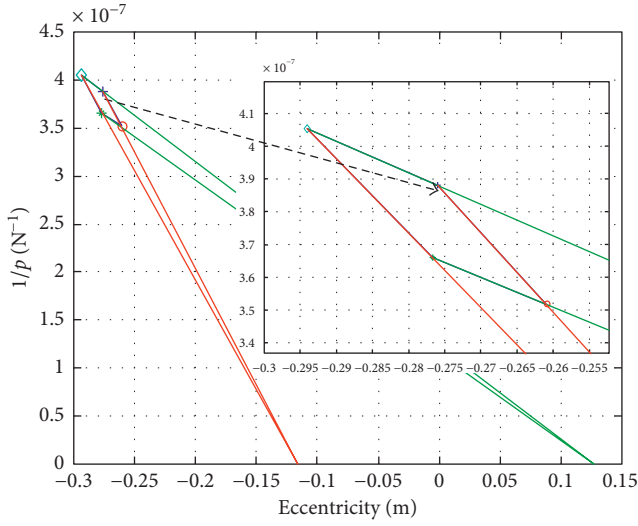


FIGURE 3: Magnel design diagram in the midspan cross section.

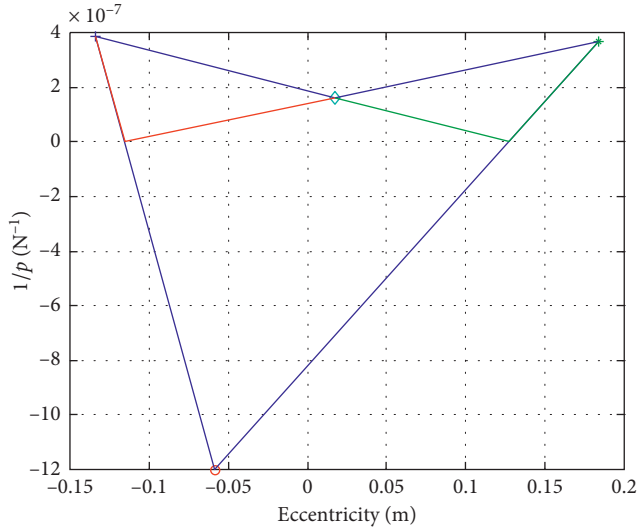


FIGURE 4: Magnel design diagram in the supporting ends.

The maximum transfer bending moment occurring at a midspan is

$$M_t = \frac{(W_t + W_a)L^2}{8} = \frac{(8.76 + 15.32) \times 18.3^2}{8} \quad (33)$$

$$= 1006.8 \text{ kN} \cdot \text{m}.$$

The Magnel diagram in the maximum bending moment cross section is drawn in Figure 3; the quadrilateral occupies a small region in the coordinate system, and for the designer, it is difficult to spot the centre, and the quadrilateral has been magnified in the figure.

In Figure 4, the design diagram is drawn at the ends, in which both the transfer moment $M_t = 0$ and service moment $M_s = 0$, we can see that the relevant quadrilateral occupies much larger region in the coordinate system plane. Although the quadrilateral loses its convexity, the centre of it is still

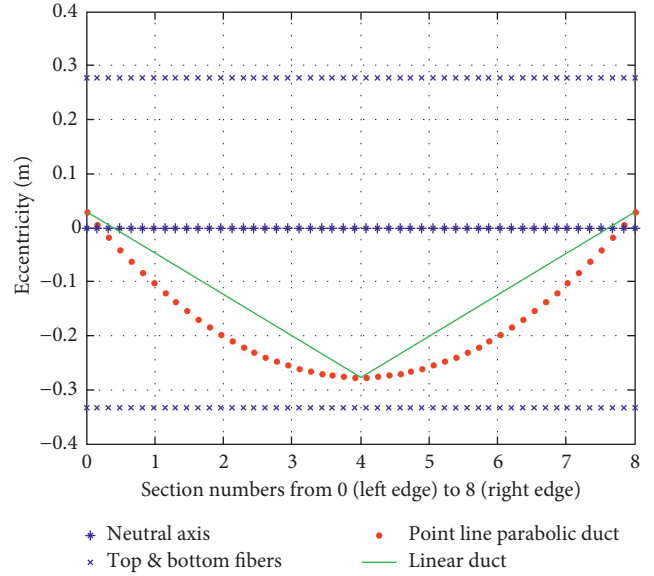


FIGURE 5: Position of the tendon, neutral axis, and top and bottom fibres across the span.

an appropriate design point. One can see that the design point will be outside the quadrilateral, but its eccentricity coordinate is in the acceptable range. The designer finally will choose a prestress level which suits all cross sections.

Based on (19) and (20), parabolic and linear tendons are designed, and the position of the strand, relative to the neutral axis in each cross section, is shown in Figure 5. The neutral axis represents zero eccentricity and is shown by dash * line; sign × represents top and bottom fibres. The linear strand position is shown by the solid line, and the point line shows the parabolic strand.

In order to see if these types of tendon profiles are accurate enough, we will draw the Magnel diagram in nine cross sections each with $L/8$ apart. Because of symmetry, we need only five Magnel diagrams, which all are drawn in Figure 6. Although we have plotted each diagram in separate figure, it is difficult to compare all quadrilaterals. However, it is easy to find out that a prestress level equal to the average of prestresses at edges of the quadrilateral of the midspan is an appropriate criterion. The horizontal line corresponding to this prestress level intersects all Magnel quadrilaterals.

This enabled (26)–(28) to be used, and in each cross section, $(e_i)_D$ could be computed. Using $(e_i)_D$, which resulted in nine points, by which a symmetric curve is produced and the tendon profile is displayed in Figure 7 by the point line, one can see that the simple linear profile in Figures 1(a) and 5 and the optimal profile in Figure 7 are very close, and in fact the parabolic and linear shape tendons can be ideal ones, if we use the expressions in (21)–(23) in this paper.

5. Conclusions

In this article, the ideal tendon profile in the posttensioned beams is investigated by multiple automatic examinations of the Magnel design diagrams. An algorithm was introduced by which one can calculate ideal parabolic and linear tendon

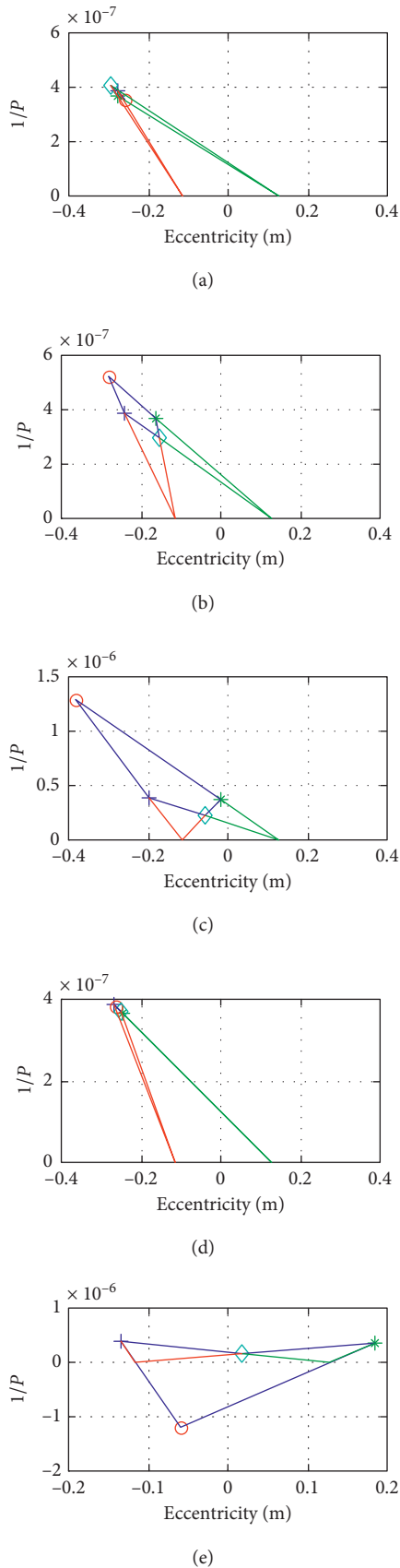


FIGURE 6: Magnel diagrams for the cross sections: (a) ($L/2$), (b) ($L/4, 3L/4$), (c) ($L/8, 7L/8$), (d) ($3L/8, 5L/8$), and (e) (ends 0, L).

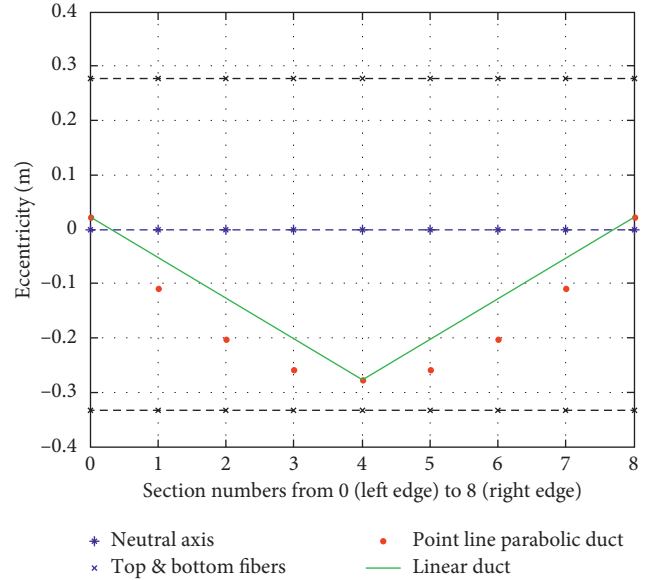


FIGURE 7: Ideal tendon profile based on the Magnel diagram of 9 cross sections each $L/8$ apart.

profiles. It is shown that ideal parabolic and linear shape tendons and ducts, calculated by the formulas in this paper, are very close to the ideal and optimal tendon profile. It is recommended that both linear and parabolic ducts can be used by designers because they do not have any disadvantage. Moreover, the design is based on simple formulas without engaging with graphical work. It can also be implemented in design of continuous girders, assuming that the moments in intermediate pier supports are found by static calculations. Moreover, the blast load as a result of car bomb and so on can be considered and added to the service load. In this case, the relevant eccentricity and prestress level can be found as shown in the numerical example. This avoids the permanent deformation (Figure 2) as a result of explosion near the bridge.

As far as that author is aware, there is not any design method which is particularly suitable for design of accessible linear-type tendons and ducts in posttensioned beams. Instead, designers use traditional methods and increase the factor of safety to compensate lack of accuracy in modelling. Therefore, the method in this paper can be used for future design applications in which bridge design should be optimised to take an extra blast load as a result of explosion due to car bomb and so on. Moreover, in future by installing sensors in the open access box girder, compression conservation can be monitored and the validity of formulas in this paper can also be checked.

Symbols

- A : Area of beam cross section
- $0 \leq \alpha \leq 1$: Prestress conservation in service
- e : Eccentricity
- e_{DM} : Design eccentricity in midspan
- e_{DC} : Design eccentricity in supporting ends
- $f_{tt} \leq 0$: Allowable transfer tensile stress

$f_{tc} \geq 0$:	Allowable transfer compressive stress
$f_{st} \leq 0$:	Allowable service tensile stress
$f_{sc} \geq 0$:	Allowable service compressive stress
i :	i th beam cross section
L :	Beam length
M_t :	Transfer bending moment
M_s :	Service bending moment
m :	Slope of the quadrilateral diagonals
n :	Total number of beam cross sections
$P \geq 0$:	Prestress compressive force
W_t :	Load distribution in transfer
W_s :	Load distribution in service
x :	Location of the cross section
$Z_t \geq 0$:	Section modulus, top fibre
$Z_b \leq 0$:	Section modulus, bottom fibre.

Conflicts of Interest

The author declares that there are no conflicts of interest.

References

- [1] D. Darwin, M. O'Reilly, J. Browning et al., "Multiple corrosion-protection systems for reinforced-concrete bridge components: laboratory tests," *Journal of Materials in Civil Engineering*, vol. 26, no. 11, Article ID 04014085, 2014.
- [2] P. Wagner, "Advanced methods for the inside protection against corrosion and the accessibility of bridges with advanced box-girder design," *Stahlbau*, vol. 85, no. 2, pp. 86–111, 2016.
- [3] H. Weiher and K. Zilch, "Usage of HD-PE in bridge construction—a corrosion protection system for steel tendons under extreme loading," in *Proceedings of the Conference on Plastic Pipes XIII*, Washington, DC, USA, October 2006.
- [4] Pipes XIII, Washington, DC, USA, October 2006. "prestressing tendons in precast segmental bridges," *PCI Journal*, vol. 47, no. 5, pp. 76–91, 2002.
- [5] Z. Hu, Y. Zhang, Z. Zeng, and L. Z. Sun, "Blast responses of bridge girders with consideration of isolation effect induced by car bomb," *Journal of Engineering Material and Technology*, vol. 139, no. 2, p. 021003, 2017.
- [6] G. F. Kinney and K. J. Graham, *Explosive Shocks in Air*, Springer, New York, NY, USA, 1985.
- [7] N. Krishna Raju, *Prestressed Concrete*, McGraw-Hill, New Delhi, India, 4th edition, 2006.
- [8] R. I. Gilbert and N. C. Mickleborough, *Design of Prestressed Concrete*, Spon Press, London, UK, 1990.
- [9] F. K. Kong and R. H. Evans, *Reinforced and Prestressed Concrete*, Chapman & Hall, London, UK, 3rd edition, 1994.
- [10] M. R. Ehsani and J. R. Blewitt, "Design curves for tendon profile in prestressed concrete beams," *PCI Journal*, vol. 31, no. 3, pp. 115–135, 1986.
- [11] G. Magnel, *Prestressed Concrete*, Concrete Publication, London, UK, 1948.
- [12] N. Krishnamurthy, "Magnel diagrams for prestressed concrete beams," *Journal of Structural Engineering*, vol. 109, no. 12, pp. 2761–2769, 1983.
- [13] C. R. Calladine, "An improvement on Magnel's diagram and an application," *Proceedings of the Institution of Civil Engineers, Structures and Buildings*, vol. 159, no. 3, pp. 145–152, 2006.
- [14] J. F. Stanton, "A simple sign convention for elastic analysis of prestressed concrete members," *PCI Journal*, vol. 52, no. 6, pp. 81–88, 2007.

Research Article

Strengthening of RCC Beams in Shear by Using SBR Polymer-Modified Ferrocement Jacketing Technique

Rajinder Ghai , Prem Pal Bansal, and Maneek Kumar 

Department of Civil Engineering, Thapar University, Patiala, Punjab 147004, India

Correspondence should be addressed to Rajinder Ghai; ghairajinder@gmail.com

Received 24 August 2017; Accepted 21 November 2017; Published 13 February 2018

Academic Editor: Lucia Figuli

Copyright © 2018 Rajinder Ghai et al. This is an open access article distributed under the Creative Commons Attribution License, which permits unrestricted use, distribution, and reproduction in any medium, provided the original work is properly cited.

There is a common phenomenon of shear failure in RCC beams, especially in old buildings and bridges. Any possible strengthening of such beams is needed to be explored that could strengthen and make them fit for serviceable conditions. The present research has been made to determine the performance of predamaged beams strengthened with three-layered wire mesh polymer-modified ferrocement (PMF) with 15% styrene-butadiene-rubber latex (SBR) polymer. Forty-eight shear-designed and shear-deficient real-size beams were used in this experimental work. Ultimate shear load-carrying capacity of control beams was found at two different shear-span (a/d) ratios 1 and 3. The sets of remaining beams were loaded with different predetermined damage levels of 45%, 75%, and 95% of the ultimate load values and then strengthened with 20 mm thick PMF. The strengthened beams were then again tested for ultimate load-carrying capacity by conducting the shear load test at $a/d = 1$ and 3. As a result, the PMF-strengthened beams showed restoration and enhancement of ultimate shear load-carrying capacity by 5.90% to 12.03%. The ductility of strengthened beams was improved, and hence, the corresponding deflections were prolonged. On the other hand, the cracking pattern of PMF-strengthened beams was also improved remarkably.

1. Introduction

With the passage of time, many of the existing RCC structures deteriorate due to increases in service loads, corrosion of reinforcement, and poor ductile detailing, which results in loss of strength, cracking, and spalling of the structural components. Such structural elements need special attention and must be retrofitted using suitable strengthening techniques to restore strength and the design life. Many researchers have worked on the development of various materials and techniques for repairing, retrofitting, and strengthening of such structural elements. The selection of a particular strengthening material and technique depends on the type, cause, and nature of distress to be addressed.

All RCC elements are designed to fail in a ductile manner by making suitable detailing of reinforcement. During an earthquake, a sudden catastrophic failure can occur due to increased shear loads [1]. In reinforced concrete beams, the shear deficiencies pop up due to many reasons such as insufficient shear reinforcement, reduction in the steel area,

increasing service loads, poor workmanship, and design faults. Shear strength of many existing structures might be deficient for present needs and requires strengthening to sustain and to satisfy current codal requirements. The engineers have experienced that shear failure of RCC beams, especially in older or heritage structures, buildings, and bridges, is a serious problem which necessitates dismantling and replacement of the structures. Hence, there is a need of developing an economical strengthening solution, which helps to restore the desired shear strength of beams.

In the recent years, the usage of different advanced materials such as ferrocement, glass fibre-reinforced polymer (GFRP), fibre-reinforced polymer (FRP), carbon fibre-reinforced polymer (CFRP), and steel plate jacketing has increased for retrofitting and strengthening of concrete structures. These materials have excellent properties such as high strength, light weight, and corrosion resistance abilities. Some researchers have explored the effect of various advanced composite bonding materials as

well as their orientation on the flexure and shear strength properties of retrofitted beams [2–15]. Many of these materials showed some flaws or shortcomings in terms of strength, cost, availability, and applicability. Hence, out of these available material options, the ferrocement has gained popularity and becomes the major structural material for strengthening and retrofitting as well for construction, especially in earthquake-prone areas because of its excellent ductility, toughness, availability, and other properties. Researchers have come to the conclusion that ferrocement is quite compatible with the existing concrete structures; apart from this, it is easy to apply [16–23].

Conventional ferrocement made with cement mortar matrix showed some deficiencies and got cracks under loads even much smaller than the ultimate loads, leading to reduced life [24–27]. The corrosion of wire mesh is also one of the primary reasons for the deterioration of ferrocement which is attributed to the permeability of cement mortar [28, 29]. To overcome these deficiencies of conventional ferrocement; it is necessary to enhance the properties of its mortar matrix with different types of additives. The addition of polymers to the conventional mortar is found to be very effective [30–39]. It further imparts some outstanding properties like resistance to corrosion, higher strength-to-weight ratio, better ductility, and tensile strength as compared to conventional ferrocement [40–44]. There are various types of polymers available worldwide, but the studies have shown that the addition of styrene-butadiene-rubber latex (SBR) polymer is very efficient in improving the properties of conventional mortar and ferrocement [45–49]. Polymer-modified ferrocement is gaining popularity in developing countries because of its excellent properties and as an economical repair alternative to the expensive process of reconstruction. Details of PMF are simple to follow and easy to execute even by local skilled workers and the ingredients being readily available [50–54]. Further developments in the field of polymer-modified ferrocement (PMF) can make a drastic improvement in the area of composite rehabilitation and strengthening of existing structures.

In the past, a few experimental studies had been carried out to gauge the effect of the high-performance ferrocement strengthening technique on RCC beams. Kumar and Vidivelli [50, 51] investigated the use of acrylic latex and styrene-butadiene-rubber latex polymer-modified ferrocement to strengthen the RCC beams in flexure. Their test results showed that the strengthened beams exhibited 79% to 85% enhancement in their general performance after the usage of polymer ferrocement jacketing, having 15% of polymer and 5% volume of wire mesh. A similar study was made by Liao and Fang [52], and they found that RC beams strengthened with high-performance ferrocement showed higher ultimate load-carrying capacities and minor cracks as compared to controlled beams. Hughes and Evbuomwan [53] also used the polymer-modified ferrocement under the soffit of beams to strengthen the beams in flexure. They resulted that the ductility and ultimate flexural load-carrying capacity of beams were increased after strengthening, without any bond failure. Zhao et al. [54] used the polymer

mortar and steel wire to strengthen the beams in shear. These strengthened beams showed the delay in crack development and improvement in the ultimate load capacity by 57% as compared to controlled beams. They also concluded that polymer mortar showed good bonding properties with the concrete members.

It is concluded that the application of polymer-modified ferrocement as an outer strengthening material is a viable technology for improving the structural performance of RCC beams in flexure. At present, there is no such research work recorded to study the effects of polymer-modified ferrocement to strengthen the beams in shear. It is the need of the hour to explore the utility of PMF as a strengthening material in the specified domain of shear. Many factors impart shear strength of RCC beams like a/d ratio, spacing of stirrups, and grade of concrete. In this experimental work, two variable factors as a/d ratio and spacing of stirrups are chosen to find their effect on strength, deflection, and cracking pattern of predamaged beams strengthened with PMF. Another study done by the authors showed that the PMF modified with 15% of SBR and three layers of square woven steel wire mesh had better flexural and tensile strength properties as compared to other compositions [45]. Therefore, three-layered wire mesh polymer-modified ferrocement with an optimum percentage of 15% SBR has been used in this experimental work to strengthen the RCC beams having three different levels of predamages.

2. Materials and Methods

A preliminary study has been done to determine the properties of ingredients required for this experimental work.

2.1. Materials. Portland pozzolana cement (PPC) with a 28-day compressive strength of 34.2 N/mm^2 , specific gravity 2.9, fineness 2.1%, consistency 34%, initial setting time 98 minutes, final setting time 240 minutes, and soundness of 1 mm conforming to IS 1489-Part 1 [55] was used in the mortar and concrete. Natural sand (FA-1) was used to prepare the mortar mix for ferrocement, and riverbed sand (FA-2) was used for concrete mix, as per IS 383 [56] specifications. Two types of coarse aggregates with nominal size of 20 mm and 12.5 mm in a ratio of 60 : 40 were used to prepare the concrete mix as per IS 2386-Part 3 [57] specifications. Detail of test results of fine and coarse aggregates is given in Table 1.

The thermomechanical-treated (TMT) 12 mm diameter bars with an ultimate tensile strength of 710 N/mm^2 were used as tensile reinforcement, and 8 mm diameter TMT bars which have an ultimate tensile strength of 697.5 N/mm^2 were used as compressive reinforcement. Plain mild steel (MS) 6 mm diameter reinforcement bars with an ultimate tensile strength of 491.5 N/mm^2 were used as shear reinforcement. Galvanised square woven wire mesh of 0.49 mm diameter with centre-to-centre spacing of 8 mm and having an ultimate tensile strength of 950 N/mm^2 was

TABLE 1: Properties of fine and coarse aggregates.

Material description	Fineness modulus	Specific gravity	Water absorption (%)	Moisture content (%)	Grading zone
Fine aggregate (FA-1)	2.24	2.67	1.9	0.22	3
Fine aggregate (FA-2)	2.65	2.675	1.35	0.16	2
Coarse aggregate (CA-1) 20 mm	6.69	2.69	1.18	Nil	All-in-aggregate
Coarse aggregate (CA-2) 12.5 mm	6.11	2.685	1.11	Nil	All-in-aggregate

used in polymer-modified ferrocement as per ACI 549.1R guidelines [58]. Details of test results are given in Table 2.

Commercially available Sika® Latex Power [59] SBR-based polymer in liquid form having 45% solid contents, pH value of 8.50 at 25°, and specific gravity of 1.01 was used to modify the current mortar matrix of ferrocement. A 0.7% silicon solid by weight of the SBR polymer was used as an antifoaming agent in the PMF matrix [60]. Potable water was used for mixing and curing purposes.

2.1.1. Concrete Mix. Concrete of grade M20 with C : FA : CA in a ratio of 1 : 2.1 : 3.4 was designed as per IS 10262 [61] guidelines. The water-cement ratio of the concrete mix was 0.55 and having an ultimate compressive strength of 26.72 N/mm². The slump value of the mix was kept as 75 mm–100 mm. This concrete mix proportion was used to cast all the beam specimens. Detail of quantities required per m³ of concrete is given in Table 3.

2.1.2. Polymer-Modified Ferrocement (PMF). Polymer-modified mortar (PMM) with a cement (C) to sand (FA-1) ratio of 1 : 2 and having 15% of SBR was used to develop the polymer-modified ferrocement (PMF). The water-cement ratio of mortar was found as 0.56 for a flow value of 105 ± 5% [62]. The 28-day compressive strength, flexural strength, and Young's modulus of elasticity of PMM were 31.53 N/mm², 8.52 N/mm², and 13.15 × 10³ N/mm², respectively [45]. This polymer-modified mortar was further used to modify the three-layered square woven steel wire mesh ferrocement. The 28-day flexural and tensile strengths of polymer-modified ferrocement were 17.01 N/mm² and 6.12 N/mm², respectively [45]. This PMF is used as an encasing material in this experimental work to strengthen the predamaged RCC beams.

2.2. Experimental Program and Methods. This experimental study was conducted on 48 full-size (127 mm × 229 mm × 2700 mm) RCC beams. Out of these 48 beams, 24 were designed for shear-designed beams (DBs), and 18 stirrups of 6 mm diameter were provided at a spacing of 150 mm c/c. The rest 24 beams were designed as shear-deficient beams (SDBs), and 7 stirrups of 6 mm diameter were provided at a spacing of 450 mm c/c. All the beams were confined with 2–12 mm diameter bars on tensile face and 2–8 mm diameter bars on compression face. Beam section and reinforcement details of both types of beams are shown in Figure 1. For casting beam specimens, the reinforcement was correctly placed in the formwork with specified cover and then poured with concrete. A steel formwork was used, and IS 456 [63] specifications were

TABLE 2: Properties of reinforcement steel bars.

Diameter (mm)	Yield stress (MPa)	Ultimate stress (MPa)	Elongation (%)
12	556.5	710.0	22.0
8	548.5	679.5	18.4
6	465.0	491.5	5.0
0.49 (square woven wire mesh)	665.0	950.0	18.2

TABLE 3: Detail of concrete mix design.

Cement (C)	Fine aggregate (FA-2)	Coarse aggregate (CA-1: CA-2) (60 : 40)	Water (W)
340	714.0	1156	187

All quantities are in Kg.

strictly followed. The detail of beams along with their designation is given in Table 4.

2.2.1. Testing of Controlled Beams. After 28 days of curing, the shear-designed and shear-deficient controlled beams were tested over a loading frame fixed with a hydraulic jack. The load test on all the beams was performed for two different shear-span (a/d) ratios 1 and 3 over a simply supported effective span of 2500 mm as shown in Figure 2. A standard set of 3 beams was taken for each load test. Load-deflection curves were observed, and the ultimate shear load-carrying capacities of controlled beams (DBs and SDBs) were worked out by applying single-point load “P” at two different shear-span ratios (a/d) = 1.0 and 3.0, respectively, where “ a ” denotes the shear span of the beam and “ d = 198 mm” denotes the effective depth of the beam. For a/d = 1.0, the value of “ a = 198 mm” was kept, and for a/d = 3.0, the value of “ a = 594 mm” was kept. These control beams were tested up to an ultimate failure to work out their average elastic, elastoplastic, and plastic load values corresponding to 45%, 75%, and 95% of ultimate load values, respectively. Details of test results are given in Table 5. Deflection of these beams was also determined and recorded by using LVDTs (linear variable displacement transducers) with a least count 0.001 mm. The LVDTs were placed under the soffit of beams which were further attached electronically with the computerised system. The location of these LVDTs was fixed according to the load position; that is, the 1st LVDT was placed under the loading point “P,” the 2nd was under the midpoint of the beam, and the 3rd was exactly at the same distance from opposite support just mirrored to the

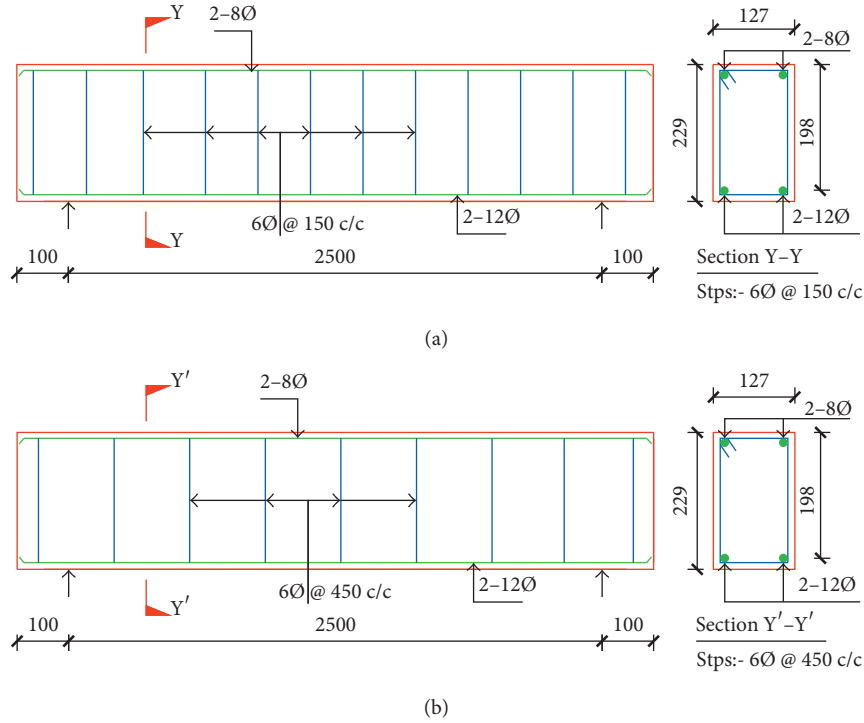


FIGURE 1: Beam section and reinforcement details: (a) shear-designed beams (DBs); (b) shear-deficient beams (SDBs).

TABLE 4: Shear-designed and shear-deficient RCC beam designation detail.

Designation of beams	Loading description	Shear-span ratio (a/d)	No. of samples
DB-ad-1	Shear-designed controlled beams	1.0	3
RDB45-ad-1	45% predamage + strengthening	1.0	3
RDB75-ad-1	75% predamage + strengthening	1.0	3
RDB95-ad-1	95% predamage + strengthening	1.0	3
DB-ad-3	Shear-designed controlled beams	3.0	3
RDB45-ad-3	45% predamage + strengthening	3.0	3
RDB75-ad-3	75% predamage + strengthening	3.0	3
RDB95-ad-3	95% predamage + strengthening	3.0	3
SDB-ad-1	Shear-deficient controlled beams	1.0	3
RSDB45-ad-1	45% predamage + strengthening	1.0	3
RSDB75-ad-1	75% predamage + strengthening	1.0	3
RSDB95-ad-1	95% predamage + strengthening	1.0	3
SDB-ad-3	Shear-deficient controlled beams	3.0	3
RSDB45-ad-3	45% predamage + strengthening	3.0	3
RSDB75-ad-3	75% predamage + strengthening	3.0	3
RSDB95-ad-3	95% predamage + strengthening	3.0	3

DB: shear-designed beam; RDB: strengthened shear-designed beam; SDB: shear-deficient beam; RSDB: strengthened shear-deficient beam.

1st LVDT (refer Figure 2). The load versus deflection curves of the 1st LVDT are only presented in this article for comparative study.

2.2.2. Predamaging of Beams. According to the test results of controlled beams, the other sets of beams were loaded on the

same setup and predamaged for three different levels of initial stresses corresponding to 45%, 75%, and 95% of the ultimate load. The DB45 and SDB45 beams were initially loaded for 45% level of damage. Similarly, DB75 and SDB75 and DB95 and SDB95 were loaded for 75% and 95% levels of damage, respectively. These damaged beams were then unloaded and strengthened with 20 mm thick U-shaped

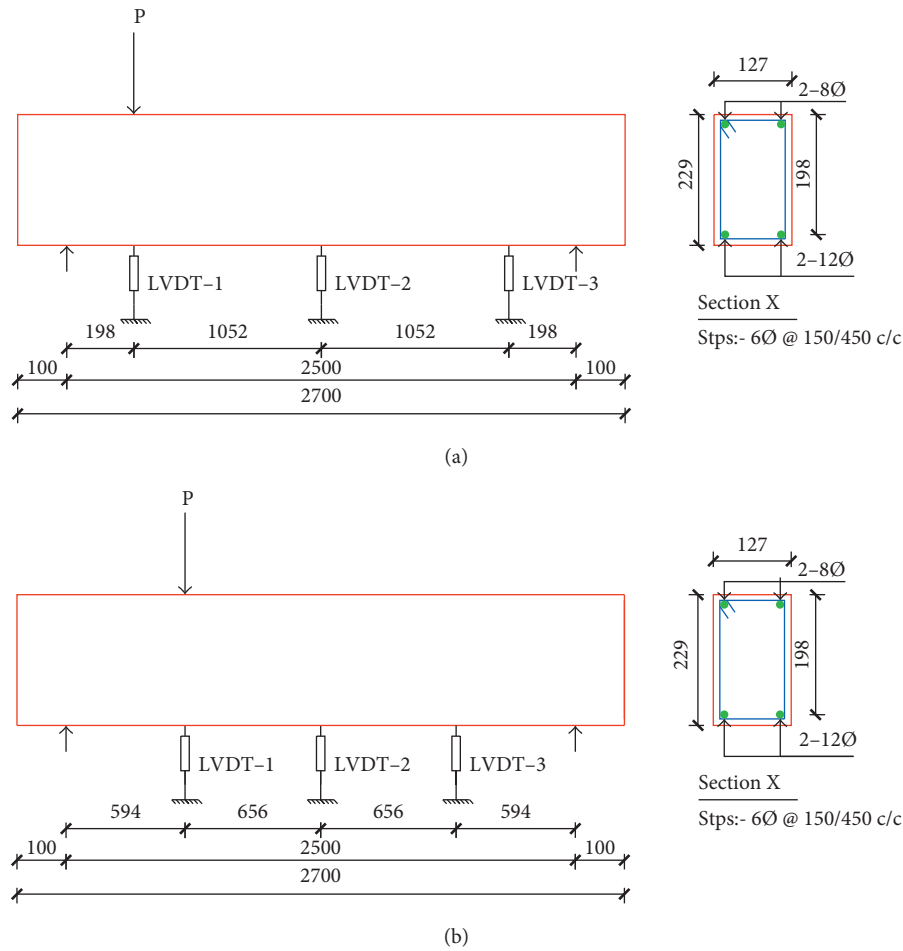


FIGURE 2: Schematic diagram of the test setup: (a) beams tested at $a/d = 1$; (b) beams tested at $a/d = 3$.

TABLE 5: Test results of controlled DB and SDB.

Designation of beams	a/d ratio	Avg. ultimate load value (kN)	Avg. deflection at ultimate load (mm)	Calculated load value for different stress levels (kN)		
				45%	75%	95%
DB-ad-1	1	145.68	5.899	65.56	109.26	138.40
DB-ad-3	3	64.53	11.674	29.04	48.40	61.30
SDB-ad-1	1	144.28	6.857	64.93	108.21	137.07
SDB-ad-3	3	59.55	10.371	26.80	44.66	56.57

polymer-modified ferrocement jacketing which contained 15% SBR latex and three layers of square woven steel wire mesh. The detail of strengthening is given in the subsequent section.

2.2.3. Strengthening Procedure. The behaviour of strengthened beams is highly dependent upon the surface preparation and application of the strengthening material. The repaired surface of the beams should be free from dirt, oil, dust, existing matter, and curing compounds. An improper preparation of the surface can result in debonding of PMF

jacketing. Before the strengthening procedure, the beams were turned upside down to expose their soffit. The particular portion of all the predamaged beams was cleaned with a wire brush at their soffit and side faces where the jacketing is supposed to be applied. The surface was cleaned with such a way to expose the aggregates and to make the surface sufficiently rough for application of repairing mortar. Water was sprayed on the prepared surface to make it wet.

The another study done by the authors resulted that the three-layered square woven steel wire mesh PMF having an optimum percentage of 15% SBR showed better strength

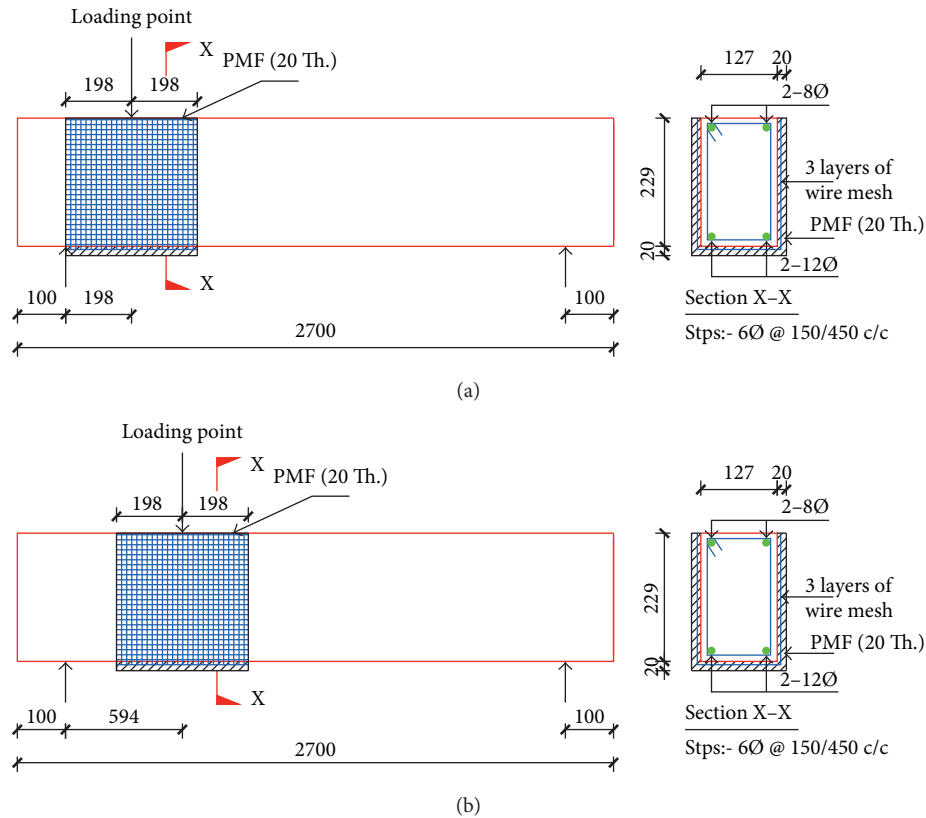


FIGURE 3: Detail of PMF strengthening: (a) beams tested at $a/d = 1$; (b) beams tested at $a/d = 3$.

properties and hence adopted in this present investigation to strengthen the predamaged RCC beams. The polymer-modified repairing mortar was constituted with cement, sand, SBR, and water in the ratio of 1 : 2 : 0.15 : 0.35 [45]. A silicon-based antifoaming agent was also added to the polymer-modified mortar matrix. Cement slurry was used as a bonding agent. First of all, three layers of wire mesh were affixed over the specified length of beams, and then, SBR-modified mortar was applied. A total of 20 mm thick PMF jacketing was applied under the soffit and side faces of the beams in a length of “ $2d = 396 \text{ mm}$ ”, centred on the loading point, for both DB- and SDB-type beams, irrespective of a/d ratios. Different sets of beam specimens were prepared for each level of initial damage. The repair material was accurately positioned with the help of wooden forms. After 24 hours of application of PMF jacketing, the strengthened portion of the beams was cured with gunny bags for further 28 days. The details of PMF-strengthened beams are shown in Figure 3 and Plate 1.

2.2.4. Reloading of Predamaged Strengthened Beams. The PMF-strengthened beams were again placed on the same loading frame setups (as specified in Figure 2) to find their ultimate shear load-carrying capacities, deflection, and cracking pattern. The locations of LVDTs were kept the same as in the case of controlled beams. The load-deflection behaviour of all sets of tested beams was recorded for conclusive study and shown in Figures 4–7. The detail of



PLATE 1: Application of PMF jacketing on the soffit and side faces of the beams (by turning the beams upside down).

observed loads, deflections, and failure modes is given in Table 6.

3. Results

In this current experimental program, a total of 48 beams were tested. The testing was aimed to achieve many objectives by comparing the behaviours of these beams. The controlled and strengthened beams were loaded up to ultimate failure. Most of the beams showed diagonal cracking patterns and the shear mode of failure. The effects of different levels of initial stresses, a/d ratios, and spacing of shear stirrups on the strength, failure modes, cracking pattern,

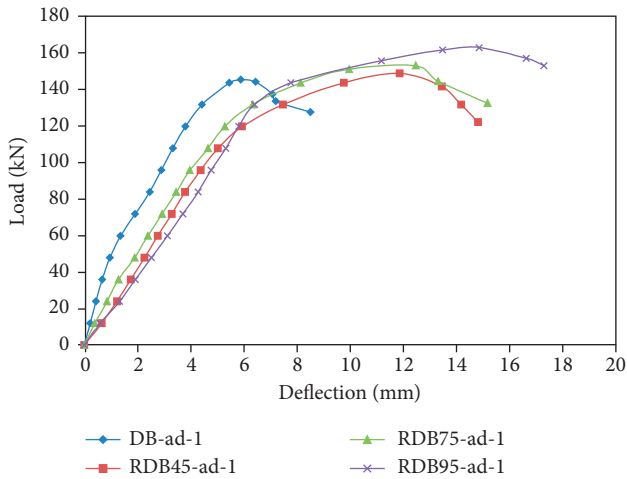


FIGURE 4: Load-deflection plot of shear-designed beams tested at a/d ratio 1.

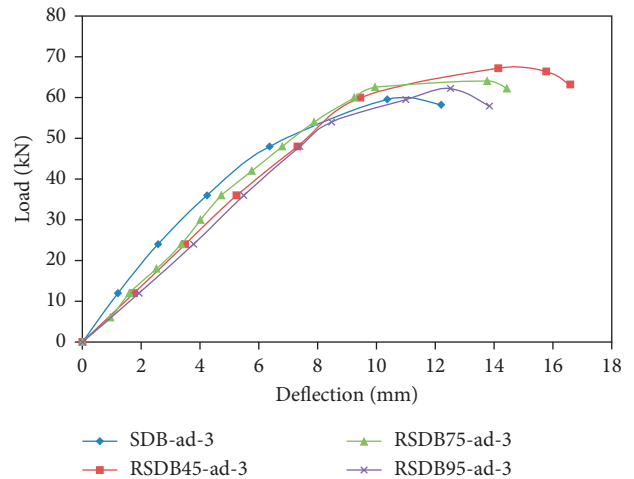


FIGURE 7: Load-deflection plot of shear-deficient beams tested at a/d ratio 3.

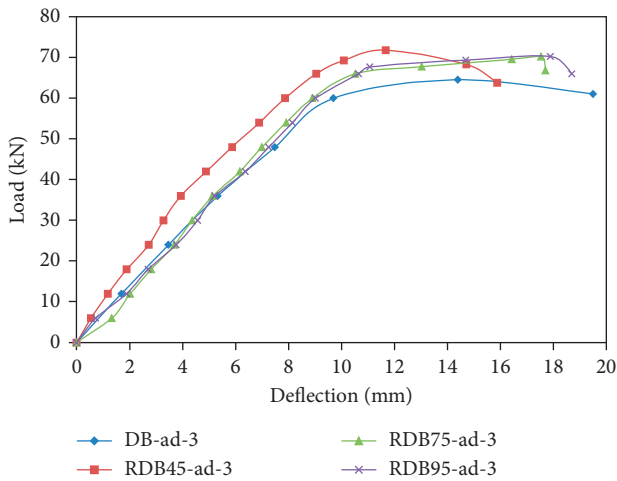


FIGURE 5: Load-deflection plot of shear-designed beams tested at a/d ratio 3.

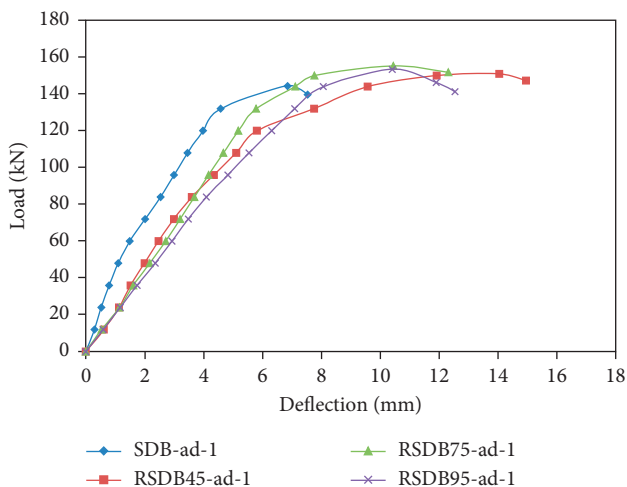


FIGURE 6: Load-deflection plot of shear-deficient beams tested at a/d ratio 1.

ductility, and deflection of strengthened beams are discussed in the subsequent sections.

3.1. Comparisons between Controlled and Strengthened Beams

3.1.1. Effect of Different Levels of Initial Stresses. All the strengthened beams which were initially damaged with 45%, 75%, and 95% of the ultimate load had showed a complete restoration and further enhancement of the original strength up to 12.03% after strengthening. The deflection behaviour of these beams was also changed after strengthening, and the beams exhibited more ductility as compared to controlled beams. Hence, higher deflection values were observed for all the strengthened beams at the ultimate failure level.

The strengthened shear-designed beams when tested at $a/d = 1.0$ and having the initial stress level of 95% (RDB95-ad-1) showed the maximum improvement in their ultimate load value by 12.03%. The results of strengthened beams with an initial damage of 45% (RDB45-ad-1) and 75% (RDB-75-ad-1) also showed a similar trend of improvement in their ultimate load values by 2.38% and 5.33%, respectively, over the controlled beam DB-ad-1. The observed figures of load values were quite less for the beams tested at $a/d = 3.0$, but these beams showed a similarly improved trend after strengthening. The strengthened RDB45-ad-3, RDB75-ad-3, and RDB-95-ad-3 beams tested at $a/d = 3.0$ demonstrated the improvement in the ultimate load by 11.19%, 8.82%, and 8.85%, respectively, with respect to the controlled beam DB-ad-3. Load-deflection comparative curves of controlled and strengthened shear-designed beams with different levels of initial damages, when tested at $a/d = 1$ and 3, are shown in Figures 4 and 5.

The strengthened shear-deficient beams having initial damages of 45%, 75%, and 95% were also tested for different a/d ratios. The strengthened RSDB75-ad-1 beams showed maximum improvement in their ultimate load by 7.57%, when compared with the controlled beam SDB-ad-1. The RSDB45-ad-1 and RSDB95-ad-1 beams also showed an improvement in their ultimate load values by 4.60% and

TABLE 6: Reloading test results of predamaged strengthened beams.

Beam description	Ultimate load (kN)	Percentage increase in ultimate load	Deflection at ultimate load (mm)	Failure mode
DB-ad-1	145.68	—	5.899	Shear
RDB45-ad-1	149.14	2.38%	11.891	Shear
RDB75-ad-1	153.45	5.33%	12.494	Shear flexural
RDB95-ad-1	163.20	12.03%	14.882	Shear flexural
DB-ad-3	64.53	—	11.674	Shear flexural
RDB45-ad-3	71.75	11.19%	14.564	Shear-flexural
RDB75-ad-3	70.22	8.82%	17.534	Shear
RDB95-ad-3	70.24	8.85%	17.887	Shear flexural
SDB-ad-1	144.28	—	6.857	Shear
RSDB45-ad-1	154.60	4.60%	14.048	Shear flexural
RSDB75-ad-1	161.87	7.57%	10.450	Shear flexural
RSDB95-ad-1	155.96	6.29%	10.412	Shear flexural
SDB-ad-3	59.55	—	10.371	Shear
RSDB45-ad-3	67.20	12.85%	14.146	Shear
RSDB75-ad-3	64.05	7.56%	13.763	Shear
RSDB95-ad-3	62.24	4.52%	12.523	Shear

6.29%, respectively, as compared to the controlled beam SDB-ad-1. At a higher a/d ratio = 3.0, the ultimate loads also exhibited enhancement, and the maximum improvement in the load was recorded for RSDB45-ad-3 beams by 12.85% over the controlled beam SDB-ad-3. The load-carrying capacities of RSDB75-ad-3 and RSDB 95-ad-3 beams were also improved by 7.56% and 4.52%, respectively. Load-deflection comparative curves of controlled and strengthened shear-deficient beams with different levels of initial stresses, when tested at $a/d = 1$ and 3, are shown in Figures 6 and 7.

Test results showed that the performance of PMF jacketing is very consistent for both shear-deficient and shear-designed beams at a/d ratios 1 and 3. Application of PMF jacketing filled the cracks which were developed during the initial damaging of beams and also helped to arrest the formation of such deformities during retesting of damaged strengthened beams. The PMF jacketing helped to enhance the ductility and caused to delay the shear failure of beams by resisting and distributing the applied loads. The proportional deflection of strengthened beams was also increased irrespective of their level of initial damages.

3.1.2. Effect of a/d Ratios. The controlled as well as strengthened shear-designed (DB) and shear-deficient (SDB) beams were tested for two different a/d ratios 1 and 3 to study the effect of shear span “ a ” on the performance of these beams. From the test results, it was found that the a/d ratio played a crucial role. The strengthened beams tested at $a/d = 1.0$ showed more improvement in their ultimate strength, cracking pattern, ductility, and deflection behaviour as compared to beams which were tested at $a/d = 3.0$, irrespective of stirrup spacing.

The controlled shear-designed beams tested at $a/d = 1.0$ (DB-ad-1) showed a higher load-carrying capacity of

125.76% as compared to DB-ad-3 beams tested at $a/d = 3$. The observed pattern for strengthened beams was also similar, and the shear load-carrying capacity of RDB45-ad-1, RDB75-ad-1, and RDB95-ad-1 beams was increased by 107.86%, 118.53%, and 132.35%, respectively, when compared with RDB45-ad-3, RDB75-ad-3, and RDB95-ad-3 beams. Graphical comparisons of ultimate loads at different a/d ratios are shown in Figure 8.

A similar trend was recorded for controlled shear-deficient SDB-ad-1 beams, and 142.28% higher load-carrying capacity was observed in comparison with SDB-ad-3 beams. The strengthened shear-deficient beams also behaved in a similar manner, and the ultimate load values of RSDB95-ad-1 beams (tested at $a/d = 1$) were improved to a maximum of 146.38%. The RSDB45-ad-1 and RSDB75-ad-1 beams showed improvement in their ultimate strength by 124.58% and 142.31%, respectively, as compared to RSDB75-ad-3 and RSDB95-ad-3 beams. Graphical comparisons of ultimate loads at different a/d ratios are shown in Figure 9.

At an a/d ratio of 1.0, the beams tend to fail in shear only, and as the a/d ratio increased, the behaviour of beams was shifted to a shear-flexure mode of failure. Shear forces were dominating in the case of beams tested at $a/d = 1.0$. All the controlled and strengthened beams showed more figurative strength values and a comparatively lesser deflection at a particular load level when tested at a smaller a/d ratio of 1.0 as compared to the beams tested at a higher a/d ratio of 3.0. As the distance of the load point from the support was increased, the relative deflection was also increased. This is due to the parabolic shape of the deflection curve, and hence, the observed deflection values were smaller for the beams tested near the support as compared to the deflection values of the beams tested at “ $3d$ ” away from the support. The observed behaviour of strengthened beams was more ductile when tested at a higher a/d ratio of 3. This improved

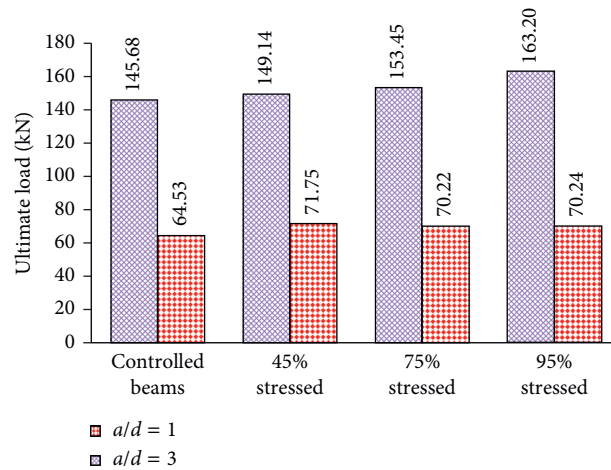


FIGURE 8: Comparison of ultimate loads of shear-designed beams tested at a/d ratios 1 and 3.

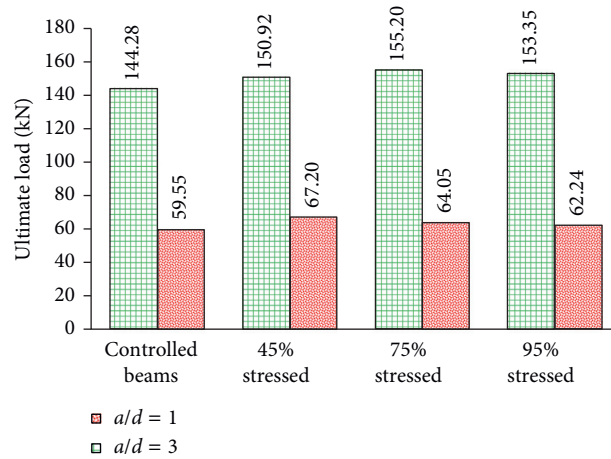


FIGURE 9: Comparison of ultimate loads of shear-deficient beams tested at a/d ratios 1 and 3.

ductility further imparts to increase the deflection of these beams.

It is concluded that the PMF jacketing technique contributes more towards improving the shear resistance of beams and further enhances the ultimate load values when the beams were tested at $a/d = 1$. Hence, PMF jacketing delays the direct shear failure, and it apparently increases the contribution of stirrups to resist higher loads.

3.1.3. Effect of Beam Type. The beams having stirrups at a spacing of 150 mm c/c were designated as shear-designed beams (DBs), and the beams have stirrups at a spacing of 450 mm c/c were designated as shear-deficient beams (SDBs). Both the controlled and strengthened beams were tested for two different a/d ratios. The controlled shear-deficient beams (SDB-ad-1) when tested at a/d ratio = 1.0 showed almost similar strength values as compared to controlled shear-designed beams (DB-ad-1) with a negligible decrement of 0.96% only. A similar trend was observed at $a/d = 3.0$, and the SDB-ad-3 beams showed 7.72% lesser

ultimate load as compared to DB-ad-3 beams. With the increase of the initial damage level, the percentage decrease in loads showed an upward trend when the beams were tested at a/d ratio 3. The observed behaviour was, however, different in the case of beams tested at $a/d = 1$, and the load values firstly improved for the beams with 45% and 75% initial damages and then decreased for beams having 95% of the initial damage. The RSDB95-ad-1 beams showed 6.04% lesser load-carrying capacities as compared to RDB95-ad-1 beams. At $a/d = 1.0$ and for a particular initial damage level, the strengthened shear-designed and shear-deficient beams showed almost equal strength with a minor variation of 1% to 6% only.

This is attributable to the arch action of the concrete element and the efficiency of PMF jacketing. The strengthening technique is observed to be more efficient in case of shear-deficient beams when tested at a/d ratio 1. In the event of beams tested at $a/d = 3.0$, a different type of behaviour was observed, and the strengthened shear-deficient beams showed a lesser load-carrying capacity as compared to shear-designed beams for a particular damage

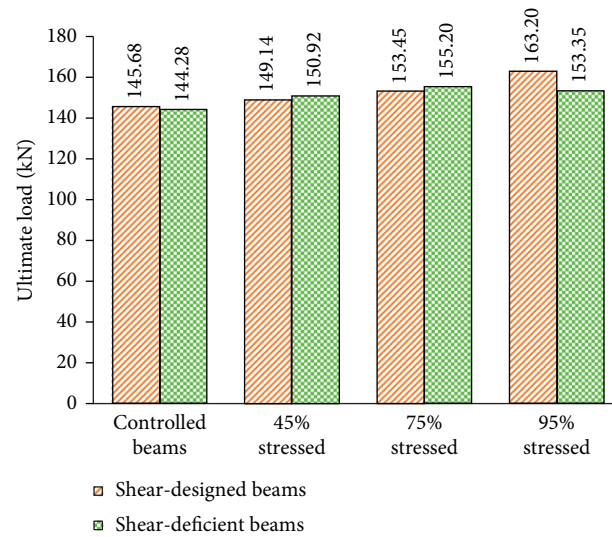


FIGURE 10: Comparison of ultimate loads of shear-designed and shear-deficient beams tested at a/d 1.

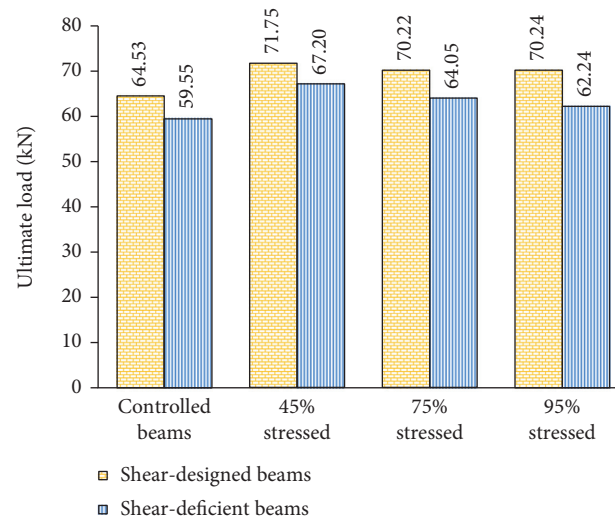


FIGURE 11: Comparison of ultimate loads of shear-designed and shear-deficient beams tested at a/d 3.

level. Deflection behaviour was also inconsistent in both the cases. Graphical comparison of ultimate loads of beams tested at a/d ratio 1 is shown in Figure 10.

The shear-deficient strengthened beams (RSDB45-ad-1 and RSDB75-ad-1) with initial stresses of 45% and 75% showed a higher strength of 1.19% and 1.14% over the shear-designed strengthened beams (RDB45-ad-1 and RDB75-ad-1), respectively, when tested at $a/d=1$. However, at the higher initial damage level of 95%, strengthened RSDB95-ad-1 beams reflected 6.04% lesser strength as compared to the controlled RDB95-ad-1 beams. It is clear from this observation that the PMF jacketing technique is more effective in the case of shear-deficient beams. Apparently, PMF enhanced the shear strength of concrete near the support by means of transferring the increased load to the stirrups and converting the brittle concrete failure into ductile. At $a/d = 3$, the strengthened shear-deficient beams (RSDB45-ad-3, RSDB75-ad-3, and RSDB95-ad-3) showed lesser strength

values by 6.34%, 8.79%, and 11.39% as compared to strengthened shear-designed beams (RDB45-ad-3, RDB75-ad-3, and RDB95-ad-3). Graphical comparison of ultimate loads of beams tested at a/d ratio 3 is shown in Figure 11.

The PMF jacketing is fully effective to restore and enhance the original strength of both types of initially damaged beams. Furthermore, in the case of shear-deficient beams, it is observed that the cracks had developed at an angle of 30° to 45° . As the stirrups were at spaced as far as 450 mm c/c, many of these cracks were not interfered by the stirrups and therefore caused failure of beams in shear. The use of PMF tends to enhance the inertia and ductility of the beam section in such cases and is thus observed to cause a delay in beam failure. Hence, the observed experimental load and deflection values are higher due to the combined strength of concrete and ferrocement jacketing. The strengthened shear-deficient beams exhibited similar elastic behaviour as the strengthened shear-designed beams,

and the beams were observed to fail in shear compression and diagonal tension.

4. Discussion

4.1. Comparison of Failure Load of Specimens. Failure load detail for all the tested beam specimens is given in Table 6. Almost shear mode of failures was observed in all the beam specimens. No debonding of jacketing appeared when the PMF-strengthened beams were tested up to an ultimate failure level. These strengthened beams showed a significant improvement in their load-carrying capacities, ductility behaviours, and cracking patterns.

The ultimate load-carrying capacity of all the strengthened beams considerably improved as compared to controlled beams at both a/d ratios 1.0 and 3.0. The percentage increase in ultimate load values of shear-designed beams RDB-45-ad-1, RDB-75-ad-1, and RDB-95-ad-1 tested at $a/d = 1.0$ was 2.38%, 5.33%, and 12.03%, respectively. As the initial stress level of strengthened beams increased, the percentage improvement in the strength was also increased. Load enhancement behaviour was also observed for the strengthened beams tested at $a/d = 3.0$, and the ultimate load values of RDB-45-ad-3, RDB-75-ad-3, and RDB95-ad-3 beams were increased by 11.19%, 8.82%, and 8.85%, respectively. At higher $a/d = 3.0$, the percentage increase of load was observed to be more consistent, and all the shear-designed beams with different levels of predamages showed almost an equal improvement of shear load-carrying capacities. Graphical comparison of ultimate load values of shear-designed beams tested at a/d ratios 1 and 3 is shown in Figure 12.

The failure loads of strengthened shear-deficient beams were also considerably improved. This improvement was found to be lesser for the beams with a higher initial damage level of 95%. The initially stressed shear-deficient beams almost got damaged at 95% stress level, but the strengthening technique showed its worth to restore and enhance the total load-carrying capacity of such beams. The percentage improvement in the failure load of beams RSDB45-ad-1, RSDB75-ad-1, and RSDB95-ad-1 tested at $a/d = 1.0$ was 4.60%, 7.57%, and 6.29%, respectively, as compared to the controlled beam SDB-ad-1. The strengthened beams RSDB45-ad-3, RSDB75-ad-3, and RSDB95-ad-3 also showed the improvement in ultimate load values by 12.85%, 7.56%, and 4.52%, respectively, as compared to the controlled beam SDB-ad-3 when tested at a/d ratio 3.0. The strengthened shear-deficient beams tested at $a/d = 3.0$ showed more percentage improvement in ultimate loads if compared with beams tested at $a/d = 1.0$. It is concluded that the PMF jacketing restores and improves the original strength of predamaged beams. Graphical comparison of ultimate load values of shear-deficient beams tested at a/d ratios 1 and 3 is shown in Figure 13.

However, it was observed that some cracks appeared even through jacketing, which indicates a good bond of PMF jacketing with the existing concrete structure. However, in some cases, no cracks developed in the strengthened length where the jacketing was applied, and the failure cracks developed only in the vicinity of the jacketing edges. It

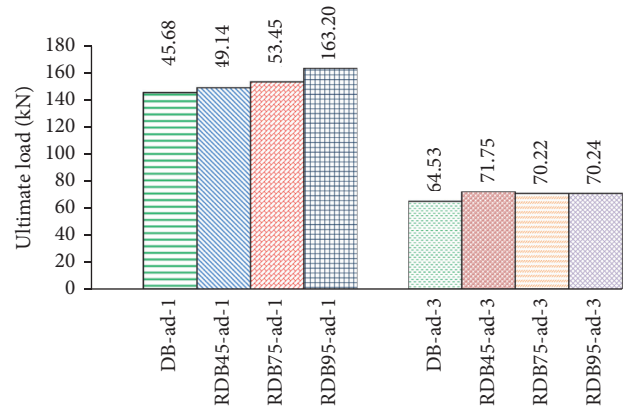


FIGURE 12: Ultimate loads of shear-designed beams tested at a/d ratios 1 and 3.

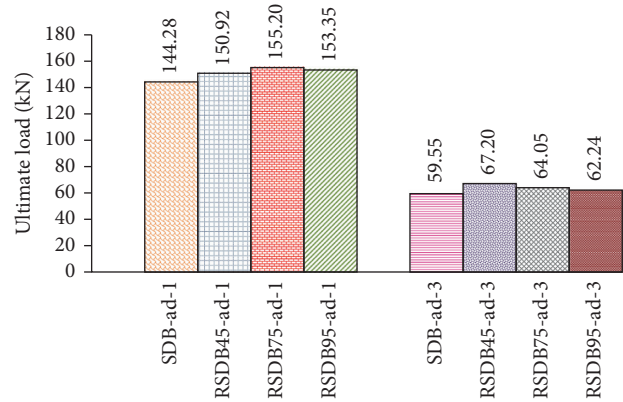


FIGURE 13: Ultimate loads of shear-deficient beams tested at a/d ratios 1 and 3.

reflected that the PMF jacketing behaved monolithically with the concrete specimens and helped to improve the ductility of beams after strengthening.

4.2. Ductility and Deflection Behaviour of Specimens. For comparative study, the deflection values under the load point are only discussed in this article. The load-deflection plots for all the beam specimens are shown in Figures 4–7. The ductility of both types of beams was improved after strengthening irrespective of whether the beams were tested at $a/d = 1.0$ or 3.0. The main reason for the increase of ductility is the strengthening technique only. Strengthening of beams improved the section modulus of beams and made the beams more ductile to resist deflection even after initial damages, and hence, the beams showed higher deflection values as compared to controlled beams at any particular load level. It is concluded that the PMF increases the ductility of predamaged strengthened beams which further imparts to sustain higher deflection and applied loads.

4.3. Cracking Pattern and Failure Mechanism. A few number of cracks of varying width and spacing were observed in

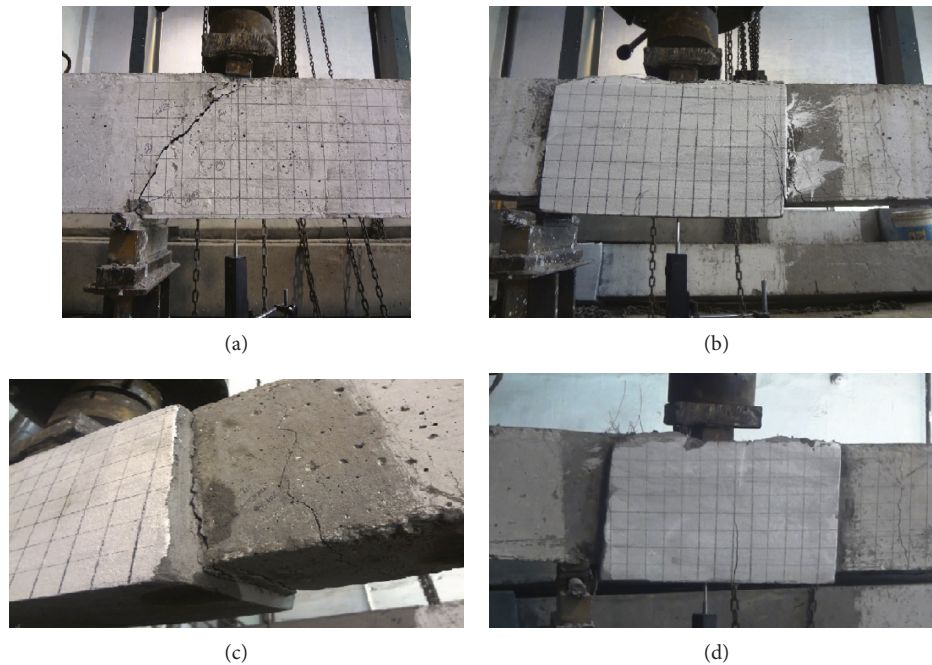


PLATE 2: Shear-designed beams tested at $a/d = 1$: (a) DB-ad-1; (b) RDB45-ad-1; (c) RDB75-ad-1; (d) RDB95-ad-1.

both types of control beams. The beams ultimately failed because of the widening of any of these cracks. On the other hand, the predamaged strengthened beams showed fewer hairline cracks during testing. The strengthened beams ultimately failed due to the formation of inclined shear cracks. These beams showed minor cracks when compared with the control beams of that particular segment. Plates 2–5 show the cracking pattern of shear-designed and shear-deficient controlled and strengthened beams tested at $a/d = 1$ and 3.

The tested beams got cracked, apparently due to two different conditions. In some cases, the cracks appeared diagonally near the support mostly because of shear forces, and in others, the cracks appeared towards centre due to shear forces together with some flexure moment. Most of the beams tested at a/d ratio 1.0 showed cracks of the first type which are described as shear compressive and diagonal tension cracks. In this mode of failure, the inclined cracks propagate rapidly due to inadequate shear reinforcement and cause the failure of concrete from the edge of the crack (refer Plates 2(a) and 4(a)). With the increase of the a/d ratio to 3.0, the observed crack pattern was of the other type which results due to a combination of shear force and flexure moment (refer Plates 3(a) and 5(a)).

In the case of both shear-designed and shear-deficient beams when tested at $a/d = 1.0$, the first crack appeared almost in the region where the shear force was maximum and the bending moment was negligible, that is, in a shear span “ a ” which is equal to “ $d = 198 \text{ mm}$ ” for a/d ratio 1.0. The cracks aligned with one another and inclined to the axis of the beam at an angle between 30° and 45° . It was observed that these cracks belonged to the first type, that

is, mostly due to shear forces. As the load increased, further cracks appeared in the zone of lesser shear stresses, that is, towards the centre of beams, and nonlinearity of the load-deflection behaviour increased. With the further increase of the load, more and more cracks developed and a dominant crack propagated towards the point of loading, resulting in ultimate failure. From the load-deflection plots, it is observed that the behaviour of beams remained linear up to a certain point, and after that, it changed into nonlinear.

The shear mode of failure was observed in the tested beams, and most of the cracks developed near the support and loading point (refer Plates 2–5). The cracking pattern of shear-designed and shear-deficient beams was changed as the a/d ratio changed from 1.0 to 3.0. It was observed that the shear-deficient controlled beams failed in a typical shear mode when tested at $a/d = 1.0$. The shear-designed controlled beam DB-ad-3 was observed to behave like DB-ad-1, but in this case, the cracks were not only in the shear zone, but some hairline cracks also developed towards the centre of the beam. These cracks were in the region of bending moment, and as such, these beams were in the combined mode condition. These cracks further grew and followed a bent path indicating a valid contribution of flexure moment in such cases. Further increasing of the load caused the development of a dominant crack towards the reduced compression zone. The response of shear-designed beams was generally ductile when tested at $a/d = 3.0$. Aggregate interlocking, dowel action of longitudinal bars, and bond strength of concrete also impart to resist the stresses which were further induced due to the widening of cracks. However, it is difficult to estimate the exact contribution of these different components.

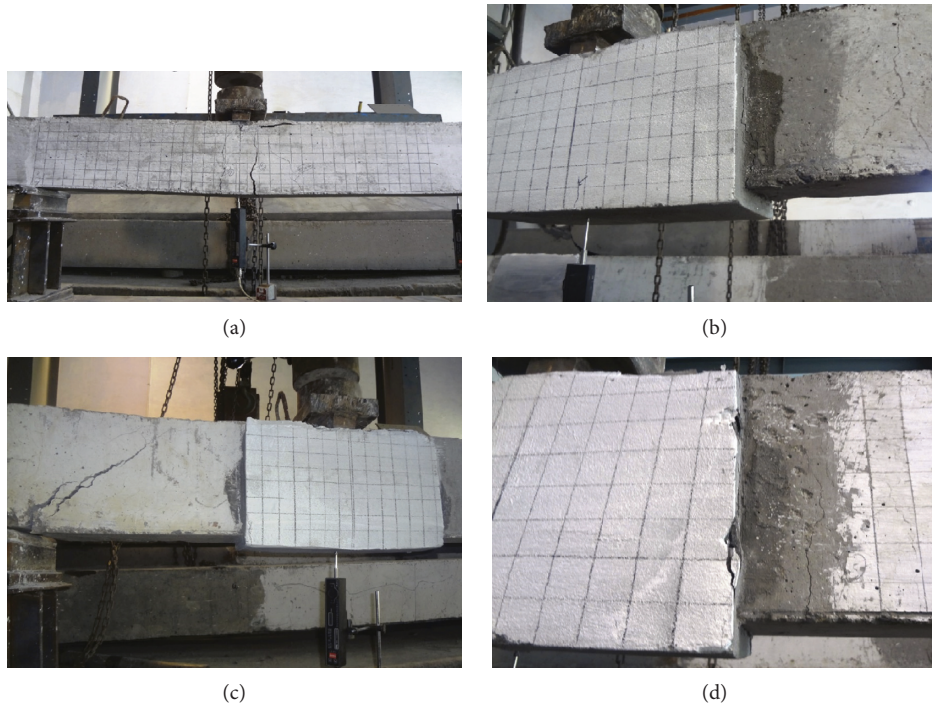


PLATE 3: Shear-designed beams tested at $a/d = 3$: (a) DB-ad-3; (b) RDB45-ad-3; (c) RDB75-ad-3; (d) RDB95-ad-3.

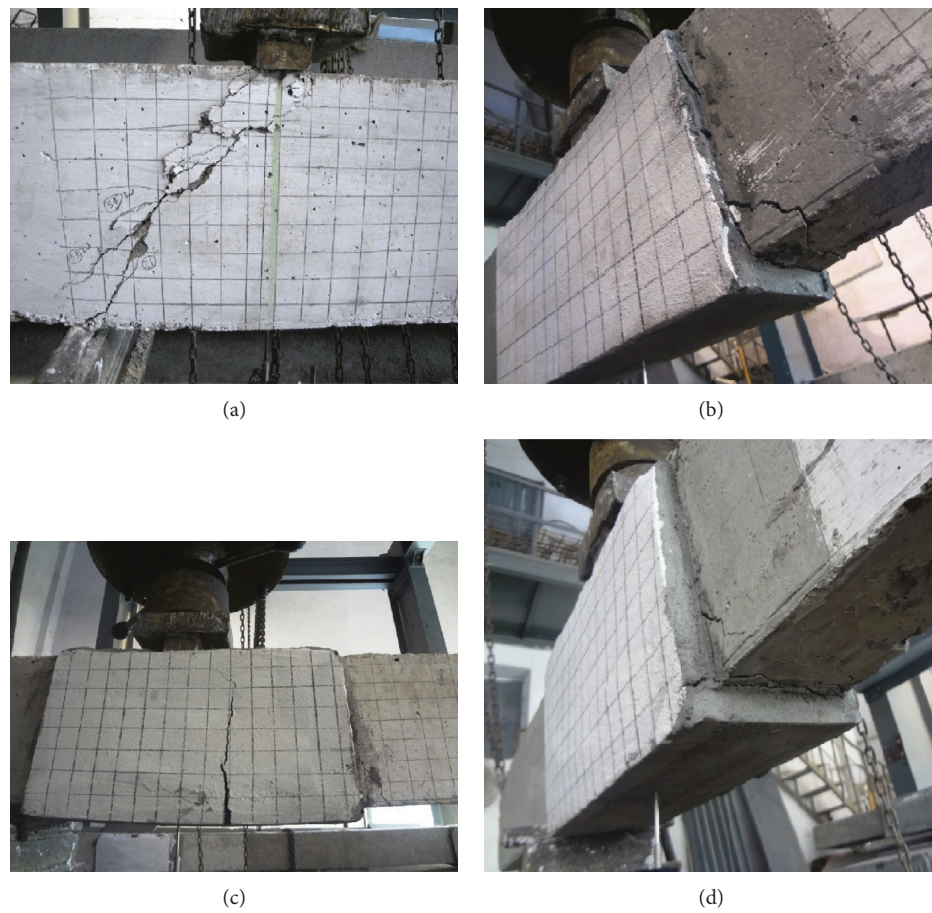


PLATE 4: Shear-deficient beams tested at $a/d = 1$: (a) SDB-ad-1; (b) RSDB45-ad-1; (c) RSDB75-ad-1; (d) RSDB95-ad-1.

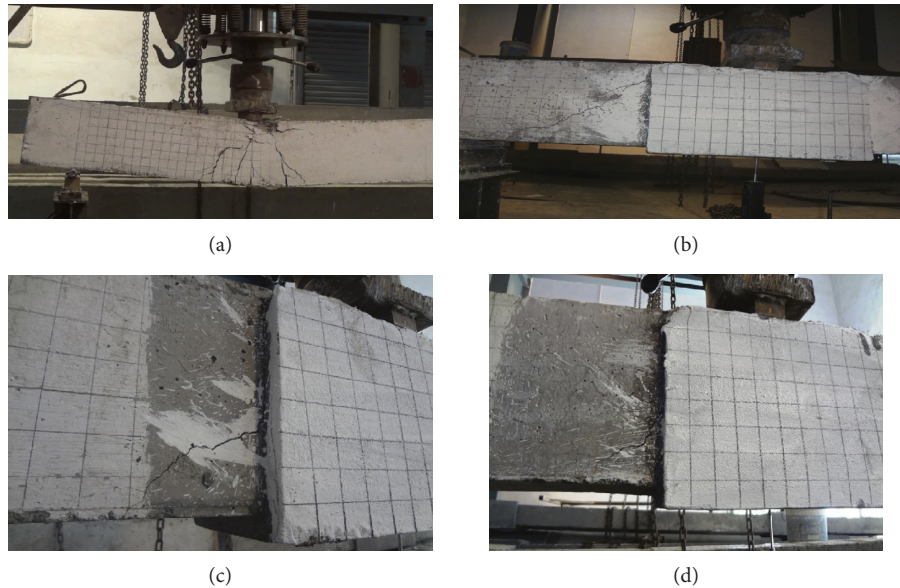


PLATE 5: Shear-deficient beams tested at $a/d=3$: (a) SDB-ad-3; (b) RSDB45-ad-3; (c) RSDB75-ad-3; (d) RSDB95-ad-3.

The behaviour of all the strengthened beams with different levels of initial damages was observed experimentally, and it was found that the jacketing neutralised the opening of cracks. The strengthened beams behaved stiffer as compared to the corresponding beams without strengthening, and the rate of crack development was also reduced. PMF-strengthened beams further displayed a lesser number of cracks when loaded to failure. This strengthening technique helps to improve the ductility of beams and causes to delay the formation of cracks. As a result, the figurative deflection of predamaged strengthened beams also enhanced. Spalling of concrete in the vicinity of the support point also reduced because of strengthening. PMF jacketing acted monolithically with the RCC beam specimens, and no bond failure was observed during the testing process. However, some cracks were found near the edge of jacketing which are attributable to the differential characteristics of strengthened beams at the newly created intersection of jacketed and unjacketed sections.

The shear failure mechanism of RCC beams is a complicated phenomenon because of interlinking of many factors such as loading pattern, shear-span ratio, beam section, the strength of concrete, and the quantity of shear and bending reinforcement. The characteristic of shear failure is abrupt as compared to the flexural failure. However, the PMF jacketing technique leads to achieve the ductile failure of strengthened beam specimens. From the abovementioned experiments, it is concluded that the PMF strengthening technique has improved the deformation behaviour, the cracking pattern, and the ultimate shear load-carrying capacity of the initially damaged beams.

5. Conclusions

The following conclusions have been drawn from this experimental study:

- (1) PMF is fully effective to restore and enhance the original strength of initially stressed beams even after 95% damage. All the strengthened beams showed a complete restoration of original strength irrespective of stirrup spacing, the level of initial damage, and a/d ratios. Maximum enhancement in the ultimate load value was observed as 12.03% for RDB95-ad-1 beams.
- (2) PMF jacketing causes to delay the direct shear failure of beams and apparently increases the contribution of stirrups to resist more loads. This technique is found to be more efficient in case of shear-deficient beams.
- (3) The PMF strengthening technique increased the ductility of predamaged beams and caused to delay the shear failure by resisting and distributing the applied loads. The beams behaved more elastically, and deflection behaviour also improved after strengthening.
- (4) The rate of crack development was also reduced, and the strengthened beams displayed a less number of cracks as compared to the corresponding beams without strengthening.
- (5) No bond failure of jacketing was observed which reflects the proper bonding and compatibility of polymer-modified ferrocement with the concrete structures.

Conflicts of Interest

The authors declare no conflicts of interest.

Acknowledgments

The authors pay the heartiest gratitude to Sika India Pvt. Ltd. for supplying the SBR latex polymer.

References

- [1] S. F. A. Rafeeqi, S. H. Lodhi, and Z. R. Wadalawala, "Behaviour of reinforced concrete beams strengthened in shear," *Journal of Ferrocement*, vol. 35, no. 1, pp. 479–489, 2005.
- [2] H. A. Ezz-Eldeen, "An experimental study on strengthening and retrofitting of damaged reinforced concrete beams using steel wire mesh and steel angles," *International Journal of Engineering Research and Technology*, vol. 4, no. 5, pp. 164–173, 2015.
- [3] M. B. S. Alferjani, A. A. B. A. Samad, B. S. Elrawaff, N. B. Mohamad, and M. H. B. Ahmad, "Shear strengthening of reinforced concrete beams using carbon fiber reinforced polymer laminate: a review," *American Journal of Civil Engineering*, vol. 2, no. 1, pp. 1–7, 2014.
- [4] S. B. Singh, "Shear response and design of RC beams strengthened using CFRP laminates," *International Journal of Advanced Structural Engineering*, vol. 5, no. 1, pp. 1–16, 2013.
- [5] S. Ahmad, A. Elahi, S. A. Barbhuiya, and Y. Farid, "Use of polymer modified mortar in controlling cracks in reinforced concrete beams," *Construction and Building Materials*, vol. 27, no. 1, pp. 91–96, 2012.
- [6] H. R. Ronagh and A. Eslami, "Flexural retrofitting of RC buildings using GFRP/CFRP—a comparative study," *Composites Part B: Engineering*, vol. 46, pp. 188–196, 2012.
- [7] H. S. Kim and Y. S. Shin, "Flexural behavior of reinforced concrete (RC) beams retrofitted with hybrid fiber reinforced polymers (FRPs) under sustaining loads," *Composite Structures*, vol. 93, no. 2, pp. 802–811, 2011.
- [8] Y. T. Obaidat, S. Heyden, O. Dahlblom, G. Abu-Farsakh, and Y. Abdel-Jawad, "Retrofitting of reinforced concrete beams using composite laminates," *Construction and Building Materials*, vol. 25, no. 2, pp. 591–597, 2011.
- [9] S. Kothandaraman and G. Vasudevan, "Flexural retrofitting of RC beams using external bars at soffit level—an experimental study," *Construction and Building Materials*, vol. 24, no. 11, pp. 2208–2216, 2010.
- [10] P. P. Bansal, M. Kumar, and S. K. Kaushik, "Effect of type of wire mesh on strength of beams retrofitted using ferrocement laminates," *National Building Materials and Construction*, vol. 2, no. 1, pp. 272–278, 2008.
- [11] S. A. Sheikh, D. DeRose, and J. Mardukhi, "Retrofitting of concrete structures for shear and flexure with fiber-reinforced polymers," *ACI Structural Journal*, vol. 99, no. 4, pp. 451–459, 2002.
- [12] Y. C. Wang and K. Hsu, "Design recommendations for the strengthening of reinforced concrete beams with externally bonded composite plates," *Composite Structures*, vol. 88, no. 2, pp. 323–332, 2009.
- [13] M. Z. Jumaat and M. A. Alam, "Behaviour of U and L shaped end anchored steel plate strengthened reinforced concrete beams," *European Journal of Scientific Research*, vol. 22, no. 2, pp. 184–196, 2008.
- [14] P. P. Bansal, M. Kumar, M. Kaur, and S. Kaushik, "Effect of different bonding agents on strength of retrofitted beams using ferrocement laminates," *Indian Concrete Journal*, vol. 80, no. 8, pp. 36–42, 2006.
- [15] S. Sheela and B. Anu Geetha, "Studies on the performance of RC beam–column joints strengthened using different composite materials," *Journal of the Institution of Engineers (India): Series A*, vol. 93, no. 1, pp. 63–71, 2012.
- [16] M. Jumaat and A. Alam, "Flexural strengthening of reinforced concrete beams using ferrocement laminate with skeletal bars," *Journal of Applied Sciences Research*, vol. 2, no. 9, pp. 559–566, 2006.
- [17] K. Eswaran, J. Sridhar, N. Karunya, and R. A. Rane, "Study on strengthening of predamaged reinforced concrete beam using ferrocement laminates—a review," *International Research Journal of Engineering and Technology*, vol. 3, no. 3, pp. 325–331, 2016.
- [18] N. Karunya, R. A. Rane, K. Eswaran, and J. Sridhar, "Study on flexural strengthening of RC beams using ferrocement laminates with Recron-3S fibre—a review," *International Research Journal of Engineering and Technology*, vol. 3, no. 2, pp. 199–205, 2016.
- [19] S. R. Dakhane, K. P. Gatlwar, A. G. Bahale, and A. D. Raut, "Review on analysis of ferrocement-construction material," in *Proceedings of the International Conference on Science and Technology for Sustainable Development (ICSTSD)—2016*, pp. 88–93, Kuala Lumpur, Malaysia, May 2016.
- [20] S. U. Khan, S. Rafeeqi, and T. Ayub, "Strengthening of RC beams in flexure using ferrocement," *Iranian Journal of Science and Technology, Transactions of Civil Engineering*, vol. 37, pp. 353–365, 2013.
- [21] S. S. Patil, R. Ogale, and A. K. Dwivedi, "Performances of chicken mesh on strength of beams retrofitted using ferrocement jackets," *Journal of Engineering*, vol. 2, no. 7, pp. 1–10, 2012.
- [22] M. V. Reddy and E. Maheshwar, "Rehabilitation of shear deficient RC beams," *International Journal of Earth Sciences and Engineering*, vol. 4, no. 6, pp. 1125–1128, 2011.
- [23] P. R. Kumar, T. Oshima, S. Mikami, and T. Yamazaki, "Seismic retrofit of square reinforced concrete piers by ferrocement jacketing," *Structure and Infrastructure Engineering*, vol. 1, no. 4, pp. 253–262, 2005.
- [24] O. Lalaj, Y. Yardim, and S. Yilmaz, "Recent perspectives for ferrocement," *Research on Engineering Structures and Materials*, vol. 1, no. 1, pp. 11–23, 2015.
- [25] A. E. Naaman, *Ferrocement and Laminated Cementitious Composites*, Vol. 3000, Techno Press, Ann Arbor, MI, USA, 2000.
- [26] N. Rengaswamy, V. Saraswathy, and K. Balakrishnan, "Studies on the effect of an inhibitor admixture in ferrocement," *Journal of Ferrocement*, vol. 22, no. 4, pp. 359–371, 1992.
- [27] C. L. C. Roxas, R. S. Gallardo, B. Teodosio, E. K. T. Ochosa, and S. E. Young, "Durability of ferrocement garbage disposal barge," in *Proceedings of the DLSU Research Congress 2013*, pp. 1–7, De La Salle University, Manila, Philippines, March 2013.
- [28] L. Andal, M. Palanichamy, and M. Sekar, "Strength and durability of polymer and fly ash modified ferrocement roofing/flooring elements," in *Proceedings of the 33rd Conference on Our World in Concrete & Structures*, vol. 25, Singapore, August 2008.
- [29] X. M. Kong, C. C. Wu, Y. R. Zhang, and J. L. Li, "Polymer-modified mortar with a gradient polymer distribution: preparation, permeability, and mechanical behaviour," *Construction and Building Materials*, vol. 38, pp. 195–203, 2013.
- [30] M. Ramli and A. A. Tabassi, "Effects of polymer modification on the permeability of cement mortars under different curing conditions: a correlational study that includes pore distributions, water absorption and compressive strength," *Construction and Building Materials*, vol. 28, no. 1, pp. 561–570, 2012.
- [31] R. Wang, P. M. Wang, and L. J. Yao, "Effect of redispersible vinyl acetate and versatate copolymer powder on flexibility of cement mortar," *Construction and Building Materials*, vol. 27, no. 1, pp. 259–262, 2012.

- [32] S. Marceau, F. Lespinasse, J. Bellanger, C. Mallet, and F. Boinski, "Microstructure and mechanical properties of polymer-modified mortars," *European Journal of Environmental and Civil Engineering*, vol. 16, no. 5, pp. 571–581, 2012.
- [33] Z. Zhang, P. Wang, and J. Wu, "Dynamic mechanical properties of eva polymer-modified cement paste at early age," *Physics Procedia*, vol. 25, pp. 305–310, 2012.
- [34] J. Chen, S. Zhang, J. Y. Liu, and X. R. Zhou, "Preparation and properties of cement mortar modified by VAE latex," *Advanced Materials Research*, vol. 306–307, pp. 913–916, 2011.
- [35] Y. Y. Wu, B. G. Ma, J. Wang, F. C. Zhang, and S. W. Jian, "Study on interface properties of EVA-modified cement mortar," *Advanced Materials Research*, vol. 250–253, pp. 875–880, 2011.
- [36] N. Žižková, R. Drochytka, and K. Nosek, "Polymer-modified mortars for surface treatment with the utilization of waste polystyrene," *Key Engineering Materials*, vol. 466, pp. 141–150, 2011.
- [37] M. Y. L. Chew, P. P. Tan, and Y. S. Yeo, "Effect of styrene acrylic ester polymer on mortar render properties," *Architectural Science Review*, vol. 47, no. 1, pp. 43–52, 2004.
- [38] B. Vektaris, E. Smetonaitė, and V. Vilkas, "The influence of polymer latex and silica fume additives on the properties of cement mortar and concrete," *Journal of Civil Engineering and Management*, vol. 9, no. 2, pp. 146–152, 2003.
- [39] Y. Ohama, *Handbook of Polymer-Modified Concrete and Mortars: Properties and Process Technology*, Noyes Publications, Saddle River, NJ, USA, 1995.
- [40] S. Sheela and N. Ganesan, "Cracking characteristics of polymer modified ferrocement flexural elements," *International Journal of Emerging Technology and Advanced Engineering*, vol. 4, no. 4, pp. 901–911, 2014.
- [41] C. B. Cheah and M. Ramli, "Load capacity and crack development characteristics of HCWA-DSF high strength mortar ferrocement panels in flexure," *Construction and Building Materials*, vol. 36, pp. 348–357, 2012.
- [42] M. Ramli and A. A. Tabassi, "Mechanical behaviour of polymer-modified ferrocement under different exposure conditions: an experimental study," *Composites Part B: Engineering*, vol. 43, no. 2, pp. 447–456, 2012.
- [43] V. Bhikshma, R. Kishore, and R. Srinivas, "Durability of polymer and fly ash modified ferro cement elements," *Procedia Engineering*, vol. 14, pp. 2642–2649, 2011.
- [44] S. Sheela and M. S. Ajith, "Flexural behaviour of polymer modified ferrocement elements in chloride environment," in *Proceedings of the 3rd International Conference on the Durability of Concrete Structures*, pp. 1–6, Queen's University, Belfast, Northern Ireland, September 2012.
- [45] R. Ghai, P. P. Bansal, and M. Kumar, "Mechanical properties of styrene-butadiene-rubber latex (SBR) and vinyl-acetate-ethylene (VAE) polymer modified ferrocement (PMF)," *Journal of Polymer Materials*, vol. 33, no. 1, pp. 111–126, 2016.
- [46] A. S. Ali, H. S. Jawad, and I. S. Majeed, "Improvement the properties of cement mortar by using styrene butadiene rubber polymer," *Journal of Engineering and Development*, vol. 16, no. 3, pp. 61–72, 2012.
- [47] R. Wang and P. M. Wang, "Application of styrene-butadiene rubber in cement-based materials," *Advanced Materials Research*, vol. 306–307, pp. 588–593, 2011.
- [48] Z. J. Wang, R. Wang, and Y. B. Cheng, "Mechanical properties and microstructures of cement mortar modified with styrene-butadiene polymer emulsion," *Advanced Materials Research*, vol. 168–170, pp. 190–194, 2011.
- [49] G. Barluenga and F. Hernández-Olivares, "SBR latex modified mortar rheology and mechanical behaviour," *Cement and Concrete Research*, vol. 34, no. 3, pp. 527–535, 2004.
- [50] D. R. Kumar and B. Vidivelli, "Acrylic rubber latex in ferrocement for strengthening reinforced concrete beams," *American Journal of Engineering and Applied Sciences*, vol. 3, no. 2, pp. 277–285, 2010.
- [51] D. R. Kumar and B. Vidivelli, "Performances of SBR latex modified ferrocement for repairing reinforced concrete beams," *Australian Journal of Basic and Applied Sciences*, vol. 4, no. 3, pp. 520–531, 2010.
- [52] H. P. Liao and S. S. Fang, "An experimental study on flexural behavior of reinforced concrete beams strengthened with high-performance ferrocement," *Advanced Materials Research*, vol. 163–167, pp. 3772–3776, 2010.
- [53] B. Hughes and N. Ebuomwan, "Polymer-modified ferrocement enhances strength of reinforced concrete beams," *Construction and Building Materials*, vol. 7, no. 1, pp. 9–12, 1993.
- [54] C. Y. Zhao, S. M. Huang, Q. L. Yao, and Y. J. Chen, "Research on shearing performance of RC beams strengthened with steel wire-polymer mortar," *Applied Mechanics and Materials*, vol. 166–169, pp. 1702–1708, 2012.
- [55] IS: 1489 (Part 1)–1991, *Portland-Pozzolana Cement Specification*, Bureau of Indian Standards, New Delhi, India, 1991.
- [56] IS: 383–1970, *Specification for Coarse and Fine Aggregates from Natural Sources for Concrete*, Bureau of Indian Standards, New Delhi, India, 2002.
- [57] IS 2386 (Part III)–1963, *Methods of Test for Aggregates for Concrete*, Bureau of Indian Standards, New Delhi, India, 1997.
- [58] ACI Committee 549 (ACI 549.1R-93), "Guide for the Design, Construction, and Repair of Ferrocement," American Concrete Institute, Detroit, MI, USA, 1999.
- [59] Sika® Latex Power, "SBR Based Multipurpose Polymer for Waterproofing and Repair," Sika India Pvt. Ltd, Kolkata, India.
- [60] M. Afridi, Y. Ohama, M. Z. Iqbal, and K. Demura, "Water retention and adhesion of powdered and aqueous polymer-modified mortars," *Cement and Concrete Composites*, vol. 17, no. 2, pp. 113–118, 1995.
- [61] IS 10262–2009, *Concrete Mix Proportioning-Guidelines*, Bureau of Indian Standards, New Delhi, India, 2009.
- [62] ASTM C 1437–07, *Standard Test Method for Flow of Hydraulic Cement Mortar*, ASTM International, West Conshohocken, PA, USA, 2007.
- [63] IS 456:2000, *Plain and Reinforced Concrete-Code of Practice*, Bureau of Indian Standards, New Delhi, India, 2000.

Research Article

Access Control Points: Reducing a Possible Blast Impact by Meandering

Martin Larcher , Georgios Valsamos, and Vasilis Karlos

European Commission, Joint Research Centre, Ispra, Italy

Correspondence should be addressed to Martin Larcher; martin.larcher@ec.europa.eu

Received 24 August 2017; Accepted 7 December 2017; Published 11 February 2018

Academic Editor: Filipe Santos

Copyright © 2018 Martin Larcher et al. This is an open access article distributed under the Creative Commons Attribution License, which permits unrestricted use, distribution, and reproduction in any medium, provided the original work is properly cited.

In response to the heightened terror threat in recent years, there is an increasing interest in the introduction of access control zones at sites that are characterized by an increased likelihood of being the target of a terrorist attack, as latest data reveal that unprotected areas of mass congregation of people have become attractive to terrorist groups. Such control zones could be located within the building that has to be protected or attached to it. The elevated security needs for these areas call for a design that will consider the risk of internal explosive events. The purpose of this article is to outline a strategy for limiting the consequences of an internal blast, while guaranteeing that the produced blast wave does not propagate into vulnerable areas. In particular, the focus is on the introduction of a protective wall system in the form of a meander that allows unobstructed access of the public and at the same time reduces the possible blast inflow to the building's interior. The performed numerical simulations show that the proposed strategy yields much smaller injury risk areas compared to a design without the addition of protective walls and is recommended for upgrading the security of buildings.

1. Introduction

1.1. Motivation. Several trends in modern terrorism need to be considered for developing an effective protection strategy against a possible attack. In the past, the focus was on the protection of *critical infrastructures*. However, recent terrorist attacks shifted towards *soft targets* due to the increased likelihood of success without the need for careful planning, big resources, and special training of the perpetrators. Soft targets are, in general, defined as unprotected areas with high concentration of people, like shopping malls, stadia, hotels, universities, urban city centres, festivals, fairs, places of worship, train and subway stations, or Christmas markets. Such targets might consist only of the attending public (e.g., markets, open-air fairs, parks, festivals, and parades) or could also entail structural components (e.g., concert halls, theatres, museums, churches, and transportation terminals). In the recent past, Jihadist perpetrators have chosen this type of targets with the intent to cause mass casualties and due to the high social, political, and/or economic impact of a successful attack. As can be seen in Figure 1, all major attacks

(involving fatalities) in Europe over the last years targeted soft targets, which is also attributed to their increased vulnerability.

It was noticed that these attacks were often performed by utilizing unconventional and/or “low-tech” weapons, such as improvised explosive devices (IEDs), knives, axes, cars, and trucks. In particular, for the attacks in Brussels (03/2016) and Paris (11/2015), IEDs were used as *modus operandi*. For instance, physical protection against vehicle-ramming attacks can be achieved by a properly designed barrier system. However, the detection of smaller weapons and explosives by specialized devices [1] is fundamental for reducing the possibility of an attack. The adoption of detection measures might be advisable for places of mass congregation of people but is crucial for controlling the access at high-risk sites. Moreover, the location of this detection zone is of great importance, since it is an area characterized by an increased likelihood of terrorist attacks (by using explosives and/or firearms). The present article concentrates on the design of such *access control points* and, in particular, their design in relation to possible attacks by the use of explosives.

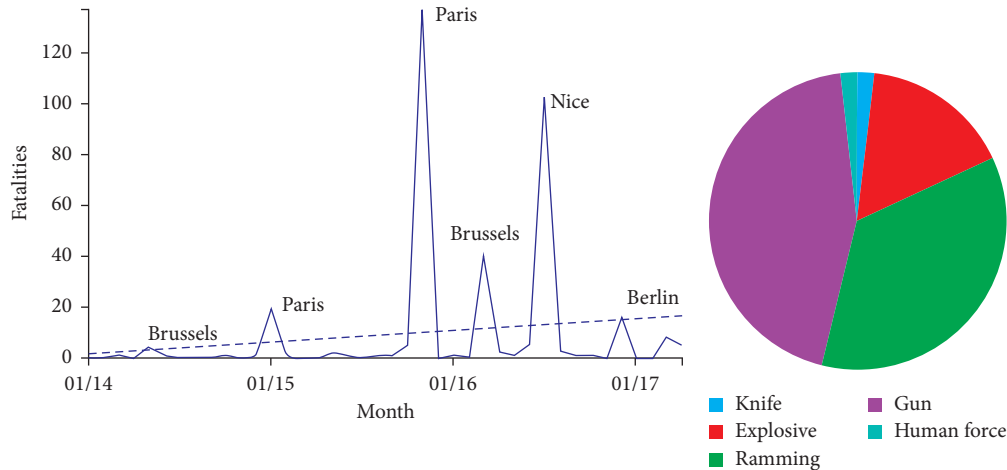


FIGURE 1: Fatalities due to terrorist attacks in the European Union 2014–2017, modus operandi.

Concerning the *physical resistance* or structural robustness of a building, a progressive collapse mechanism [2] must be avoided and glass surfaces, like windows or façades [3], should be protected against the impact of blast waves or projectiles. The physical protection of crowded places against explosive events can be performed by proper shadowing techniques, for example, by using concrete blocks [4].

1.2. Risk Mitigation. The creation of an efficient plan for the protection of critical infrastructures and soft targets starts with identifying the potential risk. To ascertain the risk of an attack, the analyst has to weigh its probable consequences, the most suitable tactic, and the weaknesses that may be exploited by the aggressors in their effort to impose damage and casualties. This means that for calculating the potential risk, the combination of threat level, vulnerability level, and target value is required. The threat level can be defined as the probability of occurrence of an attack in a specific period of time, causing abnormal loading to the structure. The vulnerability level is linked to the identification of security weaknesses and the potential damage to the system resulting from an event with a given intensity. The target value can be quantified with respect to the damage in the target's assets, such as injuries of the occupants, human life loss, capital value, reconstruction cost, and disruption of services and functions.

A carefully designed protection strategy and crisis management plan can effectively reduce the impact of an attack to the target's asset value. The implementation of a detection and investigation scheme can deter possible aggressors and decrease the threat level, while the assessed vulnerability can be reduced by strengthening the examined structure to limit the consequences of an attack.

Many buildings can be identified as potential targets of a terrorist attack. Accessibility to these buildings is often restricted, and people entering the premises (in particular external visitors) are subjected to security checks to reduce the likelihood of an attack at the building's interior. Even though an access control strategy does not guarantee detection of all possible threats, it can certainly be assumed that

perpetrators cannot enter carrying big amounts of explosives or firearms. Practically, this means that both the risk of possible attacks inside the building and their consequences are reduced.

The location of a security control zone, where people are checked for the presence of explosive materials and weapons prior entering to the building, should be carefully selected. Prior experience from military applications shows that a dedicated building (guardhouse), detached from an existing structure, reduces possible consequences in case of an attack at its interior. Such a design approach is feasible if space is available, but often in the densely built urban environment buildings occupying nearly all the available lot and construction of a detached structure is not an option. In the current article, measures for the protection of access control areas in closed environment against explosions are presented. In particular, the proposed strategy is based on the employment of a meandering wall to reduce the possible inflow of the produced blast wave to a building's interior.

1.3. Policy Context. Security is one of the recent priorities of the European Commission. The European Agenda on Security clearly advocates that the protection of critical infrastructures and soft targets presents a real challenge. The main objective is to gather best practise principles and produce guidance for mitigating the risk of terrorism. In particular, it is highlighted that the protection of soft targets and human life is of utmost importance and additional efforts are required from both state and private security stakeholders.

2. Explosion Effects

2.1. Blast Loading. Blast waves are typically characterized by a compression phase (positive phase) with a very high peak overpressure, followed by an underpressure phase (negative phase). Figure 2 shows an idealized profile of the pressure in relation to time for the case of a blast wave and presents some relevant parameters. The compression phase includes an almost instantaneous increase from the ambient pressure (p_0) to a peak pressure ($p_0 + p_{max}$) at the arrival time t_{ar} , when the

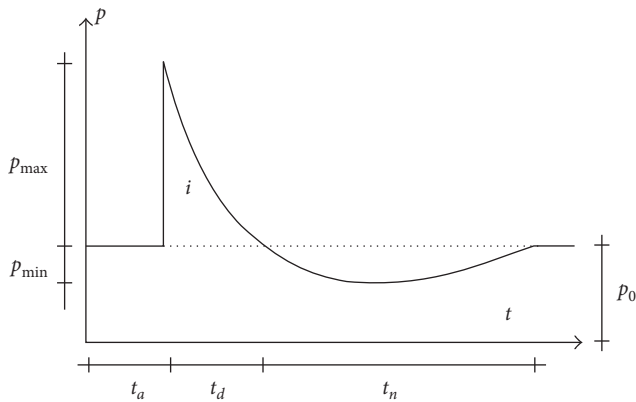


FIGURE 2: Pressure-time history for an ideal free-field air-blast wave.

shock front reaches the point of interest. The time required for the pressure to reach its peak value is very small, and for design purposes, it is usually considered as equal to zero. After its peak value, the pressure decreases at an exponential rate until it reaches the ambient value at $t_a + t_d$, t_d being called the positive phase duration. After the positive phase, the pressure drops below the ambient value, attaining its minimum value p_{\min} , before finally returning to it after t_n (negative phase duration). The positive impulse i is defined as the integral of the overpressure curve over time and is distinguished in positive and negative according to the relevant phase of the blast wave time history. More detailed information on the blast wave parameters is provided in [5–8].

The loading conditions of an externally loaded structure can be distinguished into three types: impulsive, dynamic, and quasi-static loading (Figure 3). Loads with very short duration (relative to the structure's or component's fundamental natural period) are known as impulsive loads, for example, near-field explosions of smaller charges (rucksack bombs). The structural consequences of such explosions range from shear-type failures (e.g., of fragile parts like window panes) to bending-type failures (e.g., stiffer concrete structures). Explosions with very small distances or even contact detonations could cause even spalling and scabbing [9]. If the duration of the excitation is longer than the natural period of the structure or of the component (dynamic loading), the predominant structural failure mode is bending as in the case of far-field explosions (car bombs) and gas explosions. A static load simulation approach can be used only if the examined pressure increases at a very low rate (quasi-static loading). For the other two loading conditions, sophisticated numerical models should be utilized, for example, an explicit finite element analysis. For a particular structure and load type (e.g., pressure), these loading regimes can be schematically presented by an iso-response curve in a so-called PI (pressure-impulse) diagram (Figure 3). If a probabilistic approach is of interest, the probability of damage could also be inserted in the diagram (e.g., Figure 4).

2.2. Venting/Pressure Release. The diagram shown in Figure 2 is only valid for spherical or hemispherical, free air, or

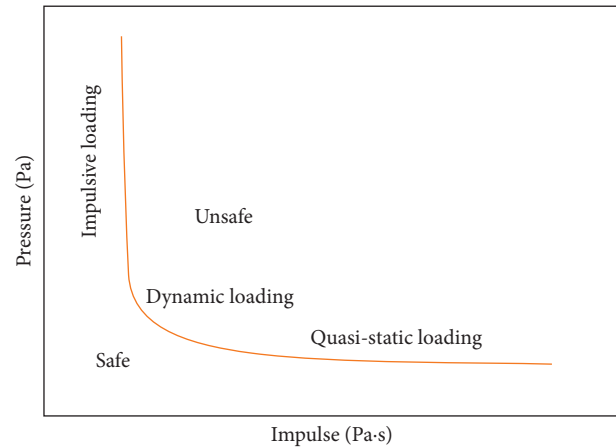


FIGURE 3: Typical PI diagram: impulsive, dynamic, and quasi-static loading (logarithmic scale).

surface bursts, respectively. Reflections, shadowing, or channelling phenomena can significantly alter the behaviour of a blast wave. In such cases, the calculation of the blast wave parameters with the empirical and semiempirical formulas proposed in [5] could result in significant errors. Thus, the use of numerical fluid-structure interaction calculations can provide a detailed identification of the loading time history of a structure or a component.

Internal explosions in confined rooms or bunkers where the pressure wave cannot escape result in a static remaining pressure after the explosion. Certain concepts for designing venting surfaces for gas explosions (e.g., [10, 11]) are publically available. However, blasts from solid explosives in confined spaces are in general faster and are characterized by much higher peak pressure and often smaller impulse values in comparison to gas explosions. The remaining static pressure from such explosions is significant and must be considered during design. Release surfaces might prove effective [12], as they are able to reduce the remaining pressure after an explosion even though their effects are not immediately evident. Nevertheless, venting surfaces cannot reduce the peak pressure associated with the first arrival of the blast wave.

2.3. Afterburning. The afterburning phenomenon may prove significant for internal explosions, depending on the type of explosive burnable products that remain after the detonation. These hot products mix with the surrounding air and burn if the conditions (in particular oxygen availability) allow combustion. Also, the presence of aluminium powder in the explosive contributes to the combustion process which leads to an additional pressure after the first peak pressure. The effect of afterburning on the resulting pressures is influenced by many factors. In numerical simulations, the approach of Miller [13] is commonly used, who proposed the addition of a certain amount of energy to the model after a specific time. Nevertheless, afterburning is not considered in the present article since injuries are most likely associated with the initial blast wave and not the afterburning.

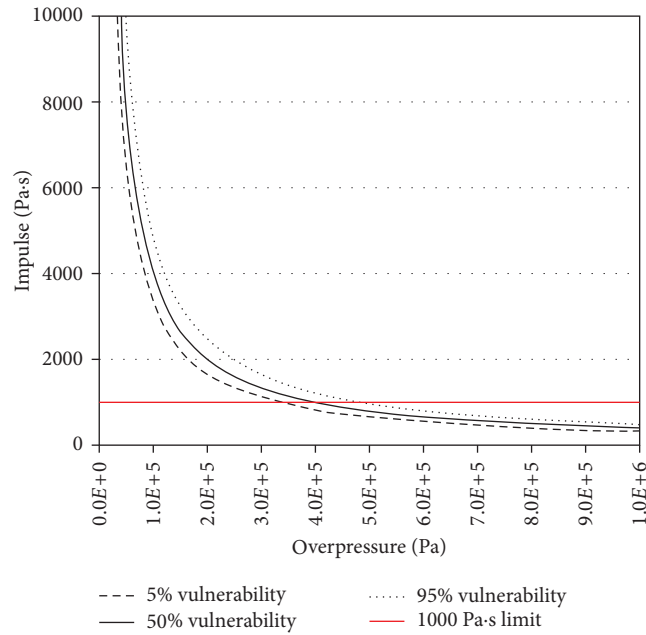


FIGURE 4: Vulnerability of humans (head impact).

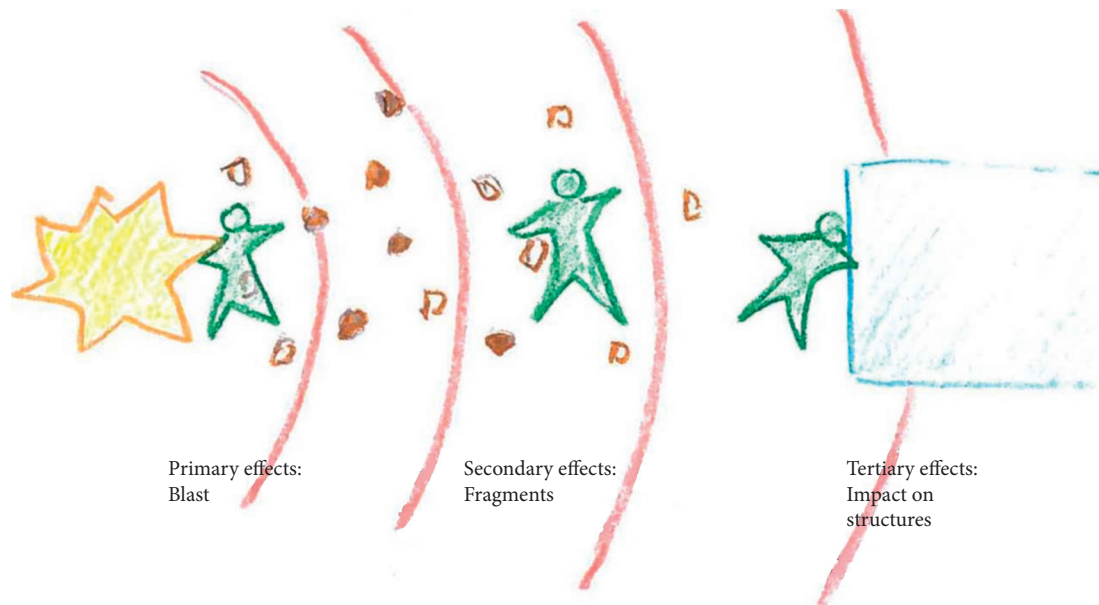


FIGURE 5: Blast effects of an explosive charge (yellow) on humans (green) due to the created blast wave (red) and fragmentation (brown).

2.4. Vulnerability of Humans. The effects of an explosion on human body can be distinguished into three broad categories (Figure 5). Concerning explosion-induced injuries, the risk due to *the primary blast effects* on humans has already been precisely described by several authors [14]. However, this is not yet the case for *secondary blast effects* that are related to the produced fragments either from the explosive charge or from the failure of structures that are propelled with high velocities striking the human body. A straightforward procedure for assessing the additional risk due to the presence of splinters as part of the secondary blast effects is currently under development [15].

In this work, the formulation of the human injury risk model is based on the work of González Ferradás et al. [16] and Mannan [17]. It utilizes the peak overpressure p_{\max} (in Pa) and the positive impulse I (in Pa·s) to determine the probability of eardrum rupture and the probability of death.

2.4.1. Causes of Death. Regarding possible causes of death, three different cases are considered: head impact, whole body impact, and lung haemorrhage. Using a PI diagram [14], it has been proven that the head impact is the dominant cause of death and its probit function can be defined as

$$Y_1 = 5 - 8.49 \ln \left(\frac{2430}{p_{\max}} + \frac{4 \cdot 10^8}{p_{\max} \cdot I} \right). \quad (1)$$

2.4.2. *Eardrum Rupture.* The probit function Y_4 of eardrum rupture is described according to the following equation:

$$Y_4 = -12.6 + 1.524 \ln(p_{\max}). \quad (2)$$

The probability of occurrence R (or the percentage of the affected population) of the corresponding injury is next determined for each death-related function using the following equation from González Ferradás et al. [16], which is a good approximation of the relevant cumulative normal distribution:

$$R_i = -3.25Y_i^3 + 48.76Y_i^2 - 206.6Y_i + 270.35. \quad (3)$$

Human risk is presented in Figure 4 as a PI diagram for a 5, 50, and 95% probability of death. Clearly, for calculating the risk of life loss at every point, both the peak pressure and the impulse values are required, meaning that a full fluid-structure interaction (FSI) analysis is required. It is noted that the influence of flying debris (secondary blast effects) is not included in these formulas.

These formulations are developed for the positive phase of spherical or hemispherical blast waves from free air and surface bursts, respectively, and can be used with both incident and reflected blast parameters. In case of confined explosions, the remaining static pressure results in an increased impulse, a phenomenon that is not considered from the available formulas. The duration of the explosions simulated in [16] is in general shorter than the time required for the effects of venting to be evident, and therefore, the above formulas can be used. In order to reduce the complexity, as an additional criterion, an impulse limit of 1000 Pa·s is used to identify critical zones at the building's interior. UFC 3-340-02 [18] proposes a limit of 1380–1725 kPa for lethal damage as a result of lung haemorrhage. This value ignores the head impact, a fact that is also recognized in UFC 3-340-02 where a much lower threshold is referenced (16 kPa). In the present study, the impulse value of 1000 Pa·s is used as an indicative limit motivated by Figure 4 and taking into account a minimum peak overpressure value of about 250 kPa. The impulse parameter is used since it is more appropriate for confined explosions. The objective of this approach is to acquire qualitative results to investigate the effects of meandering. For quantitative results, the abovementioned risk formulas should be used.

3. Blast Protective Design

Protective design of critical infrastructures against terrorist attacks is usually performed in several steps:

- (i) The first step is establishing plausible *attack scenarios*, which is a joint decision of the owner or stakeholder and the designer. Assessing the probability of occurrence of a terrorist attack through estimating sources of threat could be an appropriate

tool for defining and choosing possible scenarios. An indication is given, for example, by the North Atlantic Treaty Organization's (NATO) Standardization Agreement (STANAG) 2280 [19].

- (ii) The next step is to calculate the corresponding loads on the structure by identifying the *worst case scenario*. In some cases, this can be performed by using simple formulas for the blast wave propagation, as those proposed by Kingery and Bulmash [5] and Kinney and Graham [20], or by using a series of diagrams included in Unified Facilities Criteria such as UFC 3-340-2 [18]. Bogosian et al. [21] compared these equations with experimental data and showed that in urban environments, the propagation of the blast wave is not spherical and differences appear at the calculated blast parameters. For such complicated geometries, numerical simulations may be necessary to assess with greater precision the loading history of a structure, as described in [22].
- (iii) Subsequently, the *protection strategy* against the determined blast load according to the individual structural characteristics of the examined building (e.g., windows or facades) should be defined. Several options, validated by numerical or experimental methods, can be adopted, as described in [23].

Among the various structural and nonstructural elements, windows and facades are considered critical when facing an explosion due to their extremely fragile nature. In addition, a progressive collapse mechanism must always be prevented, as it could lead to a large death toll. In general, the explosive energy decreases rapidly by increasing the standoff distance. Hence, employing perimeter protection measures and restricting the access to a site constitute one of the most effective methods for decreasing its vulnerability. For example, protection against vehicle access can be achieved by the application of various barrier systems, as shown in [24].

3.1. *Access Point Design for Building Structures.* Depending on the security level of a site, access control measures may also be employed for the entrance of the public. The control zone should be placed in an area which should be resistant to both exterior and interior explosive events. Long queuing should be avoided to minimize the likelihood of the access point becoming a target of a terrorist attack. In case of a blast, flying debris from the failed parts of the structure (in particular from glass failure) may cause extensive injuries or fatalities. Therefore, incorporating venting in the form of release surfaces is important for mitigating the effects of a blast, in particular, if the access zone is inside the main building or attached to it. The release surfaces should be light, to be easily pushed aside by the propagating blast wave, or fragile, to instantly fail under the blast pressure. To prevent people's injury from the potential fragments of the failed opening, the release surfaces are often located at the roof of the structure. Nevertheless, the effects of venting should not be overestimated. The release surfaces (whose size is up to 10% of the

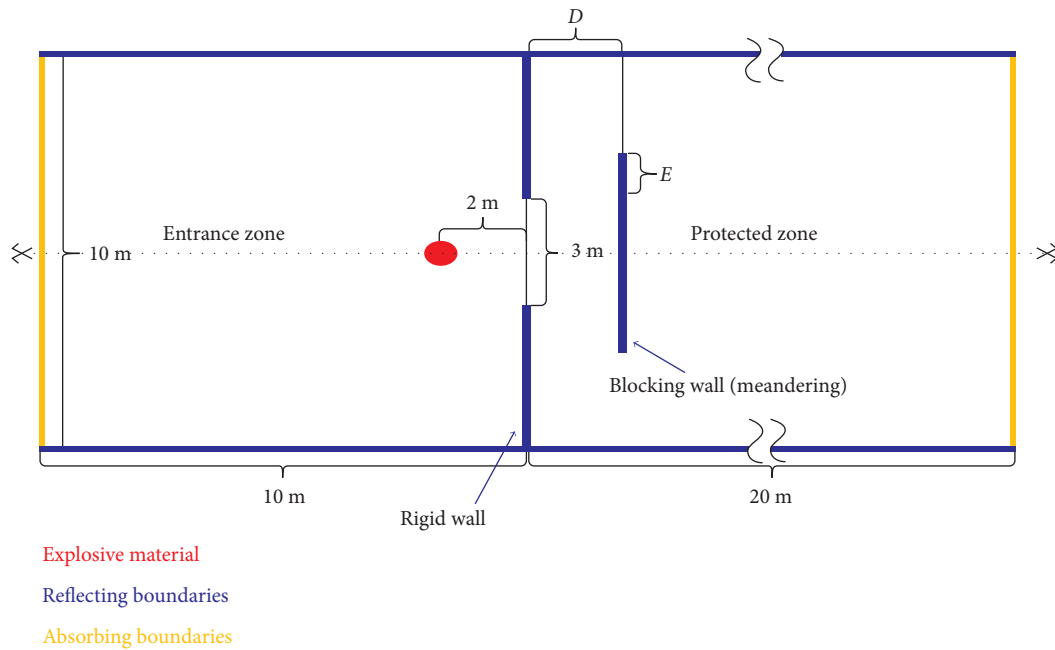


FIGURE 6: Geometry of the case study model.

room's size) have a very small impact on the peak pressure but are effective for reducing the remaining static pressure after the explosion. Clearly, the proper design of release surfaces is a challenging task since no clear indications exist in the open literature. Usually, it is advised to follow a design approach that depends on the geometry of the control zone, while the size of the openings ranges from 3% to 8% of the room's (control area's) size. Thus, these values serve only as an indication, since the actual release surface size depends also on its cross section and the determined blast scenario.

If the access control zone is located within or is connected to the main building, the propagation of the pressure wave into the adjacent structure should be avoided to confine the explosive effects only in one area. Constructions having very stiff or blast resistant doors are complicated, impractical, and space demanding since these doors must be duplicated. As shown below, a so-called meandering wall can achieve a similar protection level maintaining a design that favors the unobstructed flow of people.

4. Numerical Simulations

The current section is dedicated to the analysis of a case study simulating an explosion within an access control zone. The objective of the case study is to investigate the way a rigid (meandering) wall affects the propagation of the blast wave into an area of the building that needs to be protected. Moreover, a parametric study on the influence of the basic dimensions of the meandering wall on the attenuation of the produced detonation wave is carried out. The numerical simulations are performed with the explicit FE code EUROPLEXUS (EPX) [25], which is jointly developed by the French Commissariat à l'Énergie Atomique et aux Énergies Alternatives (CEA) and the Joint Research Centre of the

European Commission (JRC Ispra). EPX employs sophisticated fluid-structure interaction techniques and is suitable for simulating fast and severe loadings on structures such as impact and blast. The CAST3M code [26], also developed by CEA, was used to generate the mesh for the numerical models, while ParaView software [27] was used for post-processing the results.

4.1. Case Study. To reduce complexity, a simple geometry has been selected for the case study. A rectangular area is separated by a rigid wall into two parts. The first compartment is considered as the entrance zone where a possible intruder can enter carrying an improvised explosive device (IED) and walk till the opening of the rigid wall that leads to the second compartment. Just before the opening that connects the two parts, a thorough control of all persons entering the second part is considered to be implemented. The second compartment is regarded a vulnerable zone that needs to be protected, as a possible blast wave can become critical for the personnel or the structural integrity of the building.

Figure 6 shows the geometrical details of the investigated area. The entrance zone, located on the left, is connected to the protected zone, on the right, through a 3 m wide opening. The opening's width guarantees a relatively high flow of the people to avoid queuing. The height of both zones is 3 meters, while the detonation centre is located 1.5 meters from the ground level (average value for the location of a backpack in the vertical axis) and is centred to the opening, based on a worst case scenario. This is assumed to be the closest point to the protected zone that a perpetrator can reach prior to being intercepted. The mass of the IED has been selected to be equal to 25 kilograms of TNT equivalent, as an upper limit for the amount of explosives a pedestrian could carry in a backpack or small suitcase.

TABLE 1: Parameters for the JWL EOS for TNT (Dobratz and Crawford [31]).

Parameters	Description	Parameters for explosive	Parameters for air
A (Pa)	Material constant (experimental)	3.7121e11	3.7121e11
B (Pa)	Material constant (experimental)	3.23e9	3.23e9
R1	Material constant (experimental)	4.15	4.15
R2	Material constant (experimental)	0.95	0.95
Beta	Material constant (experimental)	0.25	0.25
RHO (kg/m ³)	Density	1630	1.3
EINT (J/kg)	Current internal energy		
Per unit mass	4.29e6	0.21978e6	
OMEGA	Specific heat ratio	0.3	0.3
D (m/s)	Detonation velocity	6930	—

TABLE 2: Material properties for the ideal gas law for atmospheric air.

Density (kg/m ³)	Specific heat at constant volume (J/kg.K)	Gamma ratio	Reference pressure (Pa)
1.3	716.75	1.4	1e5

As shown in Figure 6, the distance D between the opening and the introduced meandering wall and the dimension E that refers to the overlapping between the additional blocking wall and the preexisting rigid wall are not explicitly determined. These two parameters are selected as variables in the performed parametric study in order to quantify their influence on the blast wave propagation. D ranges from 1 to 3 meters, corresponding to construction specifications (e.g., wheelchair access and personnel flow). Similarly, E ranges from 0.5 to 2 meters, to allow a minimum distance of 1.5 meters between each extremity of the meandering wall and the lateral walls of the building and to guarantee comfortable access to the attached protected zone.

4.2. Numerical Model. The structural parts of the building in the case study are assumed rigid, meaning that the walls, the ceiling, and the floor of the structure are nondeformable. A postanalysis investigation of the recorded maximum pressures indicated that thick, stiff structural elements like concrete or steel walls respect this basic assumption. This hypothesis results in decreased computational power demand, since there is no need to include deformable structural parts or perform cumbersome fluid-structure interaction (FSI) calculations. Moreover, the absence of structural deformations allows an accurate study of the influence of the two parameters (D and E) on the blast wave propagation.

As already mentioned, for the numerical calculations, a purely Eulerian approach is utilized, where only the fluid part of the model is considered. The Eulerian formulation considers the computational mesh fixed while the fluid (particles) moves relative to these fixed grid points. The conservation laws of mass, momentum, and energy are expressed in a spatial framework. The discretization is based on cell-centred finite volume (FV) formulations in which the governing equations are solved in integral form. This method is conservative since the formulation ensures that the flux entering a given volume is identical to that leaving

the adjacent volume. The numerical fluxes between adjacent FVs were calculated using the Harten-Lax-van Leer-contact (HLLC) Reimann solver [28].

The fluid domain was modelled with 3D cubic finite volumes (CUVF) of 0.1 meter edge size. The size of the cubic volumes is selected after a convergence parametric study. On the extremity surfaces of the two different zones (yellow lines on Figure 6), absorbing boundaries have been introduced, in order to simulate nonreflecting atmospheric boundaries. Suitable shell elements (CL3D) that allow the introduction of an absorbing medium have been employed and from a mathematical point of view represent a supersonic outlet. As already mentioned, the rigid parts of the model are simulated as reflecting boundaries. For a 3D cubic FV, a free surface is considered by definition as a reflecting boundary. A simple duplication of the fluid nodes at the area where the rigid structure is located results into free FV surfaces that behave as reflecting boundaries.

The representation of the blast load is performed via the 1D to 3D mapping technique [29], during which a 1D numerical calculation that simulates the blast load is performed with a very fine mesh. The data obtained from the 1D calculation are mapped into a spherical shape and inserted in the coarser 3D mesh. An important detail that should be taken into account is that when transferring the results of the 1D analysis into the 3D mesh, the blast load is considered spherical, so the transformation should be performed before the wave comes to contact with any obstacles. This mapping technique can significantly accelerate the calculation time without sacrificing the accuracy of the results. For the representation of the detonation load in the 1D calculation, the Jones-Wilkins-Lee EOS law is used [30]. The material parameters for the TNT are proposed by [31] and are included in Table 1. The perfect gas law is employed for the representation of the atmospheric air in the fluid simulation. The material parameters for the atmospheric air are shown in Table 2. Finally, one

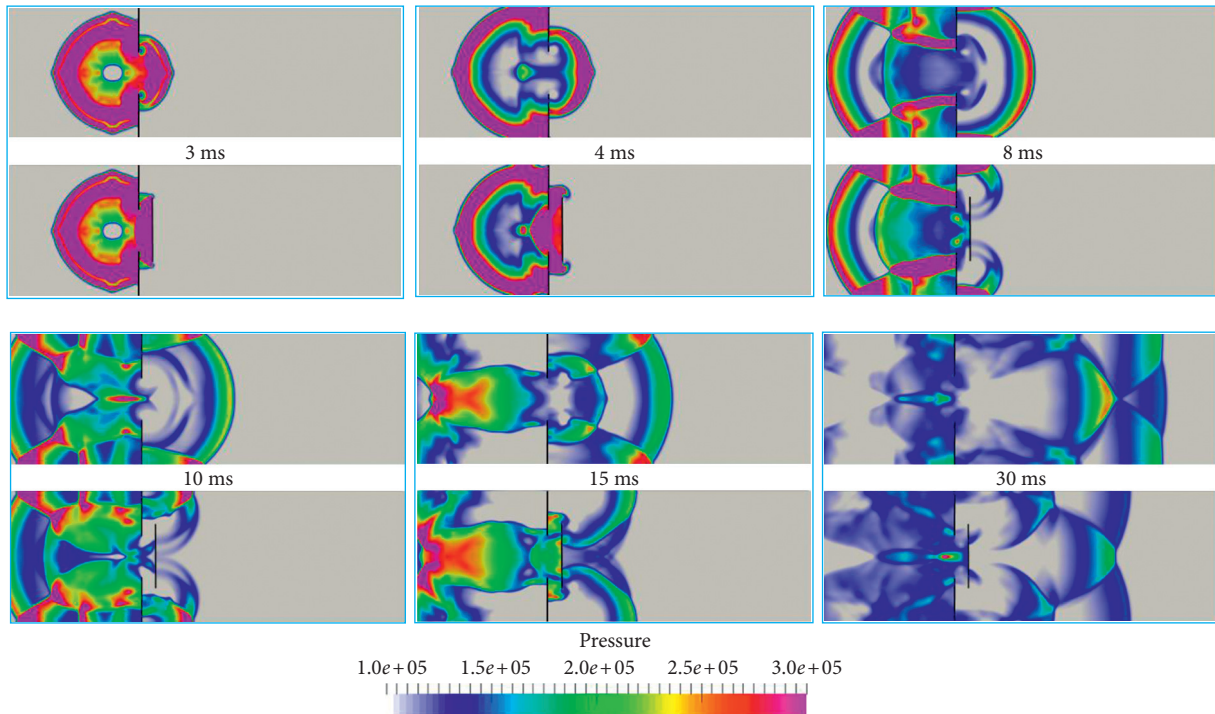


FIGURE 7: Pressure distribution of the blast wave for the “open door” model and a “meandering” model ($D = 1$ m; $E = 1$ m) for several time frames (Pa).

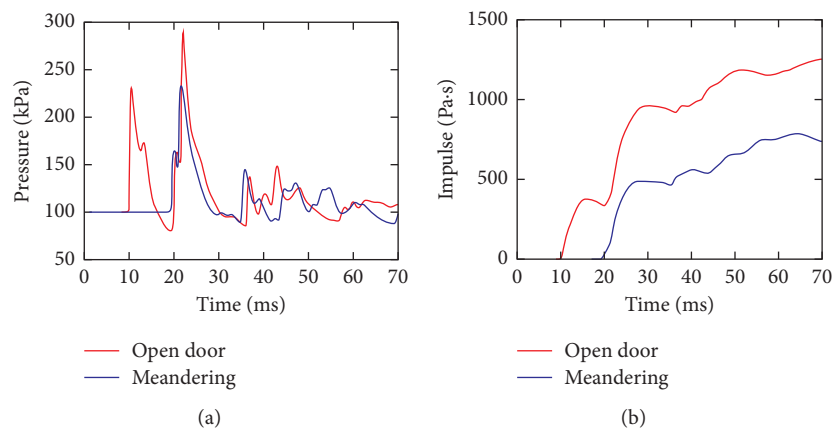


FIGURE 8: Comparison of (a) pressure and (b) impulse values for a point located in the protected zone for an “open door” model and a “meandering wall” model ($D = 1$ m; $E = 1$ m).

symmetry plane was utilized by modelling only one half of the fluid mesh.

4.3. Numerical Results. The objective of the numerical investigation is to determine the effectiveness of the introduced meandering wall. Figure 7 displays the behaviour of the propagated blast wave for the “open door” case and a “meandering” case ($D = 1$ m; $E = 1$ m) for a plane view at the height of 1.5 meters. A comparison of the two cases is performed at several time frames in order to provide a clear representation on the diversion of the blast wave from the additional wall. As already mentioned, half of the geometry was modelled in the numerical calculations so in order to

present the full model in Figure 7, special mirroring techniques are used in the postprocessing phase. The first subfigure presents the pressure field distribution at 3 ms after the detonation. At that time frame, the wave front starts being reflected on the meandering wall, as it is clear from the differences between the two models. For the “meandering” case, the blast wave starts to enter the protected zone at 4 ms and is split into two smaller waves propagating from both sides of the meandering wall. At 8 ms, it is evident that, in the “open door” case, there is one strong wave front propagating into the protected zone, while for the “meandering” case there are two weaker wave fronts. The wave propagation continues in a similar way for both cases until 30 ms after the detonation, where the two wave fronts of the “meandering”

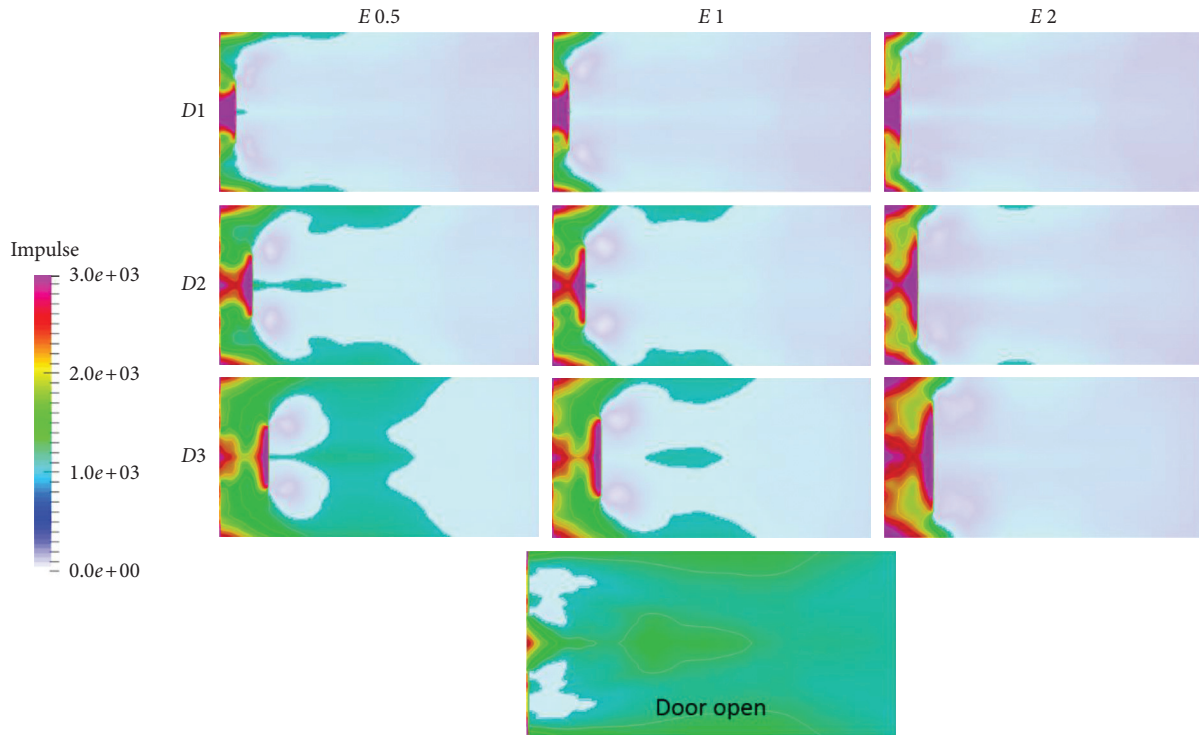


FIGURE 9: Zone of impulse higher than 1000 Pa·s for the “meandering” studied cases and the “open door” model (parameters D and E in m and impulse in $\text{Pa}\cdot\text{s}$).

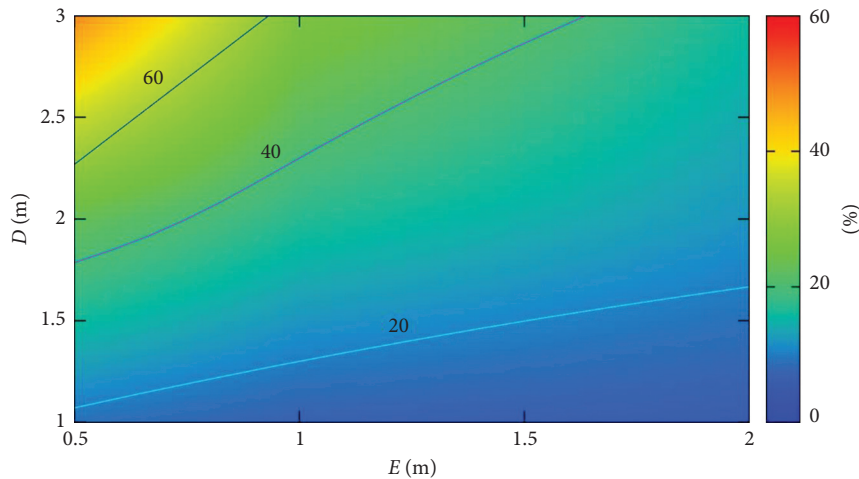


FIGURE 10: Percentage of affected area spectrum versus the investigated parameters for the “meandering” model.

case are united into one. But, as can be noticed, even in that phase the wave front of the “meandering” case is weaker than the one of the “open door” case.

The meandering wall reflects part of the initial blast wave and guides it back to the entrance area, resulting in a slightly stronger blast wave into the entrance zone. Since this zone has already been significantly affected from the initial blast wave, the additional energy due to the presence of the “meandering” wall does not affect the injury risk probability. Figure 8 presents the pressure and the impulse history for the abovementioned cases, at a point that is located at the middle of the protected zone, 7 meters from the opening, and 1.5 meters from the ground

level. From the pressure-time history, it is clear that in the “meandering” case the first peak is eliminated, while the second peak, that results from the reflection of the wave onto the lateral walls, is lower. Similar results can be derived from comparing the impulse-time histories, as there is a significant reduction of the total impulse when the meandering wall is present.

The next figures present the influence of the dimension and location of the meandering wall on the blast wave propagation. As has already been described in previous sections, areas with an impulse value larger than 1000 Pa·s are considered as high injury risk zones. Figure 9 presents the injury risk areas for the protected zone of the examined

building for several studied geometries. The results refer to the same horizontal cut that is presented in Figure 7, but the output quantity is the calculated impulse. Areas characterized by impulse values higher than 1000 Pa·s are highlighted. D and E determine the location and the size of the meandering wall as described earlier.

In the same figure, the “open door” case is also included for comparison purposes. In the “open door” case, the majority of the protected zone results in a high injury risk area. In the “meandering” case, the size of the high injury risk area varies but is always smaller than the “open door” case. It is clear that the area before the additional wall is always unprotected irrespective of the presence of the meandering wall. Moreover, in some cases, high impulse values are also recorded at the sides of the meandering wall due to the relatively strong wave fronts that are present at both those areas. Figure 10 summarizes the output of the parametric study by presenting the percentage of the injury risk area in the protected zone (above 1000 Pa·s) versus the two examined parameters. From comparing the several “meandering” cases, it can be concluded that if D is small (distance between the door and the added wall), the influence of E (dimension of overlapping length) is of minor importance. However, if D is large, the influence of E is significant (if E decreases, the blast wave that enters into the protected zone is stronger and the high injury risk areas are becoming larger).

5. Conclusions

Access control points that are located inside or attached to buildings are often adopted due to local constraints. Their design must consider possible terrorist attack scenarios (e.g., explosions) at the interior and exterior of these access control points. The mitigation of the consequences should such a terrorist attack materialize inside an access point and in the attached building can be achieved by using venting (release surfaces) and, in particular, meandering walls. The investigation shows that the reduction of the pressure is significant if meandering walls are used and that these walls can, therefore, play an important role in separating access control points from the attached buildings. Nevertheless, it is obvious that meandering walls can be considered an effective risk reduction measure and not as a full protection solution. The risk reduction concerns both blast wave effects and, for obvious reasons, fragments resulting from explosions and shooting attacks. Herein, the idealized situation that is investigated can be extended to include additional parameters. As has been presented in the current article, the presence of a rigid wall standing between an explosion’s detonation centre and a target, can effectively reduce the severity of the impacting blast wave. It is therefore recommended the addition of such elements (varying in size and geometry) in order to mitigate the risk of terrorist attacks.

Conflicts of Interest

The authors declare that there are no conflicts of interest regarding the publication of this paper.

References

- [1] A. M. Lewis, “State of the art report on European legislation relating to explosives and explosive detection system for non-aviation configurations,” Tech. Rep. JRC84076, Joint Research Centre, Ispra, Italy, 2013.
- [2] B. M. Luccioni, R. D. Ambrosini, and R. F. Danesi, “Analysis of building collapse under blast loads,” *Engineering Structures*, vol. 26, no. 1, pp. 63–71, 2004.
- [3] M. Larcher, M. Arrigoni, C. Bedon et al., “Design of blast-loaded glazing windows and facades: a review of essential requirements towards standardization,” *Advances in Civil Engineering*, vol. 2016, Article ID 2604232, 14 pages, 2016.
- [4] R. Hajek and M. Foglar, “Numerical and experimental analysis of the effect of rigid barriers on blast wave propagation,” *Journal of Structural Engineering*, vol. 141, no. 12, p. 04015061, 2015.
- [5] C. N. Kingery and G. Bulmash, “Airblast parameters from TNT spherical air burst and hemispherical surface burst,” Tech. Rep. ARBRL-TR-02555, Defence Technical Information Center, Ballistic Research Laboratory, Aberdeen Proving Ground, MD, USA, Tech. Rep. ARBRL-TR-02555, 1984.
- [6] M. Larcher, “Pressure-time functions for the description of air blast waves,” Tech. Rep. JRC46829, Joint Research Centre, Ispra, Italy, 2008.
- [7] V. Karlos and G. Solomos, “Calculation of blast loads for application to structural components,” Tech. Rep. EUR 26456EN, Joint Research Centre, Publications Office of the European Union, Luxembourg, 2013.
- [8] V. Karlos, G. Solomos, and M. Larcher, “Analysis of the blast wave decay coefficient using the Kingery-Bulmash data,” *International Journal of Protective Structures*, vol. 7, no. 3, pp. 409–429, 2016.
- [9] M. Larcher, “Development of discrete cracks in concrete loaded by shock waves,” *International Journal for Impact Engineering*, vol. 36, pp. 700–710, 2009.
- [10] J. Li and H. Hao, “Internal and external pressure prediction of vented gas explosion in large rooms by using analytical and CFD methods,” *Journal of Loss Prevention in the Process Industries*, vol. 49, pp. 367–381, 2017.
- [11] EN14494, “Gas explosion venting protective systems,” 2007.
- [12] M. Larcher, F. Casadei, and G. Solomos, “Influence of venting areas on the air blast pressure inside tubular structures like railway carriages,” *Journal of Hazardous Materials*, vol. 183, no. 1–3, pp. 839–846, 2010.
- [13] P. J. Miller, “A reactive flow model with coupled reaction kinetics for detonation and combustion in non-ideal explosives,” *MRS Proceedings*, vol. 418, 1995.
- [14] M. Larcher, R. Forsberg, U. Bjoernstig, A. Holgersson, and G. Solomos, “Effectiveness of finite element modelling of damage and injuries for explosions inside trains,” *Journal of Transportation Safety and Security*, vol. 8, pp. 83–100, 2015.
- [15] G. Valsamos, F. Casadei, M. Larcher, and G. Solomos, “Implementation of flying debris fatal risk calculation in EUROPLEXUS,” Tech. Rep. JRC94805, Joint Research Centre, Publications Office of the European Union, Luxembourg, 2015.
- [16] E. González Ferradás, F. Díaz Alonso, M. Doval Miñarro, A. Miñana Aznar, J. Ruiz Gimeno, and J. Sánchez Pérez, “Consequence analysis by means of characteristic curves to determine the damage to humans from bursting spherical vessels,” *Process Safety and Environmental Protection*, vol. 86, no. 2, pp. 121–129, 2008.

- [17] S. Mannan, *Lees' Loss Prevention in the Process Industries: Hazard Identification, Assessment and Control*, Vol. 2, Elsevier, Amsterdam, 2005.
- [18] Department of Defence USA, *Unified Facilities Criteria, UFC 3-340-2*, 2008.
- [19] "NATO. STANAG 2280: design threat levels and handover procedure for temporary protective structures," 2008.
- [20] G. F. Kinney and K. J. Graham, *Explosive Shocks in Air*, Springer, Berlin, Germany, 1985.
- [21] D. Bogosian, J. Ferritto, and Y. Shi, "Measuring uncertainty and conservatism in simplified blast models," in *Proceedings of 30th Explosive Safety Seminar*, Atlanta, Georgia, August 2002.
- [22] M. Larcher and F. Casadei, "Explosions in complex geometries—a comparison of several approaches," *International Journal of Protective Structures*, vol. 1, no. 2, pp. 169–195, 2010.
- [23] M. Larcher, A. Stolz, L. Rüdiger, and M. Steyerer, "Statische Ersatzlasten und "Ingenieurverfahren",” in *Berichte aus dem Konstruktiven Ingenieurbau Workshop Bau-Protect*, N. Gebbeken, K. Thoma, M. Rüdiger, and M. Klaus, Eds., pp. 117–130, Universität der Bundeswehr München, Neubiberg, Germany, 2012.
- [24] FEMA, "Site and urban design for security—guidance against potential terrorist attacks," Tech. Rep. FEMA 430, FEMA, Washington, DC, USA, 2007.
- [25] Joint Research Centre and Commissariat à l'énergie atomique et aux énergies alternatives, *EUROPLEXUS*, <http://www-epx.cea.fr/>.
- [26] Commissariat à l'énergie atomique et aux énergies alternatives, *CAST3M*: <http://www-cast3m.cea.fr/>.
- [27] ParaView: <http://www.paraview.org>.
- [28] F. Daude and P. Galon, "On the computation of the baer-nunziato model using ALE formulation with HLL-and HLLC-type solvers towards fluid-structure interactions," *Journal of Computational Physics*, vol. 324, pp. 189–230, 2016.
- [29] M. Larcher, F. Casadei, and G. Solomos, "Simulation of blast waves by using mapping technology in EUROPLEXUS," Tech. Rep. JRC91102, Joint Research Centre, Publications Office of the European Union, Luxembourg, 2014.
- [30] E. Lee, J. Horning, and J. Kury, "Adiabatic expansion of high explosives detonation products," University of California, Lawrence Livermore National Laboratory, Livermore, CA, USA, 1968.
- [31] B. Dobratz and P. Crawford, *LLNL Explosives Handbook: Properties of Chemical Explosives and Explosive Simulants*, University of California, Lawrence Livermore National Laboratory, Livermore, CA, USA, 1985.

Research Article

Impact Force Evaluation of the Derailment Containment Wall for High-Speed Train through a Collision Simulation

Hyun-Ung Bae ¹, Kyung-Min Yun ¹, Jiho Moon ² and Nam-Hyoung Lim ¹

¹Department of Civil Engineering, Chungnam National University, 34134 Daejeon, Republic of Korea

²Department of Civil Engineering, Kangwon National University, 24341 Chuncheon, Republic of Korea

Correspondence should be addressed to Nam-Hyoung Lim; nhrim@cnu.ac.kr

Received 23 August 2017; Accepted 12 November 2017; Published 14 January 2018

Academic Editor: Chiara Bedon

Copyright © 2018 Hyun-Ung Bae et al. This is an open access article distributed under the Creative Commons Attribution License, which permits unrestricted use, distribution, and reproduction in any medium, provided the original work is properly cited.

Fatal train accidents usually involve derailments or collisions. These derailment/collision accidents are infrequent. However, the damage due to derailment can be catastrophic. Derailment containment walls are usually used in Korea to minimize such damages. However, the impact forces that are needed to design the derailment containment walls were not well defined, and only limited studies were conducted for the behavior of the derailment containment walls. In this study, the focus was made on the impact force analysis of the containment wall through a series of 3D collision simulation after train derailment. Finite element modeling was conducted to analyze the dynamic behavior of the derailed train that collides with a structure such as containment wall using the LS-DYNA analysis software application. The FE models of car bodies, bogie frames, and wheel sets were created such that full conformity was achieved between their numerical models and actual vehicles with respect to the masses and principal mass moments of inertia. In addition, various installation situations of the containment wall were considered for the collision simulation. Finally, the economical alternative method to reduce the impact force was proposed.

1. Introduction

Fatal train accidents are usually caused by derailments or collisions. These derailment/collision accidents are infrequent. However, when they occur, the damage is catastrophic. Therefore, protection infrastructure is installed to minimize such damage. In principle, the most ideal preparation is to prevent derailments from occurring. However, it is also necessary to consider the physical means needed to reduce/minimize damage by unexpected accidents such as natural disasters or man-made hazards. This is a concept of protection for derailed trains [1, 2].

There are representative accidents that would occur if a derailed train collided with an overbridge or a surrounding building or two trains crashed into each other and then fell under a bridge substructure [2]. The main factors are the spread and amplification of secondary damage by the behavior after the derailments (primary damage). In other words, if secondary collisions with surrounding buildings by a derailed train are prevented, the damage would be

mitigated or minimized. In addition, if the secondary derailment resulting from a collision between trains or falling under a bridge is prevented, the damage would be significantly reduced or minimized [1, 2].

Since the high-speed railway was induced in Korea, “derailment containment walls” have been constructed to mitigate and minimize accident damage by preventing trains from colliding with catenary poles or falling under a bridge when they are derailed by earthquake, buckling, or defects in tracks/trains in bridge sections. At present, the derailment containment walls are uniformly designed and constructed on bridges serving train speeds of 200 km/h or higher. Accordingly, the need for judgment of effectiveness and feasibility review in terms of economics and constructability has been presented by designers and constructors.

The research related to the collision between the derailed train and the protection infrastructure is tenuous in the world. In the previous research [2], we developed the 3D collision simulation model after train derailment. In this paper, using this collision simulation model, various

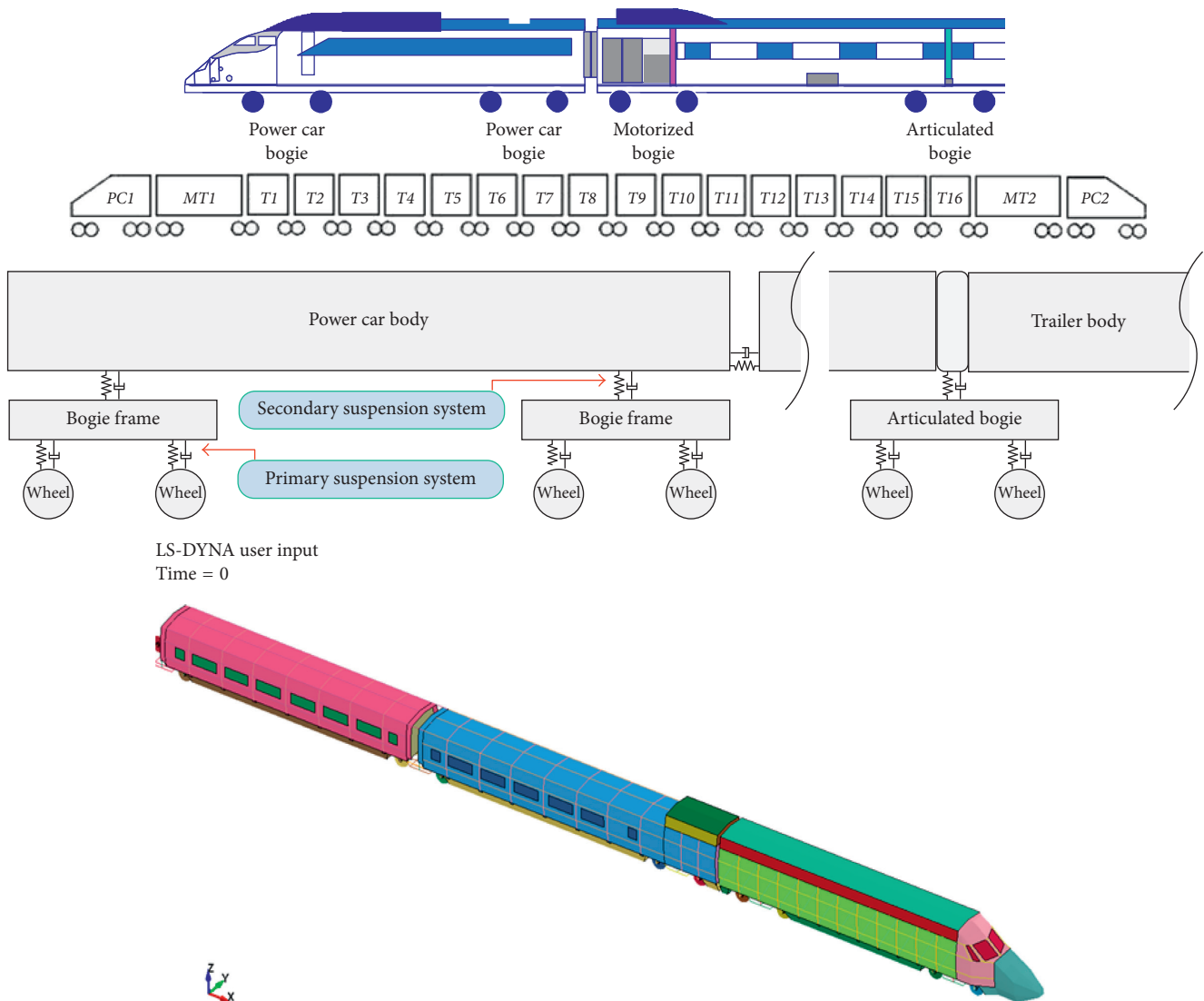


FIGURE 1: Model concept of KTX.

installation situations of the containment wall were considered by the parameters (location and height of the wall) that affect the impact force and containment effects of the containment walls. Therefore, we propose the advantageous geometric condition of the containment wall through the collision simulation (between the derailed train and the protection infrastructure) after train derailment. Finally, the economical alternative method to reduce the impact force was proposed.

2. Analysis Model

FE modeling was conducted to analyze the dynamic behavior of the three-dimensional train and structure using the LS-DYNA [3] nonlinear finite element analysis software application (Version 971). This analysis model developed in the preceding research [2] was verified by several methods. For the numerical verification about energy balance before and after collision of the train, simulations were performed for a collision accident scenario (i.e., a head-on collision

accident scenario) of the railroad cars defined by Railroad Safety Act [4]. In addition, it was confirmed that the typical derailment behavior (slip and rollover) of the train model was reproduced correctly through comparison with the theoretical wheelset derailment model by the preceding researchers [5, 6]. Moreover, the analysis model collision behavior when a derailed train collides with a structure such as containment wall was verified by results of the previous research [7].

The train model is a Korea Train eXpress (KTX) high-speed train, operated by Korean railways as shown in Figure 1. The rail was modeled by the head profile of UIC 60 Rail, and the standard gauge of a track was applied with a width of 1,435 mm as shown in Figure 2. The track types were modeled by a concrete slab. Table 1 shows the element used in LS-DYNA for modeling the track.

Contact conditions between the train and track were modeled using 3D contact elements such as surface-to-surface and node-to-surface as shown in Figure 3 and Table 2. The values of friction coefficient are based on

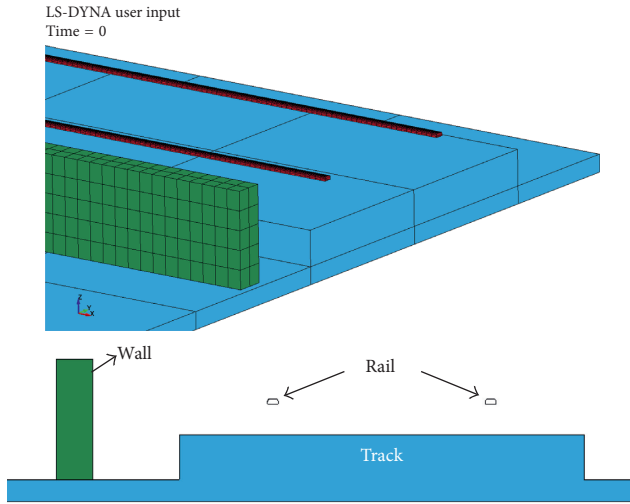


FIGURE 2: Modeling of the track.

TABLE 1: The element used in LS-DYNA for modeling the track.

Component	Element used in LS-DYNA
Rail (UIC 60/gauge 1,435 mm)	*SECTION_SHELL/*MAT_RIGID
Track and wall (concrete)	*SECTION_SOLID/*MAT_ELASTIC (i) Young's modulus: 31,000 MPa (ii) Poisson's ratio: 0.2

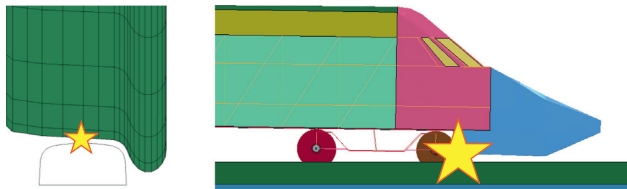


FIGURE 3: Contact conditions between the train and track.

TABLE 2: Contact conditions between the train and track.

Contact condition	Friction coefficient
Wheel~rail (general surface)	$F_{stat.} = 0.4/F_{dyn.} = 0.3$
Wheel~concrete slab (surface to surface)	$F_{stat.} = 0.55/F_{dyn.} = 0.45$
Train~wall (surface to surface and nodes to surface)	$F_{stat.} = 0.0/F_{dyn.} = 0.0$

references [8, 9]. However, in reality, measuring and identifying the frictional force between the train and the wall when collision is very difficult because it is occurred by the impact for a split second (it is supposedly close to zero). In Moyer's study conducted in the U.S. [10], the effect on impact force with respect to increase of magnitude of frictional force was investigated—"This parameter has very little effect, although higher barrier friction increases impact forces slightly." Therefore, the friction coefficients between the train and the wall were ignored in this study.

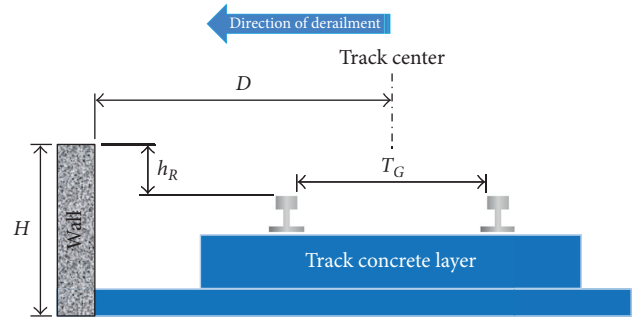


FIGURE 4: Geometric conditions of the containment wall on the railway bridge in Korea.

TABLE 3: Geometric condition of the track.

Line	H (mm)	h_R (mm)	T_G (mm)	D (mm)
Gyeongbu HSR	975	271	1,435	2,000 (1.39 T_G)
Honam HSR	940	234	1,435	1,880 (1.31 T_G)

TABLE 4: Analysis cases.

Parameter	Case	D	h_R (mm)	Remark
Effect of D	Case 1	$0.98 T_G$	271	Decrease D based on Case 3
	Case 2	$1.31 T_G$	234	Honam HSR reference model
	Case 3	$1.39 T_G$	271	Gyeongbu HSR reference model
	Case 4	$1.60-1.90 T_G$	—	Guidance by running rail
Effect of h_R	Case 5	$1.39 T_G$	436	Increase h_R based on Case 3
	Case 6	$0.98 T_G$	436	Increase h_R based on Case 1
	Case 7	$0.98 T_G$	106	Decrease h_R based on Case 1

3. Parametric Study to Evaluate the Effects of the Containment Wall

The parameters affecting the impact force and containment effects of the containment walls were selected as the location and height of the wall. The geometric conditions and material properties of the track were modeled based on the conditions of the Gyeongbu High-Speed Railway and Honam High-Speed Railway (concrete track) in Korea as shown in Figure 4 and Table 3. The details of analysis cases are shown in Table 4. The simulation train speed is 300 km/h.

Unless considering the rail to be the train derailment condition, the train is supposed as the already derailed train and only expected incident angle and speed are analyzed as variables. Therefore, the behavior after derailment becomes consistent. This study reproduced the drop of wheels from the rail to reproduce the actual derailment as closely as

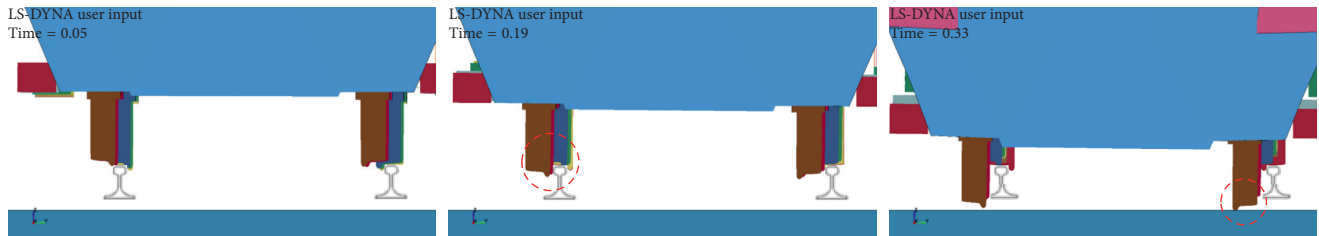


FIGURE 5: Derailment behavior by wheel climbing on simulation.

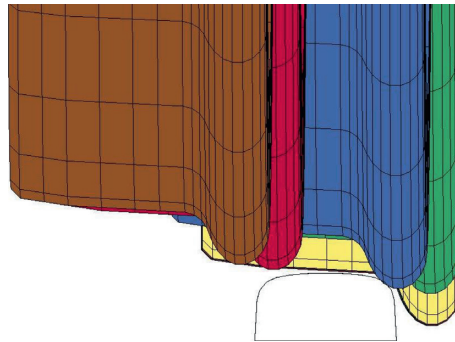


FIGURE 6: Derailment situation of wheels by wheel climbing on simulation.

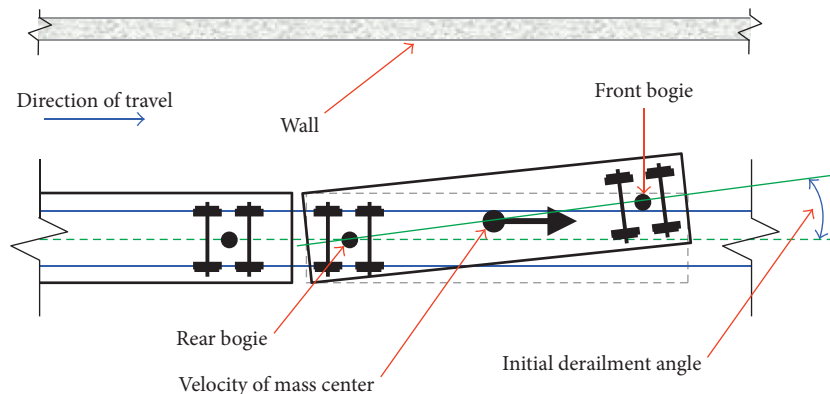


FIGURE 7: Initial derailment angle on simulation.

possible. Therefore, many changes were effected in the train behavior after derailment as the falling points of wheels were changed by the interference of the wheels and rails (Figure 5). The derailment behavior was reproduced under the slip and rollover condition by wheel climbing (Figure 6).

As soon as wheels of the front and rear bogie drop from the rail head, the car veer off to the wall and rotates about the vertical axis of the rear bogie as shown in Figure 7. At this time, angle between the longitudinal axis of the car and the track center is called "derailment angle" as shown in Figure 7. A certain initial value of the derailment angle was assumed for the convenience of the analysis. Initial derailment angles from 0.3 to 0.4° were supposed considering a rail surface. (If the initial derailment angle is less than 0.3° , the derailment does not occur well by wheel flange. Also, if the angle is greater than 0.4° , it will fall directly onto the track surface without the interference of the wheels and rails.) The initial

velocity vector (300 km/h) of the mass center of the first car remains parallel to the track centerline.

3.1. The Effect of Separation Distance from Track Center

3.1.1. $D = 1,400 \text{ mm}$ ($0.98 T_G$). Case 1 (distance effect 1) has minimized the separation distance (D) of the containment wall from the track center by putting the wall closer to the track concrete layer (TCL), as shown in Figure 8. In the case of derailment-collision behavior 1 as shown in Figure 9(a), the axlebox collides with the containment wall after the drop of the wheels on the concrete surface (TCL). Then, the first impact force is 160 kN , but the subsequent impact forces increase due to repetitive impact of the axleboxes between the rail and the wall. In the case of derailment-collision behavior 2 as shown in Figure 9(b), the axlebox collides with the containment wall before the drop of the wheels on the

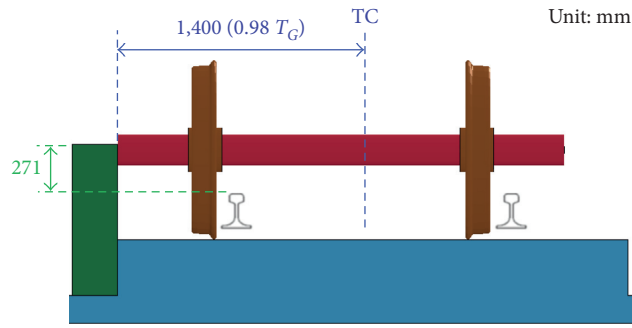


FIGURE 8: Overview of distance effect 1.

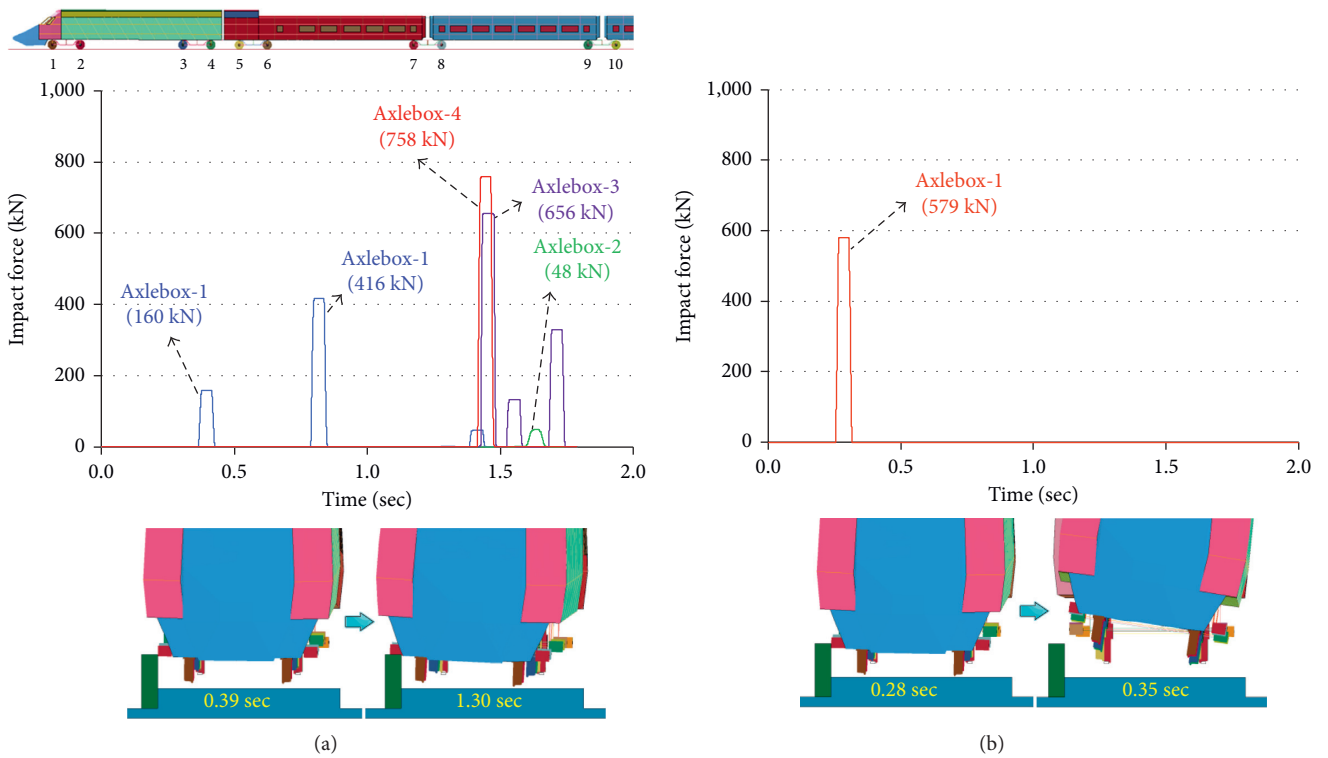


FIGURE 9: Derailment-collision behavior and impact force (distance effect 1). (a) Derailment-collision behavior 1. (b) Derailment-collision behavior 2.

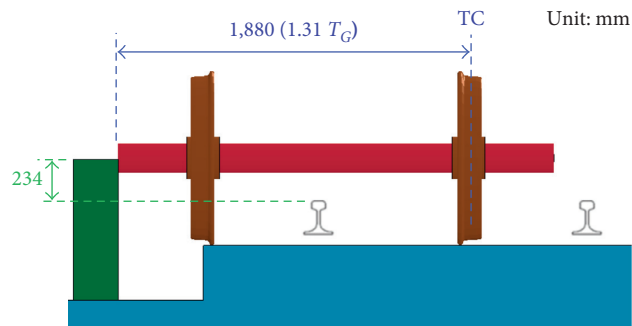


FIGURE 10: Overview of distance effect 2.

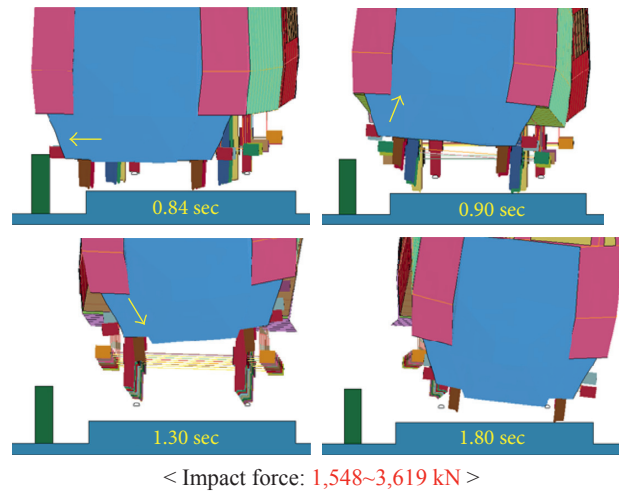


FIGURE 11: Derailed-collision behavior and impact force (distance effect 2).

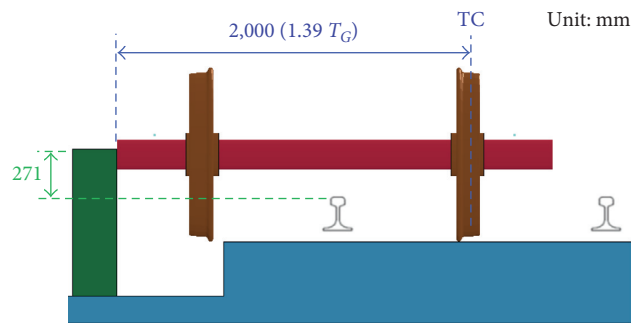


FIGURE 12: Overview of distance effect 3.

concrete surface. Then, the impact force is computed at 579 kN, and the derailed train bounces to the inner track. In both behaviors, if the containment wall is not destroyed by collision, the horizontal deviation of a derailed train is contained within the intended area (track area) after collision.

3.1.2. $D = 1,880 \text{ mm}$ ($1.31 T_G$). In Case 2 of distance effect 2, the separation distance (D) of the containment wall from the track center is set from $1.0 T_G$ to $1.5 T_G$: the condition of Honam HSR (Figure 10). In this case, the impact force is significantly greater than distance effect 1. In this case, the impact force acting on the containment wall is computed as a range of about 1,500 to 3,900 kN in accordance with collision conditions that considerably vary due to derailment conditions (interference of the wheels and rails). As shown in Figure 11, if the containment wall is not destroyed by collision, the horizontal deviation of a derailed train is contained within the intended area (track area) after collision.

3.1.3. $D = 2,000 \text{ mm}$ ($1.39 T_G$). In Case 3 of distance effect 3, the separation distance (D) of the containment wall from the track center is set from $1.0 T_G$ to $1.5 T_G$: the condition of

Gyeongbu HSR (Figure 12). In this case, the impact force is also greater than distance effect 1, like distance effect 2. In this case, the impact force acting on the containment wall is computed for the range of about 600 to 4,000 kN in accordance with collision conditions. As shown in Figure 13, if the containment wall is not destroyed by collision, the horizontal deviation of a derailed train is contained within the intended area (track area) after collision.

3.1.4. $D = \text{More than } 2,300 \text{ mm}$ ($1.60 \sim 1.90 T_G$). Case 4 (distance effect 4) has sufficiently extended the separation distance (D) until the inner wheels of a derailed train can be guided by running a rail before the outer (derailment direction) wheels collide with the containment wall (Figure 14).

The concept of this case is based on derailment containment concepts in the UK [11, 12] and Germany [13] that the primary impact damage be restricted by a running rail, and then the wall secondarily contains the horizontal deviation to a reduced force. Hence, the horizontal impact forces of the containment wall can be advantageous in terms of containment wall design.

The separation distance (D) from the track center must be more than $1.60 T_G$ in order that a wheel does not contact the containment wall and more than $1.88 T_G$ in order that an

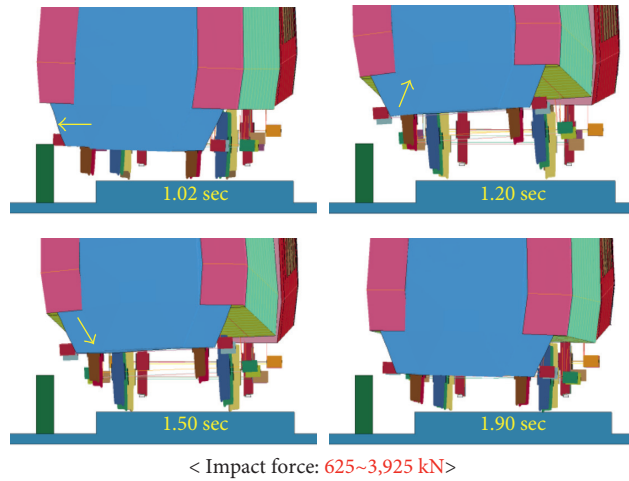


FIGURE 13: Derailment-collision behavior and impact force (distance effect 3).

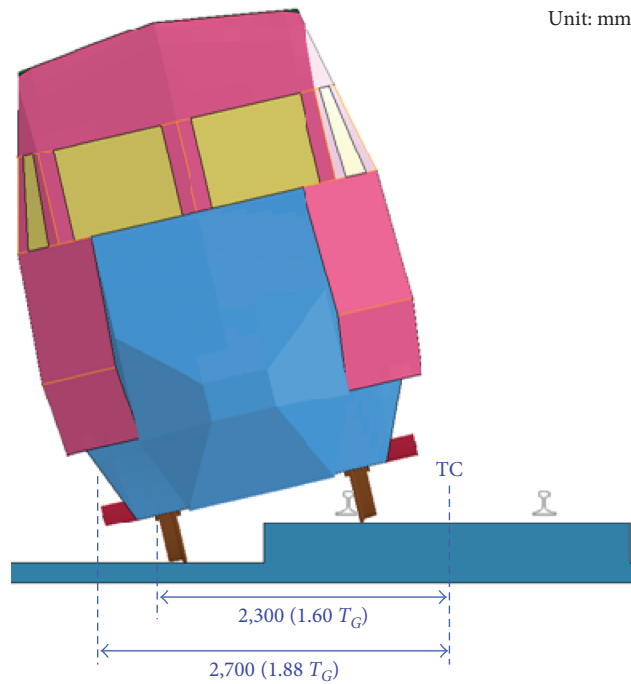


FIGURE 14: Overview of distance effect 4.

axlebox does not contact the containment wall (Figure 14). The dimensions of the wheel and the axlebox are that of the KTX train, and the track gauge (T_G) is 1,435 mm (standard gauge).

In the case of derailment-collision behavior 1 as shown in Figure 15(a), the first wheel vertically jumps after colliding with the rail, and then the 5th and 6th wheels of succeeding trailers (motorized bogie) also are sequentially guided by the rail. In case of derailment-collision behavior 2 as shown in Figure 15(b), the first wheel is vertically jumped from the ground due to severe snap behavior without contact with the rail. Hence, a derailed train has the possibility of collision with catenary ducts/poles, or falling under a bridge because of the impossibility of containment protection by the

running rail. Therefore, a containment wall of the outer side structure type is needed in this case. Also, this case shows that perfectly protecting the derailed train for all the derailment situations/conditions is impossible.

3.2. The Effect of Height above Rail Surface

3.2.1. $h_R = 436 \text{ mm}/D = 2,000 \text{ mm}$ ($1.39 T_G$). Case 5 (height effect 1) has extended the height of the containment wall (h_R) until the whole area of the axlebox can contact the containment wall (Figure 16). In this case, the collision behavior has consistency, without varying collision behaviors (the gap of impact force due to deference of contact area) according to the derailment conditions. And the containment effect of

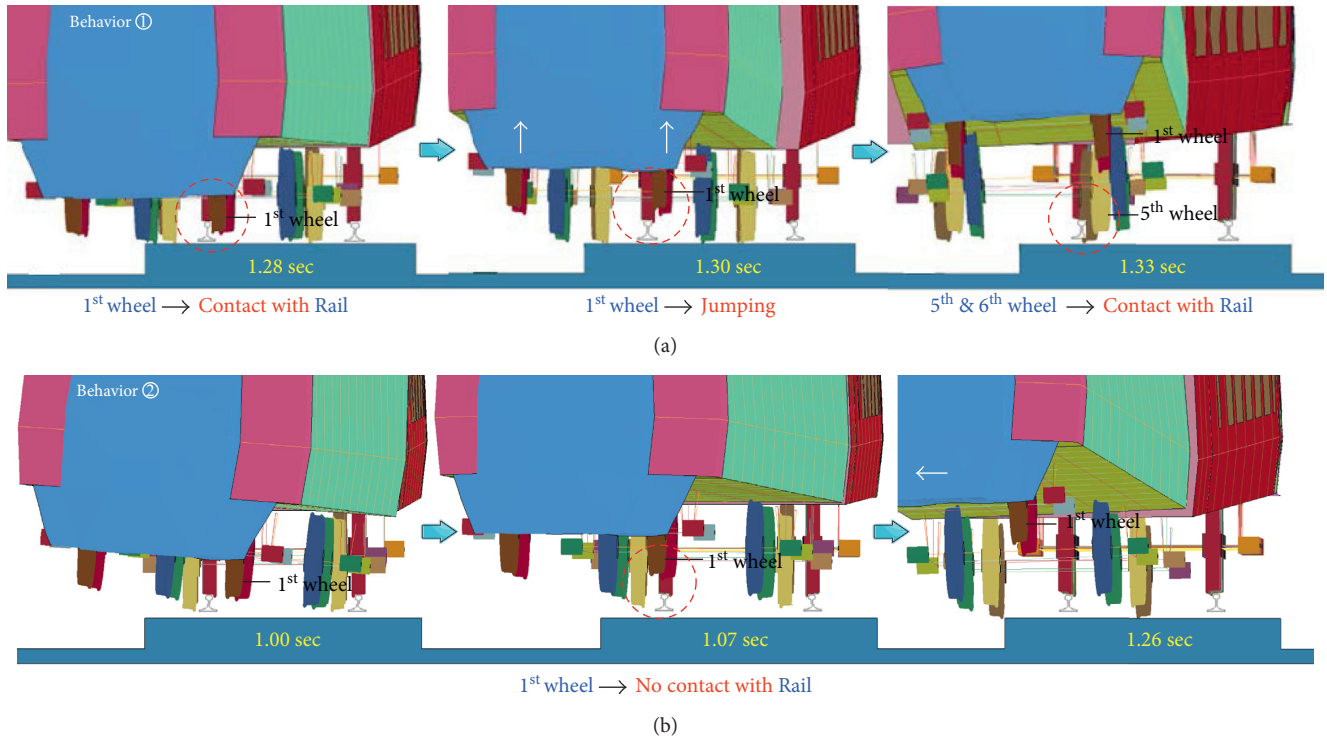


FIGURE 15: Derailment-collision behavior (distance effect 4). (a) Behavior 1. (b) Behavior 2.

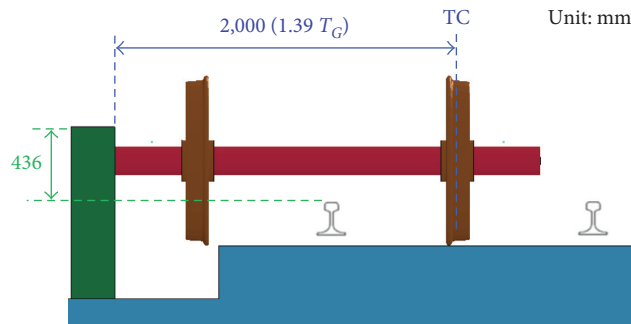


FIGURE 16: Overview of height effect 1.

a derailed train is excellent as shown in Figure 17. However, the maximum impact force acting on the containment wall is the greatest: 4,064 kN.

3.2.2. $h_R = 436 \text{ mm}/D = 1,400 \text{ mm} (0.98 T_G)$. Case 6 (height effect 2) has minimized the separation distance (D) of the containment wall from the track center by putting the wall closer to the TCL and has extended the height of the containment wall (h_R) until the whole area of the axlebox can contact the containment wall (Figure 18). In this case, the collision behavior has consistency without varying collision behaviors according to the derailment conditions. And the containment effect of a derailed train is excellent as shown in Figure 19. Also, the impact force (1,168 kN) is considerably smaller than the height effect 1 (4,064 kN)

because of reduction of inertial force due to reduced lateral behavior distance of the derailed train. However, the subsequent impact forces are likely to increase due to repetitive impact of the axlebox between the rail and the wall.

3.2.3. $h_R = 106 \text{ mm}/D = 1,400 \text{ mm} (0.98 T_G)$. Case 7 (height effect 3) minimizes the separation distance (D) of the containment wall from the track center by putting the wall closer to the TCL and has reduced the height of the containment wall (h_R) until the axlebox does not collide with the containment wall, but the wheel can contact the containment wall (Figure 20). In this case, the impact force (500 to 850 kN) is much smaller than in the height effect 1 (4,064 kN). In addition, repetitive impact is less likely to

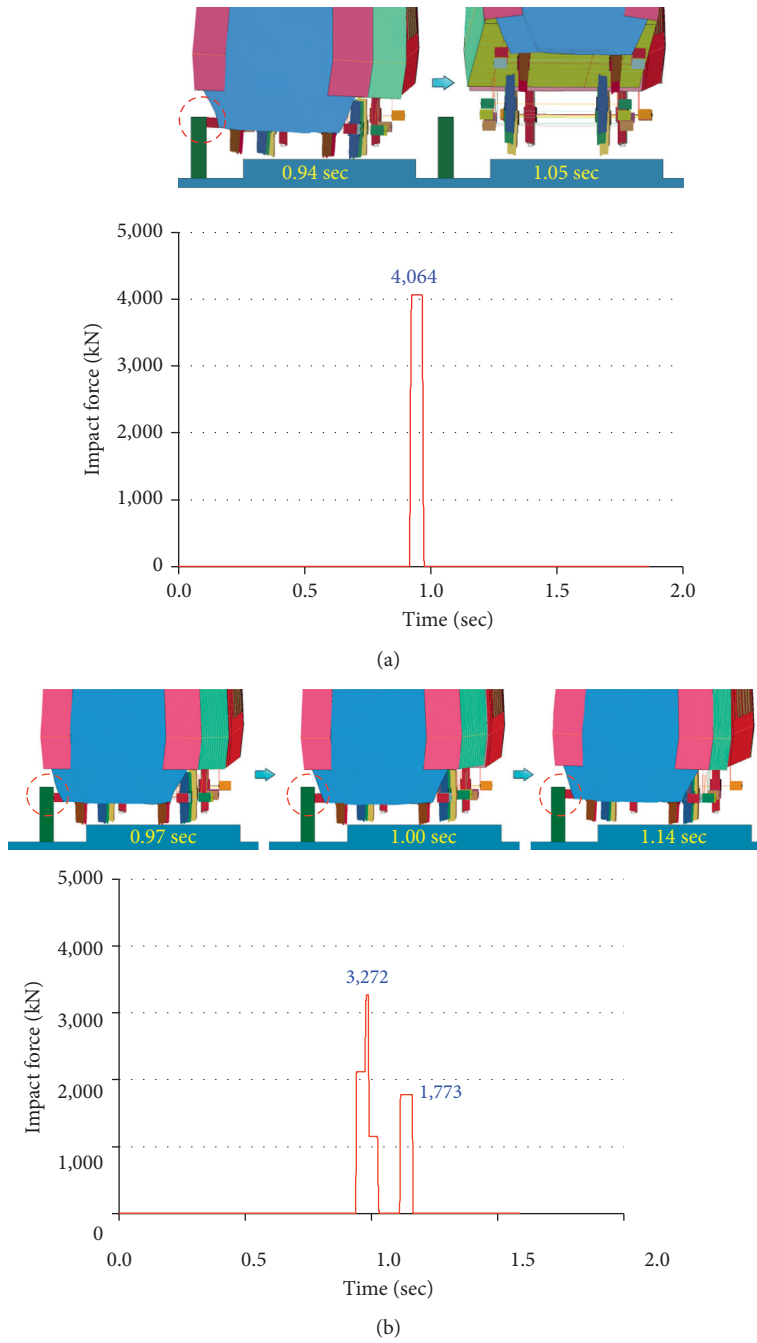


FIGURE 17: Derailment-collision behavior and impact force (height effect 1). (a) Derailment-collision behavior 1. (b) Derailment-collision behavior 2.

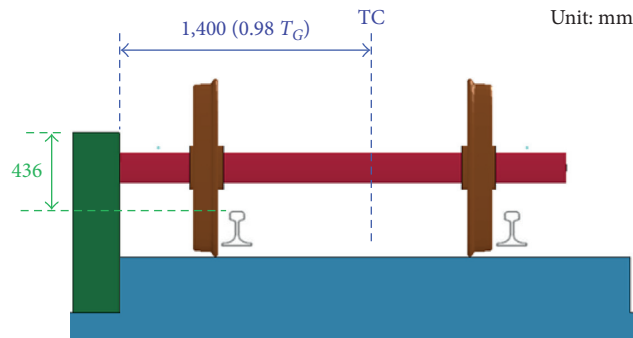


FIGURE 18: Overview of height effect 2.

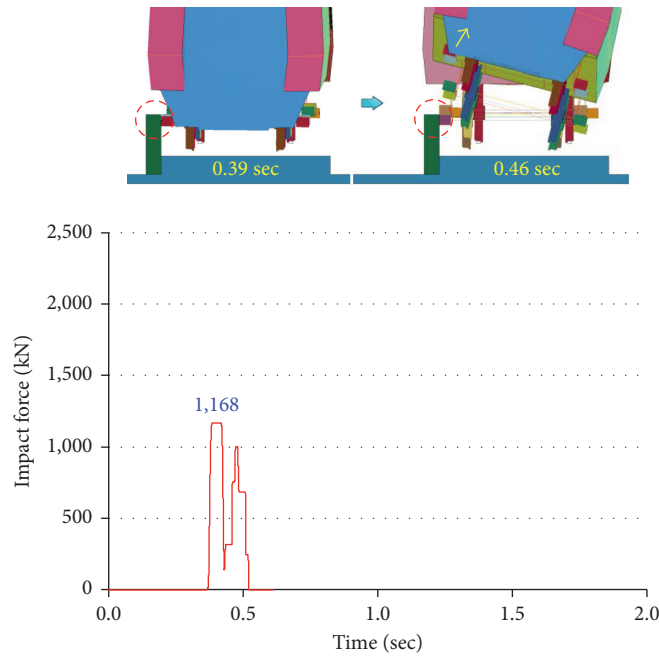


FIGURE 19: Derailment-collision behavior and impact force (height effect 2).

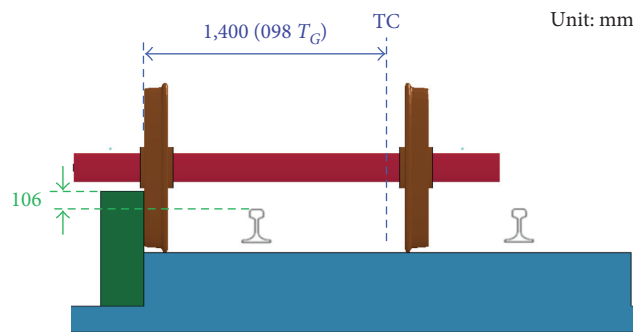


FIGURE 20: Overview of height effect 3.

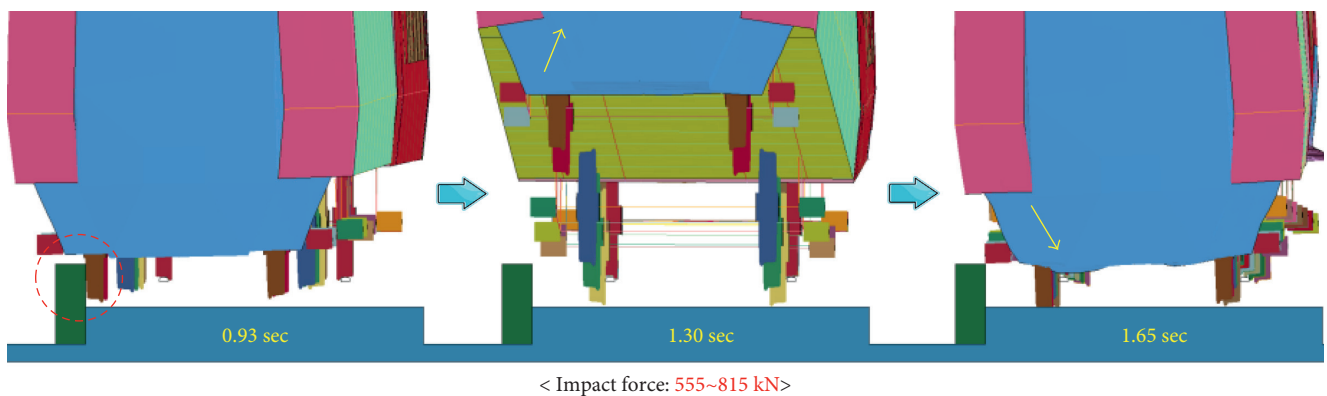


FIGURE 21: Derailment-collision behavior and impact force (height effect 3).

occur between the rail and the wall compared with the height effect 2. As shown in Figures 21 and 22, the collision behaviors due to difference of the contact area can vary according to the derailment conditions, but the impact force (500 to 850 kN) is smaller than both the height effect 2

(1,168 kN) and the distance effect 1 (160 to 1,500 kN). Also, this case has an advantage in economical efficiency since height of the wall is reduced but also has a disadvantage for the difficulty of maintenance work for the inspection of cracks on the TCL side.

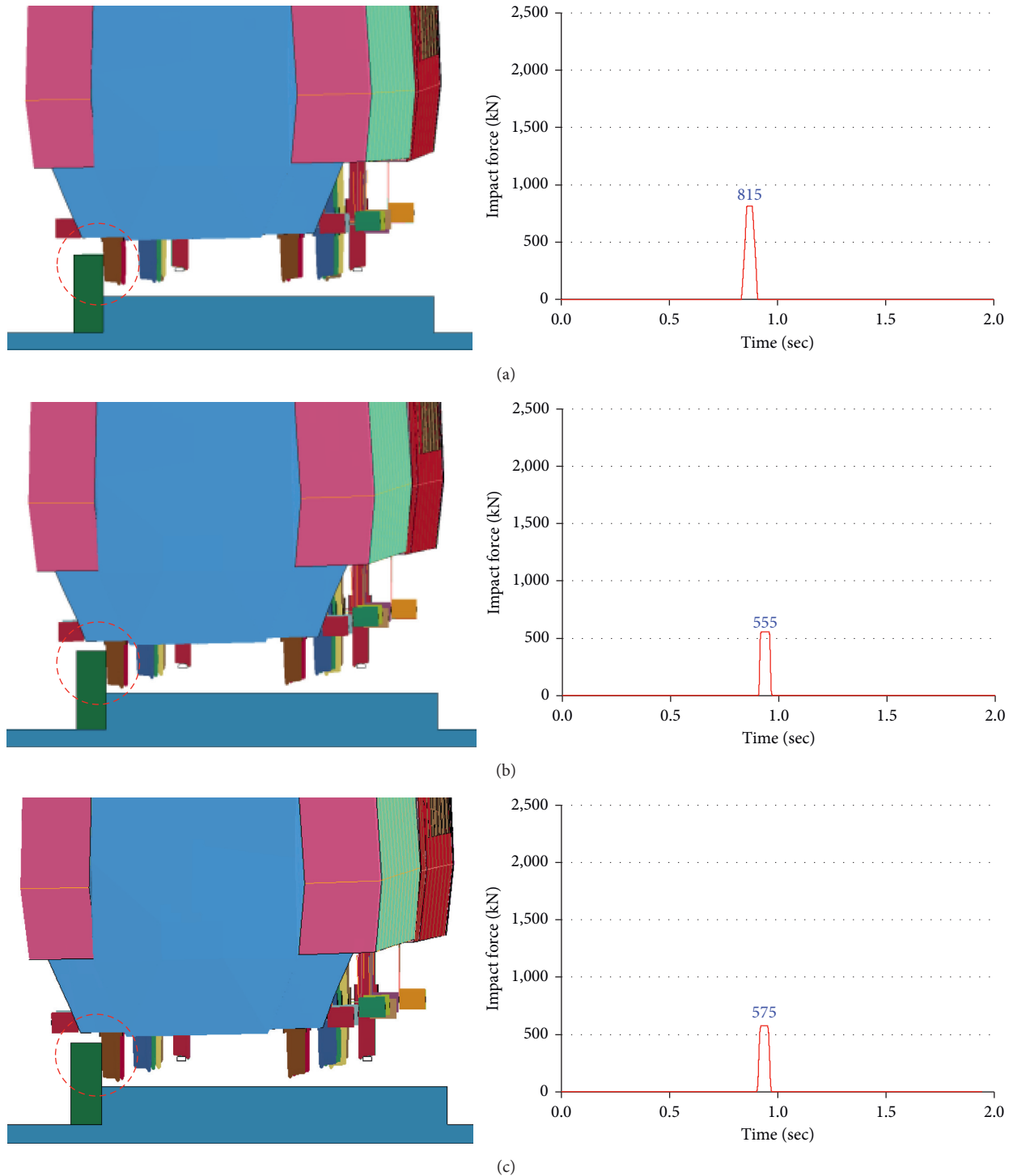


FIGURE 22: Impact force according to the collision conditions. (a) Derailment-collision behavior 1. (b) Derailment-collision behavior 2. (c) Derailment-collision behavior 3.

3.3. *Alternative Method: Containment Wall within Track Gauge.* A concrete track with the containment effect of a derailed train was modeled as shown in Figure 23 on the basis of the HSL-Zuid Project [14] that applies concrete plinth (500 × 170 mm) that is a structure type within track gauge. The horizontal deviation of a derailed train can be contained against derailment, both inside and outside of a bridge.

The impact force applied to the containment wall (or block) was computed for a range of about 100 to 250 kN depending on the difference of the contact area between the train and wall in accordance with collision conditions (Figure 24), and the containment effect of a derailed train is sufficient despite the jumping phenomenon. This containment wall (or block) has an advantage in economic and

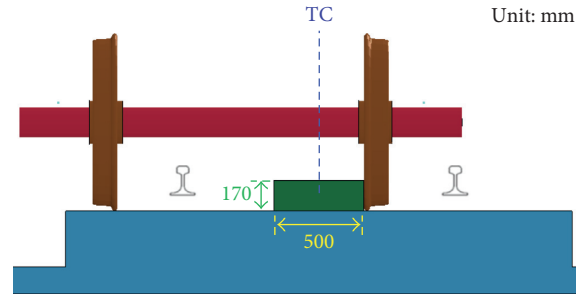


FIGURE 23: Overview of the containment wall (or block) within track gauge.

durable efficiency due to reduction of impact force (about 93% at worst case) in comparison with the containment wall (Figure 17), which is the outer side structure type of track. However, in order to apply concrete plinth above the concrete track, a new concrete track should be developed considering the interface to the track, electricity, signal, etc.

3.4. Summary of Analysis Results. This section summarizes the results according to the parametric analysis to evaluate the effects of the containment wall as shown in Table 5.

- (1) Separation distance less than track gauge ($D =$ less than $1.0 T_G$)
 - (a) Collision with the containment wall by small inertia force
 - (b) Impact forces: 160–1,500 kN
- (2) Uncertain separation distance more than track gauge ($D = 1.3\text{--}1.4 T_G$)
 - (a) Collision with the containment wall by great inertia force
 - (b) Impact forces: 600–4,000 kN
- (3) Enough separation distance ($D =$ more than $1.6 T_G$)
 - (a) The reduced force acts on the containment wall after primary guidance by the running rail
 - (b) The reasonable force level can be applied as the horizontal design load of the containment wall

As results of the analysis on distance effects, we present the optimum separation distance as follows: (1) separation distance less than track gauge or (2) enough separation distance.

- (1) Height greater than the section of the axlebox ($h_R =$ more than 440 mm)
 - (a) The whole area of the axlebox collides with the containment wall
 - (b) The containment effect of a derailed train is excellent, but the magnitude of maximum impact force is disadvantageous
 - (c) Impact forces: 1,000–4,100 kN
- (2) Height less than section of the axlebox ($h_R =$ less than 100 mm)
 - (a) The wheel collides with the containment wall

- (b) The containment effect of a derailed train is sufficient, and the magnitude of maximum impact force is advantageous
- (c) Impact forces: 500–850 kN

As results of the analysis on height and separation distance effects, we present the optimum height and separation distance as follows: (1) separation distance less than track gauge and height less than the axlebox (wheel level) or (2) enough separation distance and height less than the axlebox (wheel level).

- (1) Containment wall or block (wheel level) within track gauge
 - (a) Collision with the containment wall by very small inertia force
 - (b) Impact forces: 100–300 kN

As results of the analysis on the containment wall (or block) within track gauge, we present the alternative condition. This condition has an advantage in economic and durable efficiency due to reduction of impact force in comparison with the outer side wall type.

4. Conclusions

In this paper, a collision simulation between the derailed train and structure was carried out to evaluate impact force and containment effect of the containment walls that could be installed to minimize damage to the derailment, and the economical alternative method to reduce the impact force was proposed. The following conclusions were drawn:

- (1) As the separation distance of the containment walls is closer to the track center, the behavior range of a derailed train narrows. Therefore, the lateral inertia force decreases, thereby reducing the impact force on the wall. However, the impact force of the containment wall may increase due to repetitive collisions between the wall and the rail.
- (2) The containment effect could be assured at low walls where the wheels of the derailed train can collide with walls (not to cause the axlebox to collide with the wall). In addition, this case has an advantage in economical efficiency since height of the wall is reduced but also has a disadvantage for the difficulty

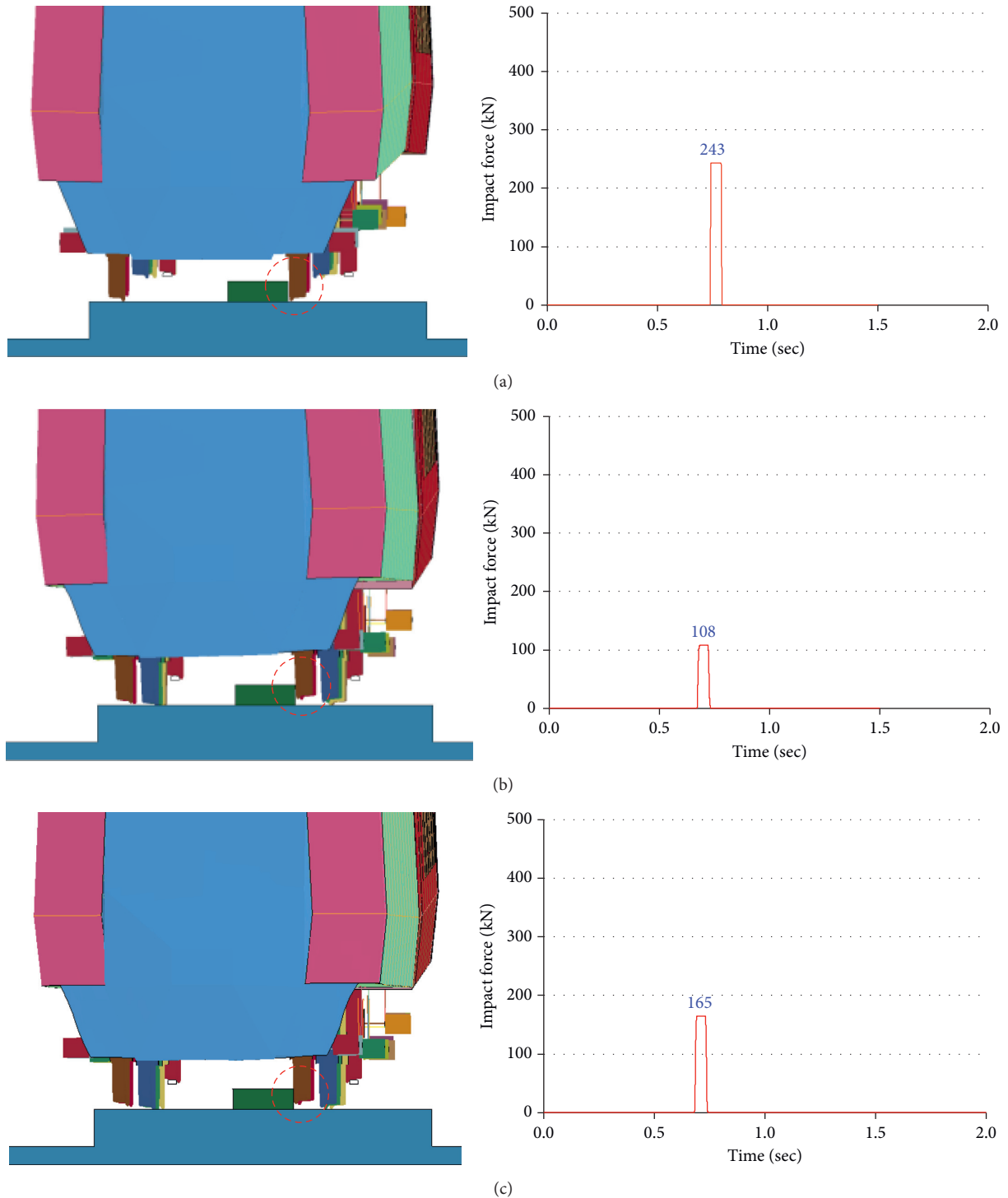


FIGURE 24: Derailment-collision behavior and impact force (alternative method). (a) Derailment-collision behavior 1. (b) Derailment-collision behavior 2. (c) Derailment-collision behavior 3.

of maintenance work for the inspection of cracks on the track concrete layer side.

- (3) The containment wall (or block) within track gauge has an advantage in economic and durable efficiency due to reduction of lateral impact force in comparison with the containment wall which is the outer side structure type of track. Moreover, the

horizontal deviation of a derailed train can be contained against derailment, both inside and outside of a bridge.

- (4) To ensure the containment effect (the derailed trains are placed within intended containment area), the derailment containment wall need to be robustly constructed to resist the impact force due to the

TABLE 5: Summary for the effects of the containment wall.

Parameter	Case	Impact force (kN)	Remark
Effect of D	Case 1	160–1,500	Reducing distance effect
	Case 2 and 3	600–4,000	Uncertain distance
	Case 4	Reduced value	Guided effect by running rail
	Case 5	3,200–4,100	Increasing height/uncertain distance
Effect of h_R	Case 6	1,168	Increasing height/reducing distance
	Case 7	500–850	Reducing height and distance
Alternative method	Case 8	100–250	Within track gauge

possibility that the succeeding trailers of the derailed train continuously collide to the wall.

Conflicts of Interest

The authors declare that there are no conflicts of interest.

Acknowledgments

This research was supported by a grant (17RTRP-B122273-02) from Railway Technology Research Program funded by Ministry of Land, Infrastructure and Transport of the Korean government.

References

- [1] H. U. Bae, *Advanced design concept of derailment containment provisions using collision simulation after train derailment [Ph.D. Thesis]*, Department of Civil Engineering, The Graduate School of Chungnam National University, Republic of Korea, 2015.
- [2] H. U. Bae, K. M. Yun, and N. H. Lim, "Containment capacity and crashworthiness estimation of derailment containment wall on high-speed train," *Proceedings of the Institution of Mechanical Engineers, Part F: Journal of Rail and Rapid Transit*, 2016.
- [3] Livermore Software Technology Corporation (LSTC), *LS-DYNA Keyword User's Manual*, vol. 1–3, Revision 2645, Livermore Software Technology Corporation, CA, USA, 2013.
- [4] J. S. Koo, H. J. Cho, and T. S. Kwon, "A study on establishing the accident scenarios for crashworthiness of rolling stocks," in *Proceedings of the Spring Conference of the Korean Society for Railway*, pp. 1–10, Korean Society for Railway, Jeju, Republic of Korea, May 2007, in Korean.
- [5] H. J. Cho, *Study on wheel-rail models for prediction of derailment behavior after collision using virtual testing model [Ph.D. Thesis]*, A Dissertation for the Degree of Doctor of Engineering, Department of Rolling Stock System, The Graduate School of Railroad, Seoul National University of Technology, Republic of Korea, 2010.
- [6] J. S. Koo and H. J. Cho, "A method to predict the derailment of rolling stock due to collision using a theoretical wheelset derailment model," *Multibody System Dynamics*, vol. 27, no. 4, pp. 403–422, 2012.
- [7] J. Fukazawa and Y. Sonoda, "Study on the crashworthiness estimation of the derailment barrier," *Journal of Applied Mechanics*, vol. 11, pp. 459–466, 2008, in Japanese.
- [8] D. Brabie, "Wheel-sleeper impact model in rail vehicles analysis," *Journal of System Design and Dynamics*, vol. 1, no. 3, pp. 468–480, 2007.
- [9] K. S. Song, S. H. Han, and Y. S. Choi, "Wheel/rail contact analysis considering friction and torque," in *Proceedings of the Spring Conference of the Korean Society for Railway*, KSR2013S073, pp. 447–452, Korean Society for Railway, Pyeongchang, Republic of Korea, May 2013, in Korean.
- [10] P. D. Moyer, R. W. James, C. H. Bechara, and K. L. Chamberlain, *Safety of High Speed Guided Ground Transportation Systems-Intrusion Barrier Design Study*, Final Report: R5021/RR593, DOT-VNTSC-FRA-95-3, DOT/FRA/ORD-95/04, U.S. Department of Transportation, Washington DC, USA, 1994.
- [11] Railtrack PLC (Safety & Standards Directorate), *Recommendations for the Design of Bridges*, Railtrack Approved Code of Practice, GC/RC5110, Railtrack PLC, London, UK, 2000.
- [12] Network Rail (NR), *Design of Bridges (Design Loading for Accommodation and Occupation Overbridges)*, NR/L3/CIV/020, Network Rail Kings Place, London, UK, 2011.
- [13] R. H. Pfeifer and T. M. Molter, *Handbuch Eisenbahnbrücken*, DVV Media Group GmbH, Eurailpress, Hamburg, Germany, 2008, in German.
- [14] Booz Allen Hamilton, *Report on the Findings of: Current Practice and Effectiveness of Derailment Containment Provisions on High Speed Lines*, Issue 1, Ref: R00673, HSL-Zuid Organisation, Zoetermeer, Netherland, 2004.

Review Article

Structural Glass Systems under Fire: Overview of Design Issues, Experimental Research, and Developments

Chiara Bedon

Department of Engineering and Architecture, University of Trieste, Piazzale Europa 1, 34127 Trieste, Italy

Correspondence should be addressed to Chiara Bedon; bedon@dicar.units.it

Received 7 August 2017; Revised 28 September 2017; Accepted 9 October 2017; Published 20 December 2017

Academic Editor: Rafik Belarbi

Copyright © 2017 Chiara Bedon. This is an open access article distributed under the Creative Commons Attribution License, which permits unrestricted use, distribution, and reproduction in any medium, provided the original work is properly cited.

Architectural design concepts incorporating glass beams, panels, or generally load-carrying elements and stiffeners for buildings, claddings, windows, and partitions are largely considered in modern high-rise constructions. A multitude of aspects, including motivations related to transparency, aesthetics, illumination, and energy conservation, progressively increased the use and interest for such a still rather innovative constructional material. However, compared to other traditional materials for buildings, standard glass is typically characterized by brittle behaviour and limited tensile resistance. The intrinsic properties of glass, moreover, together with typically limited thickness-to-size ratios for glazing elements, or the mutual interaction of glass components with adjacent constructional elements as a part of full assemblies they belong (i.e., fixing systems, sealants, etc.), as well as the combination of mechanical and thermal phenomena, make glass structures highly vulnerable. Special safety design rules are hence required, especially under extreme loading conditions. In this review paper, a state of the art on structural glass systems exposed to fire is presented. Careful consideration is paid for actual design methods and general regulations, as well as for existing research outcomes—both at the material and assembly levels—giving evidence of current challenges, issues, and developments.

1. Introduction

Glass is largely used in buildings as a construction material, to replace and/or interact with traditional structural elements composed of steel, aluminum, timber, and concrete. Major applications of glass in buildings are related to a multitude of aspects, including aesthetics, lightning, transparency, and insulation motivations (see, e.g., Figures 1(a) and 1(b)).

Generally, glass is known to behave as a brittle material with relatively high compressive resistance and limited tensile strength, hence shattering into many dangerous shards [1, 2]. Fail-safe design concepts, in this sense, are mandatory, both under ordinary loads and extreme loading conditions.

In this regard, several research studies have been dedicated over the last years to the development and/or assessment of specific design regulations and novel design concepts for structural glass systems, including extended experimental and finite element (FE) numerical

investigations related to connections, composite assemblies, and hybrid systems [3–6].

Special care has been spent also for the analysis and design of glazing systems under extreme loads, such as explosive events [7–9], seismic loads [10–13], natural hazards and climatic loads [14, 15], fire [16, 17], and impacts [18–20].

Especially in the case of fire accidents, special enhanced safety levels should in fact be ensured, to allow evacuation of buildings (Figures 1(c) and 1(d)).

Multiple aspects are however combined in the overall fire performance of a given structural glass system, such as the typical brittle behaviour of material, the high sensitivity of its mechanical properties to temperature, the high sensitivity of fire performance to geometrical features, glass type, and the mutual interactions between all the system components (i.e., the structural glass assembly, including supports and building components).

As a specific issue of glass systems, in addition, their fire performance cannot be analytically derived but requires fire testing estimations. Advanced FE modelling, in this regard,

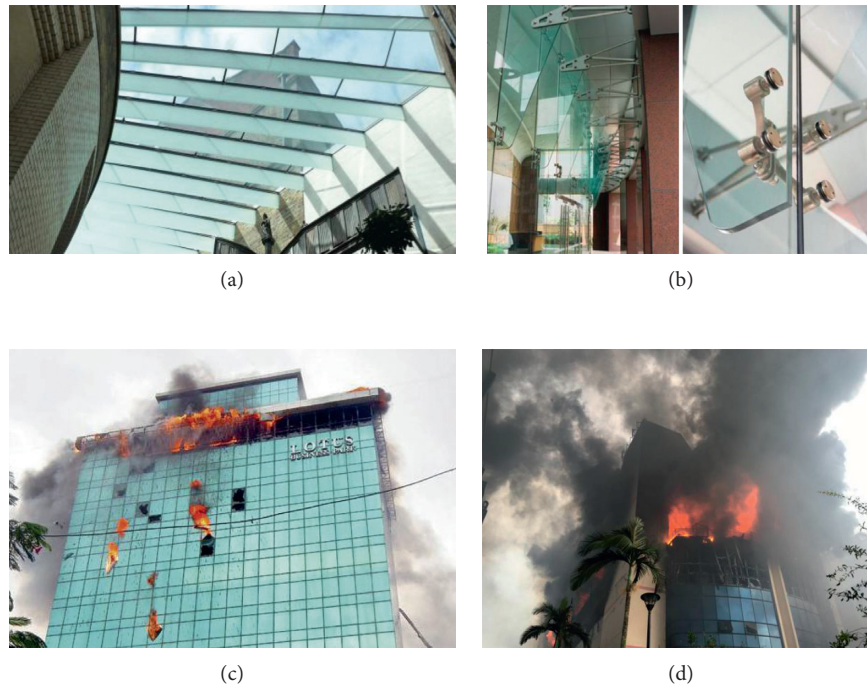


FIGURE 1: (a)-(b) Typical structural glass applications in buildings and (c)-(d) examples of recent fire event scenarios.

could represent a valid alternative to time- and cost-consuming experiments. However, major issues for the FE analysis of structural glass elements under fire derive from the current lack of standardized guidelines and general rules able to offer reliable results [21], as well as of well-established mechanical and thermal properties of materials in use. In addition, FE literature efforts related to the fire performance of structural glass systems are very limited (see, e.g., [22]).

In this paper, a review of experimental research on structural glass systems under fire is proposed. Section 2 first recalls a short overview of structural design concepts and requirements. In Section 3, mechanical and thermal properties of standard glass under high temperatures are reported, giving evidence of several literature source outcomes, as well as relatively recent fire-resistant (FR) glass solutions available on the market for special applications. Careful consideration is paid, in particular, for material properties representing key input parameters for structural design purposes. Sections 4 and 5 finally present a summary of existing experimental research related to the fire performance of glass to high temperatures, including material properties (Section 4) and structural glass systems (Section 5), such as floors and overheads, beams, facades and windows, and glazing systems retrofitted via protective films.

2. General Design Rules and Concepts

2.1. Structural Glass Systems under Ordinary Loads. Compared to traditional materials in use of constructions, one of the major factors affecting the design and verification of

structural glass elements is represented by its intrinsic features. Even without fault of the designer, a given structural glass element can in fact break unexpectedly, during its service life [1]. Whatever the reason, the structural integrity of the overall assembly it belongs must not be compromised. According to the general design concept of EN 1990:2002 [23], both ultimate limit state (ULS) and service limit state (SLS) should be properly verified.

The ULS resistance verification is intended to fulfill the structural safety of a structural glass element [1, 2]. Such a safety assessment is generally performed by limiting the maximum principal stresses achieved under relevant load combinations to do not exceed the design resistance of glass. Multiple aspects can affect, however, the design value of glass resistance (see, e.g., [1, 2]), being defined as a function of glass type, loading (i.e., in-plane and out-of-plane), loading time (i.e., instantaneous, permanent, etc.), edge effects and treatments, glass surface treatments, profile, etc. In Europe, following the recommendations of [2, 24], several national codes adopted the same design provisions (see, e.g., [25–27]). Different approaches can be found in US regulations, while further issues also derive from a combination of effects due to multiple design actions (see, e.g., [28]).

The SLS verification is aimed at the limitation of deflections. The reference limit values for such deformations mainly depend on the specific applications or support conditions. As in the case of specifications for ULS design, different SLS limit deformation values can be found in standards. A further design condition that should be properly verified (see, e.g., the CNR guidelines [29]) is then

associated to the so-called collapse limit state (CLS). Given a structural glass system to verify, in order to ensure appropriate redundancy in the case of accidental cracking, the residual CLS resistance and maximum deformations of the partially damaged system are also required.

2.2. Structural Glass Systems under Fire Loading. Fire loading represents, for glass systems as well as for constructions in general, an extreme loading configuration. As such, specific provisions should be taken into account to ensure appropriate performance levels.

Given a glazing system exposed to fire, in accordance with existing standards (see, e.g., the EN 13501-2 regulations [30]), its fire performance is generally defined on the basis of three classifications levels:

- (a) integrity (classification “E”): glass prevents flames, smoke, and hot gases from passing through. The fire remains contained;
- (b) limiting radiation (“EW”): glass restricts the amount of heat passing through it to the side which is to be protected;
- (c) thermal insulation (“EI”): the average temperature of glass on the protected side remains below 140°C; hence, the risk of self-combustion of exposed materials (due to either radiation or convection) can be minimized, and buildings can be evacuated safely and calmly.

The above FR reference criteria can only be determined on the basis of fire experiments, and typical FR rating classes are associated to 30, 60, or 120 minutes of performance. Relevant standards in use in Europe are, for example, the EN 1363-1 document [31], providing FR test requirements and methods; EN 1364-1 [32], for non-load-bearing elements and walls; and EN 1634 [33], for doors and shutters. Floors and roofs should be indeed tested in accordance with EN 1365-2 regulations [34] and then classified by following the EN 13501-2 provisions.

In addition to EU provisions, the American Underwriters Laboratory standard [35] includes a further requirement; that is, a given FR glazing system should have the ability to withstand the so-called “hose-stream test,” which assesses the system ability to remain intact after a jet of water is blasted on its surface, when exposed to fire [36].

Compared to other extreme loading conditions which may occur over the lifetime of a given structural glazing system, the main issue of FR glass systems arises from glass response to temperature variations. Conventional glass for application in buildings (Section 3), in fact, offers typically limited resistance when exposed to fire and generally shatters within minutes, giving evidence of the so-called thermal breakage phenomena (Section 4). Heat treatment can offer slightly longer resistance, but this enhancement could not be significantly enough. Special glass types, conventionally detected as “FR glasses” or “fire-rated glasses,” are indeed available on the market for specific applications (Section 3.3). On one side, besides the general fire performance of standard glasses, past experimental

research proved that ordinary glass systems can also offer interesting fire performances (Section 5). However, pure thermal effects combined with additional mechanical loads acting on a given structural glass system to verify should severely compromise its overall performance, hence requiring experimental testing and detailed investigations at the material level as well as at the component and assembly levels.

3. Glass in Constructions

3.1. Chemical and Physical Properties at Room Temperature. Most of glass solutions in existing or novel buildings are realized by using soda lime silica (SLS) glass. Special and limited in number applications only, when a certified level of fire resistance and heat resistance is required, are indeed realized with borosilicate (BS) glass, since offering better performance to temperature changes. BS glass applications in buildings are indeed limited, compared to huge SLS glass use for load-carrying elements, windows, etc. Table 1 reports the main chemical and physical features of SLS and BS glass types at room temperature. There, nominal values are also provided for characteristic resistances in tension and compression. As known, several SLS glass types are in fact commercially available [1, 2], with annealed (AN) float glass representing the reference base material. The strength of AN glass is typically limited, compared to other constructional materials, with a nominal characteristic value in tension up to 45 MPa. The mechanical properties of AN glass can then be enhanced via thermal or chemical processes, leading to strengthened (HS, with 70 MPa the nominal tensile resistance value) or fully tempered (FT, with 120 MPa its tensile resistance) glasses, respectively, with improved tensile strength as well as beneficial effects especially in terms of the shape and size of shards, in the case of accidental failure, due to the initial state of residual stresses resulting from strengthening processes. For the sake of clarity, Table 1 mentions nominal values only of material mechanical properties.

As far as the transition temperature T_g is not exceeded, glass behaves linear elastically under the assigned design loads. Given a combination of ordinary loads to verify, as a result, the knowledge of elastic mechanical properties and resistance values for SLS glass given in Table 1 allows then to perform analytical or FE structural analyses.

Crack occurrence and propagation, however, may even prematurely occur due to possible thermal stresses, hence requiring a typical multidisciplinary approach for such a constructional material. Thermal shocks, that is, cracking due to temperature gradient between heated and unheated glass regions, as well as due to relatively low thermal expansion coefficient of glass, are in fact typically expected to occur when the temperature gradient lies in the order of 40°C for AN glass, up to 100°C for HS glass, and 200–250°C for FT glass [1]. A huge number of research studies have been focused on thermal failure assessment of glazing windows, taking care of simple glass panels, double glass units, and point-fixed systems (Section 4).

TABLE 1: Chemical and physical properties of SLS and BS glass types (at room temperature), in accordance with [1].

Chemical properties				Physical properties			
	SLS	BS		SLS	BS		
Silica sand	SiO ₂	69–74	70–87	Density	ρ (kg/m ³)	2500	2200–2500
Lime (calcium oxide)	CaO	5–14	—	Young's modulus (MOE)	E (GPa)	70	60–70
Soda	Na ₂ O	10–16	0–8	Poisson's ratio	ν	0.23	0.2
Boron oxide	B ₂ O ₃	—	7–15	Tensile resistance	σ_{kt} (MPa) ^a	45–120	45–120
Potassium oxide	K ₂ O	—	0–8	Compressive resistance	σ_{kc} (MPa) ^b	1000	1000
Magnesia	MgO	0–6	—	Coefficient of thermal expansion	α_T (10 ⁻⁶ C ⁻¹) ($T < T_g$)	9	3.1–6.0 (class 1 to 3)
Alumina	Al ₂ O ₃	0–3	0–8	Specific heat capacity	c_p (Jkg ⁻¹ C ⁻¹)	720	800
Others	—	0–5	0–8	Thermal conductivity	λ (Wm ⁻¹ C ⁻¹)	1	1
				Emissivity (corrected value)	ϵ	0.837	0.837
				Transition temperature	T_g (°C)	530	530
				Maximum thermal stress	σ_T (MPa) ^a	40–250	40–250

^aDepending on the treatment of glass; ^btheoretical value, in accordance with [29].

3.2. *Laminated Safety Glass and Insulated Glass.* Further design issues and complexities arise as far as glass systems do not consist of single panes but are assembled in composite laminated sections and/or insulated glass units, as conventionally in use for buildings.

Laminated glass (LG) represents, in general terms, the combination of two or more glass plies together with foils consisting in a certain interlayer type. LG has been first developed for automotive applications, since early 1900, to avoid injuries in case of accidents, and only in the last decades, LG has been largely used in civil engineering applications for structural purposes. As a general rule of the LG concept, the resisting cross section is expected to respond as a composite system to external loads, hence having enhanced mechanical performances than single glass panes, both in the elastic stage and in the postcracked phase. From a mechanical point of view, the first implicit advantage of LG structural applications is that multiple glass layers can be bonded together; hence, the required level of resistance, stiffness, and redundancy can be obtained by using conventional glass thicknesses available on the market. In addition, thanks to the presence of bonding films, LG represents since decades the conventional safety glass solution in buildings, since able to hold together glass shards in case of failure, hence reducing possible risks for people (Figures 2(a) and 2(b)).

Bonding films typically consist of polyvinyl butiral (PVB) films, ionoplast foils (i.e., SentryGlas® (SG)), and ethylene-vinyl acetate (EVA) compounds. As a common aspect of such possible interlayers, besides their different constitutive laws, these films are generally characterized by viscous behaviour; hence, they are generally sensitive to temperature and load-time application, as also emphasized by several research efforts [37–39]. In addition, even at room temperatures, interlayers in use for LG applications are generally characterized by relatively low shear stiffness, compared to glass (Figure 2(c)). The overall structural performance of a given LG composite section is hence highly dependent on the interlayer features, including durability and resistance.

In terms of structural design of LG systems under ordinary loads, various methods are available to account for the effects of interlayer degradation over time and temperature increase (see [1, 2] for a summary of existing formulations). As a result, at the design stage, optimal resistance and stiffness behaviours for ULS and SLS are generally ensured, as well as appropriate safety performances for the CLS postcracked stage. Mostly, null contribution, given the typical mechanical degradation of interlayers for temperatures higher than 30°C (Figure 2(c)), is however expected from interlayers under fire loading; that is, the LG section is expected to behave fully uncoupled. There, specific design assumptions should be taken into account, including the use of special intumescent compounds (Section 3.3).

Multiple glass panes (monolithic and LG sections) can then be assembled together to act as insulated glass units, both double (i.e., single gas cavity interposed between glass panels) or triple (i.e., double cavity). There, design calculations should take into account the so-called *load-sharing effects* due to air or gas infill in the cavities, that is, the mutual interaction between glass panes once subjected to mechanical loads [1, 2]. Ordinary climatic loads represent an additional design condition to properly verify, due to possible variations in the cavity volume and pressure. Thermal analyses of insulated glass systems are hence required even under solar exposure only. All the mentioned aspects and variables, consequently, further increase the design complexity for glazing systems under fire.

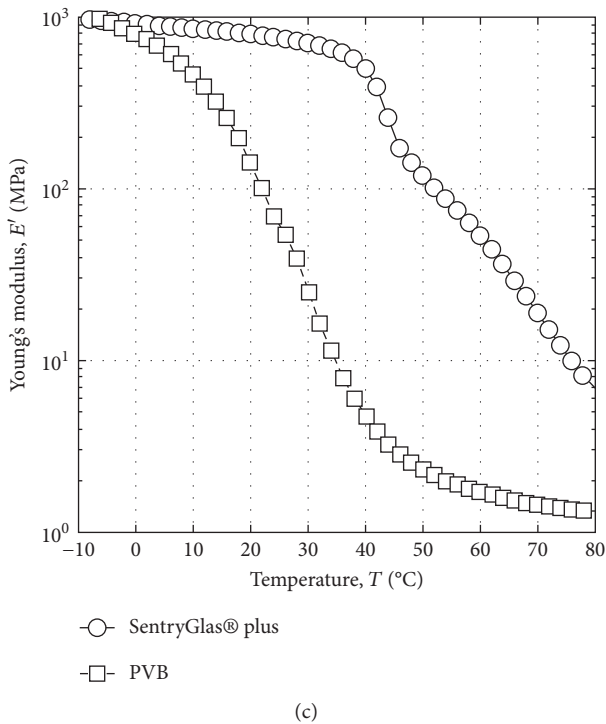
3.3. *Fire-Resistant Glazing.* FR glazing represents a relatively recent solution, known to provide excellent protection for lives and property in the event of fire, and hence may be used as a barrier for fire separation or compartmentation (for a specified duration), enabling occupants to assemble in a relatively safe compartment and acting as a part of an integrated “fire safety strategy” for the full building it belongs. As a crucial aspect of such solutions, FR glass systems require extreme attention in installation



(a)



(b)



(c)

FIGURE 2: Laminated glass: (a)-(b) examples of fractured LG panels and (c) variation of shear modulus for common LG interlayers (PVB and SG degradation with temperature [37]).

detailing. In addition, all the FR components, such as the glazing seals, beads, fixings, and frame, must be compatible and work together to achieve the required performance [36].

FR glazing, due also to relatively high costs, actually finds limited applications in buildings, especially where protected escapes must be ensured in the case of fire accidents. In

accordance with a study carried out by Yang et al. [40], for example, FR glazing was representing in 2011 less than 5% the overall China glazing applications. Major limitations in the use of FR glass derive also from current need for additional research efforts and investigation on its actual fire performance (Section 4).

In accordance with design guidelines such as [36], FR glazing solutions actually available on the market can include (i) LG composites, obtained by bonding together different glass types (e.g., SLS glass panes with enhanced and FR glass types) with special fire interlayers (i.e., intumescent films); (ii) wired glass; (iii) ceramic glass; (iv) resin laminated glass; (v) gel laminated glass; and (vi) thermally toughened alkaline earth silicate safety glass (Figure 3). Multiple glass layers according to (i)–(vi) example types can then be combined in insulated FR glazing units. Within the given list of (i)–(vi) solutions, wired glass elements do not offer enhanced fire resistance compared to ordinary glass and typically crack early due to thermal stresses. FR performance is indeed ensured by their integral wire mesh, able to hold together and in place cracked glass pieces.

Generally speaking, for structural design purposes and mechanical calculations, a given FR system can be conventionally treated as a standard, non-FR glass element (Sections 2.1, 3.1, and 3.2), with the difference of enhanced performance under fire exposure. In general terms, FR glasses are in fact considered as effective passive fire protection (PFP) tools for buildings, with specific applications like glazed internal and external fire doors (vision panels); interior partitions and compartments; roofs, floors, and ceilings; façade panels; escape and access corridor walls; and stairways, lobbies, and enclosures (to protect shafts). Juxtaposed with PFP tools, active fire protection (AFP) systems can provide further effort in combination with PFP systems but require a certain motion and response to combat fire. Typical AFP tools can be either automatic (i.e., water sprinklers, fire alarms, hypoxic air suppression systems, etc.) or manual (i.e., emergency evacuation, fire extinguishers, firefighters, water hoses, etc.). Fire design and optimization of such systems, however, is generally complex and requires specific competences. Combined PFP and AFP systems, moreover, are generally expected to provide enhanced benefits but could also lead to worst performances. So far, several research studies [41–45] highlighted, for example, that water films and sprinklers can provide high fire performance also to non-fire-rated, standard glass systems, as well as that FR glass curtains with water films can offer high fire performance, but limited heat resistance, or that the AFP systems can anticipate thermal shock failure in glazing windows and enclosures, leading them to premature collapse.

4. Existing Experimental Research on Glass Properties under High Temperatures

The performance of glass under high temperatures under heating and fire loading attracted the attention of several experimental research studies, since 1950s, due to the huge use of glazing panels in windows and fenestrations. Most of those investigations are related to thermal shock effects in

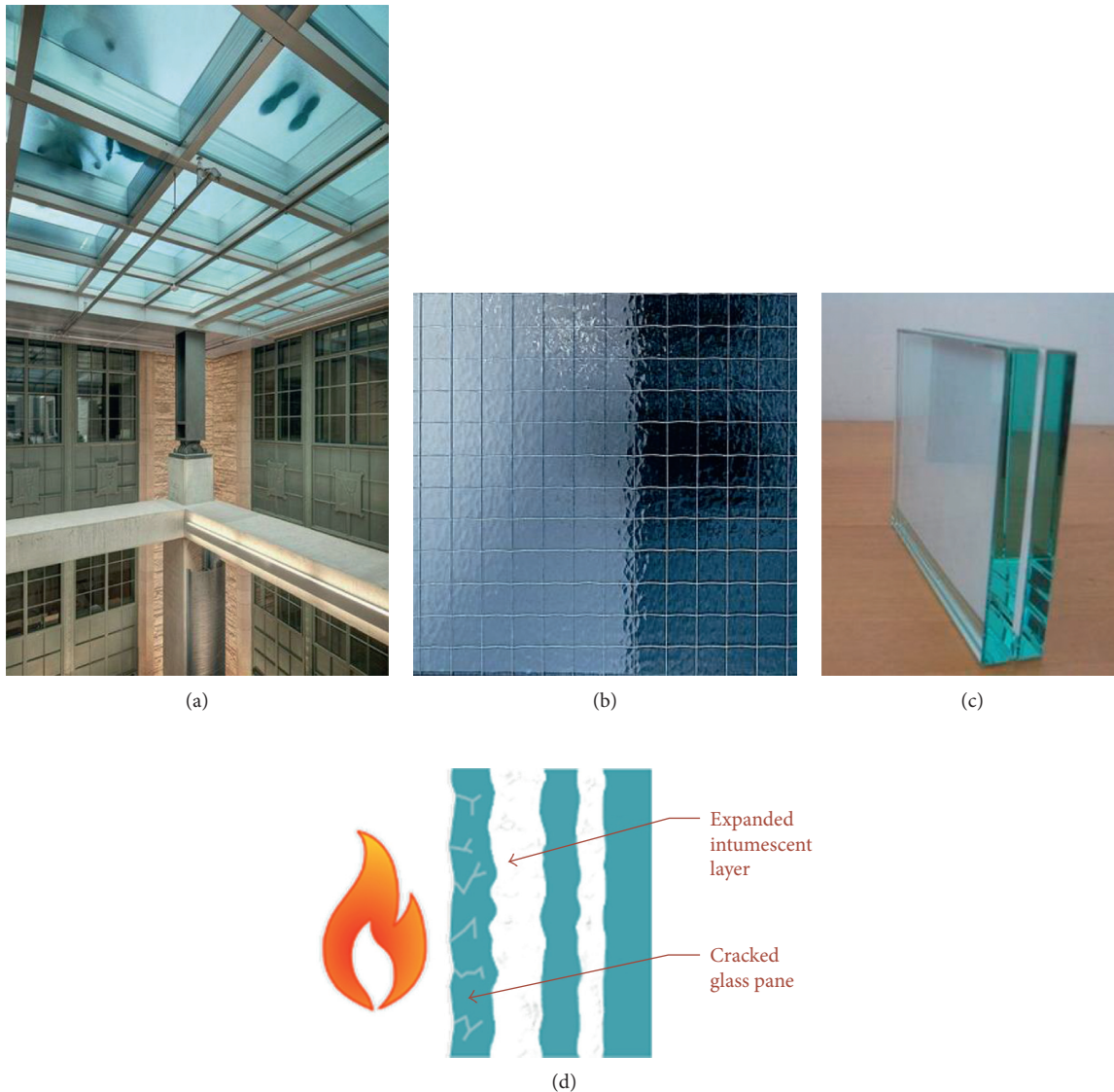


FIGURE 3: FR glass: (a) examples of application in a public building, (b) wired glass, (c) double LG with intumescent layer, and (d) working principle of a triple LG with intumescent interlayers (schematic cross section).

SLS glass, as well as to its thermal characterization in general, including variations of modulus of elasticity (MOE) and resistance with high temperatures, while only limited experimental studies are currently available for composite glass systems and assemblies under fire or combined fire and mechanical loads (Section 5). Sections 4.1 and 4.2, in this regard, present a summary of major research outcomes at the material level, giving evidence of some key influencing parameters that should be properly accounted for the assessment of the fire response of structural glass systems.

4.1. Glass Transition Temperature. As a conventional nominal value for glass transition temperature, design standards suggest a conventional value $T_g = 530^\circ\text{C}$ (Table 1). Based on experiments carried out over last decades on SLS glass, however, standard AN glass gave evidence of high variations

in T_g , with measured transition temperatures in the order of 550°C , 283°C , and 400°C [46, 47].

Rouxel and Sangleboeuf [48] measured on SLS glass specimens T_g values comprised between 450°C and 600°C , giving evidence of the thermal performance of artificially cracked specimens, including bending tests at high temperatures to monitor the MOE variations.

Due to the intrinsic properties of SLS glass, it is in fact known that, as far as the service temperature increases up to T_g , its response becomes progressively time dependent, with rapid increase of permanent deformations. Standard AN glass, based on [42–44], proved to offer a typical brittle-to-ductile (BTD) transition at high temperatures, with toughness enhancement compared to other glass types. The same BTD behaviour, however, was also observed to strongly depend on the imposed strain rate, with BTD and transition temperature increase with strain rate increase [48].

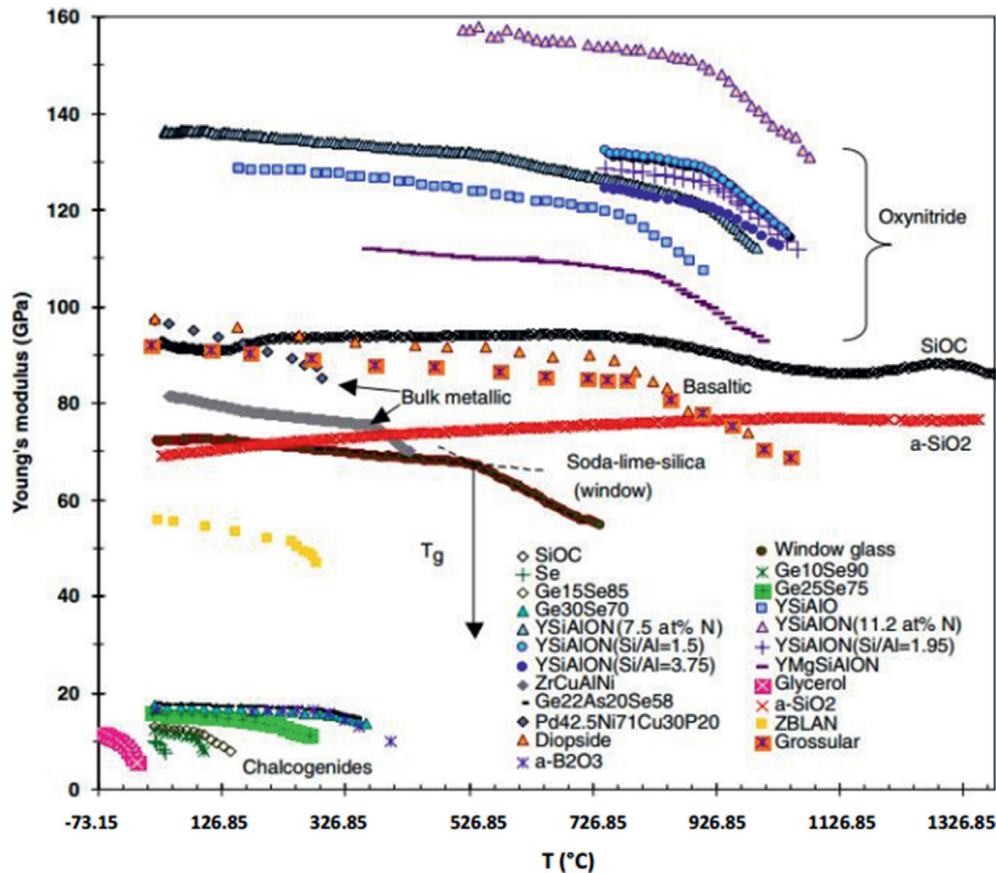


FIGURE 4: MOE variation in SLS glass and other glass types, as a function of temperature, as reported in [47].

4.2. Glass Thermomechanical Properties and Temperature Effects. The elastic properties of standard glass at elevated temperatures have been extensively assessed by Rouxel [47], by accounting for experimental data available in the literature after 1950s, giving evidence of SLS glass' MOE sensitivity to temperature, as compared with other glass types (see Figure 4, with SLS float glass labeled as "window glass"). Rather linear dependency and limited decrease can be observed for MOE values of SLS glass, as far as T does not exceed T_g , while a subsequent abrupt loss of stiffness is shown.

Earlier experiments were also carried out both on SLS and BS glass components by Kerper and Scuderi [49], with careful attention for specimens including (i) chemically strengthened SLS glass, (ii) thermally fully tempered SLS glass, and (iii) thermally semitempered BS glass. Through the experimental study, glass laths with dimensions of 254×38.1 mm (6.35 mm in thickness) and 152.4×25.4 mm (2.54 mm in thickness) were considered. Given the (i)–(iii) specimen types and a reference temperature (0–560°C the tested range), almost stable MOE values were experimentally derived, even after sequential heating and cooling cycles. MOE values were generally found to be completely relaxed for temperatures higher than 400°C.

Close correlation can be observed with MOE variations in standard AN glass specimens, as derived from different literature sources (see Figure 5, where test results from Shen et al. [50] on monolithic SLS samples (75.43×14.80 mm the

size, with 3.26 mm the nominal thickness) are also reported). The same Figure 5, finally, gives evidence of the typically increasing MOE values for BS specimens, as a function of increasing temperatures.

Worth of interest for structural design purposes is that Kerper and Scuderi [49] also assessed the resistance variations in SLS glass at high temperatures. In particular, no resistance losses were reported for temperatures up to 375°C (less than 5% losses, compared to room temperature), for thermally fully tempered SLS specimens. Substantial decrease of resistance was recorded only for temperatures higher than 500°C (fire exposure for several hours) and 550°C (15 minutes of fire exposure). Chemically strengthened SLS glass showed indeed a pronounced resistance degradation with the temperature increase, up to 5% loss at 204°C (500 hours of fire exposure), 5.8% at 260°C (500 hours), and 100% at 600°C (6 hours).

Following [49], a huge number of experimental studies related to SLS glass performance have been focused on thermal breakage assessment, being representative of the major cause of glass cracking for windows. The issue of glass thermal cracking and fallout has been first raised in 1980s by Emmons [51] and other researchers [52, 53], while in the last decades, an increasing number of experiments have been carried out on small-scale specimens, single glass panes, or double glass panes variably supported, under the effect of fire or heat radiation (see, e.g., [54–60]). Numerical investigations were, for example, proposed in [61–63],

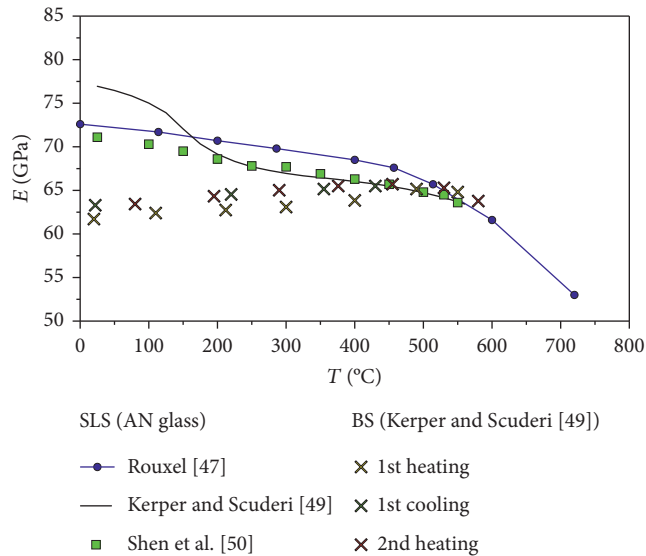


FIGURE 5: MOE variation as a function of temperature, for SLS annealed and BS glass types.

giving evidence of edge and boundary condition effects on the thermal response and breakage of standard window glass panes. Malou et al. [64] carried out thermal resistance experiments on 3 mm thick, SLS, AN glass specimens (15×50 mm their nominal size). A rather constant value was recorded for the tensile strength of glass, up to a temperature increase of 270°C (Figure 6(a)). Higher temperatures were indeed associated to a sharp decrease in the measured resistance (more than 50% the reference value at room temperature), giving evidence of thermal shock effects and damage propagation in glass specimens, as well as of generally limited performances of AN glass. A rather smooth MOE decrease was also observed (Figure 6(a)).

Later on, Xie et al. [65] experimentally investigated the tensile resistance of SLS, AN glass specimens at high temperatures. Quasi-static tensile tests were carried out on small specimens, with thickness comprised between 4 mm and 12 mm (2 mm the difference between each set of specimens). Test repetitions on specimens with the same geometrical properties were carried out at 25°C and 200°C , where the critical breakage resistance was derived as the first cracking occurrence. In Figure 6(b), evidence of such test results (average values, with minimum and maximum values for each series) is provided. In accordance with [65], a negligible decrease of resistance was noticed for specimens exposed to 200°C , compared to room temperature results, while higher sensitivity was observed especially to glass thickness (Figure 6(b)).

Worth of notice that, as far as different literature references are examined (see, e.g., [66]), even counterposed experimental findings can be derived, giving evidence of a typically high scatter and sensitivity of glass thermal resistance to elevated temperatures, hence suggesting further testing and investigations at the material level.

Moving from the material to the assembly level, such a need of further experimental assessment and investigation can be further perceived.

Experiments related to the thermal breakage of specific glazing systems under fire loading have been in fact carried out

only recently, that is, for double glazing units [58] or point-fixed glazing panes belonging to curtain walls [60]. In the case of point-fixed panes, for example, a high sensitivity of thermal breakage (i.e., time of failure and crack pattern) was typically observed, based on the position of point connectors (see an example in Figure 7). The actual performance of such a kind of specimens—as expected from the examined boundary configuration—proved to be strictly related to combined thermal exposure effects as well as to mechanical loading (i.e., self-weight of point-fixed panels, leading to additional stress peaks close to the holes), hence requiring a detailed investigation of both combined aspects.

In this regard, Chen et al. [17] studied the thermal breakage performance of standard AN windows, under the effects of combined thermal loads and wind pressures. Steel frame-supported, monolithic 0.6×0.6 m panels (6 mm their thickness) were subjected to a reference fire loading and various levels of wind pressures (up to 11 m/s the wind velocity on glass surface). Glass cracking, in some case, occurred together with fallout of samples from the supporting frame. Test results (15 specimens in total), however, generally proved that the first cracking time markedly decreases with increasing the imposed wind pressure; that is, mechanical loads (wind, in this specific case) can highly accelerate the failure of thermally loaded glass systems. As a result, detailed investigations inclusive of combined thermal and mechanical loads well representative of the actual loading and boundary configurations for the examined structural glazing system should be generally carried out.

In the case of LG systems, for example, the thermal performance of interlayers of common use should be properly taken into account. In this regard, Debuyser et al. [16] investigated the behaviour of monolithic and triple-layer LG specimens composed of standard AN glass, under the effects of radiant heating. Nominal thicknesses of glass panes of 6 mm, 10 mm, and 15 mm were taken into account, being bonded together in LG sections by PVB or SG layers (0.76 mm or 1.52 mm the thickness of interlayer foils). Low-E coated, monolithic specimens were also included in the set of experiments. Both radiant and transmittance tests were carried out, giving evidence—in accordance with earlier research efforts—of the relatively limited resistance and low thermal performance of AN glass specimens, due to the premature occurrence of thermal cracks as well as due to the poor thermal reaction of bonding interlayers (in the case of LG specimens). Critical design issues were also emphasized, by taking advantage of a 1D model able to capture the actual thermal response of the tested specimens. Thermal properties of PVB and SG foils, up to 340°C , were also reported (Figure 8). Test results collected in [16]—even limited to maximum temperatures of 340°C —generally showed a close correlation with past literature references for SLS glass [67, 68] (Figure 8). Worth of interest is also the thermal characterization of PVB and SG foils.

5. Existing Experimental Research on Glass Systems and Assemblies

Although the relatively large number of experimental studies focused on the thermal performance of glass as

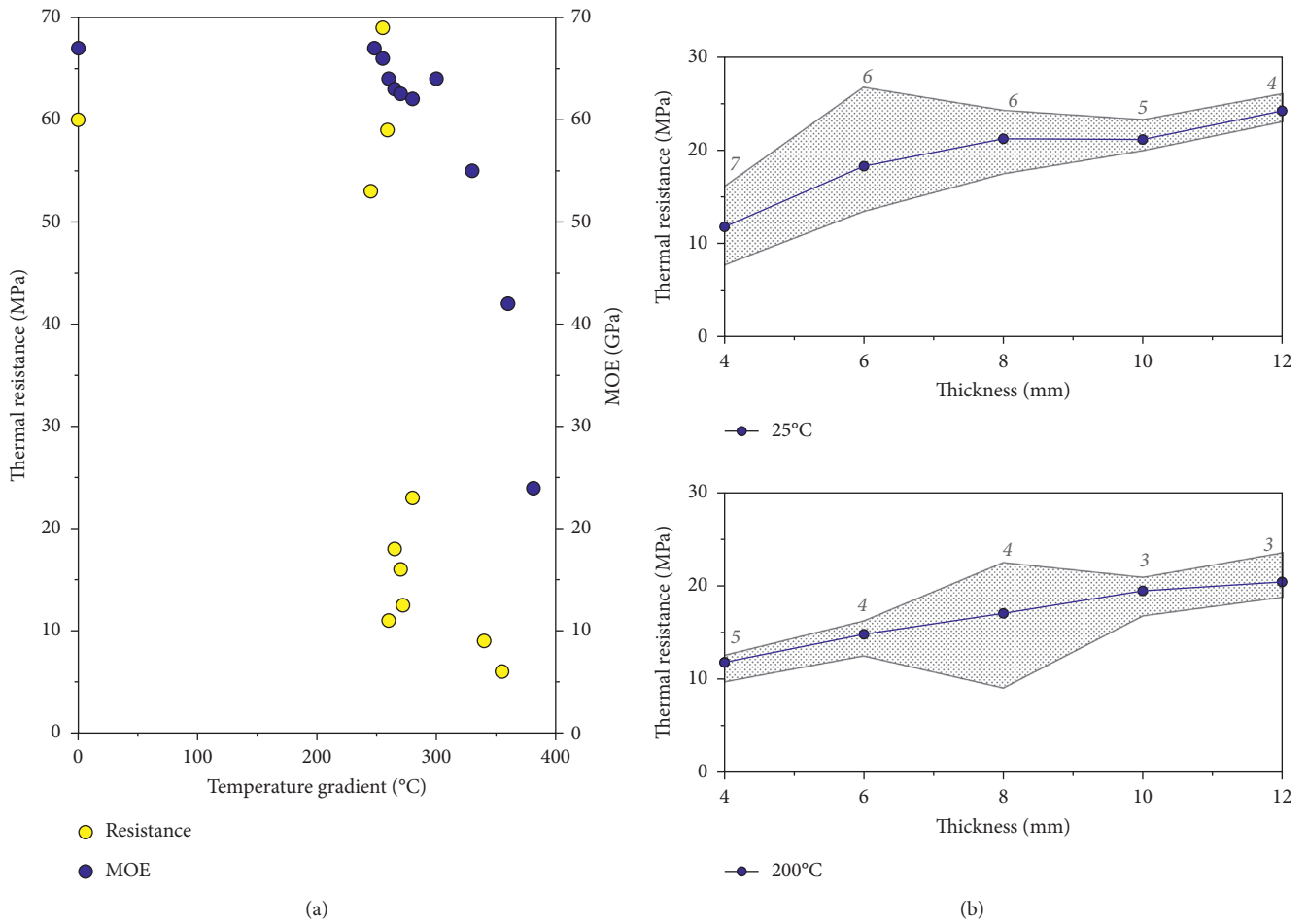


FIGURE 6: Thermal characterization of SLS glass. (a) Variation of MOE and resistance, under thermal shock [64], and (b) dependency of thermal shock resistance to glass thickness (in gray italic, the number of tests for each thickness), in accordance with [65].

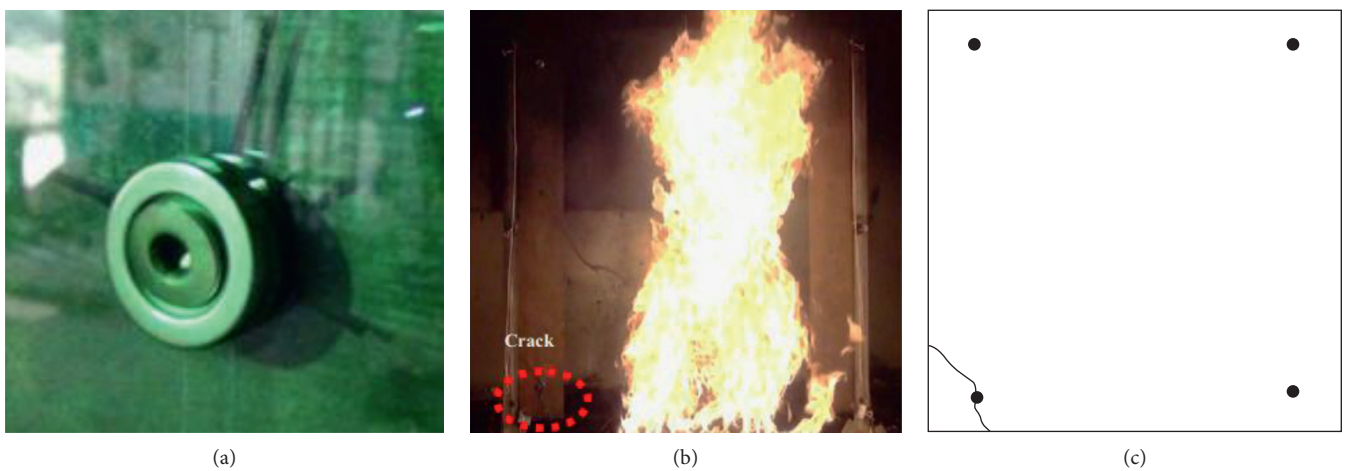


FIGURE 7: Fracture of point-fixed glass panels, in accordance with [60]. (a) Connector detail; (b) experimentally observed crack opening (front view); and (c) corresponding schematic representation.

a constructional material, limited literature efforts are still available on the fire performance of full glass systems and assemblies (see a selection in Table 2).

5.1. Glass Walls, Facades, Enclosures, and Windows. Glazing enclosures and walls attracted the attention of researchers especially during the last years, to assess the fire performance

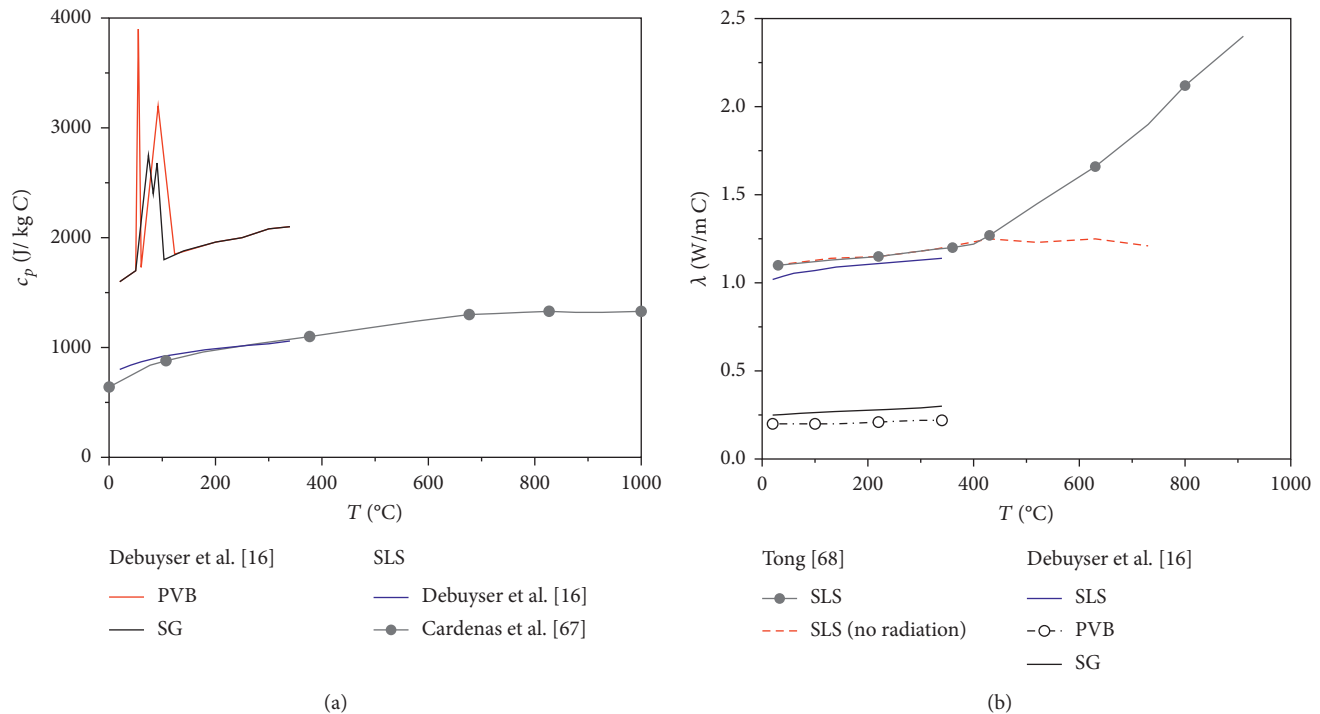


FIGURE 8: Thermal properties of glass, as a function of temperature, as derived from several literature references. (a) Specific heat capacity and (b) thermal conductivity.

of novel FR solutions in place of standard glass. In doing so, the actual boundary and loading configurations were properly taken into account in defining the test setup and methods, so as to reproduce the testing conditions of full-scale specimens as a part of full buildings and complex systems.

Glass enclosures designed for an extension of Washington Dulles International Airport (automated train system for passengers) were tested under fire conditions in 2007, as reported by Mejicovsky [69] (Figure 9(a)). Glass panels with 3.8×3.6 m high dimensions and supported by interior steel frames (4.7 m the average bay width) were investigated. Special details were defined (even using standard, non-fire-rated materials), so as to offer appropriate redundancy to the glazing system, even in the case of an accidental event. To this aim, a special mock-up was also designed, so as to simulate the actual fire-loading condition for the glazing enclosure.

Glass elements for overhangs and walls were designed in the form of LG sections, composed of two 10 mm thick FT glass panes bonded by a 1.52 mm thick PVB interlayer. Glazing joints were then realized by means of silicone rubber setting blocks and structural silicone sealant joints (Dow Corning 995™ type), while the glazing channel and edge trims consisted of minimum 3 mm thick stainless steel. The fire test was stopped after 35 minutes of exposure, with temperatures in glass over 250°C (up to 400°C in the last 5 tests of the experiment). Postexamination of the glazing system revealed no cracking or dislodgement of components, but localized melting and off-gassing of the PVB interlayer was observed, in the form of small bubbles and/or partial delamination (see details of Figure 9(a)).

A full-scale standard fire test according to EN 1363-1 and EN 1364-1 was reported by Machalická et al. [70] for a glass wall supported by an aluminum frame. The wall (3.475×4.57 m the overall size) consisted of three special FR, LG panels, gel-filled type (1.4×4.5 m the size of the central LG panel, 1×4.5 m for the lateral panels). Small gaps between adjacent glass panes were filled by means of special FR tapes and sealants. Collapse of the glass wall occurred after 49 minutes of fire exposure, with maximum temperatures in the order of 150°C (Figure 9(b)).

Both double LG panels composed of special tempered glass, gel-filled type (SAFTI SuperLite II-XL™ type, with 19.05 mm the total thickness), and monolithic glass panels (6.35 mm the thickness) were assembled together to obtain the glazing wall tested in [71]. Such a glass wall (two glass panels for each cross-section type) was frame-supported and had overall dimensions of 2.42×2.42 m. Fire experiments gave evidence of limited fire performances of simple glass panels, compared to FR components. Monolithic glass panes in fact were characterized by premature fallout from the supporting frame (i.e., 3 minutes after ignition, with 0.8 seconds elapsing between the occurrence of first cracks in glass and the final fallout of monolithic panes (Figure 10(a))). Double LG panels, in contrary, remained intact up to test conclusion (>30 minutes), without visible cracks or failure mechanisms close to connections with the framing system.

This is not the case of experimental studies carried out by Yang et al. [40] that tested monolithic, FR glass panels under standard fire curves. The experimental study gave in fact evidence of major issues deriving from framing systems and related connections. Even the FR glass panels

TABLE 2: Summary of selected experimental research studies on structural glass systems under fire.

	Reference and year of publication	Test typology/setup	Specimen size/loading	Glass type	Additional FR tools
Walls, facades, and enclosures	Mejicovsky (2007) [69]	Frame supported, double LG (special setup for heat transmission)	F/T	SLS (FT)	—
	Machalická et al. (2016) [70]	Frame supported, double LG	F/T	FR	Gel-filling layer
	Manzello et al. (2007) [71]	Frame supported, double LG + monolithic (furnace)	F/T	FR	Gel-filling layer
	Yang et al. (2011) [40]	Frame supported, monolithic	F/T	FR	—
Window retrofit	Koudijs and Csoke (2013) [72]	Double glazing unit	F/T	SLS (AN, HS)	Low-E coating
	Misawa et al. (2013) [73]	Double glazing unit	F/T	SLS (AN)	Low-E coating + refractory film
Floors and overheads	Siebert and Maniatis (2008) [74]	LG, frame supported	F/n.a.	n.a.	n.a.
	Davis (2013) [75]	LG, frame supported	F/M	SLS (FT) bonded to FR glass	Liquid laminating film
Beams	Veer et al. (2001) [22]	4 point-bending; monolithic, triple LG, insulated + segmented beams (glass frame, bespoke setup)	S/M	SLS (AN)	Intumescent protective coating
	Bokel et al. (2003) [76]	4 point-bending; triple LG (glass frame, bespoke setup)	S/M	SLS (AN), FR glass	Epoxy interlayers
	Louter and Nussbaumer (2016) [77]	4 point-bending; triple LG	F/M	SLS (AN, HS, FT)	—

S = small scale; F = full scale; M = mechanical loading; T = only thermal load; n.a. = not available.

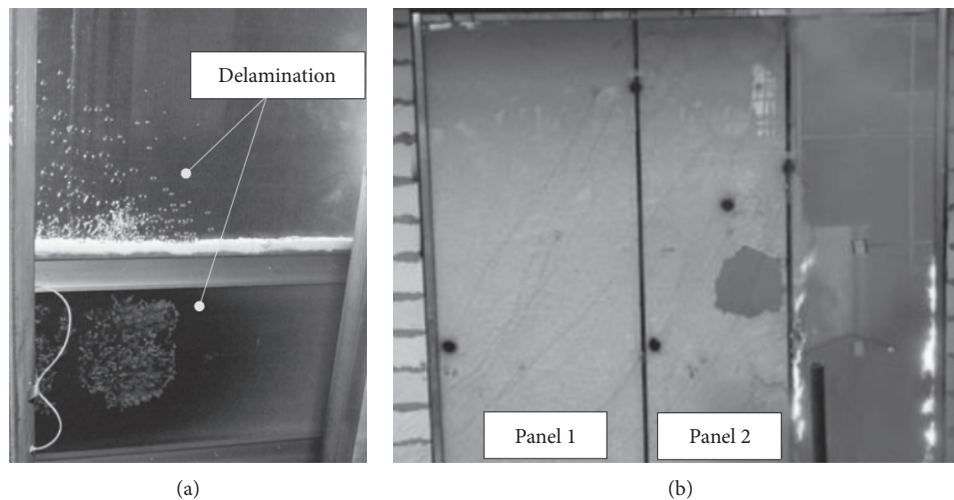


FIGURE 9: Glass enclosures under fire. (a) Evidence of partial delamination, as reported in [60] and (b) full-scale glazing wall tested in [70]. In evidence, it is possible to notice the loss of wall integrity and initiation of gel melting, after 49 minutes of fire exposure.

proved to offer high performances under fire loading; in particular, loss of integrity was observed to have origin in the glass-to-metal frame connection detailing (Figures 10(b) and 10(c)). Further fire experiments and numerical investigations on glass facade systems can also be found in [78–82], with evidence of the performance of specific glass system typologies, including cable-net systems and inclined facades.

5.2. *Retrofitting and Enhancement of Standard Glass Windows.* Several types of protective films able to improve the fire performance of existing and novel standard windows are available on the market. Although these coatings do not affect the room temperature elastic stiffness and resistance of a given glass pane to retrofit, the same films can be beneficial in delaying high-temperature effects, hence resulting in increased FR performance.

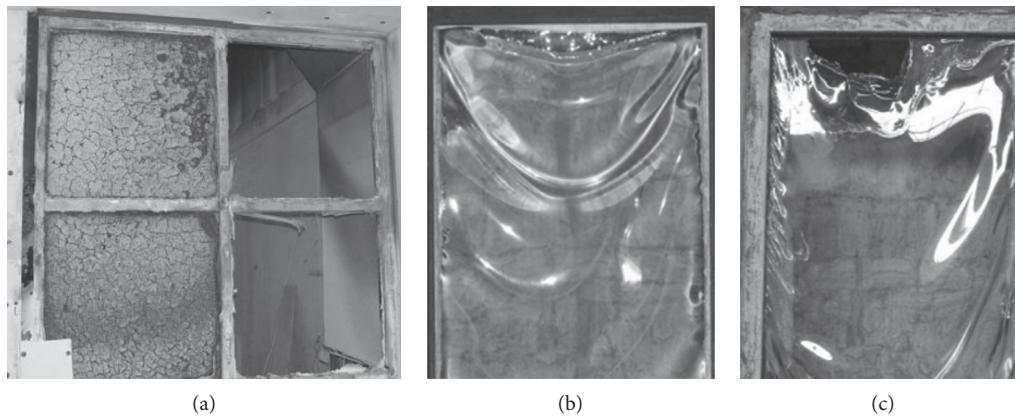


FIGURE 10: Failure mechanism in FR glass systems, as observed by (a) Manzello et al. [71], with evidence of fallout, and (b)-(c) by Yang et al. [40] on FR monolithic panes.

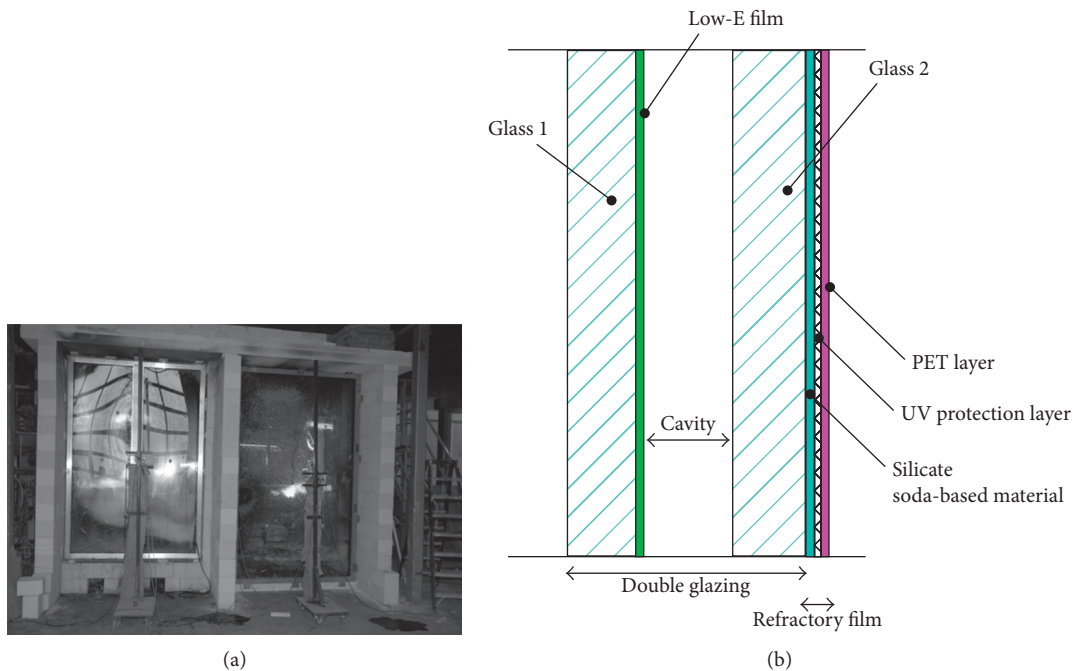


FIGURE 11: Experiments on coated glazing windows, as reported in (a) [72] and (b) [73], schematic cross-sectional view.

Koudijs and Csoke [72] first gave experimental evidence of the high potential of protective films for traditional glass systems, with careful consideration for the improved fire performance of windows composed of SLS glass, by taking into account a case study building in Rotterdam (NL) (Figure 11(a)). Low-E coatings were interposed within traditional double glazed units, by assessing the effects of their position (i.e., interior cavity face, etc.) under fire loading. The integrity of window samples was ensured for 27 minutes in the case of AN glass but increased up to 60 minutes in presence of HS glass panels, hence giving evidence of the potential fire performances of traditional insulating systems inclusive of special coatings.

Misawa et al. [73] also tested the efficacy of special refractory films, basically intended for application on the interior side of existing standard windows. The typical specimen consisted in a double glazed unit, Low-E coated, with 1×1 m the reference size. There, a novel refractory film was attached to the interior face of the glazed unit (i.e., on the glass surface expected to be exposed to fire). The refractory film consisted of (i) an external polyEthylene terephthalate (PET) film bonded to (ii) an ultraviolet protection layer and (iii) a silicate soda-based material layer (1 mm its thickness) (Figure 11(b)). 12 tests were carried out in total, including variations in AN glass supplier, thickness (8 mm or 12 mm), and specimen size (30×30 cm, 100×100 cm, and 94×94 cm) as well as Low-E film surface of application and comparisons with clear



FIGURE 12: Fire tests on glazing floor, as reported in [74]. (a) Initial state and (b) failure pattern (detail).

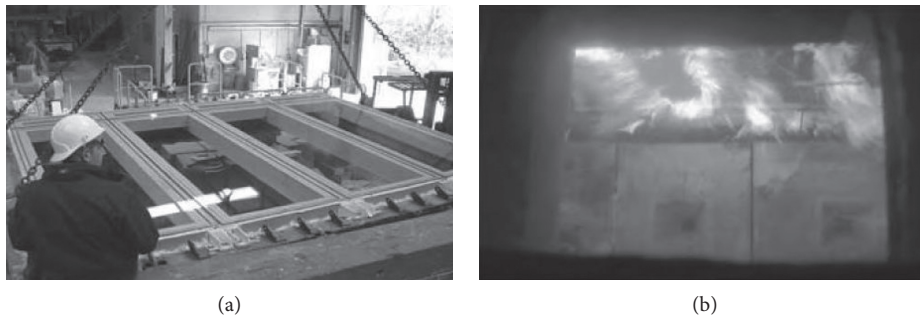


FIGURE 13: Fire tests on glazing floor, as reported in [75]. (a) Setup overview and (b) detail of the ongoing fire test.

uncoated specimens. All the experiments proved the high efficiency of refractory films, allowing Low-E double glazing units to achieve minimum 20 or 30 minutes of fire performance, as required for FR windows.

Although the mentioned research studies generally proved the potential and efficiency of such special coatings to enhance the FR of glazing systems, several aspects should be still assessed. Wu et al. [83], for example, experimentally investigated the high-temperature performance and thermal degradation of protective layers of common use for glass applications, giving evidence of gas emissions when exposed to fire.

5.3. Glass Floors and Overheads. Siebert and Maniatis [74] reported on fire tests carried out on glazing floors belonging to the subway station “Olympiapark Nord” in Munich (Germany). In the ceiling tunnel, overhead glazing accessible to person steps was made accessible by means of several openings (5×3.5 m the size). FR requirements were taken into account, as a possible configuration deriving from accidents (i.e., trains burning in the tunnel). Special multilayered safety LG panels were designed and tested under fire, in order to ensure appropriate safety levels (Figure 12). No test results and fire-performance-related data are available in the literature, however.

Similar fire experiments are summarized also in [75], referring to the glazing floor panels designed, in 2011, to be installed at a height of 130 m in the historic Blackpool Tower (UK), as a part of an ongoing refurbishment project. A full-

scale fire test was carried out (Figure 13), with 4.42×3.8 m the overall size of the flooring system. The mild steel-treated frame and related gaskets were also included within the test setup, so as to assess the fire performance of the full glazing system under its actual restraint configuration.

Aiming to ensure appropriate structural integrity as well as overall performances in the case of fire accidents, the typical glass panel (3×1.1 m the maximum size) consisted of a LG section, three 10 mm thick, FT glass layers, bonded together to a 23 mm Pilkington Pyrostop™, by using a special liquid composite bonding (Koediguard™ type). Steel-framing elements were also preliminary treated with intumescent coatings, mineral wool, and fire check boards. Additional expansion joints were finally included in the setup, in order to prevent buckling in the supporting frame members. The fire experiment was carried out in accordance with EN regulations, assigning to the flooring system a standard fire curve and a simultaneous mechanical load, being representative of crowd (5 kN/m^2 , distributed uniform pressure or 4.5 kN point load (50×50 mm foot print), resp.).

The fire performance exceeded 60 minutes of integrity (test stopped after 68 minutes), with maximum recorded temperatures of 67.6°C and no evidence of debonding or failure. Compared to fire insulation requirements (EN 1363-1), where temperature rise should not exceed 140°C (Section 2), a tolerance of $> 120^\circ\text{C}$ was hence ensured (12°C the ambient temperature during the test). Posttest deflection of 16.5 mm was measured (with $1/175$ the roof span deflection limit value provided by standards).

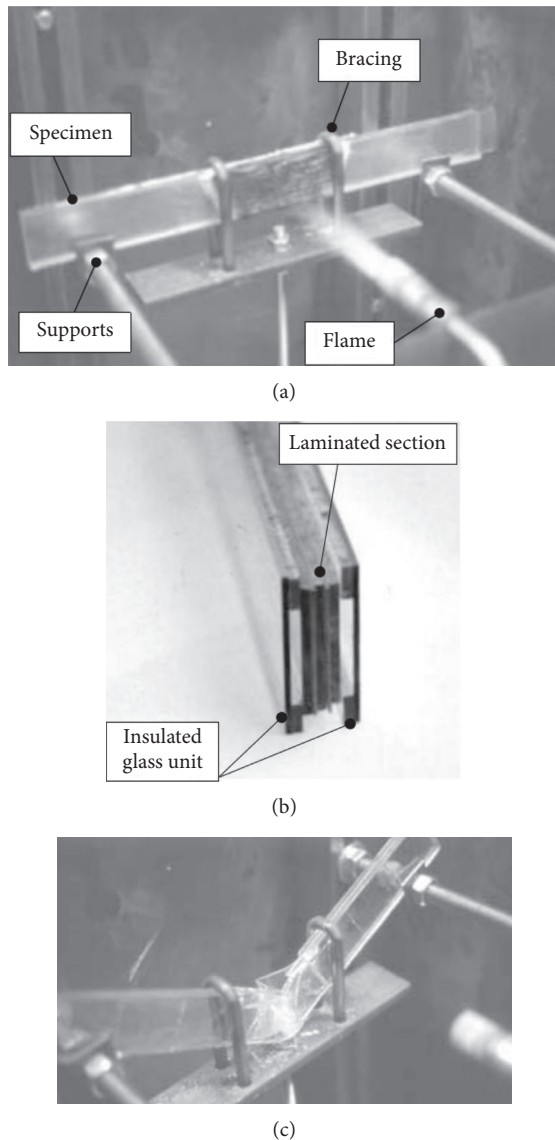


FIGURE 14: Summary of fire experiments carried out in [22]. (a) Four-point bending setup (in evidence, the foam layer provided by intumescent paint (specimens A)), (b) cross-section features of specimens E, and (c) buckling of segmented beams (type D).

5.4. Glass Beams. Limited experimental literature background can be found for structural glass elements under fire loading, due to the relatively recent demand of vulnerability assessment and protection for these systems.

Veer et al. reported in [22] on a set of bending test comparative results, experimentally obtained from monolithic and LG beams under fire, to assess the effects of intumescent coatings. The fire loading was imposed in the form of a constant flame at 650°C , with a fixed distance from the beams' lateral surface (Figure 14). Various beam geometries ($40\text{ mm} \times 400\text{ mm}$ the overall size) were tested, including specimens with different thickness and standard SLS glass types, such as

- (a) 6 mm thick, AN glass;
- (b) 6 mm thick, chemically toughened glass (120 MPa the initial stress);

- (c) 3 mm thick, chemically toughened glass, laminated with 1 mm polycarbonate (PC) foil (3 glass layers + 2 PC films);
- (d) 3 mm thick, segmented, chemically toughened glass, laminated with 1 mm PC foil (3 glass layers + 2 PC films). Compared to C, glass layers were bonded to PC foils in an overlapping pattern;
- (e) An LG beam (as in the case of C and D type specimens), including insulating cavities on the external sides.

All the (a)–(e) configurations were tested both without and after the application of intumescent coating (FlameGuard HCA-TR™ paint type).

A conventional four-point bending test setup was used for these beams. Experiments with no external mechanical loading as well as with additional weights (with up to 24 MPa the corresponding midspan bending stress) were carried out on monolithic AN specimens (type A) (Table 3).

The overall experimental investigation gave evidence of some important aspects, as, for example, the potential safety level of structural glass beams under fire.

However, critical aspects were also emphasized for the same specimens, like, for example, in the case of segmented beams (type D, see Figure 14(c)). Some preliminary FE simulations were also reported in [22], giving evidence of the temperature distribution and related stress effects for the examined beams. Worth of interest is in fact that such preliminary FE models gave evidence of temperature peaks in the adhesive layers providing structural bonding between the glass segments, hence emphasizing the crucial role of detailing.

Bokel et al. [76] later explored similar glass beam specimens, by taking into account the same overall geometrical features and test setup presented in [22]. The novel aspect was represented by testing LG beams composed of special FR glass (i.e., Pyroguard™ type as well as LG beams composed of 3 SLS glass layers, with epoxy films acting as interlayers for all the specimens). As a general outcome of the experimental investigation, epoxy layers were found to start charring after few seconds only, with limited fire performance of the beam specimens. An almost comparable behaviour was observed for all the beams, both composed of special Pyroguard layers or not, hence giving evidence (besides the limited number of tests) of the need for further extended investigations.

Louter and Nussbaumer [77] performed full-scale experimental tests on LG beams composed of standard glass layers. Differing from [18], a standard fire curve was considered for loading onto the oven, in accordance with EN regulations (Section 2). Through the experimental study, 3 full-scale beams were investigated. Given the same overall dimension of beams ($1\text{ m} \times 0.1\text{ m}$), variations were accounted in terms of glass type (AN, HS, and FT, resp.). The reference cross section consisted of 3 SLS layers, 10 mm in thickness, bonded together by SG foils (1.52 mm in thickness).

A four-point bending test setup was considered, with end supports protected from fire exposure, and the fire loading was assigned together with a simultaneous, constant

TABLE 3: Summary of bending test results reported in [22].

Specimen	Paint	Failure time (min)	Failure mode	T_{\max} (°C)	Notes
A	No	>30	I	250	—
	No*	2.4	BR	250	—
	Yes	19	BR	250	Beneficial effect of intumescent paint
B	No	>40	I	300	—
	Yes	>40	I	300	—
C	No	>30	PC evaporation	n.a.	Central 10 cm evaporated; no delamination at the beam ends
	Yes	>30	PC evaporation	n.a.	Central 7 cm evaporated; no delamination at the beam ends; beneficial effect of intumescent paint
D	No	1.45	C	n.a.	Premature failure of the adhesive layer between glass segments, with subsequent delamination, dislodgement of segments, and buckling
	Yes	4.1	C	n.a.	Beneficial effect of intumescent paint, but similar failure mechanism
E	No	>30	PC melting	n.a.	Significant thermal damage; central 7 cm PC melted (visible after 5 min)
	Yes	>39	PC melting	n.a.	Beneficial effect of intumescent paint, even with significant thermal damage; central 7 cm PC melted (visible after 10 min)

*Mechanical load included; I=integer beam; BR=broken; C=cohesive failure between glass segments and PC foils; T_{\max} =maximum temperature monitored on the beam backside, at the end of the experiment; n.a.=not available.

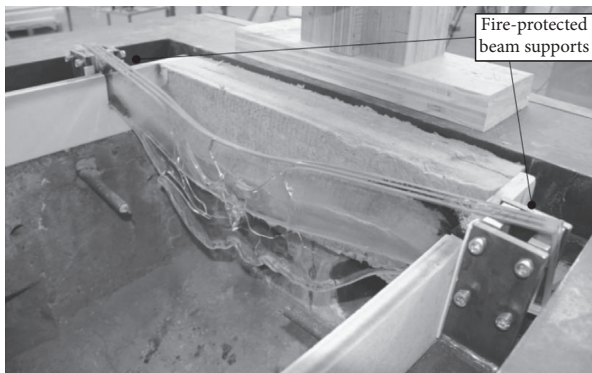


FIGURE 15: LG glass beams tested by Louter and Nussbaumer [77]. Typical failure configuration.

mechanical load taking the form of 115 kg at the midspan section. Given the limited stress effect due to the assigned mechanical load (with maximum tensile stresses in the order of 5 MPa at beams' midspan), the specimens proved to offer a rather stable behaviour under fire, for >40, >45, and >50 minutes in the case of AN, HS, and FT beams, respectively, up to collapse (Figure 15). As a general observation from such a kind of tests, the interlayer foils started melting and leaking off from their position after few minutes of fire exposure only; hence, the SLS glass panes behaved as almost fully uncoupled layers. On the other hand, protecting the beam ends from fire allowed to avoid premature collapse mechanisms.

6. Summary and Conclusions

In this paper, a state of art on structural glass systems under fire loading was presented, with careful consideration for current design methods and issues as well as

experimental research efforts. Besides the continuously increasing use of glass in buildings as a constructional material able to interact with and/or replace materials of traditional use, the actual behaviour of structural glass assemblies, in general, currently requires further investigations, as well as the application of specific fail-safe design rules. This is the case of glazing systems under ordinary loads, but especially of extreme loading conditions, as, for example, fire accidents.

As shown, the intrinsic features of glass and its interaction with other components (i.e., framing systems, boundary details, etc.) make glazing systems highly vulnerable to temperature variations, as well as combined effects of thermal and mechanical loads, hence requiring multidisciplinary approaches in their design. In doing so, appropriate structural safety levels should be in fact ensured in combination with multiple aspects, such as transparency, aesthetics, and lightning requirements.

At the material level, in particular, a wide set of experimental research can be found in the literature, aiming to assess major effects of high temperatures on MOE, tensile resistance, and thermal cracking of standard glass. Most of these experimental outcomes are in rather close agreement as far as the MOE variation with temperature is considered. But when different literature sources are accounted, however, test results can also give evidence of high scatter in the observed trends, as, for example, in the case of glass thermal resistance (Section 4). In addition, while most of glass applications in building consist of laminated or insulated glass systems, few experimental studies only are actually available to characterize the thermal effects in interlayer foils at high temperature.

As far as the attention moves from the material to the system and assembly levels, a relatively wide set of experimental investigations can also be found in the literature, with careful consideration for the fire performance of various

typologies of glass systems inclusive of a multitude of boundary configurations, fire exposure patterns, and glass types (standard and/or FR glass). As a common aspect of such experimental investigations (Section 5), connection details and restraints generally proved to have a key role in the overall observed responses, both for frame-supported and point-supported systems. Generally speaking, glass enclosures, walls, and beams proved—in most of the cases—to offer rather stable performances under fire loading, even composed of standard glass only, but requiring further extensive testing and assessment with special care for supporting details.

Finally, literature efforts have been spent in the last years also to assess the potential and efficacy of special coatings and films for the retrofitting and protection of existing glass windows and systems in general. In accordance with earlier observations, such solutions generally gave evidence of major benefits for uncoated glass specimens, but careful consideration should be still spent to properly optimize their potential.

Conflicts of Interest

The author declares that there are no conflicts of interest.

Acknowledgments

This research study has been carried out within the “Structural Task” activities of the ongoing EU COST Action TU1403 “Adaptive Facades Network” (www.tu1403.eu). In this regard, COST is gratefully acknowledged for facilitating scientific network and collaboration between the author and the Action international experts.

References

- [1] M. Haldimann, A. Luible, and M. Overend, *Structural Use of Glass*, International Association for Bridge and Structural Engineering (IABSE), Zurich, Switzerland, 2008, ISBN 978-3-85748-119-2.
- [2] M. Feldmann, R. Kasper, B. Abeln et al., *Guidance for European Structural Design of Glass Components—Support to the Implementation, Harmonization and Further Development of the Eurocodes*, Report EUR 26439, P. Dimova and D. Feldmann, Eds., Joint Research Centre—Institute for the Protection and Security of the Citizen, Brussels, Belgium, 2014.
- [3] M. Santarsiero, C. Louter, and A. Nussbaumer, “Laminated connections for structural glass applications under shear loading at different temperatures and strain rates,” *Construction and Building Materials*, vol. 128, pp. 214–237, 2016.
- [4] J. Belis, C. Bedon, C. Louter, C. Amadio, and R. Van Impe, “Experimental and analytical assessment of lateral torsional buckling of laminated glass beams,” *Engineering Structures*, vol. 51, pp. 295–305, 2013.
- [5] S. Jordão, M. Pinho, J. P. Martin, A. Santiago, and L. C. Neves, “Behaviour of laminated glass beams reinforced with pre-stressed cables,” *Steel Construction*, vol. 7, no. 3, pp. 204–207, 2014.
- [6] C. Pascual, J. Montali, and M. Overend, “Adhesively-bonded GFRP-glass sandwich components for structurally efficient glazing applications,” *Composite Structures*, vol. 160, pp. 560–573, 2017.
- [7] P. A. Hooper, R. A. M. Sukhram, B. R. K. Blackman, and J. P. Dear, “On the blast resistance of laminated glass,” *International Journal of Solids and Structures*, vol. 49, no. 6, pp. 899–918, 2012.
- [8] X. Zhang, H. Hao, and G. Ma, “Parametric study of laminated glass window response to blast loads,” *Engineering Structures*, vol. 56, pp. 1707–1717, 2013.
- [9] X. Zhang and C. Bedon, “Vulnerability and protection of glass windows and facades under blast: experiments, methods and current trends,” *International Journal of Structural Glass and Advanced Materials Research*, vol. 1, no. 1, 14 pages, 2017.
- [10] R. A. Behr, A. Belarbi, and A. T. Brown, “Seismic performance of architectural glass in a storefront wall system,” *Earthquake Spectra*, vol. 11, no. 3, pp. 367–391, 1995.
- [11] H. Sucuoğlu and C. V. G. Vallabhan, “Behaviour of window glass panels during earthquakes,” *Engineering Structures*, vol. 19, no. 8, pp. 685–694, 1997.
- [12] J. L. Brueggeman, R. A. Behr, H. Wulfert, A. M. Memari, and P. A. Kremer, “Dynamic racking performance of an earthquake-isolated curtain wall system,” *Earthquake Spectra*, vol. 16, no. 4, pp. 735–756, 2000.
- [13] C. Bedon and C. Amadio, “Enhancement of the seismic performance of multi-storey buildings by means of dissipative glazing curtain walls,” *Engineering Structures*, vol. 152, pp. 320–334, 2017.
- [14] F. J. Masters, K. R. Gurley, N. Shah, and G. Fernandez, “The vulnerability of residential window glass to lightweight windborne debris,” *Engineering Structures*, vol. 32, no. 4, pp. 911–921, 2010.
- [15] M. S. Shetty, J. Wei, L. R. Dharani, and D. S. Stutts, “Analysis of damage in laminated architectural glazing subjected to wind loading and windborne debris impact,” *Buildings*, vol. 3, no. 2, pp. 422–441, 2013.
- [16] M. Debuyser, J. Sjöström, D. Lange, D. Honfi, D. Sonck, and J. Belis, “Behaviour of monolithic and laminated glass exposed to radiant heating,” *Construction and Building Materials*, vol. 130, pp. 212–229, 2017.
- [17] H. Chen, H. Zhao, Y. Wang, Q. Wang, and J. Sun, “The breakage of float glass with four-edge shading under the combined effect of wind loading and thermal loading,” *Fire Technology*, vol. 53, no. 3, pp. 1233–1248, 2017.
- [18] C. Bedon, R. Kalamar, and M. Eliasova, “Low velocity impact performance investigation on square hollow glass columns via full-scale experiments and Finite Element analyses,” *Composite Structures*, vol. 182, pp. 311–325, 2017.
- [19] X. Zhang, H. Hao, and G. Ma, “Laboratory test and numerical simulation of laminated glass window vulnerability to debris impact,” *International Journal of Impact Engineering*, vol. 55, pp. 49–62, 2013.
- [20] A. Ramos, F. Pelayo, M. J. Lamela, A. Fernandez Canteli, M. L. Aenlle, and K. Persson, “Analysis of structural glass panels under impact loading using operational modal analysis,” in *Proceedings of the 6th International Operational Modal Analysis Conference (IOMAC)*, Gijon, Spain, May 2015.
- [21] M. Larcher, M. Arrigoni, C. Bedon et al., “Design of blast-loaded glazing windows and facades: a review of essential requirements towards standardization,” *Advances in Civil Engineering*, vol. 2016, Article ID 2604232, 14 pages, 2016.
- [22] F. A. Veer, M. van der Voorden, H. Rijgersberg, and J. Zuidema, “Using transparent intumescent coatings to increase the fire resistance of glass and glass laminates,” in *Proceedings of Glass Processing Days 2013*, pp. 392–396, Tampere, Finland, June 2001.

- [23] EN 1990:2002-Eurocode, *Basis of Structural Design*, European Committee for Standardization (CEN), Brussels, Belgium, 2002.
- [24] prEN 13474-1, *Glass in Building—Design of Glass Panes—Part 1: General Basis of Design*, European Committee for Standardization (CEN), Brussels, Belgium, 2007.
- [25] ÖNORM B 3716, *Glass in Building—Structural Glass Construction*, Österreichisches Normungsinstitut, Vienna, Austria, 2013.
- [26] NEN 2608, *Glass in Building—Requirements and Determination Method*, Nederlands Normalisatie Instituut, Delft, Netherlands, 2011.
- [27] DIN 18008:2010–12, *Glass in Building—Design and Construction Rules*, German Institute for Standardisation (Deutsches Institut für Normung), Berlin, Germany, 2010.
- [28] C. Bedon and C. Amadio, “Assessment of analytical formulations for the ULS resistance verification of structural glass elements accounting for the effects of different load durations,” *Structures*, vol. 11, pp. 218–228, 2017.
- [29] CNR-DT/210, *Guide for the Design, Construction and Control of Structures Made of Glass Structural Elements [Istruzioni per la Progettazione, l'Esecuzione ed il Controllo di Costruzioni con Elementi Strutturali di Vetro]*, National Research Council (CNR), Italy, 2013.
- [30] EN 13501, *Fire Classification of Construction Products and Building Elements. Classification Using Test Data from Reaction to Fire Tests*, European Committee for Standardization (CEN), Brussels, Belgium, 2007.
- [31] EN 1363-1, *Fire Resistance Tests—Part 1: General Requirements*, European Committee for Standardization (CEN), Brussels, Belgium, 2012.
- [32] EN 1364-1, *Fire Resistance Tests for Non-Loadbearing Elements—Part 1: Walls*, European Committee for Standardization (CEN), Brussels, Belgium, 2015.
- [33] EN 1634, *Fire Resistance and Smoke Control Tests for Door, Shutter and Openable Window Assemblies and Elements of Building Hardware*, European Committee for Standardization (CEN), Brussels, Belgium, 2008.
- [34] EN 1365-3, *Fire Resistance Tests for Load Bearing Elements—Part 3: Beams*, European Committee for Standardization (CEN), Brussels, Belgium, 1999.
- [35] Underwriters Laboratories Inc. (UL), “Fire protection systems,” <http://www.ul.com/code-authorities/building-code/fire-protection-systems/>.
- [36] Glass & Glazing Federation, “A guide to best practice in the specification and use of fire-resistant glazed systems 2011.” <http://www.ggf.org.uk/publication/FRGbest>.
- [37] S. J. Bennison, M. H. X. Quin, and P. S. Davies, “High-performance laminated glass for structurally efficient glazing,” in *Proceedings of Innovative Light-Weight Structures and Sustainable Facades Conference*, Hong Kong, 2008.
- [38] M. Santarsiero, C. Louter, and A. Nussbaumer, “The mechanical behaviour of SentryGlas® ionomer and TSSA silicon bulk materials at different temperatures and strain rates under uniaxial tensile stress state,” *Glass Structures & Engineering*, vol. 1, no. 2, pp. 395–415, 2016.
- [39] M. Meissner and V. Sackmann, “On the effect of artificial weathering on the shear bond and the tear strength of two different interlayers of laminated glass,” in *Proceedings of ISAAG 2006*, Munich, Germany, 2006.
- [40] Z. Yang, X. Zhao, X. Wu, and H. Li, “Application and integrity evaluation of monolithic fire-resistant glass,” *Procedia Engineering*, vol. 11, pp. 603–607, 2011.
- [41] Q. Shao, F. Li, T. Chen, and Z. H. Sun, “Heat resistance and water protection effectiveness for large single-pane fireproof glass,” *Journal of Central South University of Technology*, vol. 18, no. 6, pp. 2185–2191, 2011.
- [42] J. K. Richardson and I. Oleszkiewicz, “Fire tests on window assemblies protected by automatic sprinklers,” *Fire Technology*, vol. 23, no. 2, pp. 115–132, 1987.
- [43] A. K. Kim and G. D. Lougheed, “The protection of glazing systems with dedicated sprinklers,” *Journal of Fire Protection Engineering*, vol. 2, no. 2, pp. 49–59, 1990.
- [44] C. W. Wu, T. H. Lin, M. Y. Lei, T. H. Chung, C. C. Huang, and W. T. Chiang, “Fire resistance tests of a glass pane with down-flowing water film,” *Journal of the Chinese Institute of Engineers*, vol. 31, no. 5, pp. 737–744, 2008.
- [45] W. C. Hu, S. D. Nurcholik, W. H. Lo et al., “Heat resistance of a fireproof curtain with water film,” in *Proceedings of 24th National Conference on Combustion and Energy*, Article ID 080, Tainan, Taiwan, April 2014.
- [46] E. Le Bourhis and T. Rouxel, “Indentation response of glass with temperature,” *Journal of Non-Crystalline Solids*, vol. 316, no. 1, pp. 153–159, 2003.
- [47] T. Rouxel, “Elastic properties and short-to medium-range order in glasses,” *Journal of the American Ceramic Society*, vol. 90, no. 10, pp. 3019–3039, 2007.
- [48] T. Rouxel and J. C. Sangleboeuf, “The brittle to ductile transition in soda–lime–silica glass,” *Journal of Non-Crystalline Solids*, vol. 271, no. 3, pp. 224–235, 2000.
- [49] M. J. Kerper and T. G. Scuderi, “Mechanical properties of chemically strengthened glasses at high temperatures,” *Journal of the American Ceramic Society*, vol. 49, no. 11, pp. 613–618, 1966.
- [50] J. Shen, D. J. Green, R. E. Tressler, and D. L. Shelleman, “Stress relaxation of a soda lime silicate glass below the glass transition temperature,” *Journal of Non-Crystalline Solids*, vol. 324, no. 3, pp. 277–288, 2003.
- [51] H. Emmons, “The needed fire science,” in *Fire Safety Science-Proceedings of the First International Symposium*, IAFSS, pp. 33–53, Berkeley, California, 1986.
- [52] O. Keski-Rahkonen, “Breaking of window glass close to fire,” *Fire and Materials*, vol. 12, no. 2, pp. 61–69, 1988.
- [53] P. J. Pagni and A. A. Joshi, “Glass breaking in fires,” in *Fire Safety Science-Proceedings*, vol. 3, pp. 791–802, Elsevier Applied Science, London, UK, 1991.
- [54] K. Harada, A. Enomoto, K. Uede, and T. Wakamatsu, “An experimental study on glass cracking and fallout by radiant heat exposure,” *Fire Safety Science*, vol. 6, pp. 1063–1074, 2000.
- [55] T. J. Shields, G. W. H. Silcock, and M. Flood, “Performance of a single glazing assembly exposed to a fire in the centre of an enclosure,” *Fire and Materials*, vol. 26, no. 2, pp. 51–75, 2002.
- [56] T. J. Shields, G. W. H. Silcock, and F. Flood, “Behaviour of double glazing in corner fires,” *Fire Technology*, vol. 41, no. 1, pp. 37–65, 2005.
- [57] Q. Xie, X. Zhang, Y. Wan, Q. Zhang, and X. Cheng, “Full-scale experimental study on crack and fallout of toughened glass with different thicknesses,” *Fire and Materials*, vol. 32, no. 5, pp. 293–306, 2008.
- [58] Y. Wang, K. Li, Y. Su et al., “Determination of critical breakage conditions for double glazing in fire,” *Applied Thermal Engineering*, vol. 111, pp. 20–29, 2017.
- [59] Q. Wang, Y. Wang, H. Chen, H. Xiao, J. Sun, and L. He, “Frame constraint effect on the window glass crack behavior exposed to a fire,” *Engineering Fracture Mechanics*, vol. 108, pp. 109–119, 2013.
- [60] Y. Wang, Q. Wang, G. Shao et al., “Fracture behavior of a four-point fixed glass curtain wall under fire conditions,” *Fire Safety Journal*, vol. 67, pp. 24–34, 2014.

- [61] J. Virgone, P. Depecker, and G. Krauss, "Computer simulation of glass temperatures in fire conditions," *Building and Environment*, vol. 32, no. 1, pp. 13–23, 1997.
- [62] S. Dembele, R. A. F. Rosario, and J. X. Wen, "Thermal breakage of window glass in room fires conditions—analysis of some important parameters," *Building and Environment*, vol. 54, pp. 61–70, 2012.
- [63] Q. Wang, H. Chen, Y. Wang et al., "Development of a dynamic model for crack propagation in glazing system under thermal loading," *Fire Safety Journal*, vol. 63, pp. 113–124, 2014.
- [64] Z. Malou, M. Hamidouche, N. Bouaouadja, J. Chevalier, and G. Fantozzi, "Thermal shock resistance of a soda lime glass," *Ceramics-Silikáty*, vol. 57, no. 1, pp. 39–44, 2013.
- [65] Q. Xie, H. Zhang, and D. Si, "Experimental study on critical breakage stress of float glass with different thickness under conditions with temperatures of 25 and 200°C," *Fire and Materials*, vol. 35, no. 5, pp. 275–283, 2011.
- [66] Y. Wang, Q. Wang, G. Shao et al., "Experimental study on critical creaking stress of float glass under elevated temperature," *Materials and Design*, vol. 60, pp. 41–49, 2014.
- [67] B. Cardenas, N. Leon, J. Pye, and H. D. Garcia, "Design and modeling of high temperature solar thermal energy storage unit based on molten soda lime silica glass," *Solar Energy*, vol. 126, pp. 32–43, 2016.
- [68] T. W. Tong, *Thermal Conductivity 22*, Technomic Publishing Company, Ltd., Lancaster, PA, USA, ISBN 1-56676-172-7, 1994.
- [69] T. Mejicovsky, "Use of laminated glass in structural enclosures," in *Proceedings of Glass Performance Days 2007*, pp. 174–178, July 2007, <http://www.glassfiles.com>.
- [70] K. Machalická, M. Charvátová, M. Eliášová, and P. Kuklík, "The behaviour of fire resistant glass under fire," *Structures and Architecture: Beyond their Limits*, Paulo J. S. Cruz, Ed. pp. 991–997, 2016.
- [71] S. L. Manzello, R. G. Gann, S. R. Kuckak, K. R. Prasad, and W. W. Jones, "An experimental determination of a real fire performance of a non-load bearing glass wall assembly," *Fire Technology*, vol. 43, no. 1, pp. 77–89, 2007.
- [72] J. Koudijs and C. Csoke, "Fire resistance without fire resistant glass," *MATEC Web of Conferences*, vol. 9, Article ID 02001, 2013.
- [73] Y. Misawa, M. Hirota, T. Ohta, and S. Matsunobu, "Post-applied film to improve the fire resistance of existing exterior windows," in *Proceedings of Glass Performance Days 2013*, pp. 260–264, June 2013, <http://www.glassfiles.com>.
- [74] B. Siebert and I. Maniatis, "Glass constructions—applications in Germany," in *Proceedings of Challenging Glass Conference on Architectural and Structural Applications of Glass*, pp. 119–126, Delft, Netherlands, May 2008.
- [75] C. Davis, "Meeting the challenges of the modern world with liquid composite laminated glass," in *Proceedings of COST Action TU0905 Mid-Term Conference on Structural Glass*, pp. 317–322, Porec, Croatia, April 2013.
- [76] R. M. J. Bokel, F. A. Veer, and L. Tuisinga, "Fire resistance of glass," in *Proceedings of Glass Processing Days 2003*, pp. 362–363, June 2003, <http://www.glassfiles.com>.
- [77] C. Louter and A. Nussbaumer, "Fire testing of structural glass beams; initial experimental results," in *Proceedings of Glass-Con Global Conference*, Boston, PA, USA, July 2016.
- [78] W. K. Chow, Y. Gao, H. Dong, G. W. Zou, S. S. Han, and C. L. Chow, "Experimental studies on fire response of glass facade systems," *International Journal on Engineering Performance-Based Fire Codes*, vol. 8, no. 2, pp. 54–68, 2006.
- [79] W. K. Chow, Y. Gao, and C. L. Chow, "A review on fire safety in buildings with glass facade," *Journal of Applied Fire Science*, vol. 16, no. 3, pp. 201–223, 2006.
- [80] L. Peng, Z. Ni, and X. Huang, "Experimental and numerical study of fire spread upon double-skin glass facades," *MATEC Web of Conferences*, vol. 9, Article ID 03009, 2013.
- [81] L. F. Gong, Y. Bai, and S. Q. Li, "Mechanical performance calculation of single-layer cable mesh point-supported glass curtain wall under fire conditions," *Applied Mechanics and Materials*, vol. 580–583, pp. 2702–2707, 2014.
- [82] M. Quinn, A. Nadjai, F. Ali, and D. Bakirtzis, "Experimental investigation of flame impingement on vertical and inclined glazing facades," *MATEC Web of Conferences*, vol. 9, Article ID 03008, 2013.
- [83] M. Wu, W. K. Chow, and X. Ni, "Characterization and thermal degradation of protective layers in high-rating fire-resistant glass," *Fire and Materials*, vol. 39, no. 1, pp. 26–40, 2014.

Research Article

Study of Split-Flow Wall Located at Exit

Guomin Zhao,¹ Min Li,¹ Yunfeng Zhao,¹ Qingsong Zhng,² and Zhongxian Liu¹

¹School of Energy and Safety Engineering, Tianjin Chengjian University, Tianjin 300384, China

²Economics and Management College, Civil Aviation University of China, Tianjin 300300, China

Correspondence should be addressed to Guomin Zhao; guominzhao@163.com

Received 2 June 2017; Revised 17 August 2017; Accepted 29 August 2017; Published 6 November 2017

Academic Editor: Michel Arrigoni

Copyright © 2017 Guomin Zhao et al. This is an open access article distributed under the Creative Commons Attribution License, which permits unrestricted use, distribution, and reproduction in any medium, provided the original work is properly cited.

Congestion is the major cause of crowd stampede-trampling and crushing incidents. To alleviate the phenomenon of congestion in the process of evacuation, theory of split-flow wall is put forward to optimize the evacuation and the principle of it is analyzed. Based on the occupant evacuation software of buildingEXODUS, the set parameters of the split-flow wall are studied, and we find that the best range of shunt wall length is 1.5–2 times the export width and the best position of the split-flow wall is 0.5 to 0.75 times the export width far from the exit. Shunt wall can effectively alleviate and even eliminate the congestion in the process of evacuation and will not affect safe evacuation when crowd density is low.

1. Introduction

Along with the fast development of the economy, the business center, shopping plaza, large market, and comprehensive malls emerge endlessly. Their generation and progress are common product of the city, society, science and technology, finance, and other fields actually. The appearance and development of public buildings bring convenience to our life; at the same time, this kind of building with complex space structure, luxurious decoration, big fire load, big traffic, and complicated composition has brought great challenge for fire-fighting and evacuation.

In order to ensure that the people in public buildings in an emergency evacuate effectively and safely, some scholars abroad such as Kretz et al. have carried out a series of experiments on the through characteristic of bottleneck and got the relationship between export density and width of bottleneck [1]; Helbing et al., according to the mechanics model of society, found that placing a cylinder in front of the exit can reduce the evacuation crowd density near the exit and alleviate stranded phenomenon caused by excessive congestion [2]; Yanagisawa et al. found that setting obstacles in front of security exit can reduce the number of conflicts before the exit and increase number of people fleeing out of the building [3]; Kirchner et al., based on the simulation research of cellular automata model, found that the distance

between small cylinder and the exit is an important factor affecting safety evacuation time [4].

Some domestic scholars have done a lot of research. Based on cellular automata model, they studied the evacuation problems of crowd in multiexport room and analyzed the influence of rationality degree and the sensitivity coefficient to the evacuation process; Huili got a function relation between exit width and evacuation time [5]; Chen did more detailed research on critical jam density of the people stream evacuating in cross channel [6]. In recent years, in addition, some domestic researchers are also beginning to study the evacuation and diversion facilities of shunt wall; for example, Jinjing introduced a conflict function into cellular automata model and researched the set parameters of shunt wall [7].

In order to prevent the occurrence of crowd trample in the evacuation process, ensure the safe and effective evacuation of the crowd, we must reduce the population density of the bottleneck. For this purpose, we can widen the export [8], but the effect is not obvious. In view of this, it is an effective measure to improve the safety of evacuation by setting up the shunt wall at the bottleneck of evacuation. Shunt wall is usually set near the exit of the building with high-density crowd such as Movie theater and shopping center, in emergency cases which can play an important role in alleviating stranded phenomenon near the exit and ensure the safety evacuation of the crowd.

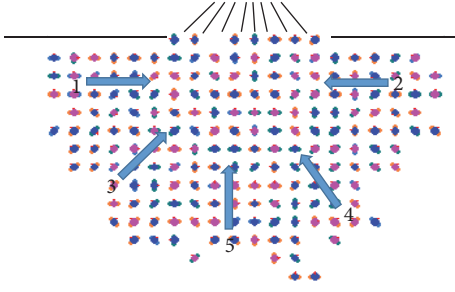


FIGURE 1: Evacuation without shunt wall.

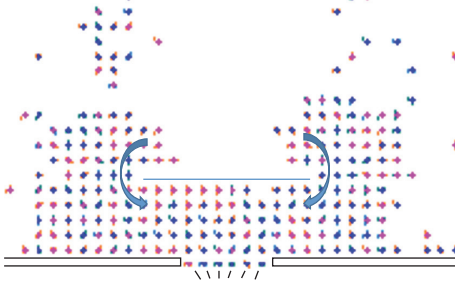


FIGURE 2: Evacuation with shunt wall.

2. Analysis of Shunt Wall

Because of the herd mentality of crowd in the process of evacuation, especially in the case of an emergency such as fire, coupled with the surrounding environment, is unfamiliar, concentrating on minority evacuation passageway, congestion, and the arching phenomenon (as shown in Figure 1) is bound to appear in the process of evacuation, which would reduce the evacuation efficiency.

Shunt wall was able to optimize evacuation, on the one hand, because shunt wall can split the stream of crowd; if there is shunt wall near the exit, the crowd would be diverted and they would evacuate along the shunt wall to the exit; as a result, the personnel density near the export is reduced, the phenomenon of congestion is alleviated, and, to some certain extent, shunt wall can also improve the efficiency of evacuation; on the other hand, in the process of crowd evacuating out of the door, there is a change in the direction of walking at the end of shunt wall, the situation where people coming from all directions flock to the core of export at the same time is changed, as shown in Figures 1 and 2, which can avoid the appearance of arch structure with balance force [9] and reduce probability of crowded stampede due to the collapsing of arch structure equilibrium state.

In addition, width of building export is constant, the evacuation capability is certain, phenomenon of congestion appears when the number of people arriving at the exports is greater than that of the largest evacuation capacity, and crowded time is t . If there is a shunt wall, the evacuation route will change and the evacuation distance will increase; extension distance is ΔL . At the same time, due to the change of path, crowd will slow down; moreover, when the crowd encounter the shunt wall in process of evacuation, they will

TABLE 1: Personnel composition.

Personnel type	Adult man	Adult woman	Children	Elders
Ratio	40%	40%	10%	10%

spend some time to choose evacuation path, thus delaying the evacuees arriving near the exit of the building; the delay time is ΔT , which is shown in (1), so that shunt wall can effectively relieve the congestion.

$$\Delta T = \Delta T_1 + \Delta T_2 + \Delta T_3, \quad (1)$$

where $\Delta T_1 = \Delta L/V$, caused by the extension distance, ΔT_2 is caused by slow speed, and ΔT_3 is the time spent during the choice of the path. The degree of congestion is expressed by η , which is shown in

$$\eta = \frac{t - \Delta T}{T}, \quad (2)$$

where T is the evacuation time and ΔT_1 , ΔT_2 , and ΔT_3 are directly affected by the D , L of shunt wall, which is shown in

$$\eta = f(D, L). \quad (3)$$

The influence of shunt wall is different to the people at different direction of the door. Just as Figure 1 shows, the crowd can be divided into 5 parts, the path of parts 1 and 2 would not change, the value of ΔT_1 and ΔT_3 will be 0, and ΔT contains ΔT_2 only because people from other parts would occupy the way which belongs to parts 1 and 2 only when there is no shunt wall, so that the shunt wall affects parts 1 and 2 slightly. While the influence on parts 3 and 4 is serious compared to that of parts 1 and 2, because ΔT of parts 3 and 4 contains the three parts all, the influence to part 5 is more serious than that of parts 3 and 4, because the extension distance ΔL of part 5 is longer than that of parts 3 and 4. The shunt wall can delay people arriving at the export in different degree and vary the situation of the people crowding into exit at the same time. The theory of using shunt wall to optimize evacuation is setting up shunt wall with reasonable parameters of D and L , making η as small as possible; at the same, the evacuation time cannot be lengthened a lot.

3. Optimization of Shunt Wall Set Parameters

Because the pretty penny of traditional full-scale evacuation experiments is prone to accidents, when determining the optimum setting parameters of the shunt wall, the evacuation experiments in this paper are conducted by the software of buildingEXODUS and take η and T as two evacuation parameters as the judgment, hoping to obtain the best setting parameter of shunt wall. Experimental design is shown in Figure 3; it is a 31×16 m square room shown in Figure 3, with exit 1, 4 m wide, and exits 2 and 3, 2 m wide. Based on the current international practical public personnel composition used in the commercial complex, the composition of evacuees of this paper is shown in Table 1. The location of the people is random. There is big difference in walking speed of evacuees

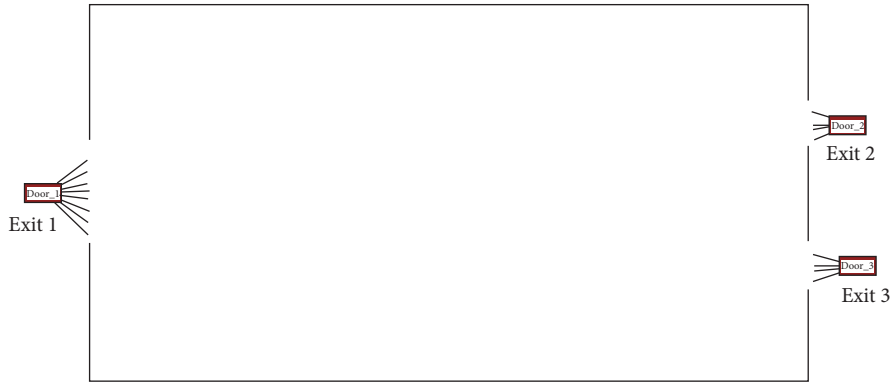


FIGURE 3: Experimental model.

TABLE 2: Evacuation speed V .

Function of building	Walking speed (m/s)		
	The ramp and stair	Shops, horizontal corridors, inward, and outward	
	Up	Down	
Adult man	0.5	0.7	1.2
Adult woman	0.43	0.6	1.02
Children	0.33	0.46	0.79
Elders	0.3	0.42	0.71

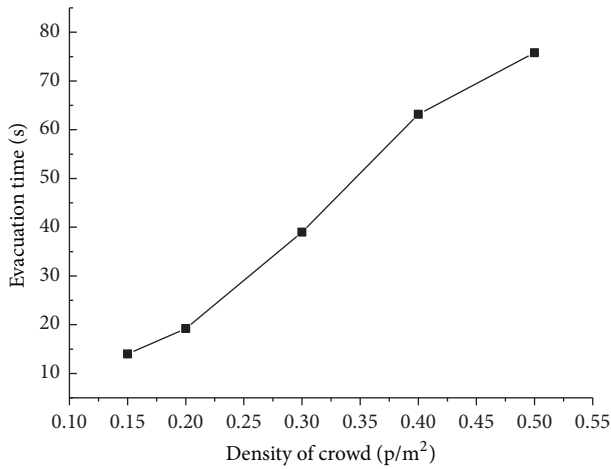


FIGURE 4: Evacuation time without shunt wall.

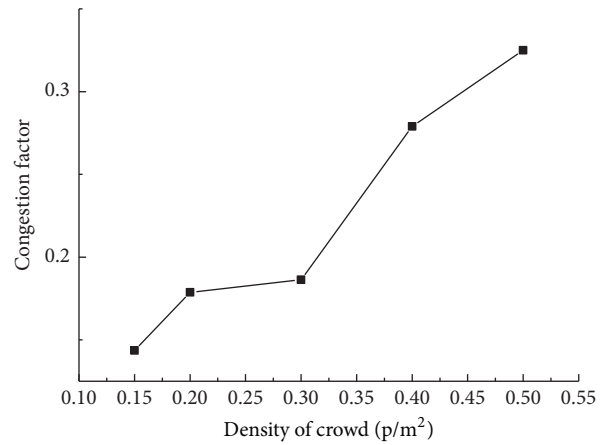


FIGURE 5: Congestion factor without shunt wall.

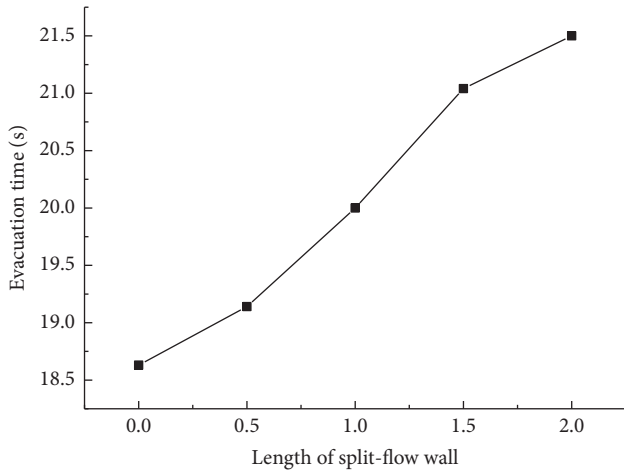
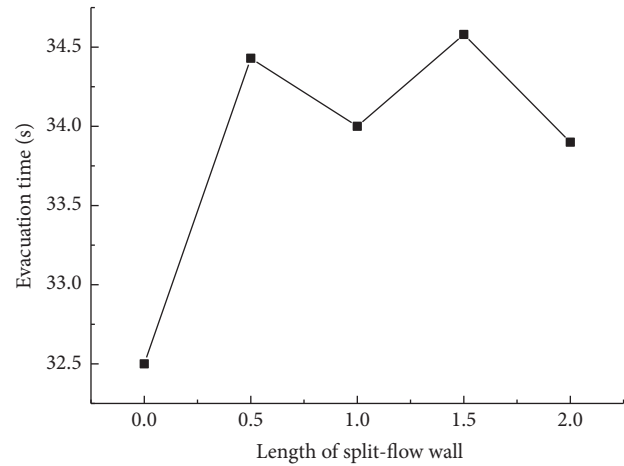
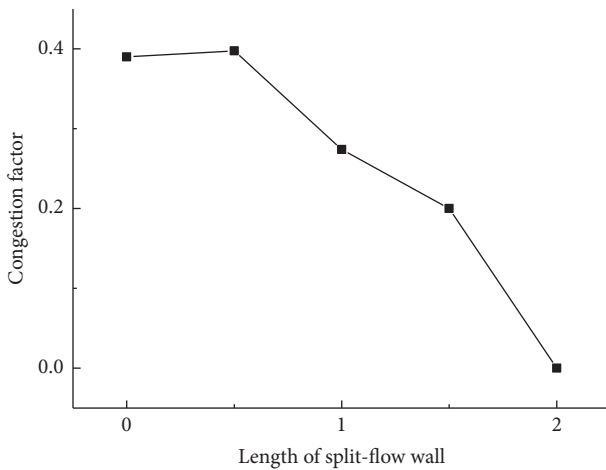
in different age and sex and different way. The project of University of Edinburgh, Scotland, mainly researched on the speed of people with different age, sex, and so on [10, 11]. The speed of evacuees in this paper is shown in Table 2. In this article, the authors views the crowd density (ρ) [12–15], length (L), and location (D) of the shunt wall and conducts comprehensive simulation experiment.

4. Analysis of Experimental Results

When there is no shunt wall, results of evacuation simulation experiment are shown in Figures 4 and 5; the figures show

that, with the increasing of population density, congestion factor increases obviously, and congestion becomes more serious with the increases of density. When population density is 0.5, η reaches 0.8. There is a great change in evacuation time too; the evacuation time changes from 15 s when the density of crowd is 0.15 p/m^2 to 35 s when the density of crowd is 0.5 p/m^2 .

Figures 6 and 7 are variation of the evacuation parameters with the change of shunt wall length, when the density of crowd is 0.3 p/m^2 and the position of the shunt wall is 0.5. As we can see from the figures, shunt wall affects η mainly, and with the increase of shunt wall length, η reduces and the speed of η reducing increases. When the range of the shunt

FIGURE 6: Evacuation time when $D = 0.5$, $\rho = 0.3$.FIGURE 8: Evacuation time when $D = 0.5$, $\rho = 0.5$.FIGURE 7: Congestion factor when $D = 0.5$, $\rho = 0.3$.

wall length is 1.5 to 2, the speed of η reducing is the fastest; when the shunt wall length is 2, η reduces to 0. In addition, as we can see from Figure 6, as the increase of the shunt wall length, evacuation time increases, and when the shunt wall length is 1.5 to 2 times the width of the exports long, the speed of evacuation time increasing slows down.

Figures 8 and 9 are evacuation parameters along with changes of the length of the wall when the population density is 0.5 p/m^2 and the position of the shunt wall is 0.5. We can see from the comparison of Figures 6 and 8 that shunt wall affects the evacuation parameters more significantly when the population density is low. Figure 8 displays that shunt wall affects η mainly, and with the increase of shunt wall length, the speed of η reducing increases. When the range of the shunt wall length is 1.5 to 2, the speed of η reducing is the fastest, and η changes from 0.72 when the length of shunt wall is 1.5 to 0.61 with the length of shunt wall being 2. In addition, as Figure 8 shows, evacuation time increases with the growth of length of the shunt wall, and when shunt wall length is 1.5 to 2, the evacuation time slightly reduces.

Consider Figures 6, 7, 8, and 9 together; with increase of shunt wall length, crowded parameter reduces. It is because when we lengthen the shunt wall, the extension distance ΔL becomes longer, and the shunt wall can interlace the arrival time of each part shown in Figure 1. But the length of shunt wall cannot be too long, because it is unrealistic and the evacuation time would become too long if the shunt wall is very long, just as Figures 7 and 9 show. And from Figures 7 and 9, we can know that, when shunt wall length increases, evacuation time grows slightly; when the crowd density is 0.3 p/m^2 , evacuation time grows by 6%; when the crowd density is 0.5 p/m^2 , evacuation time grows by 1.5%, which indicates that the increase in evacuation time due to shunt wall has little effect on evacuation. Consider η and T together; the most suitable length of shunt wall is 1.5–2.

Figures 10 and 11 are evacuation parameters varying with the shunt wall location when the population density is 0.3 p/m^2 and length of shunt wall is 1.5. Figure 10 shows that, with the distance between shunt wall and export lengthening, congestion factor increases; when the location of the shunt wall is 0.5, η is the minimum. Figure 10 shows that, with the increase of the distance between shunt wall and export, evacuation time reduces slightly.

Figures 12 and 13 are evacuate parameters vary with the shunt wall location when the population density is 0.5 p/m^2 and length of shunt wall is 2. Figure 12 shows that, with the distance between shunt wall and export lengthening, the value of congestion factor grows, congestion factor is the smallest when the location of the shunt wall is 0.5. Figure 13 shows that, with the increase of the distance between shunt wall and export, evacuation time reduces slightly.

Consider Figures 10, 11, 12, and 13 together; with shunt wall becoming far away from export, congestion factor grows. The reason is that if the distance between shunt wall and the export is too long, the area beside the door is big enough to form congestion again after people bypass the shunt wall. Figures 11 and 13 show that, with the increase of the distance between export and shunt wall, evacuation time reduces slightly, because with shunt wall being far away from the export, the extension distance ΔL becomes longer and it is

TABLE 3: Set parameters of shunt wall.

Case	(1)	(2)	(3)	(4)	(5)	(6)	(7)	(8)	(9)	(10)
ρ (p/m^2)	0.15	0.15	0.15	0.15	0.15	0.2	0.2	0.2	0.2	0.2
D	0	0.5	0.75	0.5	0.75	0	0.5	0.75	0.5	0.75
L	0	1.5	1.5	2	2	0	1.5	1.5	2	2

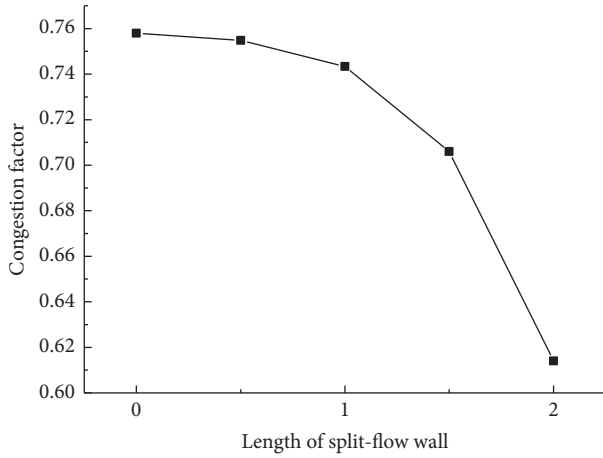


FIGURE 9: Congestion factor when $D = 0.5, \rho = 0.5$.

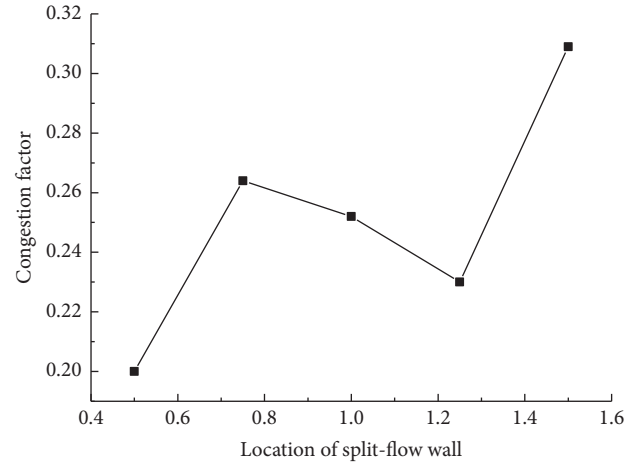


FIGURE 11: Congestion factor when $L = 1.5, \rho = 0.3$.

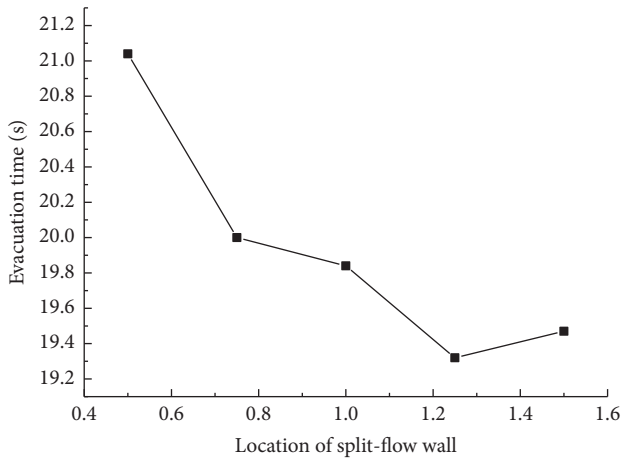


FIGURE 10: Evacuation time when $L = 1.5, \rho = 0.3$.

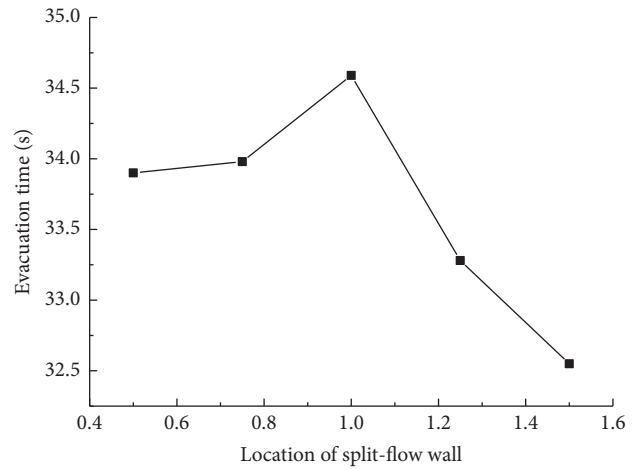


FIGURE 12: Evacuation time when $L = 2, \rho = 0.5$.

more easy to walk out of the building. But evacuation time is longer than the case without shunt wall; when the crowd density is $0.3 \text{ p}/\text{m}^2$, evacuation time grows by 8.6%; when crowd density is $0.5 \text{ p}/\text{m}^2$, evacuation time grows by 4.6%. The reason is that, when there is a shunt wall, the evacuation distance becomes longer than that of the case without shunt wall. But the increase evacuation time due to shunt wall has little effect on evacuation. According to η and T , the best location of the shunt wall is 0.5–0.75.

Figures 14 and 15 are the evacuation time when the density of the crowd is $0.15 \text{ p}/\text{m}^2$ and $0.2 \text{ p}/\text{m}^2$, respectively; the information of the shunt wall is shown in Table 3. As the figure shows, evacuation time is longer than that when there is no shunt wall. The values of evacuation time increasing due to

shunt wall are 3 s and 2 s when the crowd density is $0.15 \text{ p}/\text{m}^2$ and $2 \text{ p}/\text{m}^2$, respectively.

When the crowd density is $0.15 \text{ p}/\text{m}^2$, the value of congestion factor is 0 in any case shown in Table 3. When the crowd density is $0.2 \text{ p}/\text{m}^2$, the value of η is 0.27 with no shunt wall and 0.098 with shunt wall length of 1.5, position of shunt wall is 0.5, and η of another case is 0. It can be seen that the evacuation time of the low-density crowd increases, but it will not affect the safety of the evacuation because the evacuation time of the low density of population is short. In a word, the increasing of evacuation time due to shunt wall will not affect the safe evacuation; at the same time, shunt wall can effectively relieve congestion.

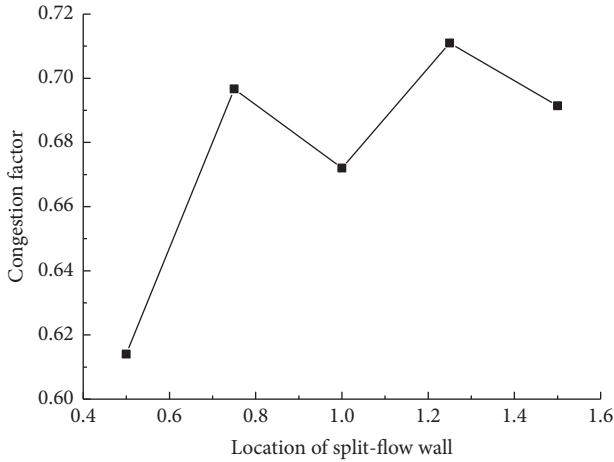


FIGURE 13: Congestion factor when $L = 2$, $\rho = 0.5$.

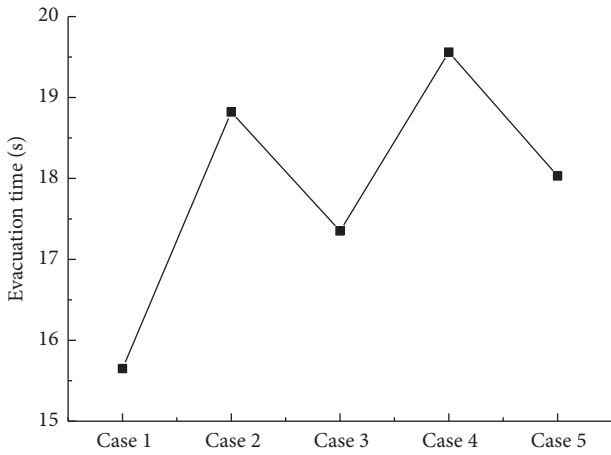


FIGURE 14: Evacuation time when $D = 2$, $L = 1.5$.

Above all, the best length of shunt wall is 1.5 to 2 times as long as the export, and the best set position is 0.5 to 0.75 times the export width far away from the exit. Shunt wall can effectively alleviate and even eliminate the congestion in the process of evacuation.

5. Conclusions and Suggestions

5.1. Conclusions. According to the statement of the simulation results, we can get the following conclusions:

(1) Shunt wall plays a significant role in alleviating the congestion, especially when the density of population is lower than 0.5 p/m^2 .

(2) The best length of shunt wall is 1.5 to 2 times as long as the export, and the best set position is 0.5 to 0.75 times the export width far away from the exit.

(3) Setting the shunt wall with relatively high-density crowd evacuation process can effectively alleviate the evacuation congestion; when the crowd density is low, shunt wall will not affect the safety evacuation.

5.2. Suggestions. It is important to ensure that the people evacuate out of the building in emergency, information of

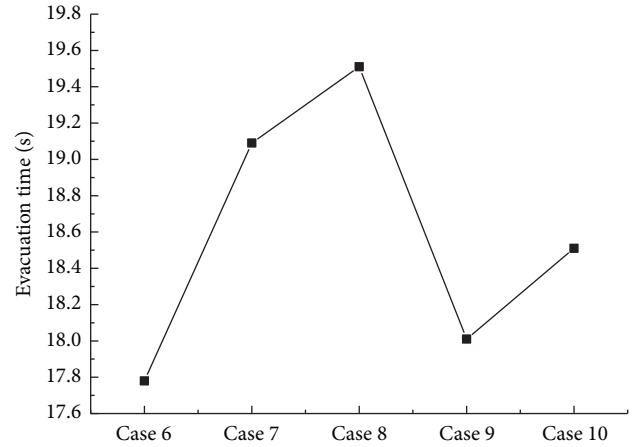


FIGURE 15: Evacuation time when $D = 2$, $L = 1.5$.

pedestrian about evacuation routes plays an important role in the evacuation, and the effect of the obstacles before export has been recognised by many researchers. Shunt wall with reasonable set parameters can improve the safety of the evacuation and improve the efficiency of evacuation effectively. But shunt wall in front of the export keeps the door out of the sight of people to a certain extent; therefore, shunt wall should be used combined with evacuation marks to achieve good effect of evacuation. In addition, there are two cases where the length of shunt wall is more than 2 times as long as the export width and the distance between the shunt wall and export is less than 0.5 times as far as the export width is not involved in this article; the main reason is that it is unrealistic in the practical buildings when the shunt wall is too long, and it is equal to the set obstacles among exports, indirectly reducing the export width, when the distance between shunt wall and export is less than 0.5 times the width and goes against the starting point of setting shunt wall to improve the evacuation safety and efficiency.

Symbols

ΔT : Delay time caused by shunt wall

t : Crowded time

ΔL : Extension distance due to the shunt wall

V : Walking speed of evacuees

T : Time from the beginning of the evacuation to the last trapped person leaving the building

η : Dimensionless quantity, crowded degree of evacuation bottleneck with the most serious congestion throughout the evacuation area, expressed by a percentage of the evacuation time being in crowded station

D : Dimensionless quantity, the position of the shunt wall which is the distance between the export and the shunt wall, expressed by the ratio of the distance and width of export

L : Dimensionless quantity, the length of the shunt wall, expressed by the ratio of the actual length of the shunt wall and width of export.

Conflicts of Interest

The authors declare that they have no conflicts of interest.

References

- [1] T. Kretz, A. Grünebohm, and M. Schreckenberg, "Experimental study of pedestrian flow through a bottleneck," *Journal of Statistical Mechanics: Theory and Experiment*, article 10014, 2006.
- [2] D. Helbing, Farkas I, and P. Molnar, "Simulation of pedestrian crowds in normal and evacuation situations," *Pedestrian and Evacuation Dynamics*, 2002.
- [3] D. Yanagisawa, A. Kimura, A. Tomoeda et al., "Introduction of frictional and turning function for pedestrian outflow with an obstacle," *Physical Review E*, vol. 80, no. 3, 2009.
- [4] A. Kirchner, K. Nishinari, and A. Schadschneider, "Friction effects and clogging in a cellular automaton model for pedestrian dynamics," *Physical Review E*, vol. 67, no. 5, 2003.
- [5] T. Huili, "A study on an improved N-S traffic flow model with partitive open boundary conditions," *Journal of Guangxi Normal University*, vol. 21, no. 2, 2003.
- [6] T. Chen, W. G. Song, W. C. Fan, and S. X. Lu, "The dependence of cross outlet width on personnel obstruction and its simulation and analysis," *Advances in Natural Science*, vol. 4, 2004.
- [7] W. Jinjing, *Research of Shunt Wall Set Optimizationbased on Safety Evacuation*, Beijing University of Chemical Technology, Beijing, China, 2012.
- [8] J. Ji, Z. Wang, K. Wang, Y. Wang, and Y. Meng, "An investigation of effects on evacuation capacity of fire-protection evacuation walk caused by internal and external door width," *Journal of Shenyang Jianzhu University (Natural Science)*, vol. 29, no. 4, pp. 698–702, 2013.
- [9] Z. Qingsong, *Study of Crowd Crushing and Trampling Accident Risk Theory and Applied to Stadium*, Nankai University, Tianjin, China, 2007.
- [10] J. Fruin, *Pedestrian Planning and Design*, Metropolitan Association of Urban Designers and Environmental Planners, New York, NY, USA, 1971.
- [11] V. M. Predtechenskii and A. I. Milinskii, *Planning For Foot Traffic Flow In Buildings, Published For The National Bureau of Standards, Amerind Publishing Co. 1978, Translated From The Russian Publication Which Appeared in 1969*, STROIZDAT Publishers, Moscow, Russia, 1969.
- [12] Z. Jianing, "Investigation and analysis of consumerflow rate in a large supermarket," *HVAC & AC*, vol. 34, pp. 53–55, 2004 (Chinese).
- [13] Y. Yuhang, "Preliminary investigation of Large supermarket personnel density," *Fire Science and Technology*, vol. 26, pp. 360–362, 2007.
- [14] D. Baoling, "Investigation and analysis of shopping malls personnel density," *Journal of Chinese Peoplesarmed Police Force Academy*, vol. 24, pp. 41–45, 2008.
- [15] L. Yong, "Investigation and analysis on personnel density in commercial complex," *Journal of Safety Science and Technology*, vol. 11, pp. 175–180, 2015.